eman ta zabal zazu

Universidad del País Vasco

Euskal Herriko Unibertsitatea

Atomistic Simulation studies of the Cement Paste Components

PhD Thesis by

Hegoi Manzano

2009

Directed by:

Dr. Jorge Sánchez Dolado

Dr. Andrés Ayuela

Dr. Fernando López Arbeloa

labein tecnalia

CENTRO DE APLICACIONES DE NANOMATERIALES EN CONSTRUCCION NANOC®

ISBN: 978-84-9860-661-4

Universidad del País Vasco Euskal Herriko Unibertsitatea

AUTORIZACION DEL/LA DIRECTOR/A DE TESIS

PARA SU PRESENTACION

Los Drs. **Jorge Sánchez Dolado**, con N.I.F. 29031543-T **Andrés Ayuela**, con N.I.F. 12748889-N y **Fernando López Arbeloa**, con N.I.F 14884371-J como Directores/as de la Tesis Doctoral: **Atomistic Simulation Studies of the Cement Paste Components,** realizada en el Departamento **Química Física, Facultad de Ciencia y Tecnología de la UPV/EHU** por el Doctorando Don **Hegoi Manzano Moro**, autorizan la presentación de la citada Tesis Doctoral, dado que reúne las condiciones necesarias para su defensa.

En Leioa a 15 de Julio de 2009

LOS DIRECTORES DE LA TESIS

Fdo.: Jorge Sánchez Dolado Fdo.: Andrés Ayuela Fdo.: Fernando López Arbeloa

Universidad del País Vasco Euskal Herriko Unibertsitatea

CONFORMIDAD DEL DEPARTAMENTO

El Consejo del Departamento de Química Física de la Facultad de Ciencia e Ingeniería de la Universidad del País Vasco UPV/EHU en reunión celebrada el día **9 de julio de 2009** ha acordado dar la conformidad a la admisión a trámite de presentación de la Tesis Doctoral titulada: **Atomistic Simulation Studies of the Cement Paste Componentes** dirigida por los Drs. **Jorge Sánchez Dolado, Andrés Ayuela Fernández y Fernando López Arbeloa** y presentada por Don **Hegoi Manzano Moro** ante este Departamento.

En **Leioa a 15 de Julio de 2009**

Vº Bº DIRECTOR DEL DEPARTAMENTO SECRETARIO DEL DEPARTAMENTO

Fdo.: Luís Manuel León Isidro Fdo.: José Luís Vilas Vilela

Universidad del País Vasco Euskal Herriko Unibertsitatea

ACTA DE GRADO DE DOCTOR

ACTA DE DEFENSA DE TESIS DOCTORAL

DOCTORANDO DON **Hegoi Manzano Moro**

TITULO DE LA TESIS: **Atomistic Simulation Studies of the Cement Paste Components**

El Tribunal designado por la Subcomisión de Doctorado de la UPV/EHU para calificar la Tesis Doctoral arriba indicada y reunido en el día de la fecha, una vez efectuada la defensa por el doctorando y contestadas las objeciones y/o sugerencias que se le han formulado, ha otorgado por_____la calificación de:

unanimidad ó mayoría

En **Leioa** a **8** de **Octubre** de **2009**

EL/LA PRESIDENTE/A, EL/LA SECRETARIO/A,

Fdo.: Fdo.:

Dr/a: Dr/a:

VOCAL 1º, VOCAL 2º, VOCAL 3º,

Fdo.: Fdo.: Fdo.:

Dr/a: Dr/a: Dr/a:

EL/LA DOCTORANDO,
Fdo.:

I believe that the scientific knowledge has fractal properties.
It doesn't matter how much do we learn; the remaining,
for small that could seem, is so infinitely complex as the whole
from which we depart. That one, I believe, is the secret of the universe.

- Isaac Asimov

Acknowledgements

Probably, the acknowledgements will be the part of the Thesis that most people will read. Thus, I was thinking to include the most important conclusions here, to asses that everybody would pass through them. Finally, I recognize that in such case people would close this document immediately. It was better try to write something informal, and that way motivate the reader to keep passing leafs. I guess that everything will be in vain...

Primeramente me gustaría dar las gracias a mis padres, Julián y Rosana. Ellos me dieron una educación más importante que el Colegio o la Universidad. Animaron mi curiosidad y me han ayudado en todo lo que he necesitado para intentar ser un científico. Sin ellos, ahora no estaría escribiendo estas líneas. Tengo que mencionar también su financiación económica durante 24 años. ¡Eso sí es una beca! También quiero dar las gracias a mi hermano Beñat por los buenos ratos y partidas de "play" que nos hemos echado (si es que estabas fuera del agua). Muchas gracias a los tres.

I met Monika almost eight years ago and she still stands me, which is a great merit! She is the person who has followed closer this Thesis, and has helped me a lot during these years, probably more than she thinks. She stands my worse moments, and *simulates* attention to my endless science ramblings. Thank you *cosa*, I love you.

I started with my PhD studies at Labein in October 2005. My first weeks there were quite hard. I spend my time reading incomprehensible articles (some of them still cryptic after 4 years), trying to learn something about cement and simulation methods. Be the only student involved in theoretical stuff implies that you spend many time alone when the others are at the laboratory. However, the members of NANOC were very nice and make me fell comfortable after few coffee breaks. Antonio Porro, Igor Campillo, Jose Antonio Ibañez, Maria Moragues, Yolanda de Miguel, Edurne Erkizia, Jorge S. Dolado, Jontxu Gaitero Yolanda Saez, Ainara Montero, Raquel Vega and Eneritz Belasko were the group members at that time. Thanks to all of them for their welcome. Most of them are still in the group, some of them have gone, and new people arrived. I

think that Gorka Pascuas, Amaia Albizu, Idurre Kaltzakorta, Irune Villaluenga, Eunate Goiti, Quim Tenas, Gemma Berriozabal, Ana Torres, Izaskun Villarias, Carlos Saéz and Raquel Gónzalez complete the list of people that have work with me in NANOC during these four years. I would like to thank all of them the nice moments we have spent, especially during the coffees (with the cookies, omelettes and “mildreds”) and the meals in the canteen. Extra thanks to Jontxu, for bringing my meal tray when I broke my leg (he took his revenge making me suffering in the mountain), and to Idurre, for stand many stupid jokes. I would like also to encourage *moleculita*, the last incorporation to the simulation field, to keep on with the nanoscience: just some coffees to gain strength and easy.

All the people in NANOC and Labein have been nice and kind with me, but a complete list would increase the printing costs. However, I must mention a group of people with a great importance: the football mates. Cobelo, Mendikoa, Eneko, Carlos, Jose Antonio, Borja, Iñaki, Quim, Jorge, Carlos, and Txutxo, I will miss our matches.

During the Thesis, I have spend three months in German Universities, first in the group of Professor Dr. Michael Griebel at the Institut für Numerische Simulation of the University of Bonn, and second in the group of Professor Dr. Gotthard Seifert at the Arbeitsgruppe für Theoretische Chemie of the Dresden University of Technology. Both groups received me warmly and made my days far from home (and from the Spanish food) more bearable. Thanks are due to Prof. Griebel, Jan Hamaekers and Frederik Herber from Bonn University, and Prof. Seifert, Andrey Enyashin, Augusto Oliveira, Sergei Yurchenko, Igor Popov and Bassem Assfour from Dresden University.

Probably the people I have to thank more are my PhD advisors Dr. Jorge Sánchez Dolado, Dr. Andrés Ayuela and Prof. Fernando Lopez Arbeloa. They have guided me during these years with dedication. At the same time they have let me to drawn my own conclusions and encouraging me to have a critic vision of science. Furthermore, the have instilled me also some values that are necessary in science but often forgotten.

I would like to thank to Fernando the opportunity he gave me to start my career as

researcher in his group, and the nice year I spent there as undergraduate student.

My first meetings with Andrés in San Sebastian were exhausting. He tried to teach me the fundaments of solid state physics and some UNIX notions. I was frightened because I couldn't understand a single word. However, he was patient and finally managed to put something in my head. Thank you Andrés for all the useful advices you have given me. I will remember with special affection our weekend as tourist in Dresden and the dinners at the Neustadt.

My relationship with Jorge has been closer. He has taught me and advice me in science, and also in other important things beyond it. I know that my future career will be extremely influence by his manners of doing research. I will always remember the nice meals we have had during these years, the moments in front of a beer, (or a patxaran, or a sider, or a wine), and our talks about science, football, films... If I have the opportunity of guide a Thesis in the future, I just hope to do it half as well as he has done it. Thank you very much.

Finally, thank you to all the people that have made this Thesis possible, to all my friends, all the people I have forgotten in these lines, and, last but not least, to you for reading this Thesis.

Hegoi

Table of Contents

Chapter 3: Assembly of C-S-H precursors

Chapter 4: Aluminium Incorporation to the Silicate Chains

Chapter 5: Elastic properties of cement phases

Chapter 6: Tricalcium Aluminate

General Introduction

Cement-based materials, such as mortars or concrete, are usually considered materials with low technological level. Although it is the most employed human made materials in the world, others such as plastics, metals, cotton, wool, wood and even stones are usually more valued in the everyday life. In fact, cement is commonly considered grey paste, with the only characteristic of becoming hard when it dries, which is employed to construct buildings. Probably the fact that cement is cheap, readily available, common, and has been employed successfully for centuries, contributes to its low technology perception.

However, that vision is far from the reality. The cement paste is a complex multi-component and heterogeneous composite, with different structural features at different length scales. The mechanism in which the clinker in contact with water becomes a hardened paste comprises hundreds of chemical reactions and physical processes. The major component of the cement paste, the C-S-H gel, is an amorphous phase with intrinsic porosity. Furthermore, its nanostructure is still undetermined. Interestingly, the C-S-H gel presents clear resemblances with other high-technological systems. For example, its nanostructure is usually described in terms of the natural tobermorite and jennite minerals. These minerals present a layered structure similar to that of the montmorillonite-smectite clays, which are employed with catalytic purposes, taking part of nano- and bio-composites, as adsorbents hazardous wastes, etc. The morphology at the microscale of the C-S-H gel also resembles that of hydroxyapatite, the main

component of the bones. Such similarities arise from their analogous composition: calcium silicate hydrate (C-S-H) in the cement matrix and calcium phosphate hydrate (C-P-H) in hydroxyapatite. In fact, both the C-S-H gel and hydroxyapatite suffer a process of decalcification, known as calcium leaching in cement and osteoporosis in bones. But there are more analogies with biological systems. The location and role of water in the C-S-H gel is similar to that in crystalline proteins. Water molecules can be at different positions, bonded with different strengths, acting as a structural part or as a pore solution, etc. These few examples are given to illustrate that the interest of the C-S-H gel structure and properties are comparable to those of other materials.

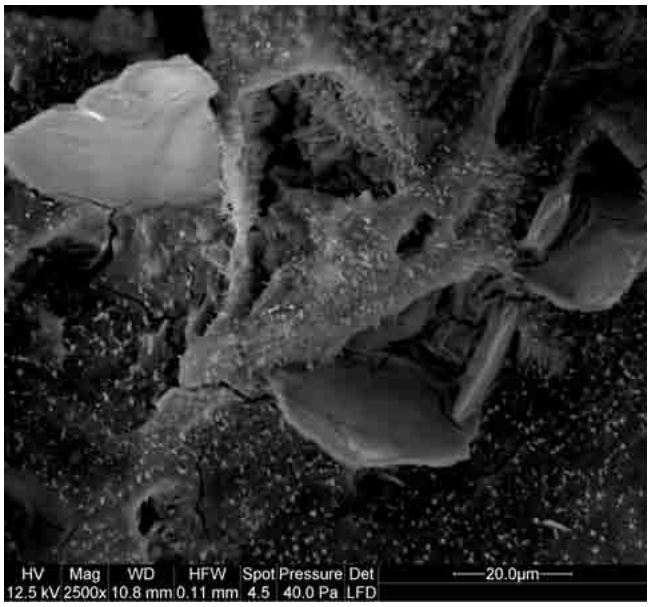

Figure 1.- SEM image of the microstructure of an ordinary Portland cement paste, courtesy of Dr. J. J. Gaitero from the Centre for Nanomaterials Applications in Construction (**NANOC**) at Labein-Tecnalia.

Cement research covers many different aspects, from reduction of green-house gases during the manufacture process, to the investigation of the material nanostructure, including the development of new cements employing wastes as raw materials, or the modification and improvement of ordinary Portland cement properties. Due to its heterogeneous nature, the cement paste is a multi-scalar material. It presents different characteristics at the nano-, micro-, and macro-scales, and its behaviour at those scales is far from being the same. Furthermore, cement research is a multidisciplinary field

where engineers, chemists, physics and geologists are involved. Such cooperative environment, as well as the multi-scale nature of the problems under study, implies that numerous techniques have been applied in cement research. The evolution of the experimental techniques in recent years has allowed us to study the cement paste at lower scales, opening the field of nanotechnology in cement materials.

In this respect, atomistic modelling has demonstrated to be an indispensable numerical instrument in nanotechnology. It allows us to study the nanoscale of a material or molecule with detail. However, the atomistic simulations methods have been used scarcely to investigate cement related problems. The same complexity that makes difficult the experimental investigations of the cement materials at the nanoscale, i.e. its amorphous and heterogeneous nature, is a problem in atomistic simulation, as the exact position of the atoms are needed as the input for the calculations. The increasing computational capabilities and the development of new approaches and methods solved partially those problems. In this Thesis, atomistic simulation methods are adopted to study several aspects of the cement paste components, such as their elastic properties, their reactivity, their structure, and their formation, with special attention focused on the C-S-H gel.

- ***Thesis Outline***

Chapter 1 is an introduction to the cement chemistry and the necessary basis in order to follow the results and discussions presented in this Thesis. It covers a description of the clinker phases, the hydration processes, the cement paste structure, and the hydration products. Special attention has been paid to the C-S-H gel, as it is the main cement paste component.

A brief overview of the atomistic simulation methods is given in ***chapter 2***. During the Thesis, several levels of theory were selected depending on their capabilities to solve punctual problems: *ab-initio*, Molecular Mechanics, and Molecular Dynamics. A discussion of their advantajes and disadvantajes is also given in this chapter.

The formation mechanisms of a C-S-H gel nanoparticle are studied in ***chapter 3*** by *ab-initio* methods. The atomic structure of these particles has not been yet determined. However, they are believed to play a key role in the properties on the cement paste, as they control the material cohesion. Here, a C-S-H precursor is suggested from the structural models of tobermorite and jennite. Then, the aggregation of those precursors to form bigger particles is analyzed depending on the calcium amount between them.

Chapter 4 is devoted to study the incorporation of aluminium to the C-S-H gel silicate chains. Aluminium is the most important guest ion that enters in the structure of the C-S-H gel. It is known to affect the silicate chain structure, and is expected to modify the C-S-H gel solubility, degradation, and elastic properties. A combination of *ab-initio* and Molecular Dynamics methods was used to study the position of aluminium within the chains and the substitution effect on the chain structure.

Chapter 5 is focused on the elastic properties of the most important cement paste components. The mechanical performance is the most relevant characteristic of the cement-based materials due to their use in construction. In this chapter, the elastic properties of the main clinker phases and hydration products are calculated by Molecular Mechanics methods. The relationship between the elastic properties and silicate chain structure, porosity, density, and water content of the C-S-H gel is also discussed.

Chapter 6 deals with the structure, elastic properties, and reactivity of tricalcium aluminate. The high reactivity of the tricalcium aluminate with water is interesting, since it is responsible of the *flash-setting*. The flash-setting is not desired because reduces the final mechanical performance of the cement paste, and retardants such as gypsum are added to the clinker. By means of *ab-initio* methods, the bulk electronic structure of tricalcium aluminate is investigated, and the differences in its reactivity when sulphate ions are added to the cement clinker are discussed.

Introducción General

El cemento y sus derivados, como los mortero o el hormigón, son generalmente considerados materiales de bajo nivel tecnológico. A pesar de ser el material manufacturado más empleado en el mundo, otros como los plásticos, los metales, el algodón, la lana, la madera e incluso las piedras, se valoran más en el día a día. De hecho, el cemento es comúnmente considerado como una pasta gris, con la única característica de endurecerse cuando se seca, y que se empleada para construir edificios. Probablemente, el hecho de que sea barato, disponible, común y haya sido empleado satisfactoriamente durante siglos, contribuye a su percepción como material de bajo perfíl tecnológico.

Sin embargo, esa visión se aleja de la realidad. La pasta de cemento es un compuesto complejo y heterogéneo, con diferentes características a diferentes escalas de tamaño. El mecanismo por el cual el clínker al entrar en contacto con el agua se convierte en una pasta endurecida incluye cientos de reacciones químicas y procesos físicos. El componente principal de la pasta de cemento, el gel C-S-H, es una fase amorfa con una determinada porosidad intrínseca, y su nanoestructura aún se desconoce. Curiosamente, el gel C-S-H presenta claras similitudes con otros sistemas de interés tecnológico. Por ejemplo, la estructura del gel es habitualmente descrita en términos de minerales naturales tobermorita y jennita. Estos minerales presentan una estructura laminar similar al de las arcillas montmorillonita-esmectita, que son utilizadas con objetivos catalíticos, como parte de los nano- y bio-composites, o como absorbentes de residuos

contaminantes. La morfología del gel C-S-H en la microescala se parece también a la de la hidroxiapatita, que es el principal componente de los huesos. Tal semejanza proviene de su composición análoga: silicato-calcico-hidratado (C-S-H) en la matriz de cemento, y fosfato-calcico-hidratado (C-P-H) en hidroxiapatita. De hecho, tanto el gel C-S-H como la hidroxiapatita sufren un proceso de descalcificación, conocida como lixiviación de calcio en el cemento y osteoporosis en los huesos. Pero hay analogías adicionales con otros sistemas biológicos. La posición y el papel del agua en el gel C-S-H y en ciertas proteínas cristalinas son similares. Las moléculas de agua pueden estar en diferentes posiciones y asociadas con fuerzas diferentes, actuando como una parte estructural o como una solución en los poros. Estos ejemplos ilustran porque el interés de la estructura y las propiedades del gel C-S-H son comparables a los de otros materiales.

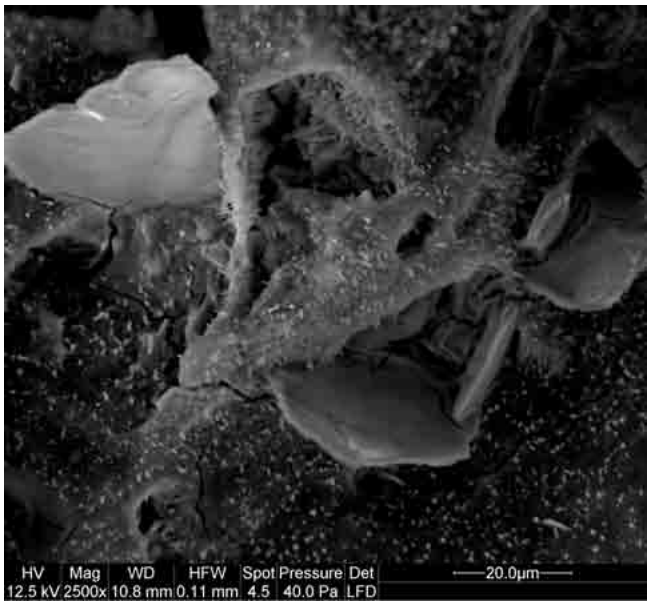

Figura 2.- Imagen SEM de la microestructura de la pasta de cemento Portland común, cortesía del Dr. J. J. Gaitero del Centro de aplicaciones de Nanomateriales en Construcción (**NANOC**) de Labein-Tecnalia.

La investigación en cemento incluye muchos aspectos diferentes, desde la reducción de los gases de efecto invernadero emitidos durante el proceso de fabricación, a la investigación de la nanoestructura del material, incluyendo el desarrollo de nuevos

cementos que utilizan desechos como materias primas, o la modificación y mejora de las propiedades del cemento Portland ordinario. Debido a su naturaleza heterogénea, la pasta de cemento es un material multiescalar. El cemento presenta diferentes rasgos y características a escalas nano-, micro- y macro-, y su comportamiento en dichas escalas dista de ser el mismo, Además, la investigación del cemento es un campo multidisciplinar en el que están implicados ingenieros, químicos, físicos y geólogos. Ese ambiente cooperativo, así como la naturaleza de multiescalar de los problemas a estudiar, implican el uso de numerosas técnicas experimentales en la investigación del material. La evolución de las técnicas experimentales en los últimos años nos permite estudiar la pasta de cemento a escalas cada vez más pequeñas, con la apertura al cemento de un campo como la nanotecnología.

En nanotecnología, los métodos de simulación atomística han demostrado ser un instrumento numérico indispensable. Estos métodos nos permiten estudiar la nanoescala de un material o molécula con gran detalle. Sin embargo, los métodos de simulación atomística apenas se han aplicado en la investigación de aspectos relacionados con el cemento. La misma complejidad que dificulta las investigaciones experimentales de los materiales en base cemento en la nanoescala, como su naturaleza amorfa y heterogénea, es un problema en la simulación atomística, ya que la posición exacta de los átomos es información necesaria para los cálculos. No obstante este problema ha sido parcialmente solucionado por el incremento de la capacidad computacional y el desarrollo de nuevas técnicas y métodos de cálculo. En esta Tesis, se han empleado métodos de simulación atomísticos para estudiar diversos aspectos de los componentes de pasta de cemento, como son sus propiedades elásticas, reactividad, estructura y formación, prestando una atención especial al gel C-S-H.

- ***Contenido de la Tesis***

El ***Capítulo 1*** es una introducción a la química del cemento, donde se dan las bases necesarias para seguir los resultados y discusiones presentados en esta Tesis. Incluye una descripción de las fases del clínker, los procesos de hidratación, la estructura de la pasta de cemento y los productos de hidratación. Se ha prestado una atención especial al

gel C-S-H, ya que es el pricipal componente de la pasta de cemento.

En el ***Capítulo 2*** se incluye una breve descripción de los métodos de simulación atomística. Durante la Tesis, se emplearon varios niveles de teoría en función de sus características para resolver el problema a estudiar: *ab-initio*, Mecánica Molecular y Dinámica Molecular. En este capítulo también se incluye una discusión sobre sus ventajas y desventajas.

Los mecanismos de formación de las nanopartículas del gel C-S-H son estudiados en el ***Capítulo 3*** mediante métodos *ab-initio*. La estructura atómica de estas partículas no ha sido determinada. Sin embargo, se cree que juegan un papel clave en las propiedades de la pasta de cemento y que controlan la cohesión del material. En este capítulo se propone un precursor del gel C-S-H a partir de los modelos tobermorita y jennita. Posteriormente, se analizan los mcanismos de agregación de dichos precursores para formar partículas mayores en función de la cantidad de calcio presente.

El ***Capítulo 4*** está dedicado a la incorporación del aluminio en las cadenas de silicatos dentro del gel C-S-H. El aluminio es el ión más importante que se incorpora en la estructura del gel C-S-H. Se sabe que esta incoporación afecta a la estructura de las cadenas de silicato, y se espera que modifique la solubilidad, la degradación y las propiedades elásticas del gel C-S-H. Se ha empleado una combinación de métodos *ab-initio* y de Dinámica Molecular para estudiar la posición del aluminio dentro de las cadenas y el efecto de la sustitución sobre su estructura.

El ***Capítulo 5*** se centra en las propiedades elásticas de los componentes más importante de la pasta de cemento. El comportamiento mecánico es la característica más relevante de los materiales en base cemento debido a su empleo en la construcción. En este capítulo, se han calculado las propiedades elásticas para las fases del clínker y los productos de hidratación mediante métodos de Mecánica Molecular. Se ha estudiado también la relación entre las propiedades elásticas y la estructura de la cadena de silicatos, la porosidad, la densidad y el contenido del agua del gel C-S-H.

El ***capítulo 6*** se ocupa de la estructura, las propiedades elásticas y la reactividad del aluminato tricálcico. La alta reactividad del aluminato tricálcico con agua es de gran interés tecnológico, ya que es responsable del *flash-setting*. El *flash-setting* es un proceso no deseado, ya que disminuye las propiedades mecánicas de la pasta de cemento. Para retardar este proceso se añaden aditivos como el yeso al clinker. Mediante métodos ab-initio, se ha investigado la estructura electrónica del aluminato tricalcico, y se han discutido las diferencias en la reactividad en presencia de iones sufato del yeso.

Cement chemistry Notation

Along this work, cement notation has been preferentially used; however, in some cases, it has had to be combined with chemical notation. It will be evident to distinguish between them attend to the context.

C = CaO	H = H_2O	$\hat{S}$ = SO_3	F = Fe_2O_3
S = SiO_2	M = MgO	K = K_2O	
A = Al_2O_3	N = Na_2O	P = P_2O_5	

- ***Some common abbreviations in cement research employed in this work:***

C-S-H: Calcium Silicate Hydrate. The dashes indicate a variable stoichiometry.
CSH: Crystalline Calcium Silicate Hydrates family of compounds
LD- C-S-H: Low Density C-S-H gel
HD- C-S-H: High Density C-S-H gel
OPC: Ordinary Portland Cement
w/c: Water to Cement ratio
C/S: CaO to SiO_2 ratio
AFm: family of crystals with the general stoichiometry Al_2O_3-Fe_2O_3-monosulpho
Aft: family of crystals with the general stoichiometry Al_2O_3-Fe_2O_3-trisulpho

- ***Other acronyms in this thesis:***

DFT: Density Functional Theory

HF: Hartree-Fock

MD: Molecular Dynamics

MM: Molecular Mechanics

K: Bulk modulus

G: Shear modulus

E: Young modulus

v: Poisson's ratio

Chapter 1:

Introduction to Cement Chemistry

1.1. Introduction to cement-based materials

The general meaning of the word “cement” is binder, any substance capable to stick things together. However, the term cement is normally used to designate the construction material. Nowadays, cement is the most employed material by the humankind, just after water. Furthermore, it is one of most ancient ones. Its origin dates back to the Egyptian civilization, which employed a mortar made of gypsum in their buildings. The Romans went a step further, inventing the first hydraulic cement by mixing lime with fly ashes from the Vesuvius. Most of the Roman knowledge was lost during the dark days of the Middle Age, going back to the use of badly mixed mortars and poorly burnt lime. The beginning of cements modern history started in 1754, when John Smeaton rediscovered the material in order to repair the Eddystone lighthouse (England) in a durable manner. Other key event in cement-based materials development was the patent of Portland cement in 1824 by Joseph Aspdin. Aspdin fixed a

predetermined combination of limestone and clay, as well as a studied manufacturing process, very similar to the one used currently [1].

Today cement-based materials are by far the leaders in the construction sector, in terms of both investments and production volume. Just as example, the overall production during 2007 in the world reached 2770 millions of metric Tons, see ***figure 1.1.1(a)***. The economic impact of cement industry is in general positive, especially for developing countries. Half of the world production corresponds to China, with Brazil, India, Indonesia and Thailand as other important producers [2]. However, the environmental impact is in his turn considerable. The cement industry is responsible for approximately 5% of global anthropogenic carbon dioxide emissions. Half of the emissions arise from the decarbonation of raw materials, 40% from the burning process, and the rest correspond to other aspects such as transport. The overall rate of emissions is nearly 900 kg of CO_2 for every 1000 kg of cement [3].

Due to the economical and environmental magnitude of cement industry, there is an increasing interest in both basic and applied research of cement-based materials. The

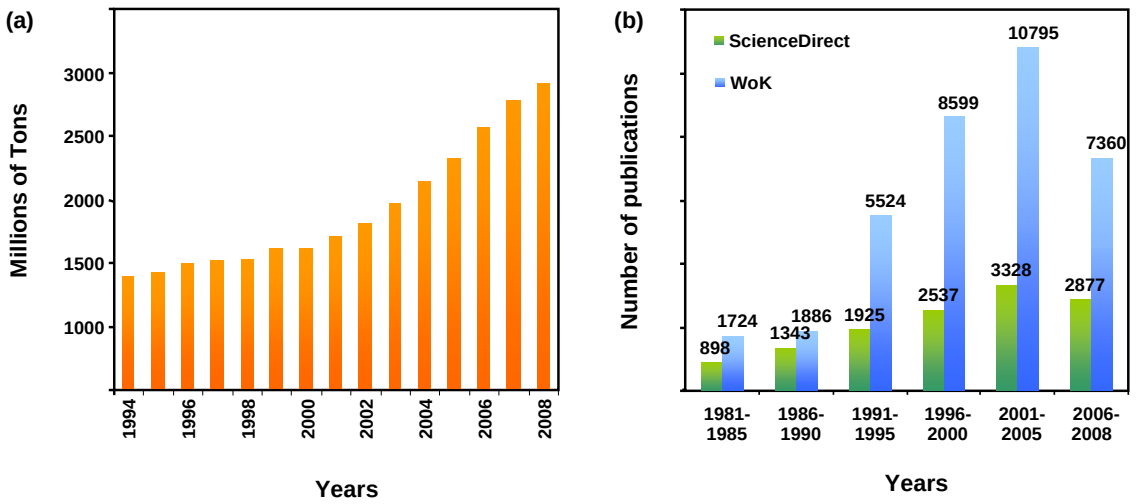

Figure 1.1.1 (a) The world production of cement since 1994 to 2008 is displayed (2008 data are an estimation [2]). **(b)** Evolution in the number of cement-related papers published in scientific journals since 1981 up to these days. The results were obtained searching the word "cement" in titles, keywords and abstracts employing ScienceDirect and The web of Knowledge (WoK) as search engines.

evolution in the number of cement-related papers published in scientific journals since 1981 up to these days is shown in ***figure 1.1.1(b)***. Despite its ubiquity and the daily uses, and contrary to most people belief, cement is a very complex and still not fully understood material. Cement research is a multidisciplinary field where many aspects are under study, covering from the intrinsic nature and properties of the material, to the manufacture and performance of the manufacturing product, and going through the improvement of its characteristics or development of innovative cements.

There are many different types of cements. The first classification could be done by looking if they need water to set, hydraulic cements, or not, non-hydraulic cements. The first group is the one employed in construction, due to its better performance. Some examples of hydraulic cements are Portland, pozzolan-lime, calcium sulphoaluminate and geopolymeric cements [1]. Among them, the Portland cement and its derivates are the most common ones. *Ordinary Portland Cement* (OPC) clinker is a material composed by two thirds by mass of calcium silicates and one third of aluminium and iron oxides. Different classifications of Portland cement depend on the exact composition and additives employed (Type I, II, II, IV and V), as well as the final compressive strength (32.5 N-R, 42.5 N-R and 52.5 R) [1]. However, the manufacture process can be generalized for all of them as follows. The raw material for Portland cement production is a mixture of limestone and clays. The mixture, with the appropriate proportion of each component, is finely grinded and stirred until a homogeneous and fine powder is obtained. Then, it is introduced in a cement kiln, a slowly rotating and sloped cylinder, where is heated up to temperatures of 1400ºC. At this temperature, the mixture melts and several chemical processes take place: lose of free water, decarbonation, and formation of the clinker. Finally, the clinker nodules are milled to get the desired particle size, and additives such as gypsum are added [1, 4].

In the specialized bibliography, the term cement strictly refers to the clinker including additives. When cement is mixed with water, the correct term to name it is *cement paste* or *cement matrix* if speaking of the pure material, or *mortar* and *concrete* if aggregates are incorporated. The hydration process is a very complex transformation, during which a myriad of chemical reactions take place, and the powder transforms progressively in a

grey paste which sets and hardens. In few words, cement paste can be described as a multiphase matrix, where crystalline agglomerates of different sizes are bound by an amorphous hydration product of variable stoichiometry, the *Calcium Silicate Hydrated* (C-S-H) gel [4]. The crystalline agglomerates could be either hydration products such as portlandite and ettringite, or unreacted clinker grains which persist after the hydration process. The C-S-H gel is the most important hydration product, accounting for the 70% of the cement paste volume, and it is the principal responsible for the cement paste cohesion and properties. It is heterogeneous in morphology and composition, depending on the local environment [5-9]. Hydrated cement pastes have associated a pore structure with different hierarchical levels depending on the size. Macropores (100 μm - 5 mm) are associated to air inclusions during the setting process, capillary pores (10 nm - 5 μm) to empty space shaped during the hydration, and nanopores (<10 nm) are an intrinsic characteristic of the C-S-H gel due to the spatially random packing of its particles [1, 4, 10].

1.2. Clinker phases

Portland cement clinker is the result of the heating process of clays and limestone ($CaCO_3$) up to 1450ºC. As the temperature progressively increases, a series of transformations take place. From 70 to 110ºC free water absorbed in the minerals evaporates. From 400 to 600ºC clays decompose in their basic oxide components, mainly SiO_2, Al_2O_3. In the next step, from 600 to 1100ºC, limestone reacts with silica dioxide to form belite (Ca_2SiO_4), while the excess of $CaCO_3$ decomposes into calcium oxide (CaO) and carbon dioxide (CO_2). Those reactions, altogether with the fuel burning to heat the mixture, are the principal responsible for the carbon dioxide emission during the cement manufacturing. Finally, from 1100 to 1450ºC, partial melting occurs, and belite reacts with calcium oxide to form alite (Ca_3SiO_5). The final composition of a typical Portland cement clinker is given in ***table 2.2.1***. It can be seen that the most abundant oxides are CaO and SiO_2, the main components of the predominant phases, alite (C_3S) and to a minor extend belite (C_2S). Other oxides (Al_2O_3, Fe_2O_3 and MgO) are present in smaller but not negligible quantities, corresponding to

Table 1.2.1.- Distribution of oxide components among phases in a typical Portland cement clinker. Discrepancies in totals arise from rounding [4]

	Na_2O	MgO	Al_2O_3	SiO_2	P_2O_5	SO_3	K_2O	CaO	TiO_2	MnO_3	Fe_2O_3	Total
Alite	0.1	0.7	0.7	16.8	0.1	0.1	0.1	47.7	0.0	0.0	0.5	66.8
Belite	0.0	0.1	0.3	4.1	0.0	0.0	0.1	8.2	0.0	0.0	0.1	12.9
Aluminate	0.1	0.1	2.2	0.3	0.0	0.0	0.0	4.0	0.0	0.0	0.4	7.1
Ferrite	0.0	0.3	2.2	0.4	0.0	0.0	0.0	4.7	0.2	0.1	2.1	10.0
Free lime	0.0	0.0	0.0	0.0	0.0	0.0	0.0	0.9	0.0	0.0	0.0	0.9
Periclase	0.0	0.5	0.0	0.0	0.0	0.0	0.0	0.0	0.0	0.0	0.0	0.5
Sulphates	0.1	0.0	0.0	0.0	0.0	0.9	0.8	0.1	0.0	0.0	0.0	1.9
Total	0.3	1.7	5.4	21.6	0.1	1.0	1.0	65.6	0.2	0.1	3.1	100

mineral phases like tricalcium aluminate (C_3A), and ferrite ($C_2A_xF_{1-x}$ with $0 < x < 0.7$). A general description of these four main phases is given below.

- ***Alite, C_3S***

Alite is the main component of Portland cement, accounting for the 70 %wt. It is the chemically modified form of pure tricalcium silicate (Ca_3SiO_5 or C_3S). Pure C_3S exhibits the following set of reversible phase transitions upon heating [1, 4, 11-14]:

$$T_1 \overset{620^oC}{\leftrightarrow} T_2 \overset{920^oC}{\leftrightarrow} T_3 \overset{980^oC}{\leftrightarrow} M_1 \overset{990^oC}{\leftrightarrow} M_2 \overset{1060^oC}{\leftrightarrow} M_3 \overset{1070^oC}{\leftrightarrow} R$$

The letter indicates the crystal symmetry of the polymorph (T = triclinic, M = monoclinic and R = rhombohedral) and the subscript variants in the structure for a particular symmetry. Although the stable phase at room temperature is the T_1, the incorporation of guest ions in the clinker prevents the polymorphic changes under cooling, and the most common phases are the monoclinic variants. Furthermore, mixtures of monoclinic variants are usually found, even in the same crystal, with a core of M_1 surrounded by a shell of M_3 [15]. Triclinic and rhombohedral structures can be present in some clinkers. The impurities play also a key role stabilizing alite from

decomposing into dicalcium silicate and lime (CaO) at temperatures below 1250ºC. The most common substitutions are those of Mg^{+2} for Ca^{+2}, but $2 \cdot Al^{+3}$ or $2 \cdot Fe^{+3}$ for $Ca^{+2} + Si^{+4}$, and $4 \cdot Al^{+3}$ for $3 \cdot Si^{+4}$ also take place [4].

The crystal structure of the different alite polymorphs is similar, all of them closely related to the R phase [14, 16-19]. The structure consists in SiO_4^{-4} tetrahedra and Ca^{+2} and O^{-2} ions, see ***figure 1.2.1***. The polymorphs differ in the orientation of the SiO_4^{-4} tetrahedra, which affects to the symmetry and the coordination of the Ca and O atoms. Even for a given polymorph, the high disorder in the orientation of those SiO_4^{-4} groups causes also different Ca-O coordination.

- ***Belite, C_2S***

Belite is the second phase of importance in ordinary Portland cement. Similar to alite, belite is a chemically modified form of dicalcium silicate (Ca_2SiO_4 or C_2S), and presents a sequence of reversible polymorphs with the temperature [1, 4, 14, 20]:

$$\gamma \overset{500ºC}{\leftrightarrow} \beta \overset{630\text{-}680ºC}{\leftrightarrow} \alpha_L' \overset{1160ºC}{\leftrightarrow} \alpha_H' \overset{1425ºC}{\leftrightarrow} \alpha$$

The greek letters represent different phases of the structure, and the L and H subscripts denote a low temperature and high temperature variants respectively. The α, α_H', α_L' and β polymorphs have very similar structures, belonging all of them to the family of glaserite, while the γ phase is different and belongs to the family of olivine. The crystal structure of belite is composed by SiO_4^{-4} tetrahedra and Ca^{+2} ions, differing from alite in the absence of O^{-2} ions, see ***figure 1.2.1***. The α_H', α_L' and β polymorphs are derived from the α form by a decrease of the symmetry due to the disorder of SiO_4^{-4} groups and slight changes in the position of Ca atoms [20-23]

Although the γ form is the most stable at room temperature, it is not present in the clinker due to stabilization of other phases by guest ions, as in the alite case. The most important incorporation of guest ions is that of Al and Fe atoms. Furthermore, the

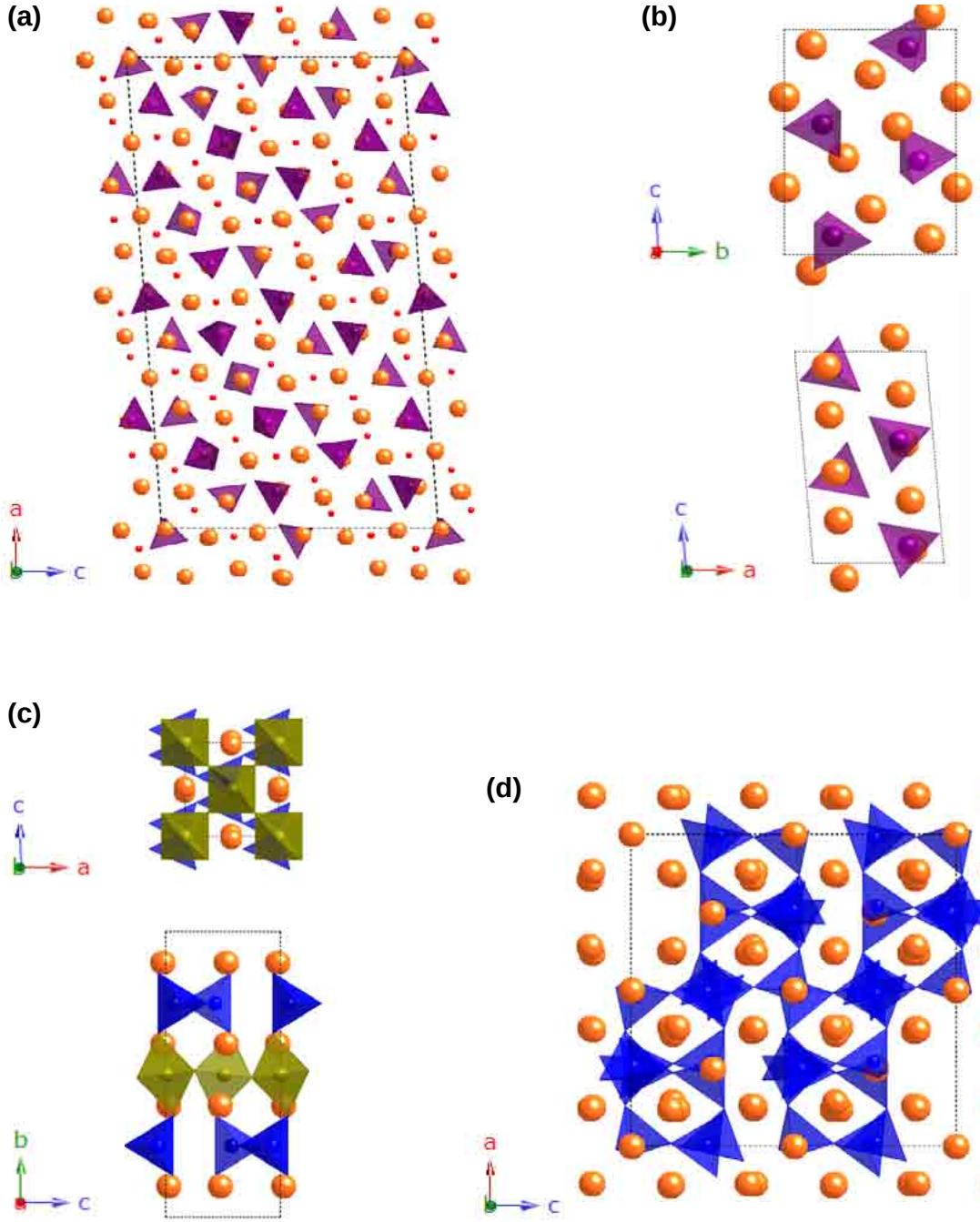

Figure 1.2.1.- Crystalline structure for the main components in the clinker **(a)** tricalcium silicate monoclinic superstructure, **(b)** β dicalcium silicate, **(c)** aluminoferrite with stoichiometry C_4AF (x = 0.5) and **(d)** tricalcium aluminate. The view directions are represented by the lattice vectors in the down left corner of each phase. The unit cell is showed by a dotted line. Ca is represented in orange, silicon in purple, aluminium in blue, iron in green and oxygen in red. Atoms with irregular coordination are shown as balls. Whenever an atom (X) has regular coordination to oxygen, X-O, it is represented as a ball inside the corresponding coordination polyhedron. Oxygen atoms occupy the vertex of the polyhedra, though they are not shown for a clearer view.

transition between the similar polymorphs α, α_H', α_L' and β requires little energy and is completely reversible, while the rearrangement from β to γ is more sluggish. Consequently, when cooling the clinker, the β form persists in metastable equilibrium. This implies an advantage, due to the higher reactivity of the β variant with respect to the γ form. At laboratory conditions, where the cooling can be slow enough, the transformation involves cracking of the β crystals when some zones transform to the γ form. This phenomenon is know as *dusting*, and it is caused by the lower density of the γ polymorph [1, 4].

- ***Tricalcium Aluminate, C_3A***

The third significant component in Portland cement is tricalcium aluminate ($Ca_3Al_2O_6$ or C_3A). Pure tricalcium aluminate has a cubic symmetry and is stable in all the range of temperatures until melting. Its unit cell is composed of $Al_6O_{18}^{-18}$ rings, with their charge counterbalanced by Ca^{+2} ions located in the space between rings, as can be seen in ***figure 1.2.1*** [24-26]. However, the substitution of 2 Na^+ for Ca^{+2} induces a decrease in the symmetry, and orthorhombic and monoclinic polymorphs appear. For Na_2O contents < 2%, the cubic symmetry is kept, and over it the orthorhombic variant persists until ~4.5%. Substitutions of Al^{+3} by Fe^{+3} or Si^{+4} could also take place. The former is the most significant, though it has little effect in the phase transition, still controlled by the amount of Na [27].

In the ordinary Portland cement clinkers at room temperature the cubic and orthorhombic polymorphs appear, alone or in combination, while the monoclinic form has not been detected. The cubic form usually is mixed with dendritic crystals of ferrite phases [4].

- ***Aluminoferrite, C_4AF***

The aluminoferrite phase is a modification of ferrite (C_2F), in which aluminium atoms enter to the structure. The stoichiometry of the solid solution is $Ca_2(Al_{(1-x)}Fe_x)_2O_5$ or

$C_2A_{(1-x)}F_x$ in cement chemistry notation. At room temperature and pressure, the composition of the solid solution can vary from x = 1 to ~0.3, although x = 0 can be achieved at high pressure [28]. In the unit cell of pure C_2F, there are two different positions occupied by iron ions, one with tetrahedral coordination and the other one with octahedral coordination, being the number of the latter twice the number of the former. Aluminium has a preference for the tetrahedral sites, which are completely occupied for x ~0.67. When the aluminium substitution starts to take place in the octahedral sites, both the unit cell parameters and the symmetry change [1, 4].

For composition in the range x = 0.3 - 0.7, the structure is similar to that of perovskite, Ca_2TiO_3 [29]. It is composed of layers of octahedrally coordinated atoms alternated by tetrahedrally coordinated ones, together with Ca^{+2} ions in the remaining space, see ***figure 1.2.1***. Probably owing to this structural similarity, the most relevant guest atom which takes part in ferrite is titanium. When high amount of titanium enters the structure, perovskite-like zones appear mixed with ferrite [1, 30].

1.3. The hydration process

In cement chemistry, the term *hydration* comprises the myriad of chemical reactions, physical changes, and thermodynamic processes that take place when the clinker is put into contact with water. During the hydration, the system evolves to form an amorphous paste which sets and hardens. It is a process of huge complexity due to the great number of involved variables. One must keep in mind that the cement powder contains a wide variety of components, clinker phases and additives, each of them with impurities and random particle sizes and shapes, distributed heterogeneously among the cement, and with different reaction rates. Other external factors, such as the water to cement ratio (w/c, in % wt) and curing temperature, play also a key role in the final properties.

Although it seems to be simple from a technological viewpoint, just a mixture of cement with water in a given proportion, the hydration process is still not fully understood, due to the aforementioned complexity. The process has been studied from a

scientific point of view since the early 1900´s [31] and it is still object of many investigations [32-35]. In order to decrease the large number of variables, the hydration process is frequently studied independently for each component of the clinker. The most important reactions are those of the main phases described in ***section 1.2***, and they will be discussed below.

1.3.1 Hydration reactions of the clinker phases

- ***Alite, C_3S***

Alite hydration is the main responsible for the strength development during the first days. It reacts moderately fast with water. After 28 days, it is considered that about the 70% of the alite has reacted, while the process is virtually complete after 1 year. The reaction of the pure tricalcium silicate can be written as:

$$2 \cdot C_3S \; + \; 6 \cdot H \; \rightarrow \; C_3S_2H_3\left(C\text{-}S\text{-}H \; gel\right) \; + \; 3 \cdot CH \qquad (1.3.1)$$

Portlandite (CH) and especially the C-S-H gel are the main components of the cement paste and the principal responsible for the material properties. When the previous reaction is analysed, it must be noted that the stoichiometry of the C-S-H gel is not fixed [9], and the proposed reaction has to be taken as an approximation. Other stoichiometries that end in the C-S-H gel have been suggested [1]:

$$3 \cdot C_3S \; + \; (3+m-n) \cdot H \; \rightarrow \; C_nSH_m \; + \; (3-n) \cdot CH \qquad (1.3.2)$$

For a given particle size and water to cement ratio, the C_3S hydration process is similar to that of the clinker itself, which will be discussed later.

- ***Belite, C_2S***

The hydration reaction of β dicalcium silicate is comparable to that of tricalcium

silicate in terms of final products and stoichiometry, with the difference that less portlandite is formed:

$$2 \cdot C_2S \; + \; 4 \cdot H \; \rightarrow \; C_3S_2H_3\left(C\text{-}S\text{-}H \; gel\right) \; + \; CH \qquad (1.3.3)$$

A remarkable difference is that the reaction rate of belite is much slower than that of alite. Only the 30% of belite reacts after 28 days, and the process is still incomplete after 1 year, when nearly the 90% has reacted [1, 4]. There are not large differences between the hydration kinetics of the β and α forms, while the γ phase presents an almost negligible hydraulic activity [1, 4].

- ***Tricalcium Aluminate, C_3A***

Tricalcium aluminate reacts very fast with water. This process, known as *flash setting*, is not desired, since it affects the rheology of the paste at early ages. It reduces the workability of the paste and hinders the homogeneous mixing of cement with water. The first hydration products are the unstable calcium hydroaluminates, which evolve rapidly to hydrogarnet (C_3AH_6) [1, 4]:

$$C_3A + \; 21 \cdot H \; \rightarrow \; C_4AH_{19} \; + \; C_2AH_8 \; \rightarrow \; 2 \cdot C_3AH_6 + \; 15 \cdot H \qquad (1.3.4)$$

To avoid the *flash-setting*, retardants such as gypsum are added to the clinker. In the presence of gypsum, the reaction products are calcium sulphoaluminates, mainly ettringite $C_6A\bar{S}H_{32}$:

$$C_3A + \; 3 \cdot C\bar{S}H_2 + \; 26H \rightarrow \; C_6A\bar{S}H_{32} \qquad (1.3.5)$$

When there is no more gypsum available in solution, tricalcium aluminate starts to consume the created ettringite, and forms monosulphoaluminate, $C_4A\bar{S}H_{12}$, a crystalline phase richer in aluminium:

$$2 \cdot C_3A + C_6A\bar{S}H_{32} + 4H \rightarrow 3 \cdot C_4A\bar{S}H_{12} \quad (1.3.6)$$

There is a controversy in the nature of the retardation mechanism. Some authors propose that the sulphoaluminate phases cover the C_3A surface with a more or less impermeable layer that prevents the contact with the solution [36-38], while others suggest that sulphate groups block the reactive points in the crystal surface [39, 40].

- ***Aluminoferrite, C_4AF***

Hydration of the ferrite phase is very similar to the aluminate one. The main product is $C_4(A,F)H_{19}$, but evidences of amorphous iron oxides or hydroxides are found. In the presence of gypsum, the reaction products follow the same sequence as the one of C_3A, with the only difference that the hydration products (ettringite and monosulphoaluminate) present a partial substitution of aluminium by iron [1, 4].

1.3.2. Hydration process

The hydration process has been followed by many different techniques, like conductimetry, thermogravimetry, light and electron microscopies, NMR, X-Ray diffraction, etc [4, 41]. The recorder evidences from those studies agree that in the hydration of ordinary Portland cement, five different periods or stages can be distinguished [42]. Those stages are easily differentiated monitoring the heat rate evolution during the hydration, as can be seen in ***figure 1.3.1***. In this figure, the Ca^{+2} ion concentration in solution is also shown.

- ***Stage I (Pre-induction)***

When cement powder is put in contact with water, there is an initial fast dissolution of the clinker grains releasing Si^{+4}, Ca^{+2} and OH^- ions to solution. This stage lasts for a few minutes and is characterized by an elevated heat production. The concentration of Si^{4+} ions reaches a maximum value and begins to reduce as the first C-S-H gel is formed. On the contrary, the concentration of Ca^{2+} and OH^- increases continuously, as

the formed gel has a lower Ca/Si ratio than the clinker phases. As the saturation level of Ca^{2+} and OH^- ions in solution is not reached, portlandite does not precipitate. Therefore, the solution pH increases. During this stage the first ettringite ($C_6A\bar{S}H_{32}$) crystals appear due to C_3A dissolution, or, if gypsum is not present, flash setting occurs [1].

- ***Stage II (Induction or dormant period)***

As the hydration continues, the reactions slow down, and the paste remains plastic and workable for a few hours. There are different theories which attribute the decrease in the hydration rate to different reasons. Some authors suggest that the main cause formation of an impermeable layer which reduces the dissolution rate is [43, 44]. For others, the

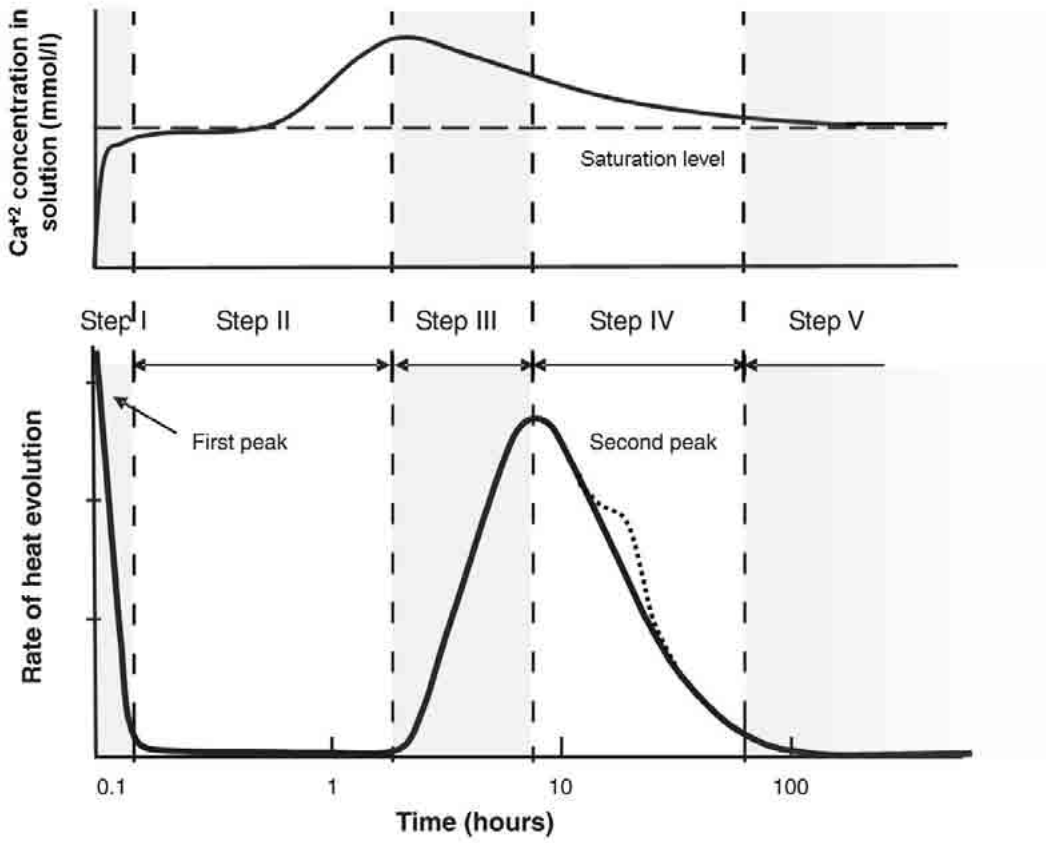

Figure 1.3.1.- Idealized curves of the Ca^{+2} concentration in solution (top) and the rate of heat evolution (bottom) versus the hydration time of ordinary Portland cement pastes. The different stages are explained in the text. Note that the time scale is logarithmic.

slow nucleation of portlandite [45] and the C-S-H gel [46, 47] due to the low concentration of ions in solution controls this stage. The concentration of Ca2+ and OH^- ions increases over the saturation level, when portlandite begins to precipitate. At the end of this stage the pH value is 12-13, [1].

- ***Stage III (Acceleration)***

The precipitation of portlandite decreases the concentration of Ca^{2+} and OH^- in the liquid phase. Thus, the dissolution of calcium silicates and aluminates is accelerated again, with the consequent increase in the released heat. A second stage C-S-H gel is formed, while portlandite and ettringite continue growing [1]. The C-S-H gel formed on the surface of adjacent clinker particles coalesces. This point, known as the cohesion point, matches with the maximum heat release, and corresponds to the setting period end [4].

- ***Stage IV (Deceleration)***

After several hours of reaction, the hydration products cover the cement grain surfaces, and the kinetics is no longer controlled by the dissolution rate or crystal nucleation and growth, but rather by the diffusion of calcium and silicate ions through the already formed produtcs. Therefore, the reaction slows down as more hydration products are formed. Due to the consumption of sulphate ions, ettringite evolves to monosulphoaluminate, what can produce a shoulder on the heat evolution curve [1].

- ***Stage V (Diffusion)***

In this stage the microstructure of the C-S-H gel is developed, and the gel becomes denser. Other crystalline species, especially portlandite and monosulphoaluminate, could keep growing. As a consequence, the diffusion of the solution becomes smaller and reactions slow down as the paste becomes stronger. It is considered that the hydration is virtually finished after one year, though the process could continue over years, as well as the evolution of the C-S-H gel and cement paste microstructure [1].

1.4. Structure of the cement paste

Ordinary Portland cement pastes, and in general all the types of cement pastes, are truly complex materials, porous, multi-component, and multi-scalar. In the cement paste crystalline hydration products, such as portlandite or the AFm and AFt phases, co-exist with unhydrated clinker particles of different sizes which may persist after the hydration, surrounded by the amorphous C-S-H gel. The spatial location of the crystalline phases and the structure of the C-S-H gel depends on the initial distribution and composition of clinker particles, and therefore, inherit its heterogeneity. Furthermore, as the hydration products have a very dissimilar structure and sizes, the cement paste itself has different hierarchical levels of organization at different scales. Each length scale is a random composite, and has associated a characteristic pore structure, which will be determinant in the net paste properties. Thus, the description of the cement paste structure will be presented separately for each scale. The most usual classification divides the multi-scalar structure in three size ranges: macro-scale, micro-scale, and nano-scale.

- ***Macro-scale***

At the macro-scale (> 10^{-3}m) the cement paste is considered as a homogeneous material with bulk properties and characteristics. At this level, aggregates and reinforcements can be easily distinguished, bounded by the cement paste, see ***figure 1.4.1 (a)***. In this scale, pores with sizes between 0.1 and 5 mm of diameter appear. They have their origin in air inclusions entrapped in the cement paste during the hydration process. These pores are generally detrimental for the mechanical properties and service life, as they constitute naturally open paths for chemical attacks [48].

- ***Micro-scale***

The multi-phase composition of the cement paste becomes evident at this scale, between 10^{-3} and 10^{-6} m. Electron microscopy techniques are the most used methods to investigate the cement paste structure within this size [41], see ***figure 1.4.1 (b)***.

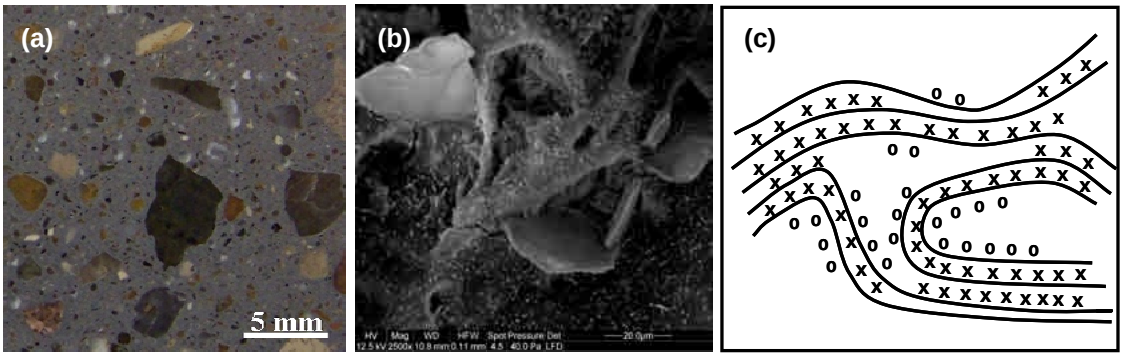

Figure 1.4.1.- Structure of the cement paste at different length scales, from the macro-scale to the nano-scale. **(a)** In the macro-scale, the aggregates are the most visual features, surrounded by the homogeneous cement paste. **(b)** In the micro-scale, the heterogeneous nature of the paste becomes evident, with many crystalline phases embedded in the amorphous C-S-H gel. Image provided by Dr. Gaitero from from the Centre for Nanomaterials Applications in Construction (**NANOC**) at Labein-Tecnalia. (**c)** Proposed model for the C-S-H gel nanostructure [49].

At this scale the C-S-H gel can be described essentially as an amorphous product which surrounds all the crystalline aggregates. Many different morphologies of the C-S-H gel have been described in the literature: flakes, honeycomb-like, needles, foils, grains or unshaped agglomerates are some examples [4]. These morphologies seems to appear depending on initial parameters, such as the w/c ratio and cement types [9], as well as depending of the hydration stage when C-S-H gel is formed and the available space [50]. Nevertheless, it is well-known that in view of the microscopy images, the C-S-H gel can be classified as *inner* product and *outer* product [1, 4, 51-53]. The inner product refers to the C-S-H gel that grows inwards the boundaries of the clinker grains, occupying the place of the anhydrous phases. On the contrary, the outer product is the C-S-H gel that is formed outwards the boundaries of the clinker grains, in the water filled space. In general, the inner product has a more compact and amorphous structure, while the outer product has been found to form bundles of fibres radiating from the cement grains [4]. The composition of both products seems to be similar, although some authors report slight differences in the C/S ratio, that is higher for the inner product [7].

Among the crystalline phases, portlandite is the most easily recognizable. Portlandite crystals could reach several micrometers in size, depending on several factors such as

temperature or w/c rate. It grows together with the outer product and in the pore space. Under ideal conditions, portlandite forms hexagonal plates, due to its preferential grow direction. In the cement paste, although perfect hexagonal crystals may be present in the pore space, it is more common to find it as unshaped crystals, conserving the characteristic layered structure. AFm and AFt crystals are smaller, and form needles of ~1 μm long preferentially on the surface of the cement grains, though they have also been found far from them [4, 54].

The pores associated to this scale are called meso-pores or capillary voids. They are a consequence of the empty space that appears when hydration products replace the space initially occupied by water and cement. In general, the higher the initial w/c ratio, the more porous the cement paste is. As the hydration rate increases, the pore volume decreases, and the initially connected pores undergo a percolation transformation, and become disconnected [10, 48, 55]. In early pastes, the capillary voids may reach 5 μm, whereas they range between 10 nm to 50 nm in well cured mature samples [48].

- ***Nano-scale***

The cement paste structure at the nano-scale (< 10^{-6} m) is basically that of the C-S-H gel, although AFm and AFt crystals of small sizes can also be included in this scale. The C-S-H gel is the most important product of hydration and it is the responsible for most of the cement paste properties. It is amorphous and heterogeneous in composition. Consequently, the C-S-H gel characterization is not straightforward, and its structure has not been fully elucidated despite the large amount of experimental techniques employed: NMR, SEM, TEM, AFM, SANS, SAXS, sorption measurements, etc. [41].

The pores at the nanoscale are intrinsic to the C-S-H gel structure. The high surface area of the C-S-H gel and many processes such as creep and shrinkage depend on these pores [48, 56]. However a quantitative characterization of their net volume is very difficult. Intrusion porosimetry techniques using Hg or N_2 do not reach such low pore sizes, while drying the cement paste to measure the water loss has in his turn many problems due to the presence of several types of adsorbed water [10, 56]. Due to its

importance, the structure and models of the C-S-H gel will be discussed at length in the next section.

1.5. The C-S-H gel

The C-S-H gel is the most important hydration product. It constitutes up to the 70% vol. of the solid phase, and is, therefore, the main responsible for the material properties. The C-S-H gel is an amorphous and porous material with variable stoichiometry. In fact, the acronym C-S-H stands for Calcium-Silicate-Hydrated with no fixed stoichiometry, equivalent to write $C_xS_yH_z$. In the beginning of past century, Le Chatelier suggested a variable composition, referring to the C-S-H gel as CaO·SiO·Aq [57]. Due to its complexity, the accurate C-S-H gel structure characterization at the nanoscale is a very complicated and still unresolved task. The microscopy techniques do not have enough resolution to reach the small sizes necessary to investigate the disordered C-S-H gel structure. Therefore, indirect methods are the only available techniques to investigate it. Recently, NMR, IR-spectroscopy, X-Ray methods, SANS, SAXS, nanoindentation or gas sorption techniques have been applied to characterize the C-S-H gel [41, 58].

A basic picture of the C-S-H gel structure is presented in *figure 1.5.1*, and it could be described as follows. The gel is composed of silicate chains joined together by calcium oxide layers, forming layered structures. The interlayer space is occupied by water molecules and ions such as Ca^{+2} or Na^{+1} [5, 6, 8, 52]. The silicate chains follow a *Dreierketten* or wollastonite-like arrangement, in which the structure repeats every three silicate tetrahedra, with finite lengths of 2, 5, 8, …, $3n - 1$ units, with n an integer. Each unit is an orthosilicic acid group, $Si(OH)_4$, which has polymerized via condensation reactions to form the chains. In young ordinary Portland cement (OPC) pastes, most of the chains are dimers, although they continue growing and the mean chain length after 23 years is 4.8 [59]. To explain such fixedlengths, Richardson et al. proposed a growth model in which a dimer could not continue growing to form a trimer, but two dimeric structures merged by means of an bridging monomer to form the pentamer [6, 8, 52, 60].

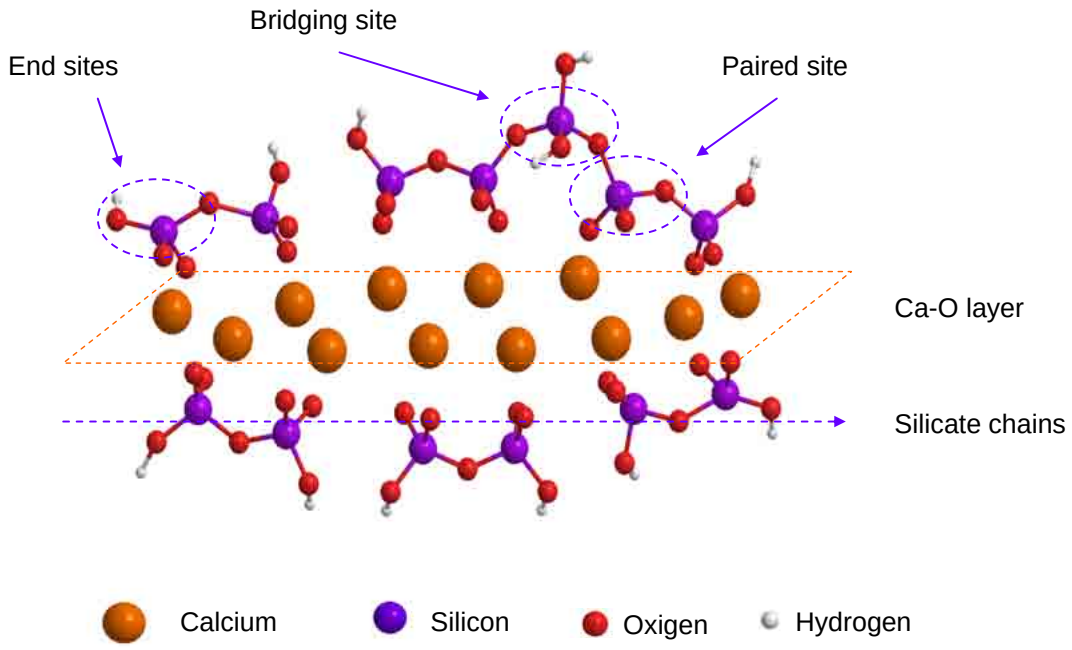

Figure 1.5.1.- Schematic representation of the C-S-H gel atomic structure. Silicate chains of lengths according to the 3n-1 rule (dimers and pentamer) are held together by a Ca-O layer. The different positions within a chain (end, paired and bridging) are represented. The legend in the bottom shows the colour and size of the involved atoms.

As the C-S-H gel structure is not fixed, its composition is usually characterized by its calcium to silicon ration, C/S. In OPC pastes at early hydration times, the C/S ratio range from 1.2 to 2.1, with a binodal distribution of values. As the hydration progresses, the C/S ratio evolves to an normal distribution with a mean value of 1.75 [6, 61].

Although the C-S-H gel is an amorphous material, it has some short-range order at the atomic scale, and many of the knowledge about it has been gained from the comparison with fully crystalline Calcium Silicate Hydrates. Therefore, in the next section the structure of high ordered phases related to the C-S-H gel will be described.

1.5.1. Ordered structures related to the C-S-H gel

Around 30 different crystalline Calcium Silicate Hydrates have been reported in the

literature [62]. At room temperature and pressure, the calcium silicate hydrate thermodynamically stable in equilibrium with water and portlandite is afwillite [63], even though it does not present any parallelism to the C-S-H gel. However, the tobermorite family and jennite show many similarities with the C-S-H gel.

- ***Tobermorite***

The tobermorite family is composed of four members: tobermorite 9 Å or riverseidite, clinotobermorite, tobermorite 11 Å, and tobermorite 14 Å or plombierite. In general, these phases are built of calcium oxide layers ribbed on both sides by silicate chains, forming layered structures, with water molecules and extra Ca^{+2} ions in the interlaminar space. The distance that labels the different members of the family identifies the basal spacing between two consecutive layers. By a dehydration process on progressive heating, tobermorite 14 Å, the most hydrated specimen of the series, evolves to tobermorite 11 Å and later to tobermorite 9 Å. Clinotobermorite is closely related to tobermorite 11 Å, but with a different symmetry in the layers [64-66].

Although 9 and 11 Å tobermorites could be useful models for C-S-H gel with low C/S ratios, the variety with more resemblances to the cementitious C-S-H gel is tobermorite 14 Å, probably as a consequence of the high water content [5, 9]. Tobermorite 14 Å, $Ca_5Si_6O_{16}(OH)_2 \cdot 7\ H_2O$, is a natural mineral which has been found in many locations, an it is also synthesized under hydrothermal conditions from different materials [64]. It has a monoclinic unit cell with space group B11b. As mentioned before, the structure of tobermorite 14 Å is composed of central calcium oxide layers connected with silicate chains in both sides. The silicate chains follow the already cited wollastonite-like or Dreierketten arrangement, that is, the structure repeats every three silicate tetrahedra. Two of three silica tetrahedra are closely connected to the calcium oxide layer while the remaining one is oriented to the interlaminar space, see ***figure 1.5.2***. These chains are shifted between them by *b*/2, being *b* the lattice parameter. Each layer has an stoichiometry $[Ca_4Si_6O_{16}(OH)_2]^{-2}$, due to a non hydroxilated oxygen atom in the bridging silicon tetrahedra. The charge is counterbalanced by Ca^{+2} ions located in the interlaminar space. Each Ca^{+2} ion is coordinated to the oxygen atoms in the bridging

tetrahedra of consecutive layers and to four water molecules. The C/S ratio is 0.83, with a density of 2.20 g·cm^{-3} [64].

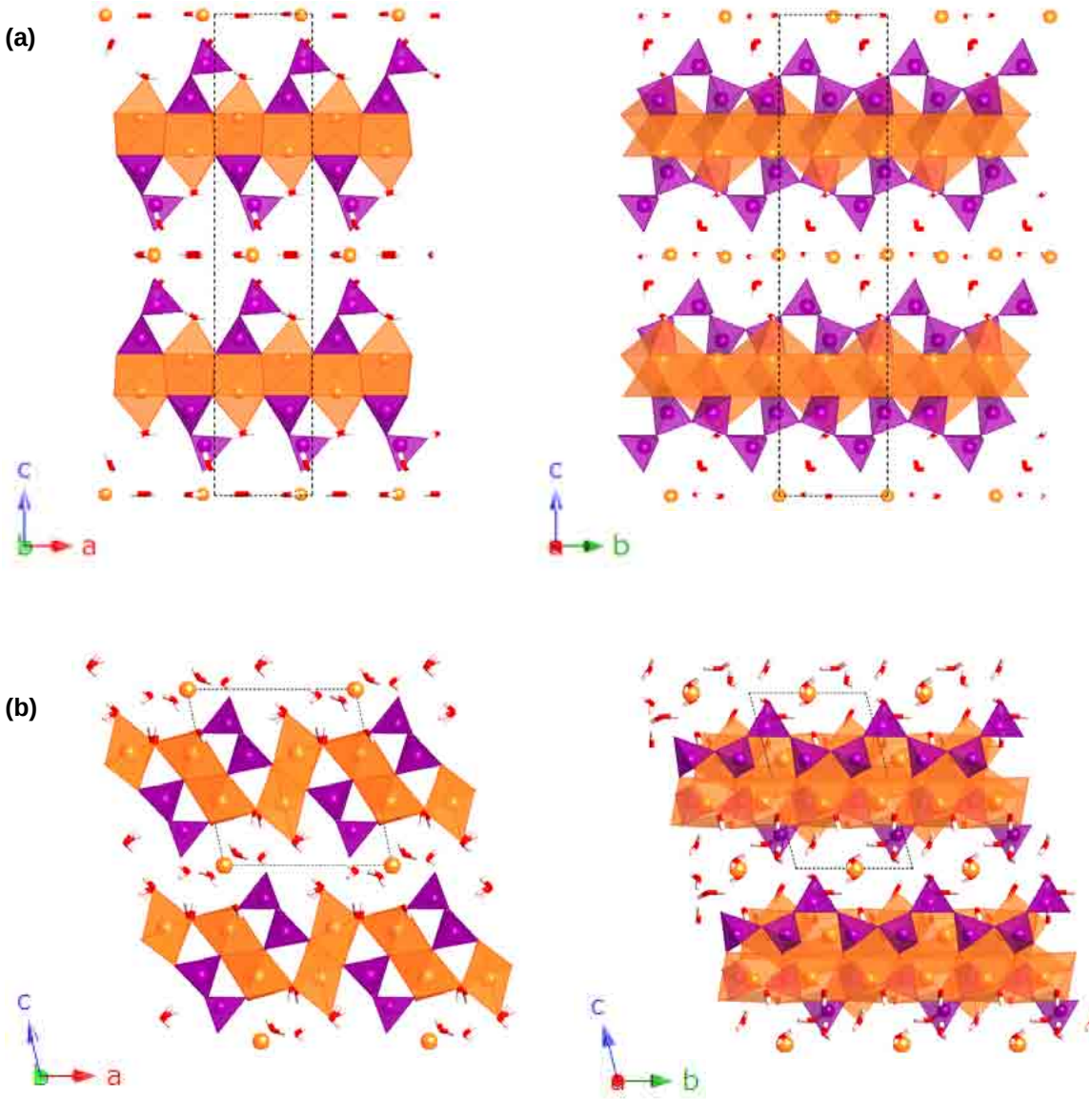

Figure 1.5.2.- Structures of the crystalline phases related to the C-S-H gel **(a)** tobermorite and **(b)** jennite. The unit cell is represented by the dotted lines and the view direction by the l The left panels show the crystals in a parallel view to the chain direction, while the right ones show them in a perpendicular view. Silicate groups are represented by purple tetrahedra and water molecules by a pair of joined red and white sticks. Intralayer Ca atoms are in orange, inside the corresponding coordination polyhedra, while interlaminar Ca atoms are given as balls for a better view, even though they also present regular coordination.

- ***Jennite***

Jennite is a rare mineral which appears in nature associated to tobermorite [67]. As tobermorite, jennite can be synthesized under hydrothermal conditions and losses water molecules upon heating, which gives raise to a related structure called meta-jennite [68]. Jennite's structure is similar to that of tobermorite with two significant differences as seen in ***figure 1.5.2***. First, the bridging tetrahedra of the silicate chains are also connected to the calcium-oxide layer. Second, due to the higher calcium content in the layer, only half of the Ca atoms are linked to the oxygen atoms of the silicate groups, while the rest are coordinated to the hydroxyl groups which join the calcium oxide layer. As in tobermorite, the silicate chains are shifted, but this time by *b*/4, and the layers are charged negatively, counterbalanced by the Ca^{+2} ions placed in the interlayer space together with water molecules. The empirical formula of jennite is $Ca_9Si_6O_{18}(OH)_6 \cdot 8\ H_2O$, with a Ca/Si ratio of 1.5 and a density of 2.325 $g \cdot cm^{-3}$ [68].

- ***Calcium silicate hydrates type I and II***

Attempts to synthesize tobermorite 14 Å at room temperature resulted in an ill crystalline product called C-S-H (I). This phase could be described as a tobermorite 14 Å with multiple imperfections, mainly the omission of the bridging tetrahedra in the silicate chains. Thus, finite chains with variable lengths following the $3n - 1$ rule are formed, and the C/S ratio increases [1, 4]. It has been synthesized C-S-H(I) with C/S ratios ranging from 0.8 to 1.5. The X-ray diffractograms show that the basal spacing of C-S-H(I), i.e. the distance between consecutive layers, is not well defined. As the C/S ratio increases, the basal space decreases and the structure becomes more irregular, with a reduction of the mean silicate chain length [1, 4].

Under certain special conditions and water excess, a second poorly crystalline product may be formed, called C-S-H (II), with C/S ratios that can reach a value of 2. X-ray powder diffraction patterns show similarities in the lattice parameters with those of jennite. Thus, the C-S-H (II) is depicted as an imperfect and disordered version of jennite, with finite chain lengths due to the omission of the bridging silicate group.

Posterior efforts to synthesize C-S-H (II) under controlled conditions have failed, and, therefore, its formation and characteristic are not fully understood [1, 4].

1.5.2. Models for the C-S-H gel atomic structure

Numerous models have been proposed to explain the atomic structure of the C-S-H gel, based all of them in an imperfect and disordered versions of the crystalline phases tobermorite, jennite or portlandite. Two detailed reviews on this topic are those of Richardson [9, 62]. Below, the main aspects of these models will be described.

Some early models are based on the portlandite structure with the incorporation of monomeric silicate groups [69, 70]. The hydroxyl groups of three $Ca(OH)_2$ units would undergo a condensation reaction with those of the silicate monomers, and they form a compound with formula $Ca_3(OH)_3O_3Si(OH) \cdot 3\ H_2O$. It was also proposed that the gel could be a variety of C-S-H (I) and (II) compounds with only monomeric silicate units [71]. Although monomeric silicate chains may appear in the C-S-H gel at early hydration ages, they evolve to polymeric chains following the $3n - 1$ rule [59, 72]. Consequently, these models are inconsistent with the experimental data.

The analogy between the C-S-H gel and tobermorite was first proposed in 1952 [73] after X-ray diffraction studies on hydrated C_3S pastes. Such analogy became the base of most of the models proposed afterwards. However, the C-S-H gel has a mean C/S ratio ~1.7, which is higher than that of tobermorite, C/S = 0.83. In view of such disagreement, some authors proposed that the C-S-H gel was actually a solid solution of tobermorite and portlandite [74], tobermorite-like layers sandwiched between portlandite sheets [75], or tobermorite with more Ca^{+2} and OH^- ions in solution in the interlaminar space [76]. Hence, the C/S ratio was higher, with a suggested compositions similar to that of tobermorite with an excess of Ca and OH, i.e. $Ca_5Si_6O_{18}(OH)_2 \cdot [Ca(OH)_2]_x \cdot 7\ H_2O$, with x = 5, 6, 7.

The previously mentioned models do not take into account the finite chain length of the C-S-H gel, and propose structures built from monomers or infinite chains. At an

intermediate approach to these limit cases, Taylor suggested [77] that higher C/S ratios could be reached by the partial removal of bridging tetrahedra in the silicate chains and their replacement with interlaminar calcium ions. In this process finite chains are created. Stade et al. extended this idea and propose a model with two varieties of C-S-H gel, one entirely made of dimers, and another one made of polymeric chains. Each gel variety had different stoichiometry, and they assumed a total protonation of the end silicate chains, as well as a variable amount of ions in the interlayer region to asses the charge neutrality [78]. Thirty years later from his first model, Taylor introduced the possibility of jennite-like structures to account for the higher C/S ratios in C-S-H gels [5].

A most general and flexible model is the one proposed by Richardson and Groves [6, 9, 52, 61]. Their model reconciles the tobermorite-portlandite and tobermorite-jennite visions of the C-S-H gel by considering both the calcium atoms and hydroxyl groups in the interlayer space or in the structure as follows:

$$\left\{Ca_{2n}H_wSi_{(3n-1)}O_{(9n-2)}\right\}\left(OH\right)_{w+n(y-2)}Ca_{\frac{n\,y}{2}}\cdot m\,H_2O \qquad (1.5.1)$$

The stoichiometric formula is build up by two terms. The first term, represented between brackets in the equation (1.5.1), is the central part which accounts for the silicate chains of $3n - 1$ units and the corresponding calcium packed between them. The second term includes the extra Ca^{+2} and OH^-, with no distinction if they are in the interlayer region as free ions, portlandite, or as a second structural layer of Ca-OH for jennite like structures. Some extra conditions are necessary to impose the charge neutrality:

$$\begin{aligned} &0 \le y \le 2 \;\rightarrow\; n(2-y) \le w \le 2n \\ &2 \le y \le 4 \;\rightarrow\; 0 \le w \le 2n \\ &4 \le y \le 6 \;\rightarrow\; 0 \le w \le n\,(6-y) \end{aligned} \qquad (1.5.2)$$

These conditions balance the hydroxyl calcium ratio for any protonation degree of the

silicate chains. The model has also been extended to the incorporation of guest ions in the structure, mainly the replacement of Si^{+4} by Al^{+3}:

$$\left\{Ca_{2n}H_w\left(Si_{1-a}R_a\right)_{(3n-1)}O_{(9n-2)}\right\}I^c_{\frac{a}{c}(3n-1)}\left(OH\right)_{w+n(y-2)}Ca_{\frac{3n\,y}{2}}\cdot m\,H_2O \qquad (1.5.3)$$

where *R* is aluminium (or other trivalent guest ion) and *I* is a monovalent or divalent ion that balances the charge excess in the chain resulting from the ion substitution.

Other models based on finite Dreierketten-type chains have been discussed in the literature [79-82]. Essentially, they are specific cases of the general formulation proposed by Richardson. In addition, some authors have suggested three composition ranges in which C-S-H has different structures, α (0.66 < C/S < 1.0), β (1.0 < C/S < 1.5) and γ (1.5 < C/S < 2.0) [82]. Nevertheless, the proposed stoichiometry of the C-S-H gel in these ranges is also equivalent to the Richardson's formulation.

1.5.3. Models for the C-S-H gel nanostructure

So far, the structure of the C-S-H gel at the atomic scale has been explained. The atomic structure of the C-S-H gel is formed by layered structures of tobermorite-like and/or maybe jennite-like disorder crystals with a short range order. The question that now arises is how the structure of the hardened cement paste develops from the growth and arrangement of these disordered crystals, something which is not completely understood. The tobermorite/jennite-like "crystalloid" point of view seems to be, in principle, contrary to the idea of a colloidal C-S-H gel. However, the colloidal nature of the C-S-H gel was already mentioned by Michaelis [83] in the beginning of the last century, and the description of the gel as a colloidal material is nowadays the most accepted one.

One of the first models to describe the nanostructure of the C-S-H gel was the one due to Feldman and Sereda [49]. It was based on sorption measurements, porosity, and the relationship between physical properties and water content of mature cement pastes. As

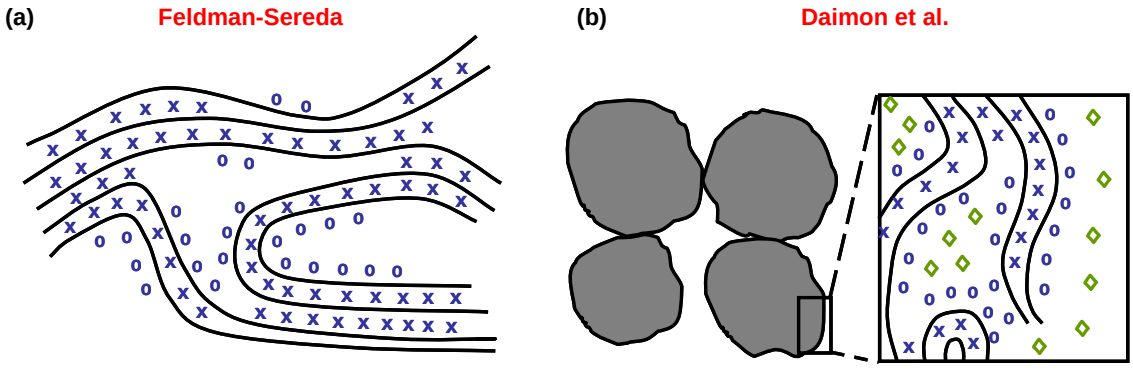

Figure 1.5.3.- Models for the C-S-H gel nanostructure. **(a)** Feldman-Sereda model. Each line represents a tobermorite layer as proposed for the atomic scale (see ***figure 1.5.1***), the interlaminar water is represented by an (**x**), and the physically absorbed water by a circle (**o**). **(b)** Daimon et al. modification of the Feldman-Sereda model. Each C-S-H particle has the structure proposed by Feldman and Sereda, but including water in the inter-particle a and intra-particle pore space, represented by a rhombus (◇).

can be seen in the representation of ***figure 1.5.3***, the model proposes that the C-S-H particles are composed of tobermorite layers which tend to group in modules of several layers-thick, with interlaminar water between them. In some cases, the interlaminar water is missing, which gives place to local disorders due to the layer proximity. Finally, absorbed water is present in the free surfaces that are not in contact with other layers. Later Daimon et al. modified this model with a refinement of the pore structure. In their description they included the pores between the C-S-H particles proposed by Feldman and Sereda, as well as the internal pores within the particles [56]. Thus, the water in the particle could be interlaminar, absorbed in the surface of the layers, or in the internal pores.

At the moment, the most successful model is the one developed by Jennings and co-workers. The model proposed by Jennings [84, 85] aimed to explain the contradictory experimental data about surface area, porosity, density and water content of the C-S-H gel found along the years by several groups. From a reinterpretation of the N_2 sorption data, together with new Specific Surface Area (SSA) measurements by Small Angle Neutron Scattering (SANS) [86], they proposed the existence of two different types of C-S-H gel differing on the porosity. This model rationalizes the incongruent results

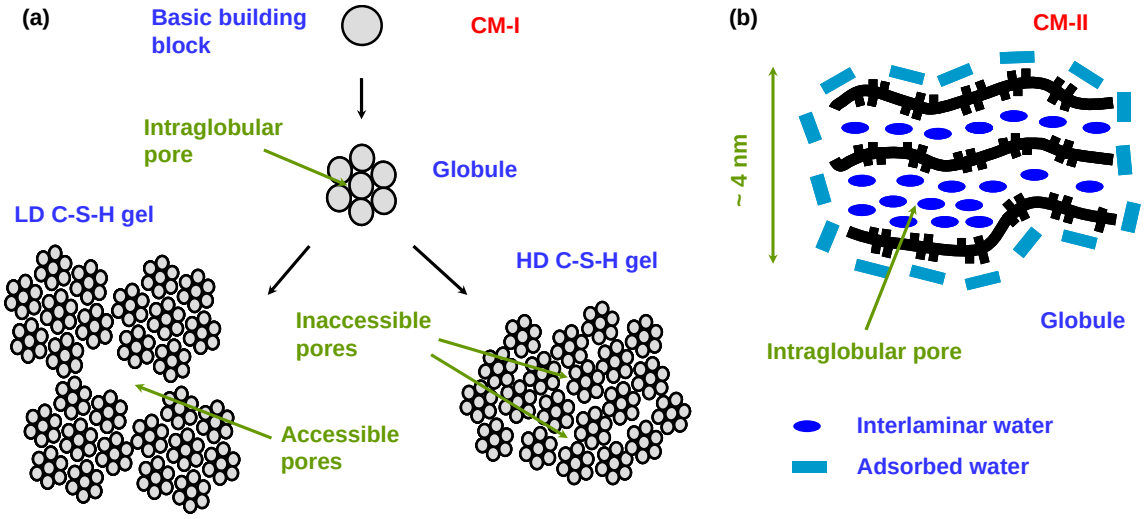

Figure 1.5.4.- Colloidal model of Jennings. **(a)** CM-I with the different structural levels, starting from the basic building block and the evolution to two types of C-S-H gel with low and high densities. The accessible and inaccessible pores for N_2 penetration and SANS resolution are shown. **(b)** Structure of a globule in the CM-II model. Black lines represent the calcium silicate skeleton of the particles. The intraglobular pores are filled by intralaminar water more weakly bonded to the structure.

obtained by previous researches under different conditions, due to the fact that each technique measures the C-S-H gel features at different length scales. In that model, called later CM-I by the author, the starting point were some spherical basic-building-blocks with a radius of approximately 1.2 nm and a density of ~2.8 g cm^{-3}. The author suggested that the particles were not spherical but roughly equiaxed structures, although spheres were easier to model. Those basic blocks formed bigger structures called "globules" about 3 nm of radius with a variable density dependent of the water content. The globules packed themselves, in two different ways, loose or tight, which give rise to a Low Density (LD) and High Density (HD) varieties of the C-S-H gel respectively. The HD C-S-H gel had a very compact structure in which N_2 cannot penetrate and that SANS cannot resolve, while the LD variety can be fully observed by those techniques. In addition to this pore or surface configuration, there was another level at smaller scales within the globules. The structure at this level is common to both types of gels, as they are built up from the same initial particles, and would be equivalent to the intraparticle pore space of the Feldman-Sereda model. The non-linear relationship

between the SSA measured by SANS and the degree of hydration made the author suggest that the LD C-S-H gel was developed mainly during the first hydration stage (stages I-IV), while the HD C-S-H during the diffusion period (stage V). The authors also commented the possible connection between the inner product and the HD gel and between the outer product and the LD gel. Posterior nanoindentation measurements of cement pastes indicated the presence of a bimodal distribution of elastic modulus [58, 87, 88]. Such results have been attributed to the presence of the two C-S-H gel varieties with different porosities [58, 87, 88].

Recently, the same author has proposed a refinement to the CM-I, after new data about the C-S-H particles obtained by SANS and SAXS [89]. It was found that the water-saturated particles have a density of 2.604 g cm^{-3} and a chemical formula $C_{1.7}SH_{1.8}$. They also identified some nanocrystalline domains of portlandite [89]. In the new model, called CM-II to indicate that is an improvement of the previous one, the nature of the globules was modified, while the concept of HD and LD gel varieties remains [90]. This time, the globules are taken as the smallest particle, without the basic building blocks. These particles are stated to be platelets of ~4.2 nm thick, although the name globule is used for the notation. The structure of the globules is, in many senses, similar to that of the Feldman-Sereda model, composed of tobermorite and/or jennite-like sheets and water. The water could be located in several positions. Moving from the inside to the outside, the water could be interlaminar, filling the intraglobular pore space, adsorbed in the surface of the particles, and finally in the interglobule pore space [90]. Through the CM-II, the author interpreted the sorption isotherms at different water contents, and some processes that occur in the cement paste such as creep and shrinkage. These processes are explained in terms of water loss, as well as rearrangement of both the globules and the chains within the globules [90].

Although there is an overall agreement in the validity of the CM-II, the interpretation of sorption data has been the object of some discussion [91, 92]. The rearrangement of the chains within C-S-H particles has been also proposed to explain the elastic properties of the C-S-H gel with different water contents and porosities [93]. Contrary to many previous models, Nonat stated that the C-S-H gel is not necessary a very

disordered material at the nanoscale [82]. This assumption was based in atomic force microscopy (AFM) images showing long range order in synthetic C-S-H gel nanoparticles, about 60 nm in their largest direction [94].

1.6. Other hydration products

Although the C-S-H gel represents up to the 70% wt. of the cement matrix, the chemistry of other hydration products has also an important role in the product performance, the degradation processes and the material service life. The most important hydration products have been already in ***section 1.2***. A short description of their main characteristic will be given below.

- ***Portlandite***

Portlandite is the mineral name of crystalline calcium hydroxide, with chemical formula $Ca(OH)_2$, or CH in cement chemistry notation. It is the crystalline product present in major quantities in the cement matrix, up to the 25% in volume, and appears as massive crystals which can reach sizes of micrometers [4]. Portlandite has a layered structure, with calcium atoms octahedrally coordinated to OH groups. The oxygen atoms themselves are linked to three Ca^{+2} ions and to a hydrogen atom perpendicular to the sheets, see ***figure 1.6.1***. The layers interact by weak dispersive forces because the distance between them is too large to establish hydrogen bonds or other types of stronger interaction [95].

The contribution of portlandite to the mechanical performance of the cement paste is unimportant compared to the C-S-H gel. However, portlandite plays an important role in some degradation processes such as calcium leaching or the corrosion of metals. Calcium leaching consists in the progressive dissolution of the cementitious matrix as the calcium ions migrate to the pore solution. This process depends on the equilibrium between the free calcium concentration in the pore solution and the C/S ratio of the hydration products. Portlandite is the first hydration product that dissolves during

calcium leaching, so that the porosity increases, in detriment of the mechanical properties [48, 96, 97]. On the other hand, the corrosion of metals embedded in concrete (conductions, pipes or reinforcements) is usually prevented by the high pH of the pore solution. The presence of large portlandite amounts ensures the high alkalinity levels of the cement paste, and protects the metals [48].

- ***Ettringite***

Ettringite, $C_6A\bar{S}H_{32}$, is the result of the hydration processes of aluminate and ferrite clinker phases in the presence of gypsum. When all the gypsum content is consumed during the hydration reactions, the continuous dissolution of aluminate and ferrite phases consumes the ettringite to form a second product with lower sulphate content. However, ettringite crystals may persist in mature cement pastes [98]. In such cases, they present a rod-like morphology and may reach lengths up to 10 μm [4]. Ettringite belongs to the AFt family of compounds (Al_2O_3-Fe_2O_3-trisulpho). As can be seen in ***figure 1.6.1***, the ettringite structure is based on columns arranged parallel to the z axis. The columns are formed by aluminium atoms octahedrally coordinated to hydroxyl groups alternated with three calcium atoms in a plane. The Ca atoms share and are coordinated to the hydroxyl groups of aluminium and to four water molecules placed in the space between columns. The stoichiometry of the columns leads to a charge excess, which is neutralized by sulphate ions placed in the channels between these columns [99, 100].

A secondary formation of ettringite may occur in mature cement pastes. Sulphate ions coming from the environment could react with portlandite and monosulphoaluminate to form new ettringite [48]. Furthermore, monosulphoaluminate is not stable at temperatures higher than 70º. If the cement paste is exposed to those temperatures, the monosulphoaluminate dissolution releases Al^{+3} and SO_4^{-2} ions. The first ions are likely to enter the silicate structure of the C-S-H gel, and therefore, when the temperature decreases again, the Al^{+3} to SO_4^{-2} ratio is lower, and ettringite is formed [48, 98]. Both processes, known as sulphate attack and delayed ettringite formation, are associated to an expansion of the cement paste and the apparition of micro-cracks, although the mechanism is not fully understood [48, 98].

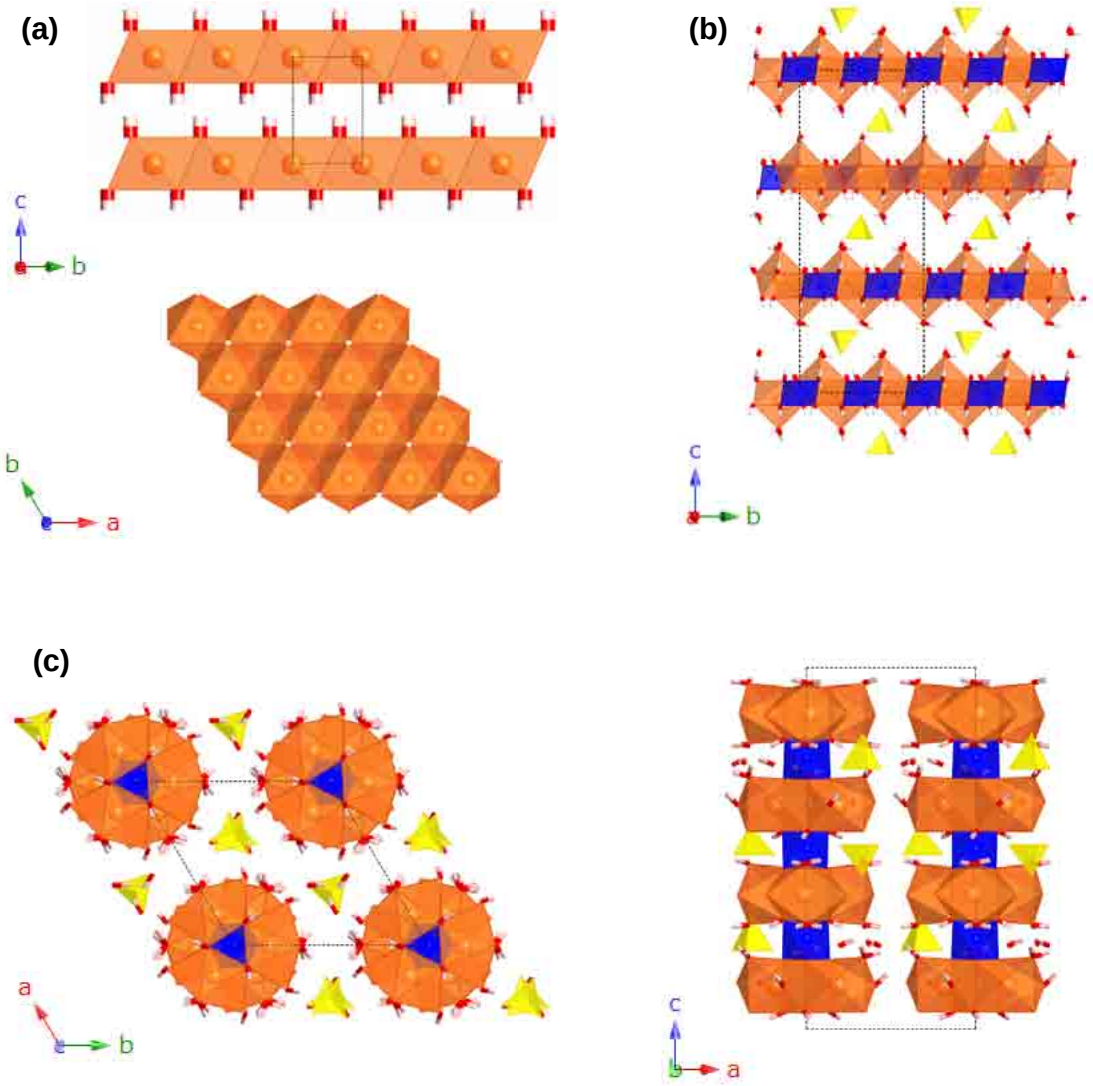

Figure 1.6.1- Main crystalline species formed during the clinker hydration. **(a)** Structure of portlandite, showing the layered structure and the hexagonal coordination of Ca to OH groups. **(b)** Structure of kuzelite, a natural analogous to the monosulphoaluminate present in the cement paste, with 18 water molecules per unit cell. **(c)** Two views of the crystalline structure of ettringite, where the arrangement in columns can be easily seen. The colour code and representation follow those given in ***figure 1.5.2*** and ***figure 1.2.1***. The sulphur atoms are shown in yellow, inside a tetrahedron due to its specific coordination.

- ***Monosulphoaluminate***

Monosulphoaluminate is an AFm compound (Al_2O_3-Fe_2O_3-monosulpho), which is formed in the cement paste after the dissolution of ettringite, when the gypsum content

has been consumed. It has a stoichiometry $C_4A\bar{S}H_{12}$, with a layered structure derived from that of portlandite. One in three Ca^{+2} ions are replaced by Al^{+3}, distorting the principal layer and displacing alternate calcium atoms in opposite directions from the centre of the sheet. The charge defect is compensated by the inclusion of SO_4^{-4} ions in the intralayer space, surrounded by water molecules, see ***figure 1.6.1***. The water content is uncertain, variable in the range between 12 to 18 molecules per unit cell [4]. The structure of low water content varieties has not been yet determined. However, the most hydrated variety (with 18 water molecules in the interlaminar space) has a natural analogue called kuzelite, for which the structure is fully resolved [101].

The monosulphoaluminate phase is strongly linked to ettringite. The former has greater Al/Si ratio that the latter and all the processes involving the dissolution and the formation of ettringite and monosulphoaluminate are determined by this ratio. The monosulphoaluminate is formed by dissolution of ettringite when the Al content decreases during the hydration due to the gypsum consumption. Opposite, when the Al content increases by sulphate attack, monosulphoaluminate dissolves giving rise to ettringite. Therefore, they are intimately tied.

1.7. Computational simulation in cement research

The development of computational models to describe the microstructure and properties has been a constant in material science and technology. The case of cement-based material is not an exception. Many efforts have been made in the modelling of its elastic properties, transport properties, degradation, hydration, microstructure development, etc [96, 102-107]. The random and complex nature of cement-based materials makes difficult a complete and realistic model of their properties. In fact, it has been stated that "*there is no hope that it would ever be possible to describe the properties of cement-based materials realistically, i.e., in the same way as this can be done for, for example, with metals and other well-structured materials*" [108]. However, some progress have been made [109]. Among the most successful models, the NIST [55, 110], the DUCOM [111] and the HYMOSTRUC [112, 113] models can be cited. In

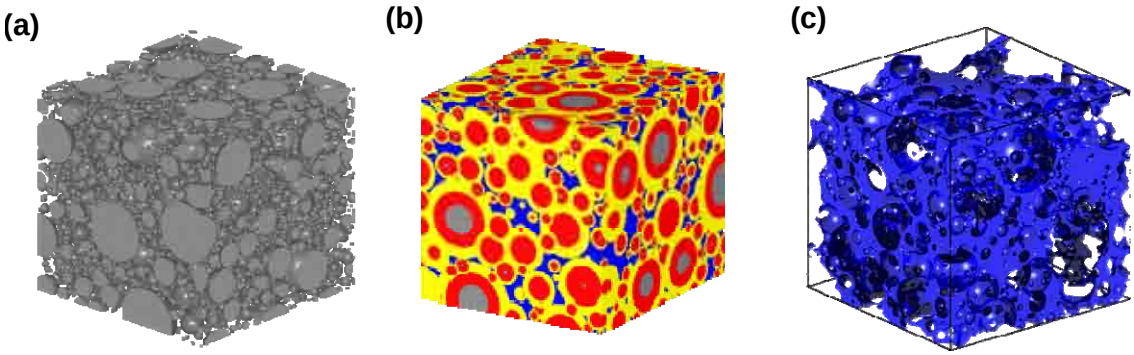

Figure 3.7.1.- Simulation boxes showing the virtual structures during a microstructure development simulation with the HYMOSTRUC code from the TU Delft. **(a)** Generated clinker particle distribution. **(b)** Development of the inner product (red) and outer product (yellow) around the clinker particles (grey). **(c)** Capillary structure obtained after removing the solid phase.

these models the formation of the cement paste microstructure is modelled explicitly, and the mechanical, physical, and transport properties are calculated as a function of the developed microstructure. Recently, a microstructural model based on chemical kinetics and the cellular automaton algorithms has been reported, called HydratiCA [114]. One of the advantages of HydratiCA is that it can be adapted to different materials if some physical properties of the material (density, diffusivity, volume) and the chemical reaction rates are known [114].

Atomistic simulation methods have been scarcely applied to cement research. Opposite to the microstructural models mentioned above, atomistic simulation methods are not developed to simulate a specific material. These methods model the interaction between the atoms, and can be applied in general for any atomic system. The unsettled nature of the C-S-H gel and the big number of atoms in cement related problems are probably the main obstacles for the use of atomistic simulations in this field.

The main subject under study employing atomistic simulation methods has been the C-S-H gel, usually employing tobermorite as structural model. Using Monte Carlo methods, Pellenq et al. studied the electrostatic attraction between charged surfaces [115-117] . They calculate the perpendicular pressure between two charged parallel sheets

neutralized by different counterions in the interlaminar space. They found that for the values of a C-S-H gel fully protonated layer and Ca^{+2} as counterion, the necessary pressure to separate the layers was the maximum compared to other compositions. The same authors also carried out force field simulations of tobermortite-like Hamid´s structure [118]. They found three energy minima as a function of the lattice parameter perpendicular to the layers, corresponding to 9, 11 and 14 Å varieties of the tobermorite family [117, 119]. They calculate as well the Young modulus of Hamid's structure and tobermorite 14 Å, obtaining values of E = 71.8 GPa and 63.5 GPa respectively [119].

Molecular Dynamics methods have been also applied to the study of the C-S-H gel. Faucon et al. analysed the chain breakage and interlaying crossing of the silicate chains for different C/S ratios and the effect of the Al^{+3} for Si^{+4} substitution in tobermorite [120, 121]. Dolado et al. [122] studied the polymerization of $Si(OH)_4$ groups in presence of variable amounts of $Ca(OH)_2$. They obtained a good correlation with the experimental data in the mean chain length and polymerization degree of the formed cluster versus their C/S ratio. They concluded that the C-S-H gel presents a tobermorite-like structure for low C/S ratio and jennite-like structure for high C/S ratios. Kalinichev et al. focused their work in the study of the mineral – water interfaces [123-127]. They developed a suitable force field for clay systems (CLAYFF [124]), and studied the water-surface interactions and the diffusivity of dissolved ions within the surface [123, 126, 127].

Ab-initio methods have been not so extensively applied to the study of cement materials. The C-S-H gel silicate chain stability was studied by Ayuela and co-workers using DFT methods [128], confirming the $3n - 1$ rule for the most stable lengths. Rhaman et al. utilised HF methods and concluded that for isolated chains the Al^{+3} and Si^{+4} substitution is always thermodynamically stable independently of the position within the chain [129]. Finally, Yamanaka et al. employed semiempirical, HF and DFT methods to calculate the stability of Al in Hamid's structure. Their results were in disagreement with the experimental data, fact that they attributed to the differences between the real structure and their model [130].

Chapter 2:

Overview of Atomistic Simulation methods

2.1. Introduction to Atomistic Simulation Methods

The philosophical hypothesis of atoms as the tiniest and indivisible particle that composes matter was proposed by early Greek and Indian academics. However, it was Dalton in 1808 who finally established, from experimental findings, the modern concept of the atoms. During the second half of the XIX century, Clausius, Maxwell, and Boltzman developed the kinetic theory of gases. This model was one of the first and more successful applications of the concept of atoms and molecules to describe a real system. Unfortunately, there are very few systems for which the equilibrium properties can be calculated with models (ideal gases, harmonic crystals, or ferromagnetic materials employing the Ising model are some examples). Typically, the systems, and the interactions that govern them, are too complicated to be evaluated analytically [131]. The arrival of computers was, therefore, of relevance, as they were able to solve numerically large systems of equations. The first computational simulation of liquids was carried out in 1953 at Los Alamos with the *Monte Carlo* (MC) method [132], and the first *Molecular Dynamics* (MD) simulation of hard spheres was reported in 1956 [133].

The mentioned simulation methods assume that the atomic behaviour can be described by classical models and equations. However, in the early 1900, Planck, Einstein, Dirac, Pauli, Born, de Broglie, Schrödinger and others, established the basics of quantum mechanics. Quantum phenomena are relevant when the dimension of the system under study is small, in the size of atoms and molecules. Based on previous findings, Schrödinger discovered heuristically in 1926 its equation for the hydrogen atom [134]. This equation plays the same role as Newton's equation in classical systems, and tells how the wave function of a system evolves with time. After further development and several approximations [135], the numerical resolution of the time independent Schödinger equation was possible using computers. The first *ab-initio Hartree-Fock* (HF) calculations on diatomic molecules were carried out in 1956 at the Massachusetts Institute of Technology [136].

The theories underlying atomistic simulation methods were independent from the existence of computers. However, the mathematical complexity of the algorithms to be solved made the computers indispensable in any atomistic simulation. Since computers were available for non-military purposes in the 50's, atomistic simulation methods have become essential in many different research areas, such as drug design in organic chemistry, protein and DNA studies in biochemistry, or magnetism, electronics and optics in material science. In the present Thesis different levels of theory were employed, each of them chosen to solve specific questions in view of their capabilities. Thus, the simulation details for each problem are included in the corresponding chapter. The aim of this chapter, then, is just to provide a rough idea of the theory and capabilities of the computational methods employed during this research. A more complete and technical description of the formalisms would be too long, and is beyond the scope of this Thesis. However, the references to get further information are given through the text.

2.2. *Ab-Initio* Methods

Ab-initio methods, also called first principles methods, owe their name to the fact that

are derived directly from theoretical principles, and do not fit any empirical parameter during the calculation. There are different levels of approximation depending on the treatment of the electronic correlation and on the influence of relativistic effects. The usual starting point for any discussion of *ab-initio* calculations is the time independent *Schrödinger equation*:

$$\hat{H}\,\Psi_i(\vec{r}) = E_i\,\Psi_i(\vec{r}) \tag{2.2.1}$$

Here $\hat{H}$ is the *Hamiltonian* operator, which acts upon the *wave function* of the system in a determined state $i, \Psi_i(\vec{r})$, and returns the system energy at that state, E_i.

The Hamiltonian is a differential hermitical operator corresponding to the total energy. For a general system of *N* electrons and *M* nuclei, in absence of external fields [137, 138] it can be written in atomic units as:

$$\hat{H} = -\frac{1}{2}\sum_{i=1}^{N}\nabla_i^2 - \frac{1}{2}\sum_{A=1}^{M}\frac{1}{m_A}\nabla_A^2 - \sum_{i=1}^{N}\sum_{A=1}^{M}\frac{Z_A}{r_{iA}} + \sum_{i=1}^{N}\sum_{j>i}^{N}\frac{1}{r_{ij}} + \sum_{A=1}^{M}\sum_{B>A}^{M}\frac{Z_A Z_B}{r_{AB}} \tag{2.2.2}$$

where *i* and *j* run over the electrons in the system, *A* and *B* run over the nuclei and ∇_i is the Laplacian operator. The two first terms in equation (2.2.2) take into account the kinetic energy of the electrons ($\hat{T}_{ele}$) and nuclei ($\hat{T}_{nuc}$). The remaining terms are the potential energy due to interactions between electrons and nuclei ($\hat{V}_{ele-nuc}$), interaction between electrons ($\hat{V}_{ele-ele}$), and interaction between nuclei ($\hat{V}_{nuc-nuc}$). Thus, the previous equation can be abbreviated as:

$$\hat{H} = \hat{T}_{ele} + \hat{T}_{nuc} + \hat{V}_{ele-nuc} + \hat{V}_{ele-ele} + \hat{V}_{nuc-nuc} \tag{2.2.3}$$

The wave function $\Psi_i(\vec{r})$ contains all the information of a system in a determinate state *i*. The wave function is not an observable itself; only its square has physical interpretation as the probability distribution to find the system in a determined state. For

instance, the square of an electronic wave function gives us the electronic density [135, 139].

The analytical resolution of the Schödinger equation is not possible with few exceptions [135]. The *variational principle*, gives the recipe for a systematic approach to the correct solution [135]. Considering a trial wave function $\Psi_{trial}(\vec{r})$, the variational principle says that the corresponding energy, E_{trial}, will be equal to the minimal possible energy of the system, i.e. the ground state energy E_0, only if $\Psi_{trial}(\vec{r})$ is the wave function of ground state. Otherwise, E_{trial} will be always higher than the ground state energy E_0. The construction of an acceptable wave function must track the objective of obtaining an energy as low as possible, and thus, closest to the ground state value.

The evaluation of the Schrödinger equation can be further simplified for molecules according to the *Born-Oppenheimer approximation* [140]. The wave function of a system can be separated in two terms, the electronic (Φ_{ele}) and the nuclear (Φ_{nuc}), and both can be studied separately:

$$\hat{H}\,\Phi_{ele}(\vec{r})\,\Phi_{nuc}(\vec{r}) = E_{total}\,\Phi_{ele}(\vec{r})\,\Phi_{nuc}(\vec{r}) \qquad (2.2.4)$$

This is often justified in a rough manner by saying that under typical physical conditions, the nuclei are considerably heavier than the electrons (neutrons and protons are approximately 1800 times heavier than electrons) and consequently the nuclei move slower than the electrons. In fact, the nuclei can be considered fixed while computing the electronic states. As a first step, the kinetic term of fixed nuclei in the Hamiltonian $\hat{T}_n$ is equal to zero, and the potential term due to inter-nuclei interactions $\hat{V}_{n-n}$ is constant. Then, the Schrödinger equation (2.2.1) for the electrons is written as:

$$[\hat{T}_{ele} + \hat{V}_{ele\text{-}nuc} + \hat{V}_{ele\text{-}ele}]\;\Psi_{ele}(\vec{r}) = E_{ele}\,\Phi_{ele}(\vec{r}) \qquad (2.2.5)$$

In a second step the interaction between frozen nuclei and the nuclei kinetic energy are

considered. The energy obtained for the electronic part also contributes as a potential term:

$$[\hat{T}_{nuc} + \hat{V}_{nuc\text{-}nuc} + E_{ele}]\ \Phi_{nuc}(\vec{r}) = E_{total}\ \Phi_{nuc}(\vec{r}) \qquad (2.2.6)$$

Due to the Born-Oppenheminer approximation, the *Potential Energy Surface* (PES) of a molecular system can be defined. The PES is the surface defined by the electronic energy over all the possible nuclear coordinates. Some concepts such as the local stability and the geometries of equilibrium and transition states are defined as critic points of the PES [141, 142].

2.2.1. The Hartree-Fock Method

The Schrödinger equation can be solved analytically for hydrogen-like atoms, with a nucleus and one electron. In such cases, the equations describe the system as a radial force problem with the electron distance from the nucleus as the unique variable [135]. The eigenfunctions of the Schödinger equation are called *hydrogen-like wave functions*. For systems with more than one electron, the electrons are not independent, and the problem cannot be solved analytically (the so called *many-body problem*). The first approximation to overcome the problem is the *Hartree method* or *independent particle approximation*. In such method, each electron is treated separately, splitting up the wave function as a product of one-electron wave functions. Thus, the Hamiltonian is that which corresponds to one electron, and the electron-electron interaction is calculated separately, as one electron moving in the average potential of the rest (known as the *mean-field* approach). The total electronic Hamiltonian is:

$$\hat{H}_{ele} = \hat{T}_{ele} + \hat{V}_{ele-nuc} + \hat{V}_{ele-ele} = \sum_{i}^{N} \hat{h}_1 + \sum_{i,j\neq i}^{N} J_{ij} \qquad (2.2.7)$$

where $\hat{h}_1$ is the one electron Hamiltonian and J_{ij} is the *Coulomb integral* which represents the classical repulsion between two charge distributions [135, 137, 141].

Despite the Hartree is a useful approximation, the obtained wave function violates the indistinguishability of electrons. Moreover, electrons are fermions, so their wave function must be *antisymmetric*. They have associated a *quantum angular momentum* (spin) with values = ±1/2, and must obey the *Pauli´s exclusion principle*. Therefore, no more than two electrons can be in the same orbital. The way of representing the antisymmetric electronic wave functions for a system of *N* electrons is the *Slater determinant*:

$$\Psi_{ele}(\vec{r}_1,\vec{r}_2,...,\vec{r}_N) = \Psi_{SD} = \frac{1}{\sqrt{N!}}\begin{vmatrix} \chi_1(1) & \chi_2(1) & \dots & \chi_N(1) \\ \chi_1(2) & \chi_2(2) & \dots & \chi_N(2) \\ \vdots & \vdots & \ddots & \vdots \\ \chi_1(N) & \chi_2(N) & \dots & \chi_N(N) \end{vmatrix} \qquad (2.2.8)$$

where χ_i are the spin-orbitals, a one electron wave function product of a spatial part and a spin part. The *Hartree-Fock method* (HF) is an extension of the Hartree method, where the electron wave function is described by a Slater determinant. Again, each electron is considered to move independently for the others in the spin orbital space. The kinetic energy and the repulsion between electrons and nuclei is evaluated as in the Hartree method. However, the interaction with other electrons has now a new contribution due to the spin, the *exchange integral* K_{ij} without classical analogy. The *Fock operator* for each electron is:

$$\hat{f}_i = -\hat{T}_{ele} + \hat{T}_{nuc} + V_i^{HF}\{j\} = \hat{h}_i + \sum_j^N (J_j - K_i) \qquad (2.2.9)$$

where $V_i^{HF}\{j\}$ is the Hartree-Fock potential, $\hat{h}_i$ is the Hartree Hamiltonian for one electron, and J_j and K_i are the operators defined so as to give the corresponding Coulomb and exchange integrals respectively.

In 1951 Roothaan proposed to represent each one electron orbital χ_i as a *linear*

combination of atomic orbitals (LCAO) [143]:

$$\chi_i = \sum_{j=i}^{N} a_{ij}\varphi_i \tag{2.2.10}$$

where a_{ij} are the coefficients in the linear combination of the atomic orbitals φ_i. Although called atomic orbitals, the functions φ_i are usually a set of known functions as those proposed by Slater, Pople, Gaussian functions, etc., [144]. If the Schrödinger equation is written using the Fock operator and the LCAO approach, we get:

$$\hat{f}_i \sum_{j=1}^{N} a_{ij}\varphi_i = \varepsilon_i \sum_{j=1}^{N} a_{ij}\varphi_i \tag{2.2.11}$$

where ε_i are the corresponding energies for the orbitals χ_i. Multiplying the equation in both sides by the φ_i atomic orbitals, integrating over all the space and rearranging the terms, the Roothaan-Hall secular equation is reached:

$$\sum_{j=1}^{N} a_{ij}(F_{ij} - \varepsilon_i S_{ij}) = 0 \tag{2.2.12}$$

where F_{ij} and S_{ij} are the *Fock* and *overlap integrals*. This set of equations can be represented in matrix notation:

$$\begin{pmatrix} F_{11}-\varepsilon_i S_{11} & F_{12}-\varepsilon_i S_{12} & \dots & F_{1N}-\varepsilon_i S_{1N} \\ F_{21}-\varepsilon_i S_{21} & F_{22}-\varepsilon_i S_{22} & \dots & F_{2N}-\varepsilon_i S_{2N} \\ \vdots & \vdots & \ddots & \vdots \\ F_{N1}-\varepsilon_i S_{N1} & F_{N2}-\varepsilon_i S_{N2} & \dots & F_{NN}-\varepsilon_i S_{NN} \end{pmatrix} \begin{pmatrix} a_{11} & a_{12} & \dots & a_{1N} \\ a_{21} & a_{22} & \dots & a_{2N} \\ \vdots & \vdots & \ddots & \vdots \\ a_{N1} & a_{N2} & \dots & a_{NN} \end{pmatrix} = 0 \tag{2.2.13}$$

or in a more compressed form as $\mathbf{F}\boldsymbol{A_i}=\varepsilon_i\mathbf{S}\boldsymbol{A_i}$, where **F** and **S** are the Fock and overlap matrices respectively [141]. The secular equation is solved by finding the various roots ε_i. Then, the energy is calculated as a sum of the energies for the *N* occupied orbitals, minus a correction term that arises from the double counting of the electron-electron

interaction due to the one electron Hamiltonian in the Fock operator:

$$E = \sum_{i=1}^{N} \varepsilon_i - \sum_{i=1}^{N/2} \sum_{j=1}^{-N/2} (2J_{ij} - K_{ij}) \qquad (2.2.14)$$

The Hartree-Fock method neglects the electron correlation due to the mean-field approximation. The so called *post-Hartree Fock* methods were devised to include electron correlation to the multi electron wave function [141, 142]. For example, the Møller–Plesset perturbation theory treats correlation as a perturbation of the Fock operator. Other methods such as the configuration interaction (CI), the multi-configurational self-consistent field (MCSCF), and the complete active space SCF (CASSCF), expand the true multi-electron wave function in terms of a linear combination of Slater determinants [141, 142]. However, the computational cost of post-HF makes them unviable to treat a moderate number of atoms. An alternative is the Density Functional Theory method, which includes an approximate solution to the exchange and correlation effects.

2.2.2. Density Functional Theory

The wave function plays a key role in HF methods. Although the wave function has not physical meaning itself, its square has the physical interpretation as the probability to find the electrons in a determined volume. Thus, the electronic density is the square of the wave function integrated over all the space for $N - 1$ electrons, being N the total number of electrons of the system. To calculate the energy through the electronic density seems to be, therefore, a way to overcome the manipulation of the wave function. After the early work of Thomas-Fermi-Dirac and their *free electron gas approximation* [145, 146], Hohenberg and Kohn established the basis of Density Functional Theory with two theorems [147]. First, the *existence theorem* demonstrates that the wave function of a system in the ground state is a functional of the electronic density, $\Psi_i(\vec{r}) = f\left[\rho(\vec{r})\right]$, and therefore, the ground state properties are also density functionals. Second, the *Hohenberg and Kohn variational principle* states that the energy obtained from a wave function constructed from a guess electronic density is

always greater than or equal to the real ground state energy. It must be noted that DFT mainly concerns the ground state properties [146].

In 1965 Kohn and Sham proposed a self-consistent method to solve the variational problem of minimizing the energy [148]. Using the Born-Oppenheimer approximation, the density-dependent energy can be divided in three parts:

$$E\left[\rho(\vec{r})\right] = T_{ele}\left[\rho(\vec{r})\right] + V_{ele-nuc}\left[\rho(\vec{r})\right] + V_{ele-ele}\left[\rho(\vec{r})\right] \tag{2.2.15}$$

Parallel to the operators in the HF methods, T_{ele}, $V_{ele\text{-}nuc}$, and $V_{ele\text{-}ele}$ are the density functionals which account respectively for the electron kinetic energy, the potential energy due to the electron-nucleus interactions, and the potential energy due to the interaction between electrons. Kohn and Sham simplify the problem taking as starting point an ideal system of non-interacting electrons with the same density as the ground state density of the real system. The equation (2.2.15) is rewritten then as:

$$\begin{aligned} E\left[\rho(\vec{r})\right] = {} & T_{n.i.\ ele}\left[\rho(\vec{r})\right] + V_{ele-nuc}\left[\rho(\vec{r})\right] + \\ & + V_{n.i.\ ele-ele}\left[\rho(\vec{r})\right] + \Delta T_{ele}\left[\rho(\vec{r})\right] + \Delta V_{ele-ele}\left[\rho(\vec{r})\right] \end{aligned} \tag{2.2.16}$$

The first term in the right hand side of equation (2.2.16) is the kinetic energy of electrons derived by Thomas and Fermi for an infinite homogeneous gas made of non-interacting electrons. The second term is the potential energy due to the interaction of a charge density (electronic density) and point charges (nucleus). The third term is the potential energy due to repulsion between two densities of charge [145, 146]. The last two terms include all the non-classical interactions of the electrons. They are collected together as the exchange-correlation energy, E_{xc}, and include the correlation and exchange energies, as well as all the corrections to the one electron kinetic energy between the ideal non-interacting system and the interacting one. If orbitals are considered, similar expressions to those of the HF method are achieved, called Kohn-Sham equations:

$$\hat{h}_i^{KS}\chi_i = \varepsilon_i\ \chi_i \tag{2.2.17}$$

where χ_i are the Kohn-Sham set of one electron orbitals that reproduce the ground state electronic density, ε_i their corresponding energies, and $\hat{h}_i^{KS}$ the one electron *Kohn-Sham operator*:

$$\hat{h}_i^{KS} = \hat{T}_{ele} + \hat{V}_{ele-nuc} + \hat{V}_{ele-ele} + \hat{V}_{xc} \tag{2.2.18}$$

The V_{xc} is the functional derivative for which the value of the *Kohn-Sham determinant* is equal to E_{xc}. The one electron orbitals can be expressed as LCAO:

$$\hat{h}_i^{KS}\sum_{j=1}^{N} a_{ij}\varphi_i = \varepsilon_i \sum_{j=1}^{N} a_{ij}\varphi_i \tag{2.2.19}$$

and a secular equation of the form $\mathbf{H_{ks}}\boldsymbol{A_i}=\boldsymbol{\varepsilon_i}\mathbf{S}\boldsymbol{A_i}$ is obtained, where $\mathbf{H_{ks}}$, and **S** are the Kohn-Sham and overlap matrices respectively. The numerical procedure to solve the secular equation is analogous to that of Hartree methods, with the exception of the exchange-correlation part that depends on the density and therefore must be solved numerically by grid integration methods [149].

Although not employed in this Thesis, it should be mentioned that there are other methods in DFT calculations to calculate the one electron electronic states, such as the Atomic Sphere Approximation (ASA), as grids samplings, and Plane Waves (PW). Plane waves are popular in solid state physics as they implicitly involve the concept of periodic boundary conditions. They are the solutions of the Schrödinger equation for a free particle, and they are not centred at the nuclei but extend through the complete space [149, 150]. Each orbital wave function is expressed as a linear combination of plane waves which differ by reciprocal lattice vectors (G) of the periodic cell:

$$\psi_i^k(r) = \sum_G a_{i,k+G}\cdot e^{i(k+G)r} \tag{2.2.20}$$

where *i* is the imaginary unit and *k* the wave vector. The use of PW's present the advantage that they are a complete basis set, i.e. when the number of basis set increases, the orbital wave function is described more accurately, condition that is not necessary fulfilled by the LCAO approximations [149]. Their main disadvantage is that usually many PW are necessary to obtain accurate results for the core orbitals localized around the nucleus and, hence, they have a high computational cost. This problem is partially solved with introduction of pseudopotentials that describe the core electrons and nucleus with effective potentials [149].

Up to this point, the spin component has not being taken into account. It is common to deal with the spin by splitting the density in two components, ρ^{α} and ρ^{β}. By convention, the spin density at a point is given by the *normalized spin polarization* [149]:

$$\zeta(\vec{r}) = \frac{\rho^{\alpha}(\vec{r}) - \rho^{\beta}(\vec{r})}{\rho(\vec{r})} \qquad (2.2.21)$$

The spin polarization is important when the spin symmetry is broken, as in the case of systems with unpaired electrons and magnetic materials [149]. That is not the case of the systems under study in this Thesis, and therefore the spin polarizability was not included in the calculations.

Unfortunately, the V_{xc} functional in equation (2.2.18) is unknown (with the exception of the free electron gas). Thus, an approximated expression for the E_{xc} that describe reasonably well the expected real value of E_{xc} must be found. The exchange-correlation energy is commonly expressed as:

$$E_{xc}\left[\rho(\vec{r})\right] = \int \rho(\vec{r})\,\varepsilon_{xc}\,d\vec{r} \qquad (2.2.22)$$

where ε_{xc} is called *energy density*. There are different approaches to obtain ε_{xc}, usually as a sum of the different contributions (ε_x and ε_c). First, the *Local Density Approximation* (LDA) assumes that the value of ε_{xc} can be calculated from the local

value of the electron density at that point. Going further, it seems clear that the electronic density in a molecule is far from being uniform. Thus, an extension of the LDA, the *General Gradient Approximation* (GGA), makes the functional dependent on the local density at one point and its gradients. Finally, *Hybrid Methods* makes a mixture between HF and DFT to obtain an accurate E_{xc}. Note that in HF the exchange is considered exactly, while the correlation is completely ignored. These hybrid methods are the *Adiabatic Correction Formula*, a relationship between HF and DFT exchange and correlations using empirical constants.

For each approximation there are many different exchange and correlations functionals, which can be found in the literature [137, 141, 144-146]. Note that once approximations and empirical parameters are included, the method is no more variational and even energies lower than the exact ground state energies can be obtained.

2.3. Molecular Mechanics Methods

Molecular mechanics methods are based in two basic assumptions. The first one is the Born-Oppenheimer approximation. In *ab-initio* methods, nuclei can be assumed frozen during the first step with respect from the electronic motion. Then, the electronic arrangement is studied. In other words, it could be considered that electrons can adjust instantaneously to the nuclei position for any movement. The system energy in a configuration can be, therefore, calculated as a function of the nuclear positions, with the electrons around them in an optimal distribution [137].

The second assumption is that each nucleus can be studied as a classical particle. Therefore, the potential energy surface (PES) of the system can be evaluated according to Newtonian mechanics. The presence of electrons is not taken into account explicitly but it is implicit in the description of the atoms. They are simulated as spheres, with an assigned radius and charge, interacting by means of a collection of two or many body interatomic potentials [141, 144].

The main advantage of molecular mechanics methods is that they can deal with a large number of particles (atoms), with a relative low computational effort. If the employed force field describes well the system, it could provide accurate information on structures, thermodynamics, and mechanical properties with a low computational cost. Nevertheless, they present two main drawbacks. On the one hand, there is no guarantee that certain potentials could simulate properly structures different from the originals used to fit them. The potentials are usually built up to describe the interactions of atoms under a given neighbourhood. The same atoms in different environments are expected to interact with each other in different ways. Therefore, before any simulation, the employed sets of potentials must be carefully checked with the experimental data to assess their transferability. On the other hand, molecular mechanics methods cannot provide information of the electronic structure as they omit the electronic nature of the atoms. It must be also noted that the total energy obtained by this method (called *Lattice energy* for crystalline systems) has no physical sense for most force fields, although relative differences in energy have proved to be useful in conformational analysis.

2.3.1. Potential energy functional forms

The energy of a system in a molecular mechanics calculation is defined as the sum of all the interactions present. The functional form of the explicit interaction between a given pair or group of atoms is usually chosen based on physical insights, as to the nature of the forces between the particles. The parameters of the force field are chosen to fit *ab-initio* calculations or experimental data. Hereafter, the most common interactions and potentials are described. A large collection of functional forms can be found in the literature [151].

- ***Coulomb interaction***

Long-range Coulomb interaction is the most important contribution in ionic solids. The functional form for the energy is given by the Coulomb's law:

$$U_{AB}^{Coulomb} = \frac{qA \cdot q_B}{r_{AB}} \qquad (2.3.1)$$

where q is the charge of the corresponding atom and r the distance between them. Although being simple, the practical evaluation of this term is complicated due to convergence problems in systems with low symmetry. The energy decays with the inverse of the distance r_{AB}, while the number of ions increases proportionally to the surface of a sphere, $4\pi r^2$. Thus, the energy increases rather than decrease. Among the different techniques employed to overcome the problem [131], the Ewald's summation [152] is the most widespread. The Coulomb term is divided by a Laplace transformation in two terms, one of which converges rapidly in the real space and the other one in the reciprocal space.

- ***Dispersive interaction***

Dispersive interaction (London forces, attractive van der Waals forces) is the second long-range interaction [153], usually important in systems where the coulomb interaction is not large, such as molecular crystals. This force arises from the fact that the distribution of the electrons around the nucleus is not uniform. Even in absence of permanent charge, the fluctuations in the electron densities can create induced dipolar and higher multipolar moments [154, 155]. The interaction is given by a series of terms increasing with the inverse of the 6^{th}, 12^{th}, 18^{th}, … power of the interatomic distance. However, the most important force is due to dipolar moments, and usually only the first term of the series is employed to represent the dispersion:

$$U_{AB}^{Disp} = -\frac{C}{r_{AB}^6} \qquad (2.3.2)$$

which inversely depends on the 6^{th} power of the interatomic distance r_{AB} , and C an is empirical parameter. As in the case of Coulomb interactions the Ewald-like summation technique is often employed to speed up the convergence [131, 151].

- ***Repulsive interaction***

The repulsive energies at short distances arise from the overlap of the electronic clouds when two atoms are close. The most employed representations of the force are as an exponential function, or as a positive terms varying with the 12th inverse power of the distance. Usually, the repulsive and dispersive forces are included in the same functional forms. For instance, the Buckingham form is given as:

$$U_{AB}^{buckingham} = A\, e^{\left(-\frac{r_{AB}}{\rho}\right)} - \frac{C}{r_{AB}^{6}} \tag{2.3.3}$$

or alternative, the Lennard-Jones form as:

$$U_{AB}^{Lennard-Jones} = \frac{C_m}{r_{AB}^{m}} - \frac{C_n}{r_{AB}^{6}} \tag{2.3.4}$$

where A, ρ and C are empirical parameters, r_{AB} is the interatomic distance, and m is typically chosen as 12 in the Lennard-Jones functional form (eq. (2.3.4)). The potentials have a minimum at some internuclear distances, increasing rapidly at short distances and smoothly at high distances [155]. In some particular cases, the energy component of the dispersive potential decreases faster than the repulsive component increases. In this situation, the net potential would be attractive and the atoms would collapse. To avoid this unphysical behaviour, the dispersive potential is dumped at short distances, assuming that the functional form of the dispersive potential is not valid when the electronics cloud start to overlap too much [156].

- ***Bonding interaction***

Unlike ionic systems, covalent bonds imply a localized distribution of electrons between atoms, forming a bond network. Thus, empirical functions with other physical dependence are employed to define the energy potential, such as the Morse potential:

$$U_{AB}^{Morse} = D_e\left[(1-e^{-\alpha(r-r_0)})^2 - 1\right] \tag{2.3.5}$$

In this equation, r_0 is the interatomic equilibrium distance, D_e is the energy of the bond at the equilibrium distance (depth of the potential), and α is the curvature of the potential around the equilibrium distance, determined from vibrational frequencies. As the functional form describes all the contributions for the chemical bond, the coulomb interaction is frequently subtracted when these bonding potentials are used.

Covalent bonding entails specific shapes in many cases due to the hybridization of the bonds, such as tetrahedral bonds in carbon and silicon [144]. In such cases, three body potentials are taken to describe these forces, such as the harmonic potential, which penalize deviations from the optimal angle:

$$U_{ABC}^{harmonic} = \frac{1}{2}k\left(\theta-\theta_0\right) \tag{2.3.6}$$

where θ_0 is the equilibrium angle and k is a force constant.

2.4. Molecular Dynamics Methods

Note that all the methods explained so far calculate the system properties for a given configuration. Aditionally, Molecular Dynamics methods calculate the equilibrium properties of a system following the atoms over a certain time period.

In a classical system, any state can be completely described from the position (q) and momentum (p) of all the particles that composes the system.

$$\begin{aligned}\mathbf{q} &= (q_x^1, q_y^1, q_z^1, q_x^2, q_y^2, q_z^2, ..., q_x^N, q_y^N, q_z^N)\\ \mathbf{p} &= (p_x^1, p_y^1, p_z^1, p_x^2, p_y^2, p_z^2, ..., p_x^N, p_y^N, p_z^N)\end{aligned} \tag{2.4.1}$$

In the phase space each point represents the **q** and **p** of the particles in the system, and the evolution of them can be followed as a trajectory. The imaginary collection of the system copies in each state or phase points, considered all at once, is called *ensemble*. Any system property, lets say *A*, of the system at the equilibrium can be calculated as an average:

$$\langle A \rangle = \iint A(\mathbf{q},\mathbf{p})\, P(\mathbf{q},\mathbf{p})\, d\mathbf{q} d\mathbf{p} \qquad (2.4.2)$$

where $A(\mathbf{q},\mathbf{p})$ is the property value in one phase space point, and $P(\mathbf{q},\mathbf{p})$ is the system probability to be in that point. The quantity computed from equation (2.4.2) is an *ensemble averag*e. However, the probability for a system being in some of the phase space points is near-zero, and therefore, those points do not contribute to the *A* property expected value. Thus, the $\langle A \rangle$ average value can be calculated checking the most probable configurations of a system, instead all the possible configurations. This methodology is followed in Monte Carlo (MC) methods, not covered here as it is not used in this Thesis

In the case of Molecular Dynamics the methodology is different. If a system starts in a phase space configuration close to the equilibrium configuration, and its trajectory is followed at constant energy, it seems likely that the system will evolve sampling the most probable points of the phase space. If the starting point is correct, the *A* property average can be calculated as:

$$\langle A \rangle = \frac{1}{N} \sum_{i}^{N} A(\mathbf{q},\mathbf{p},t_i) \qquad (2.4.3)$$

where *N* is the number of measurements at different times t_i. In the limit of continuous sampling and during an indefinitely time, the equation (2.4.3) becomes:

$$\langle A \rangle = \lim_{t \to \infty} \frac{1}{t} \int_{t_0}^{t_0+t} A(t)\, dt \qquad (2.4.4)$$

The *ergodic hypothesis* states that, for an isolated system at the equilibrium, all the accessible states are equally probable over a long time period, independently from the starting time, initial positions (**q**), and momenta (**p**) for a given number of atoms (*N*) in a volume (*V*) and at constant energy (*E*). Thus, the property average over time and the average over all the states (*ensemble average*) at the equilibrium are equal [131, 137, 141, 157].

In Molecular Dynamics simulations, the desired property must be computed from the particles position and momentum in the system. For example, the system density can be calculated as the average number of particles in a certain volume. Other quantities are measured by means of classical principles. For instance, the temperature is calculated from the equipartition principle:

$$\left\langle \frac{1}{2} m v_i^2 \right\rangle = \frac{1}{2} k_B T \qquad (2.4.5)$$

Thus, only the positions (**q**) and the momenta (**p**) must be known at each time. The particles in the system evolve following the classic Newton's motion equation:

$$F_i = m \cdot \frac{\partial^2 q_i}{\partial t^2} \qquad (2.4.6)$$

To integrate this equation, the forces acting on every particle must be known. Usually the same functional forms as in the Molecular Mechanics methods mentioned in the previous section are employed in Molecular Dynamics simulations. They allow the study of large systems during long time periods. However, the use of a force field implies some disadvantages already mentioned, such as their transferability. Furthermore, according to de Broglie's matter-wave duality, the quantum nature of atoms becomes evident for light particles at very low temperatures. As an example, the wavelength of a hydrogen atom in an OH bond vibration with duration of ~0.2 ps and a distance ~1 Å is approximately 2.2 Å, about the same order of the particle size, and therefore the quantum nature could be important. In such cases, the forces can be also

obtained from *ab-initio* calculations. For each step, the electronic problem is solved by *ab-initio* methods in a conventional way, and the resulting ionic forces are employed in the MD calculation. Other possibility to perform *ab-initio* molecular dynamics is the *Car-Parrinello method*. It introduces explicitly the electronic degrees of freedom as fictitious dynamical variables. An extended Langrangian for the system leads to a system of coupled equations for both the nucleus and electrons [158]. Unfortunately, the computational cost limits *ab-initio* MD methods to small systems and short time periods. For large systems, hybrid *Mechanics/Molecular Dynamics* (QM/MD) schemes calculate a small part of the system using *ab-initio* Molecular Dynamics, while the rest is treated classically [141].

- ***Integration algorithms***

Many algorithms have been developed to integrate Newton's equation (2.4.6). All of them present advantages and disadvantages. Problems in the energy conservation, energy drifts, irreversibility, high dependences of the starting point, or the need of short time steps are some of them [131]. The most employed due to its simplicity and performance is the Verlet algorithm [159]. The initial velocities are usually adjusted to a desired value of the (kinetic) energy, conserving the total momentum equal to zero. The coordinates of each particle are first expanded in Taylor series around the time up to the fourth term, in both "directions", backwards (t-Δt) forward (t+Δt) and. Summing both equations we get:

$$q(t+\Delta t) \approx 2q(t) - q(t-\Delta t) + \frac{F(t)}{m}\Delta t^2 \pm O(\Delta t^4) \qquad (2.4.7)$$

where q is the particle position, F are the forces acting on the particle, m is the mass of the particle, t is the current time, and Δt is the time step. The velocities are not needed to calculate the next positions, only the forces together with the current and past positions. However, the velocities can be derived from the rest of the Taylor series, forward and backward:

$$v(t) = \frac{r(t+\Delta t) - r(t-\Delta t)}{2\Delta t} + O(\Delta t^2) \qquad (2.4.8)$$

Note that the numerical error of the algorithm is in the order of Δt^4 for the positions and in the order of Δt^2 in the velocities.

Other algorithms are alternatives to the Verlet scheme, such as the Euler, the Leap Frog, and the velocity Verlet algorithms. Higher-Order schemes as the predictor-correction algorithm employ information from higher order derivatives of the Taylor expansion. For a detailed description of algorithms and their capabilities see references [131, 157, 160, 161].

- ***Ensembles***

The ergodic hypothesis states that the time average in MD is equal to the ensemble average in Monte Carlo (MC) methods. In MD simulations the time average properties of a system of *N* particles, are calculated while keeping constant the volume and the energy are measured. Those are the conditions of a *microcanonical ensemble* (*NVE*). However, in many cases it is convenient to perform calculations at constant pressure or temperature. For that purpose there are some alternatives that will be explained in the following.

One way to carry out MD simulation in the *canonical ensemble* (*NVT*), is by coupling the system to an imaginary heath bath [162]. The temperature is preserved constant by exchanging energy with this bath. The energy exchange is done applying impulsive forces on randomly selected atoms at a certain frequency. This process can be considered as a MC step which varies the energy between the usual MD steps in the microcanonical ensemble. The coupling strength between the system and the bath is controlled by the frequency of the energy exchange steps.

Other possibility is based on a modification of the Langrangian equations of motion. As shown in equation (2.4.5), the temperature depends on the average kinetic energy.

Thus, the temperature can be modified tuning the velocity, which in his turn can be modified changing the time step [163, 164]. A new variable which relates the real time of the system and the new rescaled one is introduced:

$$\partial t = s(t')\partial t' \tag{2.4.9}$$

and the equation of motion then reads:

$$F_i = m \cdot \frac{\partial^2 q_i}{\partial t'^2} + \frac{1}{s}\frac{\partial s}{\partial t'}\frac{\partial q_i}{\partial t'} \tag{2.4.10}$$

where the second term determines the friction between the system and the heat bath.

Under constant pressure and temperature, in the so-called *isobaric-isothermal ensemble* the pressure can be maintained constant at each time step varying the size and the shape of the simulation box [162, 165]. Then, the atomic coordinates are rescaled for the new box. As in the previous case, the Langrangian equations of motion are modified and they yield the following expression:

$$F_i = m \cdot V^{1/3} \cdot \frac{\partial^2 q_i}{\partial t'^2} + \left(\frac{\partial s}{\partial t'} + \frac{2}{3V}\frac{\partial V}{\partial t'} \right) \frac{\partial q_i}{\partial t'} \tag{2.4.11}$$

This formula is deduced for cubic boxes. Anyhow, the method can be extended similarly to non-cubic systems [157].

Chapter 3:

Assembly of C-S-H precursors

3.1. Introduction and computational method

The C-S-H gel is the most important component of the cement matrix. It can reach 70% by weight of the material, and it is the principal responsible for most of the cement paste properties, including the mechanical ones. However, the exact nature and composition of the C-S-H gel is unknown, due to its amorphous and variable structure. In the introductory chapter, some models proposed to describe the C-S-H gel at the atomic- and nano-scale have been already explained in detail. At the atomic scale, the C-S-H gel is depicted as a distorted version of tobermorite and/or jennite-like structures with very short range order [9, 62]. At a higher scale (1-100 nm), the starting point for the accepted models are some globules that pack themselves in different ways to form bigger structures. These globules have a characteristic length of ~4 nm, and they are not precisely described at the atomic scale [85, 90].

It must be noted that the existing models take into account intraglobular

characteristics, such as the presence of silicate chains, porosity, and water content, to explain experimental sorption isotherms and processes like creep and shrinkage [90, 93]. Thus, it is assumed that the internal structure of the particle is crucial for the properties of the gel, and hence for the cement paste. Furthermore, the cohesion among the C-S-H gel particles is a consequence of the iono-covalent nature of the chemical bonds, and therefore it is dependent on the surface structure [117, 119, 166]. However, the growth and arrangement of tobermorite and/or jennite-like particles to form these globules is unknown. It is clear that establishing the internal structure and the surface area of the globules would be important to understand the physico-chemical properties of the C-S-H gel.

In this chapter, the growth of the C-S-H gel particles is studied following an aggregation approach. The starting unit is a structure called *CSH precursor*, extracted from the crystal structure of tobermorite 14 Å and jennite [64, 68]. It is composed of two dimeric chains held together by calcium atoms, and could be considered the smallest identity unit of the C-S-H gel, see ***figure 3.1.1***. Then, the aggregation of two precursors with calcium ions is studied for two limit cases, analyzing the atomic charges, bond distances, and dipolar moments.

- ***Computational method***

The aggregation of precursor units was studied employing first principles methods, both in the Hartree-Fock (HF) and Density Functional Theory (DFT) approaches. On the one hand, the HF method was employed to perform the optimization calculations and the atomic Mulliken population analysis [167]. It was applied as it is implemented in the GAMESS code [168, 169]. After some tests, a Dunning-Hay double zeta basis set plus one polarization function with Dunning exponents was chosen [170]. The structure optimization was done using the quadratic approximation (QA) algorithm, a quasi-Newton-Raphson method in which the Hessian inversion is done approximately [142].

On the other hand, the DFT simulations were carried out with the Gaussian code [171]. With this program, the Fukui functions [146, 172] were calculated, as well as the

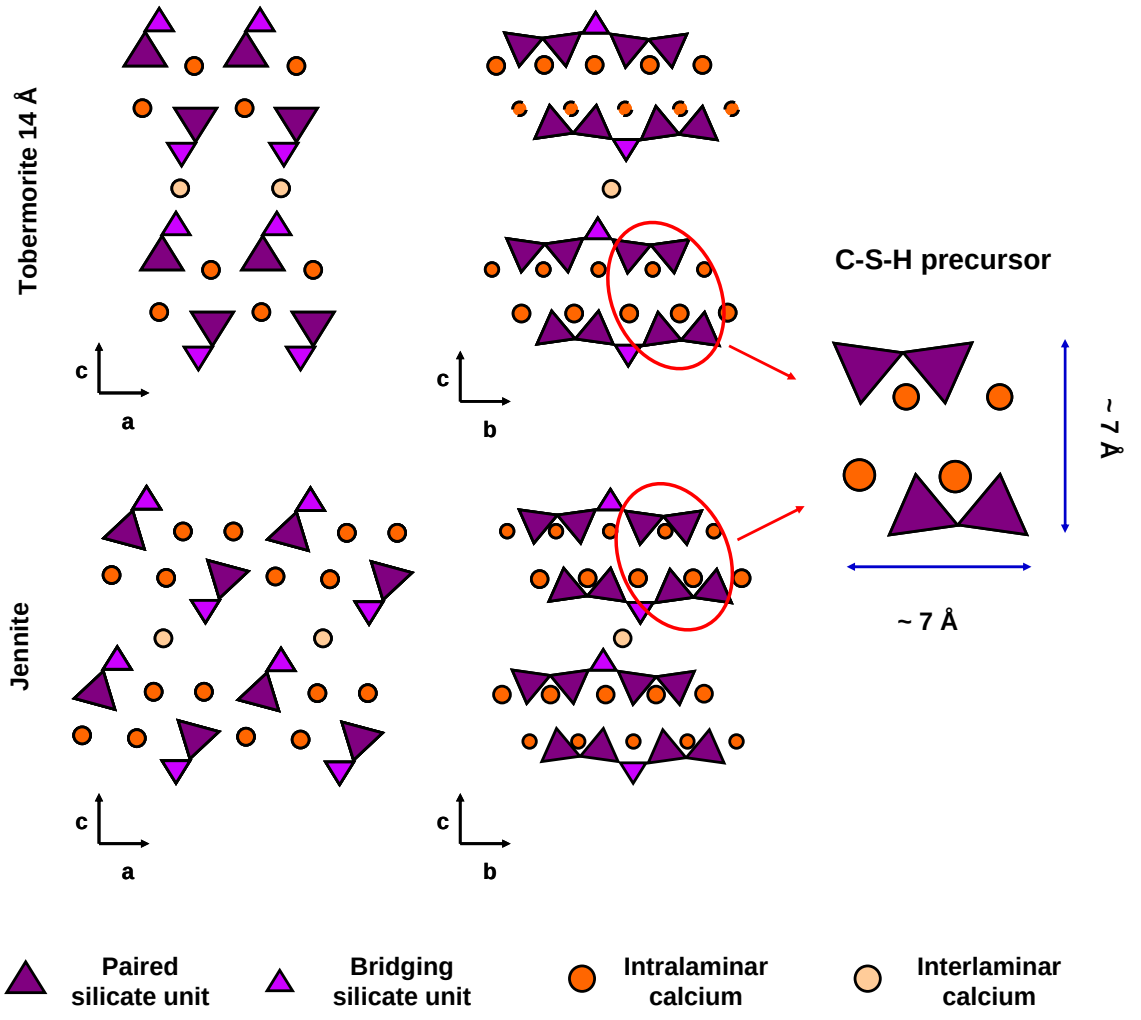

Figure 3.1.1.- Representation of tobermorite 14 Å and jennite. They present a similar arrangement in the partial structure composed of two dimeric units with calcium between them. Hence, it was isolated from the crystals and proposed as CSH precursor, shown in the right. This CSH precursor could be the smallest building block of the C-S-H nanoparticles.

population analysis following the ChelpG procedure, which is less dependent from the basis set than the Mulliken analysis [173]. A B3LYP hybrid functional which includes a mixture of the HF exchange and the DFT exchange-correlation in the LDA approximation was used [174], together with a Pople 6-31G plus one polarization function basis set [175, 176].

3.2. The C-S-H precursor

The structure of tobermorite 14 Å was employed to build the basic unit or precursor of the C-S-H gel, as it is represented in ***figure 3.1.1***. The initial structure isolated from the crystal is composed of two silicate chain-like dimers, hold together by a layer of calcium. The silicate chains are shifted by ~2.7 Å in the chain direction and ~2 Å in the perpendicular direction to the chain. The calcium atoms between the dimers form two differentiated layers, alternated up and down and shifted in the same directions than the silicate chains. The structure dimensions are around 7 x 7 x 4 $Å^3$, with a calcium to silicon ratio (C/S) of 1. In order to achieve a structure in a neutral charge state, the terminal oxygen atoms of the silicate chains were saturated with hydrogen. In tobermorite, those terminal oxygen atoms would be linked to the bridging tetrahedra. The structure fulfils the stoichiometry of the C-S-H gel proposed by Richardson [9]:

$$2\cdot\left[\left\{Ca_{2n}H_wSi_{(3n-1)}O_{(9n-2)}\right\}(OH)_{w+n(y-2)}\,Ca_{\frac{n\,y}{2}}\cdot m\,H_2O\right] \qquad (3.2.1)$$

$$n=1; w=2; y=0; m=0 \rightarrow 2\cdot\left\{Ca_2H_2Si_2O_7\right\}$$

The grown energy structure for the precursor is shown is ***figure 3.2.1***. The initially displaced silicate chains and CaO layer reorganize themselves into a very symmetric arrangement. Calcium atoms are coplanar and the silicate chains are in specular positions up and down from the calcium plane. The iono-covalent character of the interatomic bonds follows a clear trend independently of the population analysis employed (now on, the ChelpG values are given if the contrary is not specified). The Ca and O atoms of the middle layer have a mean charge of +1.7 e^- and –1.27 e^- respectively. It implies a strong ionic character of the Ca atoms and a partially ionic bond for O atoms, which is probably less ionic because the oxygen atoms are also bonded to silicon. The O atoms that belong to the silicate dimers have a mean charge of 0.9 e^-, and therefore a more covalent nature. Although the structure is almost completely symmetric, the position of the terminal hydrogen atom was dissimilar in the silicate chains. Such unexpected irregularity was checked with more simulations, obtaining the

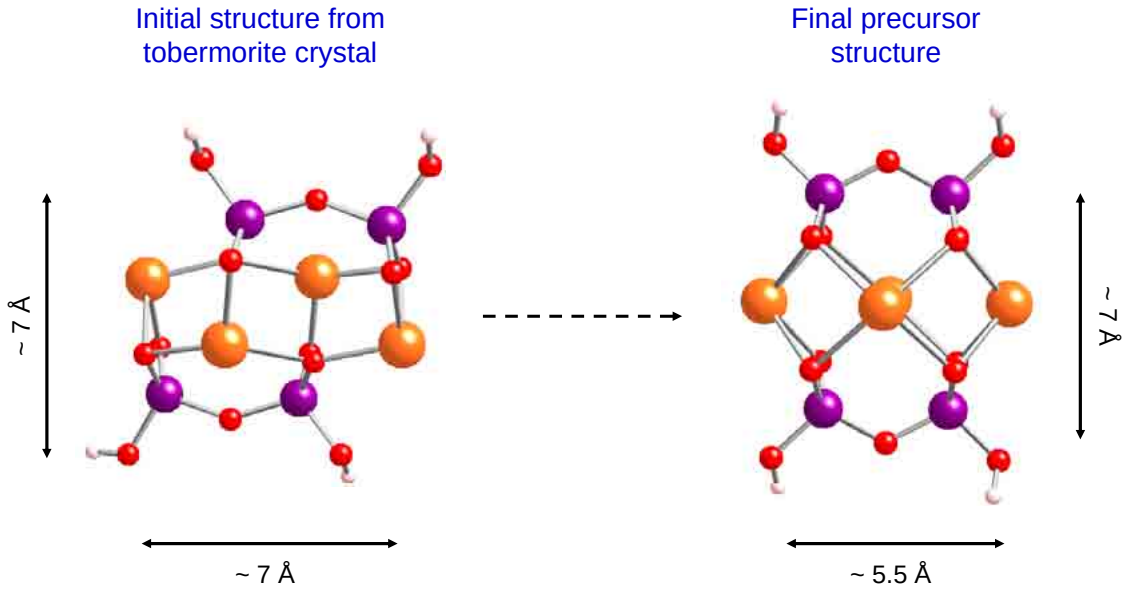

Figure 3.2.1.- Picture of the input geometry for isolated from tobermorite 14 Å (left) and the ground state structure (right) of the C-S-H gel precursor. They are composed of a Ca-O layer ribbed by two silicate dimers. The originally shifted structure evolves to a very symmetric structure. Si atoms are represented in purple; Ca, in orange; O, in red; and H, in white.

same result. The asymmetry induces a dipolar moment on the precursor of ~1.6 D (as reference, the dipolar moment of the water molecule is 1.85 D). The dimensions of this basic unit are similar to those of the initial structure, with the only difference of 1.5 Å reduction of the length in the direction of the chains, see ***figure 3.2.1***.

3.3. Assembly of precursors at low C/S ratio

Once the structure and properties of the C-S-H gel precursor were determined, the assembly of two units was studied. Although merging could happen between neutral structures due to Van der Waals interactions, it was considered a case in which two negatively charged units are linked together by an external Ca^{+2} ion. This assumption is in agreement with the existing models for the C-S-H atomic structure that predict the presence of calcium ions in the space between tobermorite-like layers, acting as a bond between different layers or replacing the bridging tetrahedron in a given layer [5, 9, 80,

82]. It is also in agreement with the stoichiometry proposed by Richardson [9]:

$$4\cdot\left[\left\{Ca_{2n}H_wSi_{(3n-1)}O_{(9n-2)}\right\}(OH)_{w+n(y-2)}\,Ca_{\frac{n\,y}{2}}\cdot m\,H_2O\right]$$
$$n=1;w=\frac{3}{2};y=\frac{1}{2};m=0\rightarrow 4\cdot\left[\left\{Ca_2H_{\frac{3}{2}}Si_2O_7\right\}\cdot Ca_{\frac{1}{4}}\right] \qquad (3.3.1)$$

Thus, a negatively charged precursor was built, by omission of a terminal H atom from the silicate chain, and relaxed. The resulting arrangement is similar to the neutral one, with a slight change in the position of the oxygen previously linked to the hydrogen atom. Although the main charge increase is localized in such oxygen (– 0.2 e^-), both population analysis (ChelpG and Mulliken) show a partial delocalization of the charge between the nearest oxygen atoms. Nevertheless, the effect of the H atom omission is especially important in the dipole moment of the structure, which increases up to 14.85 D, pointing in the contrary direction to the charged oxygen atom.

Although an insightful analysis said that the Ca^{+2} ion would be placed between the charged oxygen of the precursor, the relative position of the precursors with respect to each other was less intuitive. In order to start the simulation from a reasonable guess configuration, the *Fukui functions* of the charged precursor were calculated. The Fukui functions evaluate the areas of the system where electrons are likely to be removed ($f^-_{\rho(r)}$) or added ($f^+_{\rho(r)}$). Thus, they are a measurement of the reactive points under electrophilic and nucleophilic attack respectively [146, 172]. They are defined as follows:

$$f^+_{\rho(r)} = \rho_{(r)}(n+1)-\rho_{(r)}(n)$$
$$f^-_{\rho(r)} = \rho_{(r)}(n)-\rho_{(r)}(n-1) \qquad (3.3.2)$$

where n is the total number of electrons of the system and $\rho_{(r)}$ is the electronic density for that system. In the case under study, the positively charged Ca^{+2} ions would react with the specific zones of the system with high electron donor capacity. Therefore, the Fukui functions of interest in this case were the positive function ($f^+_{\rho(r)}$) for the calcium

ion (electron acceptor) and the negative Fukui function ($f^{-}_{\rho(r)}$) for the precursor (electron donor).

The spatial location of the Fukui functions is shown in ***figure 3.2.2***. In the case of calcium ions, a radial distribution of the Fukui function around the nucleus was obtained, as it was expected. For the precursor, the reactive area is mainly located in the charged oxygen atom. However, the remaining oxygen atoms of the silicate chain also

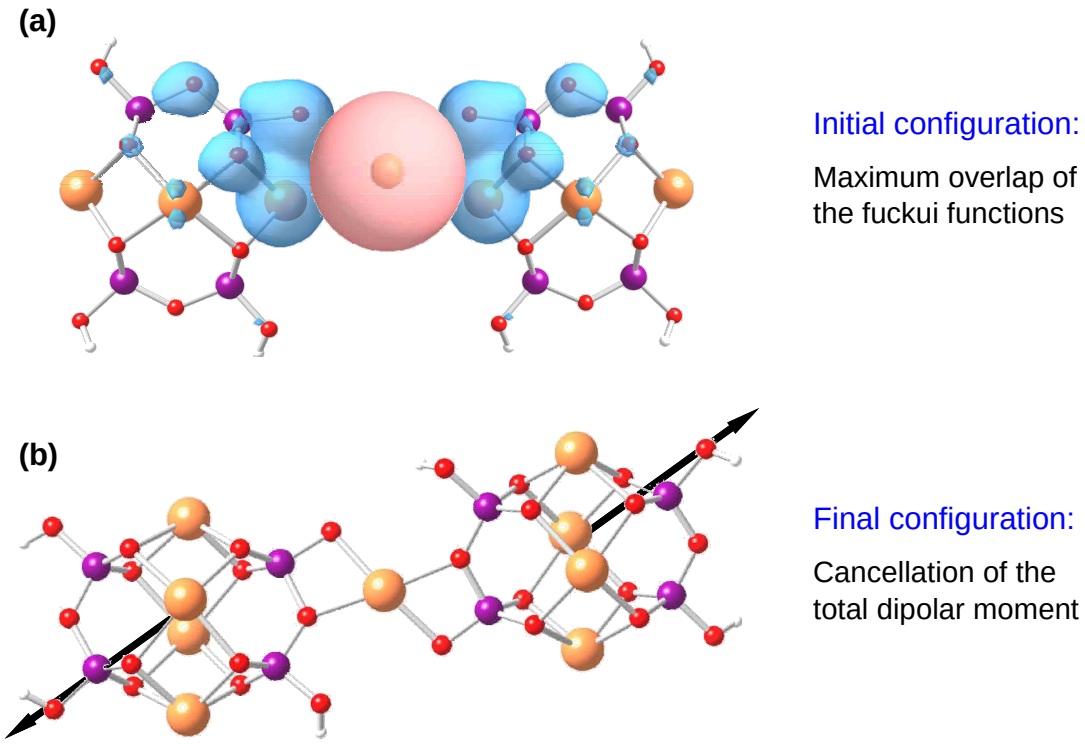

Figure 3.2.2.- Assembly of two negatively charged precursor units with a Ca^{+2} ion. The guess starting point **(a)** was chosen looking for a maximum overlap between the Fukui functions, which represent the most likely places to react. The Fukui functions are represented by red and blue density contours, corresponding to $f^{+}_{\rho(r)}$ and $f^{-}_{\rho(r)}$ respectively, and the surface plot threshold value is 1% of the maximum value. **(b)** The final configuration after the relaxation procedure. The dipolar moments of the precursors are represented by black arrows. The cancellation of the net dipolar moment can be the mechanism responsible of the rearrangement. The colour code is the same than in previous figures.

contribute to the Fukui function, decreasing their importance with the distance. This is a consequence of the previously mentioned partial delocalization of the negative charge among neighbouring oxygen atoms. Interestingly, the closest calcium atom to the charged oxygen also has a tendency to give electrons. This might be due to an increase of its electronic population when the charged structure was built. This effect is described by the Mulliken analysis, with a slight decrease of the charge with respect to the remaining calcium atoms (0.8 e^-).

After the analysis, the precursors were placed looking for the highest overlap of the Fukui functions clouds. The initial guess configuration and the final optimized structures are presented in ***figure 3.2.2***. The precursor units rearranged themselves into a very regular structure with the calcium ion between them. The driving force to reach this configuration might be the cancellation of the high dipolar moment that a single charged precursor presents. In fact, the calculated dipolar moment of the new system is 1.0 D, even lower than that of the neutral precursor.

It has been suggested that the presence of water molecules inside C-S-H nanoparticles could be the responsible of some properties, such as creep and shrinkage [90, 177, 178]. Current models situate the water molecules in the interlaminar space, probably coordinated to calcium ions [9]. According to the Ca-water coordination in the interlaminar space of tobermorite, four water molecules were added surrounding the ion, with the free electron pair of the oxygen atoms pointing towards it, and the structure was relaxed again. The inclusion of these water molecules implies a charge increase of the linker calcium, ~0.2 e^- higher, which indicates a more ionic bond character. Water molecules have little effect on the structure of the precursor aggregate. Only a slight increase of the distance between precursors was observed, from 1.1 nm to 1.2 nm (taking the central Ca-O layer of each precursor as the point of measurement). This effect can be attributed to a decrease of the bond strength due to the aforementioned increase of the ionic character of the precursor-Ca-precursor bonds, as well as to the steric hindrances due to the presence of water. Nevertheless, both distances are in good agreement with the experimental data of the crystalline species [64, 66] and other theoretical studies [119].

3.4. Assembly of precursors at high C/S ratio

In mature ordinary Portland cement pastes, the C/S ratio is around 1.7 [59]. In agreement with this value, the average composition of a single C-S-H nanoparticle estimated by small angle neutron scattering (SANS) is $C_{1.7}SH_{1.8}$ [179]. The C/S ratio of the system studied in the previous section, two precursors plus one calcium atom, is 1.125, a value considerably lower than the experimental data. Therefore, the aggregation of the precursors for higher calcium content should be considered. To that end, three more Ca^{+2} ions were placed between two precursors, taking the previously relaxed structure with two precursors and one calcium atom as starting point, so that the C/S ratio increases up to 1.5. Many possible configurations fulfil the Richardson's stoichiometry for this composition [9], especially if hydroxyl groups are included to counterbalance the charge. Nevertheless, to facilitate the initial guess no hydroxyl groups were included. The selected stoichiometry is:

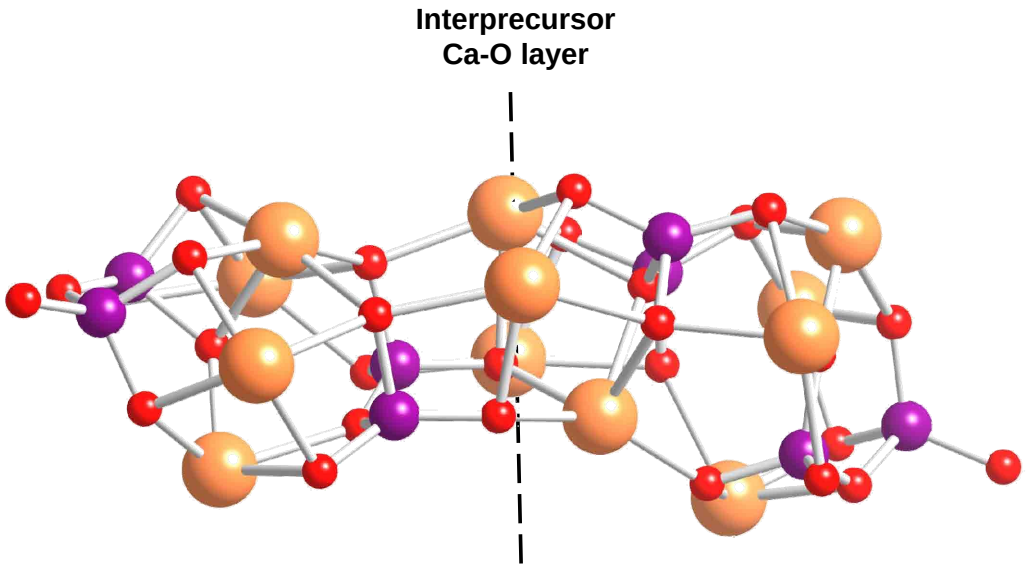

Figure 3.2.3.- Relaxed structure of the assembly of two precursors with high calcium content (C/S = 1.5). The starting point was that of figure 3.2.2, with the inclusion of three Ca^{+2} atoms between the precursors, and removing the correspondent hydrogen atoms to obtain a neutral system.

$$4\cdot\left[\left\{Ca_{2n}H_wSi_{(3n-1)}O_{(9n-2)}\right\}(OH)_{w+n(y-2)}\,Ca_{\frac{n\,y}{2}}\cdot m\,H_2O\right] \qquad (3.3.3)$$

$$n=1; w=0; y=2; m=0 \rightarrow 4\cdot\left[\left\{Ca_2Si_2O_7\right\}\cdot Ca_1\right]$$

The relaxed structure after the optimization (***figure 3.2.3***) has a very poor symmetry, in comparison with the low C/S ratio case. Consequently, the total dipolar moment of the particle is very high, 13.72 D. It can be suggested that the energy gain of the multiple bond formation primes over the dipole cancellation in the present case. Each precursor can be still distinguished, although their structure is distorted. The added calcium atoms are coordinated not only to the terminal oxygen atoms of the silicate chains, but also to those of the Ca-O layer of each precursor. Thus, the silicate dimers are now linked to two different Ca-O layers, within the precursors and between them. The mean charge of the calcium ion of the layer formed between the units is slightly smaller than the one within the precursor, just about 0.1 e^- lower. This small decrease indicates that the iono-covalent nature of both layers is similar.

3.5. Discussion of the assembly mechanism

The formed structures after the assembly of precursors can be related to the crystalline species tobermorite 14 Å and jennite. A schematic representation is presented in ***figure 3.2.4***. When the dipole-dipole interaction is the responsible of the system organization, a tobermorite-like structure is formed. The configuration can be identified as a precursor assembly in the perpendicular direction of the silicate chains, with the Ca^{+2} ion acting as a linker between layers. However, when the formation of multiple Ca-O bonds primes, the silicate chains rearrange themselves and are coordinated to two Ca-O layers. This would be equivalent to a jennite-like structure, growing in the laminar plane and perpendicular to the silicate chain direction. Thus, starting from a single precursor, tobermorite or jennite-like structures can be reached, depending on the mechanism, which in its turn depends on the calcium to silicon ratio. The growth mechanisms are consistent, therefore, with the calcium content of the crystalline species.

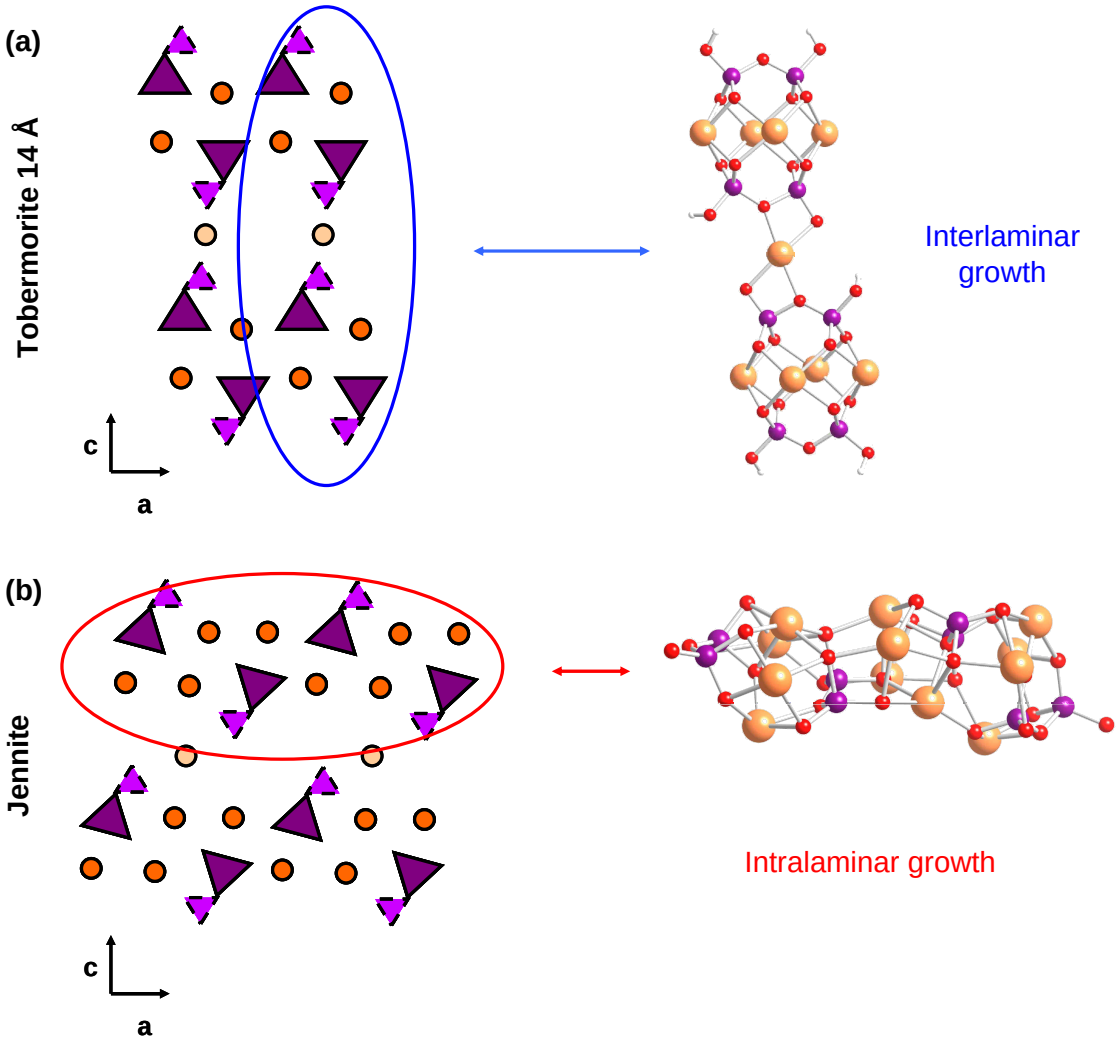

Figure 3.2.4.- Possible growing mechanisms of the precursors depending on the C/S ratio. **(a)** For low Ca contents the minimization of the dipolar moment is the determinant factor, and tobermorite-like structures are formed trough an interlaminar growth. **(b)** For high Ca contents, the bond formation takes preference over the dipole cancellation, and jennite-like layers are formed trough an intralaminar growth.

A subsequent growth between the so formed particles could depend again on the same factors. Particles with high dipolar momentum could interact between them to form bigger systems, while the formation of a calcium oxygen bond network could be the driven force for particles with low dipolar moment. This mechanisms do not necessarily imply a long range ordering, and the particles could therefore be X-Ray amorphous. Just as a comment, if the characteristic size of a particle is ~4nm [90, 179], about 6 precursor units would form the particle in that direction.

The C/S ratio of the precursor is one. Although it is lower than the mean value for OPC pastes (1.7), it must be note that any aggregation of precursor units following the proposed mechanisms would imply an increase of the C/S ratio. In view of the crystalline structures of tobermorite and jennite, the only way to decrease the calcium to silicon ratio is to increase the silicate chain length. A merging process in which silicate groups could link two silicate chains by condensation reactions has been stated as the growth mechanism for the silicate chains in the cement paste [6, 52, 61, 128, 180]. This would be the remaining possible growth direction in the crystal, parallel to the silicate chain. The merging process could take place once the precursors have already reacted, and therefore, the silicate chains and the particle growth can be considered as separate processes. This suggestion is consistent with the experimental observations. In Portland cement young pastes, most of the chains are dimers, although they continue growing and the mean chain length after 23 years is 4.8 tetrahedra [59].

3.3. Conclusions

In this chapter the formation of a C-S-H nanoparticle starting from a single precursor unit has been studied. First of all, a precursor consistent with the existing models and stoichiometry has been proposed. Its structure has been built isolating a piece of tobermorite formed by a calcium oxide layer ribbed in both sides by silicate dimers. After relaxing the structure, the aggregation of two precursors was studied for two limit cases:

a) A case with low calcium content (C/S = 1.125), in which a single Ca^{+2} atom was included between two precursors. The precursors assembly is characterized by a high symmetry geometry in which the individual dipolar moment of the precursors are cancelled, and the net dipole moment of the formed structure is very low (around 1D). The process would be equivalent to a growth of tobermorite-like structures in perpendicular direction to the layers.

b) A case with high calcium content (C/S = 1.5), in which three more Ca^{+2} atoms are added to the previously formed system. A new calcium-oxide layer appears, and the silicate chains rearrange themselves to form a Ca-O bond net. The structure resembles a jennite-like structure that has growth in the layer plane but perpendicular to the silicate chains. This structure is characterized by a high dipole moment (around 13 D) due to the poor symmetry of its relaxed geometry.

The study of the aggregation mechanisms could be continued up to the proposed sizes for C-S-H nanoparticles. The inclusion of a third precursor or the aggregation between the already formed systems could be considered, as well as variable amounts of interlaminar Ca^{+2} ions or even water molecules. However, the high number of variables and computational cost of the simulations make this task impractical. Different approximations and/or other levels of theory such as force field or *ab-initio* Molecular Dynamics could be employed to study the C-S-H nanoparticles formation [122].

Chapter 4:

Aluminium Incorporation to C-S-H gel Silicate Chains

4.1. Introduction and computational method

Among all the guest ions that might enter into the C-S-H structure, aluminium is the most common one. By looking at ***table 1.2.1*** in ***chapter 1***, it can be seen that Al_2O_3 is the third oxide in amount in the ordinary Portland cement clinker. Although aluminium takes part in several AFm and AFt crystalline phases, Copeland et al. shown that these hydration products do not account for all the aluminium present in the cement paste [181], and therefore aluminium should take part in the C-S-H gel. The aluminium incorporation is expected to modify the C-S-H gel properties and many processes such as ion exchange behaviour, the solubility, and the reactions during delayed ettringite formation [182-184]. Furthermore, slag- and fly ash-based cements, which employ residual wastes as raw materials, have a high aluminium content [185]. Hence, the mechanism and effect of aluminium incorporation to the C-S-H gel is of great technological interest, and must be investigated.

Many experimental works can be found in the literature devoted to determine the nature of the aluminium present in the C-S-H gel and related species, employing techniques such as X-Ray diffraction, X-Ray fluorescence, trimethylsilylation, and especially ^{27}Al and ^{29}Si Nuclear Magnetic Resonance (NMR) [186]. The atomic sites of the silicate chains have inherited the nomenclature employed by this technique. The sites are identified by the chemical shift in the spectrum signal, and classified according to the number and nature of the atomic bonds. A Q^n position denotes a silicon atom linked to *n* other silicon atoms via oxygen atoms, Si-(O-Si)$_n$. The nomenclature can be widened to incorporate aluminium, and specify the bond number to an Al atom. For example, Q^2 indicates a Si atom bonded via oxygen atoms to two silicon atoms, while Q^2_{1Al} indicates a Si atom bonded via oxygen atoms to a silicon and an aluminium. It is also common to assign the position in a linear silicate chain considering the *Dreierketten* arrangement of tobermorite, jennite, wollastonite and other crystals. The silicate chain extremes, Q^1 positions, are called end sites. The internal chain places, Q^2 for linear chains, are divided in paired sites (those with are linked to the calcium-oxide layer in the minerals) and bridging sites (those oriented to the interlayer space in the minerals). The chain arrangement has been explained in detail in the introductory chapter (***section 1.5***). A graphical representation of this notation is shown in ***figure 4.1.1***.

The study of Al incorporation in crystalline tobermorite is useful to understand that of the amorphous C-S-H gel. It has been reported that aluminium enters the silicate chain up to Al/Si ratios of 0.15. At higher ratios, aluminium appears hexacoordinated due to the formation of hydrogarnet [184]. Synthetic tobermorite prepared in the presence of aluminium has a basal distance of 11.37 Å. Thus, tobermorite 11 Å was obtained where aluminium formed interlaminar crossings. For low aluminium contents its substitution occurs mainly in Q^3 sites across silicate chains of different layers, although Al in Q^2 positions was found when increasing the Al/Si ratio [184, 187].

Regarding the C-S-H gel, several sites with different aluminium coordination have been identified. The general classifications name these sites as Al[*n*] where *n* is the coordination number, equal to 4, 5 and 6. There is an overall agreement that

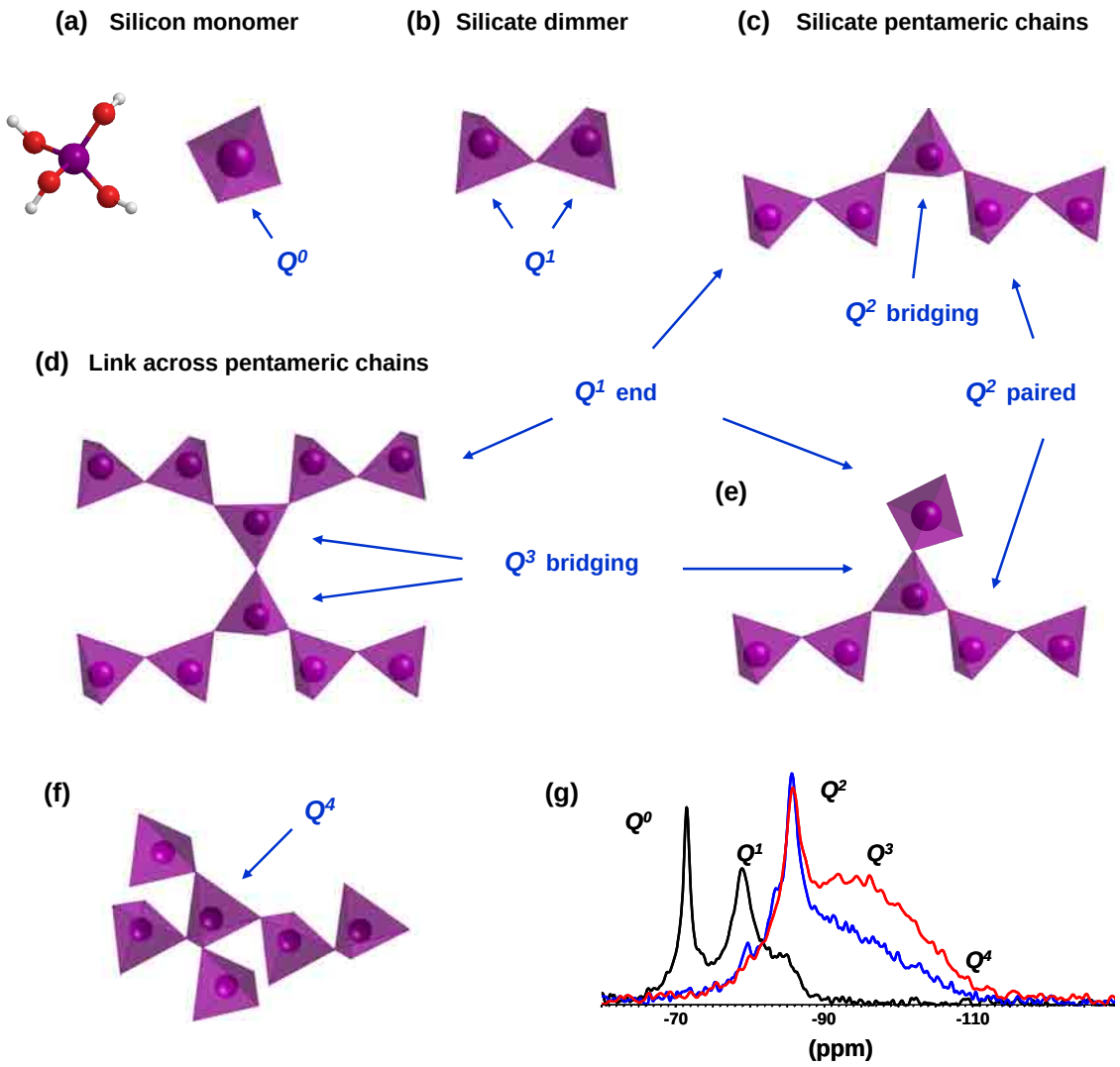

Figure 4.1.1.- Schemes of the Q^n nomenclature for the atomic sites in silicate chains. The panels **(a)**, **(b)**, **(c)** and **(d)** are typical structures in cement pastes or synthetic C-S-H phases, while **(e)** and **(f)** are more polymerized species that may appear in degraded pastes or systems with low or no Ca content such as fly ash and slag cements. **(g)** ^{29}Si MAS NMR spectra. The experimental spectra have been collected from non degraded (black) cement pastes and degraded (blue and red) cement pastes by calcium leaching [97]. Each purple tetrahedron represents a $Si(OH)_4$ tetrahedra, with the Si atom in the centre and the OH groups in the vertexes. A Si-O-Si bond between tetrahedra is represented sharing a corner. A Q^0 position implies a non-reacted silicon monomers. For linear chains, the extreme points are always Q^1 positions while the inner positions are Q^2. Within the Q^2 sites, paired and bridging positions can be distinguished due to the *Dreierketten* arrangement. Q^3 and Q^4 sites appear when the polymerization degree increases in 2D and 3D features, as the interlaminar crossing. Q^n_{mAl} would name any of the previous structure linked to m Al atoms, and $n - m$ Si atoms.

tetracoordinated aluminium (Al[4]) arises from the substitutes of Al^{+3} by Si^{+4} in the silicate chains, while pentacoordinated (Al[5]) and hexacoordinated aluminium (Al[6]) are at the interlaminar space [52, 60, 61, 180, 182, 188-194]. The position of Al[4] within the chains is also restricted to certain sites. Richardson et al. for slag containing cement pastes [6, 52, 60, 61, 180, 193], Andersen et al. for white cement pastes and precipitated C-S-H pastes [190-192], and Sun et al. for a series of synthetic samples with a wide range of composition [182], conclude that Al[4] substitute silicon only in the bridging chain positions. In particular, for synthetic samples two sites have been identified: a Q^3 site with interlaminar crossing and a Q^2 site counterbalanced by ions (Na^+, Ca^{+2}, H^+, etc) or by Al[5] and Al[6] by means of Al-O-Al bonds [182]. The charge balance mechanism has been suggested to play a key role in the substitution, especially in the case of Na^+ cations [182, 195-200]. Additionally to other authors findings, Faucon and co-workers suggested that Al[4] might occupy even paired sites [195-200]. Their model also proposed the incorporation of Al[6] substituting calcium in the intralaminar space between silicate chains [195-199]. Most authors disagree with this suggestion and attribute the Al[5] and Al[6] to aluminate phases that may grow in its surface or interlaminar space of the C-S-H gel [182, 190-193].

The most significant effect of the aluminium incorporation to the silicate chains is an increase of the mean chain length. The growth mechanism proposed by Richardson [6, 52] states that two dimeric chains are merged by a monomer to form a pentamer. Thus, the tendency of aluminium for the bridging position enhances the formation of pentameric chains, acting as the linker in the merging reactions [8, 9, 52, 60, 61, 180]. It has been also reported an increase in the polymerization degree of the chains and interlaminar crossing due to aluminium Q^3 positions [184, 187]. The maximum content of Al[4] depends on the calcium to aluminium plus silicon ratio, Ca/(Al+Si). The Al[4] content decreases as the Ca/(Al+Si) increases, and it favours the formation of Al[5,6] structures [182, 188]. The calculated maximum Al[4] content for equilibrated samples with Ca/(Al+Si) ratio from 0.88 to 1.4 has been ~ 0.17 [182], although much larger values, up to 0.26, have been also reported for Ca/(Al+Si) ratios of 0.66 [195].

Besides these experimental works, the incorporation of aluminium to the silicate chain

structure of the C-S-H gel has been studied by atomistic simulation methods. Faucon et al. employed Molecular Dynamics (MD) to study the position of aluminium in a tobermorite structure. They found that the substitution in bridging positions is more stable than in paired ones. Furthermore, a chain break occurs for the substitutions in paired sites. Regardless the position and chain break, Al is always flanked by Si [121]. Yamanaka et al. performed semi-empirical, Hartree-Fock and Density Functional Theory calculations on a finite cluster isolated from tobermorite structure [118]. Opposite to the experimental findings, their results shown that the paired Q^2 sites were the most stable ones for Al, and they attribute the disagreement to the differences between the real structure and their model [130]. Finally, Rahaman et al. concluded from HF calculations of isolated silicate chains that the substitution of Al^{+3} and SO_4^{-2} is always thermodynamically possible for dimeric and pentameric chains, independently of the position [129].

Here, the aluminium incorporation to the silicate chains has been studied at two different levels of approximation. First-principles calculations have been used to study energetically the stability, growth mechanism, and position of aluminium within isolated *Dreierkette*n-like silicate chains. With Molecular Dynamics simulations the polymerization mechanisms of $Si(OH)_4$ and $Al(OH)_3$ in presence of Ca^{+2} has been studied, as well as the structure of the formed chains.

- ***Computational method***

First principles simulations have been performed using the Density Functional Theory (DFT) approach as implemented in the SIESTA code [201]. The general gradient approximation (GGA) has been adopted to describe the electronic exchange-correlation, using the Perdew-Burke-Ernzerhof (PBE) functional [202]. A suitable double-ξ polarized basis set (DZP) has been used to describe the valence electrons. The presence of the core electrons and nucleus is mimicked by means of atomic pseudopotentials, parameterized following the Troullier-Martins method [203]. The reference configuration for the parameterization and the basis set parameters are detailed in ***appendix 1***, and their transferability was previously checked in similar systems by other

authors [128]. The SIESTA method works with periodic boundary conditions. To avoid the interaction between a given silicate chain and its periodic images (especially in the case of charged systems), large enough cubic boxes were taken as simulation cells. The SIESTA default was adopted for the cell parameters, i.e. the minimum size to include the system without intercell interactions, plus a 10% [201]. The simulations were performed at the Γ point with a mesh cut-off of 100 Ry. These parameters were chosen after convergence tests of the energy below 10^{-3} eV/atom.

The structure for silicate chains with lengths ranging from 1 (silicic acid) to 9 tetrahedra were relaxed. The initial chains were obtained by isolating them from the crystalline structure of tobermorite 14 Å [64] and saturating the terminal oxygen atoms with hydrogen atoms. Calcium atoms were not included in the simulation although their presence was mimicked by the initial *Dreierketten* arrangement, and by relaxing the structure only to the nearest energy minimum with a conjugate gradient method [137]. The inclusion of Al^{+3} was done by replacing directly a Si^{+4} in the initial structure. According to the maximum aluminium to silicon ratio calculated experimentally, Al/(Al+Si) = 0.17 [182], only one Al per chain was included, obtaining a Al/(Al+Si) ratio from 1 to 0.11. This range switches to 0.2 - 0.11 if chain lengths larger than 5 are considered, those with a bridging atom are likely to suffer the substitution in view of the experimental data [60, 180, 182, 190].

With the DFT approximation, the obtained results were also cross-checked with the Gaussian03 code [171]. Single point calculations on the optimized structures were performed, employing the Becke 3-parameter, Lee, Yang, and Parr (B3LYP) hybrid scheme, which includes a mixture of the Hartree-Fock exchange with DFT exchange correlation at the local density approximation (LDA) level [174]. A 6-31G basis set plus an extra polarization d function has been chosen for an improved description of the oxygen polarizability [175, 176]. The results obtained by Gaussian show the same trends than those of SIESTA in all the studied parameters (stability index, Mulliken populations, HOMO-LUMO gaps, condensation energies, and merging reactions). Hence, the results obtained by SIESTA are given through the text unless otherwise is stated.

The Molecular Dynamics simulations were carried out with the TREMOLO code [204]. Within the canonical ensemble, this is, at constant number of particles, volume, and temperature (NVT), a Nosé Langrangian [205] was chosen. with a thermostat coupling value of 100 uÅ^2. The equations of motion were solved using a third order predictor-corrector algorithm in the Beeman and Refson approach [206, 207], with a time step of 0.1 fs. The total simulation time for each system was 2200 ps, with the following temperature profile. First, the system was kept at 300 K during 10 ps to equilibrate the initial random configuration. Then, the temperature was raised linearly during 90 ps up to 1800 K, and kept at that temperature during 1500 ps. The high temperature was adopted to accelerate the condensation reactions between $Si(OH)_4$ and $Al(OH)_3$. The thermal energy correspondent to this temperature (KT = 3.57 Kcal mol^{-1}) is ~20 % of the barrier energy for $Si(OH)_4$ monomer S_n^2 condensation (E = 18.7 Kcal mol^{-1}) [208], and therefore it not is expected to introduce other perturbation than to speed the reactions. The duration of this period ensures that the condensation reactions rate is complete. Finally, the temperature was decreased linearly to 300 K during 500 ps, and the system was equilibrated at that temperature during 100 ps. The data collection to average the system properties of the system was done during the last 50 ps.

Several systems with different compositions, Al/(Al+Si) and Ca/(Si+Al) were studied. The Al/(Al+Si) = 0.125, 0.167, and 0.250 ratios represent respectively the substitution of Si by Al in 3, 2, and 1.5 each 4 bridging positions of a tobermorite-like chain. The values were chosen in agreement with the reported maximum Al content in the silicate chain structure [182, 195]. The Ca/Si ratios were 0.85, 0.95, 1.20, 1.50, 1.75 and 2.00, and the resulting Ca/(Si+Al) cover the range between 0.64 and 1.75, according to the experimental ranges [190-192]. $Na(OH) \cdot 5\ H_2O$ groups were included in a proportion of 1:1 to Al, as it has been suggested that they play a key role counterbalancing the charge [182, 195, 198, 199]. The appropriate amount of $Si(OH)_4$, $Al(OH)_3$, $Ca(OH)_2 \cdot 4\ H_2O$, and $Na(OH) \cdot 5\ H_2O$ groups to get this ratios were placed in a 66 Å length cubic simulation cell, with periodic boundary conditions.

The interaction between atoms followed the potentials and parameters developed by Garofalini and co-workers to simulate the polymerization via condensation reactions of

alumino-silicate glasses, water interaction with alumino-silicate surfaces, as well as the properties of intergranular films on ceramic materials [209-214]. This force field consists in a modified Born-Mayer-Huggins two-body potential to simulate the short range repulsion and the coulombic interaction, together with a three-body potential to simulate the angle of the covalent bonds in the silicate and aluminate groups. A screened coulombic potential was added for the Ca-Na, Ca-H and Na-H pairs, not included in the force field previously. The functional form and parameters are given in ***appendix 2***.

4.2. Stability of the alumino-silicate chains: the 3*n* – 1 rule

First the condensation energies of a monomer-by-monomer linear growth were calculated. A silicate chain of length *m* might grow by condensation reactions of a silicon monomer $Si(OH)_4$, an aluminium monomer $Al(OH)_4^-$, or even with a charged silicon monomer $Si(OH)_3O^-$ [215]. The OH group of monomers reacts with a terminal hydroxyl of the alumino-silicate chain, and it loses a water molecule to form a Si-O-Si bonds. For instance, for a $Si(OH)_4$ monomer the reaction is:

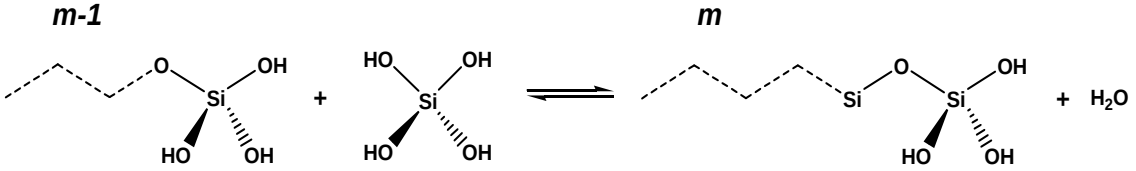

The condensation mechanism proceeds equally when $Al(OH)_4^-$ or $Si(OH)_3O^-$ monomers are considered instead of $Si(OH)_4$. The condensation energies for the linear growth were calculated as the energy difference between products and reactants:

$$E_{condensation} = (E(m) + E_{H_2O}) - (E(m-1) + E_{monomer}) \qquad (4.2.1)$$

Following equation (4.2.1), the higher the condensation energy the more favourable the reaction. The obtained condensation energies for these processes are shown in ***figure 4.2.1***. All the condensation energies are positive, which indicates that all the reactions

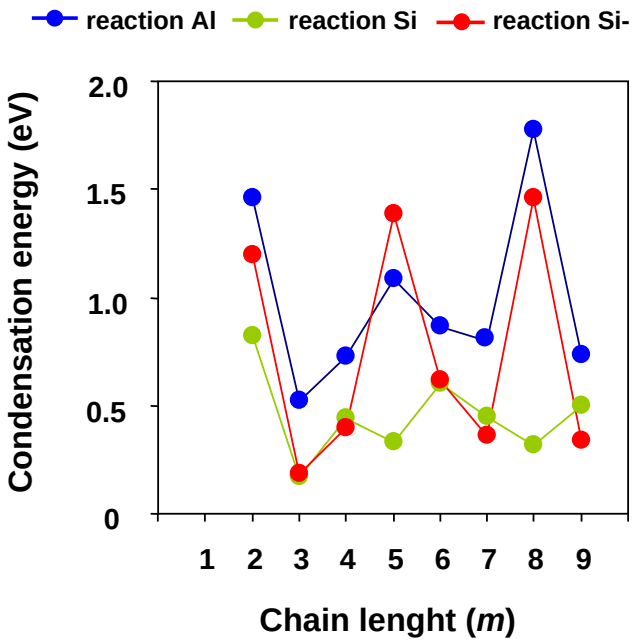

Figure 4.2.1.- Condensation energies of alumino-silicate chains of length m – 1 with a $Al(OH)_4^-$ (blue), $Si(OH)_3O^-$ (red), and $Si(OH)_4$ (green). These energies are plotted against the length of the formed chain (m).

are exothermic independently of the chain length. Therefore, a linear growth by condensation of monomers in the chain extremes would be possible from a thermodynamical point of view. The condensation energies of neutral species (in green) are the smaller ones, so it is the less favourable one, and it follows even a different trend from the one of charged species. In the charged species case, it is clear that the most favourable reactions are those that form a chain of tetrahedron length 2, 5 and 8, i.e. according to the $3n$ – 1 rule. Furthermore, the condensation of aluminium leads to the higher energy gains, with the only exception of the pentameric chain.

However, the experimental results show that the stable lengths follow the $3n$ – 1 rule, and that it is maintained when aluminium substitutes for silicon [190, 191, 197]. To study this fact theoretically, the *stability index* (S) of the alumino-silicate chains were calculated. It has been previously reported that the incorporation of Al to dimeric and pentameric chains is always thermodynamically possible [129]. In a dynamic process as the chain formation via condensation reactions, the existence of a certain size depends

not only in its local stability, but also in its stability with respect to their neighbouring sizes. The stability index of an alumino-silicate chain with the length *m* evaluates the stability of that chain with respect to the addition or removal of one alumino-silicate unit. It is the chemical potential of the system against the number of particles. This methodology is generally employed in the study of the stability with the cluster sizes [216], and it has been applied successfully to investigate the stable lengths of silicate chains [128]. To calculate the stability index, all the possible growing mechanism must be identified and taken into account. A silicate chain of length *m* might grow reacting with other silicon monomer $Si(OH)_4$, an aluminium monomer $Al(OH)_4^-$, or even with a charged silicon monomer $Si(OH)_3O^-$ [215]. If only one charged silicon tetrahedra unit or one aluminium per chain are considered, the chains of length *m +1* could continue growing by adding neutral silicon monomer. The same reasoning can be applied to the inverse process, when a silicate chain losses a unit. All the possible growth paths that were considered in this study are given in ***figure 4.2.1***. It must be noted that once the aluminium enters the chain, the next $Si(OH)_4$ may be incorporated in both sides of the chain. Then, they are several growth paths due to the asymmetry arising from the presence of aluminium. In order to deal with a unique growth path, the $-Al(OH)_4^-$ unit was always located at the end of the chain, assuming that subsequent silicon units would react in the opposite chain side.

The neutral and charged silicate chains (orange, blue and red paths of ***figure 4.2.1***) were explored in a previous work by Ayuela and co-workers [128]. They found that the stable chains were those which fulfil the $3n - 1$ rule, in agreement with the experimental data [6, 8, 52], and that the charged chains contribute more than the neutral ones to the global stability. In this work, the growing paths involving aluminium (green and purple in ***figure 4.2.2***) were studied. The stability index of these new channels is defined as:

$$S_{Al}(m) = E(m-1)_{Al} + E(m+1)_{Al} + E(m-1)_{Si} - 3 \cdot E(m)_{Al} \qquad (4.2.2)$$

where the subscript denotes a silicate ($_{Si}$) or alumino-silicate chain ($_{Al}$), the term in parenthesis indicates the length of the chain, and *E* is the energy of the corresponding chain. A detailed derivation of the stability index from reaction transition rates and the

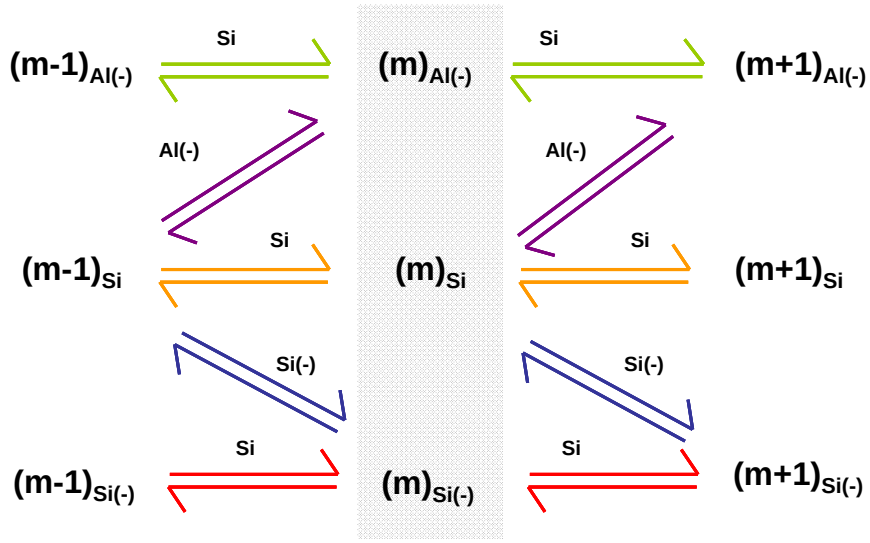

Figure 4.2.2.- Growth paths considered in this chapter represented by the coloured arrows, with the involved monomer written on top. The subscript Si represents a neutral $Si(OH)_4$ group; Si(-), a charged $Si(OH)_3O^-$; and Al(-), a $Al(OH)_4^-$. The chain length is shown in parenthesis. Each column represents a fixed chain length, while each row represents a type of chain.

Boltzmann population distribution function is given in ***appendix 3***. The result of the analysis is clear: for a given length *m*, if the stability index is higher than that of the neighbouring sizes $m + 1$ and $m - 1$, the chain is stable with respect to addition or removal of another unit. However, if $S_{Al}(m)$ is lower than that of the neighbouring sizes $m + 1$ and $m - 1$, the silicate chain would evolve increasing or decreasing its size to reach more stable structures.

In ***figure 4.2.3 (a)*** the total result for aluminium (in red), the total result for silicon calculated in reference [128] (in blue) and the global stability index (in black) of all the considered mechanisms are given. The global stability index a certain length *m* ($S(m)$) can be written as a sum of the processes that involve alumino-silicate chains ($S_{Al}(m)$) and pure silicate (neutral or charged) chains ($S_{Si}(m)$):

$$S(m) = S_{Si}(m) + S_{Al}(m) \tag{4.2.3}$$

It can be seen that the tendency of the alumino-silicate chains and pure silicate chains is

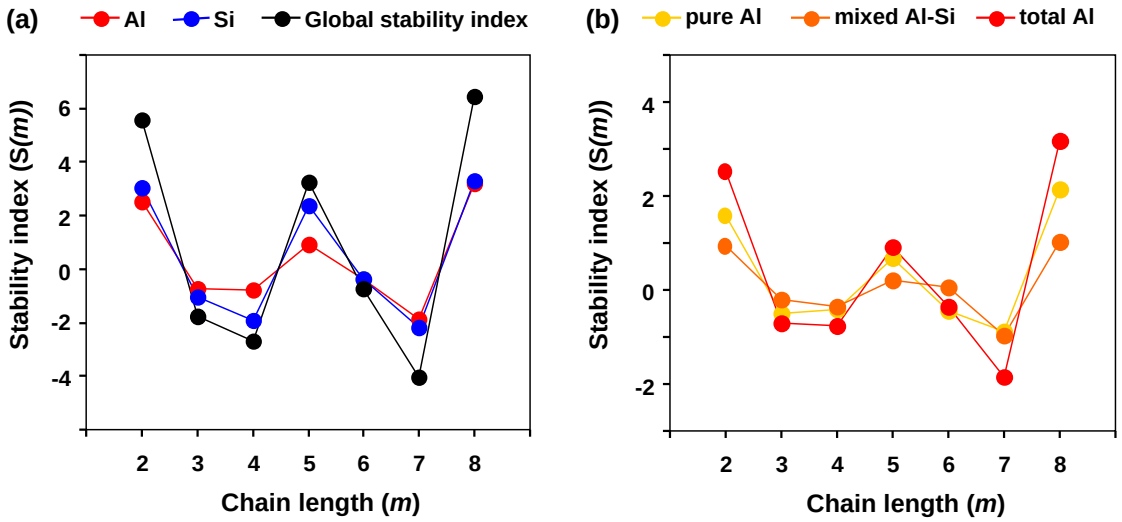

Figure 4.2.3.- **(a)** Stability index of pure silicate chains (in blue), alumino-silicate chains (in red), and the Global Stability index of all the considered paths (in black) versus the silicate chain length. **(b)** Decomposition of the stability index for the channels that involve aluminium (green and purple in ***figure 4.2.1***).

the same, and, therefore, the only effect of the growth paths that involve aluminium is to enhance the global stability of the silicate chains with $3n - 1$ tetrahedron units.

The aluminium process can be further decomposed in two contributions: the channel involving the growth of alumino-silicate chains, shown in green in ***figure 4.2.2***, and the channel involving the growth of pure silicate chain, shown in purple in ***figure 4.2.2***. These decomposed results for aluminium channels are shown in the ***figure 4.2.3 (b)***. The total stability index of the chains, given in red, fulfils the $3n - 1$ rule is higher than those of their neighbouring sizes are. Thus, the stable chain lengths when aluminium is incorporated are the same as in the Al-free case, maintaining the $3n - 1$ rule, in agreement with the experimental results [190, 191, 197]. Furthermore, both considered channels, i.e. a silicon chain growth by condensation of a $Al(OH)_4^-$ group or a alumino-silicate chain growth by condensation of a $Si(OH)_4$ group (orange and yellow respectively in ***figure 4.2.3 (b)***), have the same trent. In both situations the incorporation of aluminium to the chains favours the stable lengths. According to these results, dimeric chains with aluminium are stable. It implies that aluminium could be located at

a Q^1 position. This disagreement with the experimental data will be discussed later in ***section 4.4***, when discussing the growth processes of the alumino-silicate chains.

To study the reason for the stability of the 3*n -1* alumino-silicate chain lengths, their structure and electronic properties have been discussed. To this end, the structure and electronic properties of the alumino-silicate chain are now studied. The energy difference between the *Highest Occupied Molecular Orbital* (HOMO) and *Lowest Unoccupied Molecular Orbital* (LUMO) quantifies the chemical stability of a system: a higher gap indicates higher stability [146, 172]. In ***figure 4.2.4*** the HOMO-LUMO gap of the alumino-silicate chains versus the chain length is shown. DFT methods are known to underestimate the experimental value of the HOMO-LUMO gap by certain amount. Nevertheless, the gap values of the chains are big enough to asses their stability. It can be seen that the chains with length equal to 2, 5 and 8 units have a higher gap than their

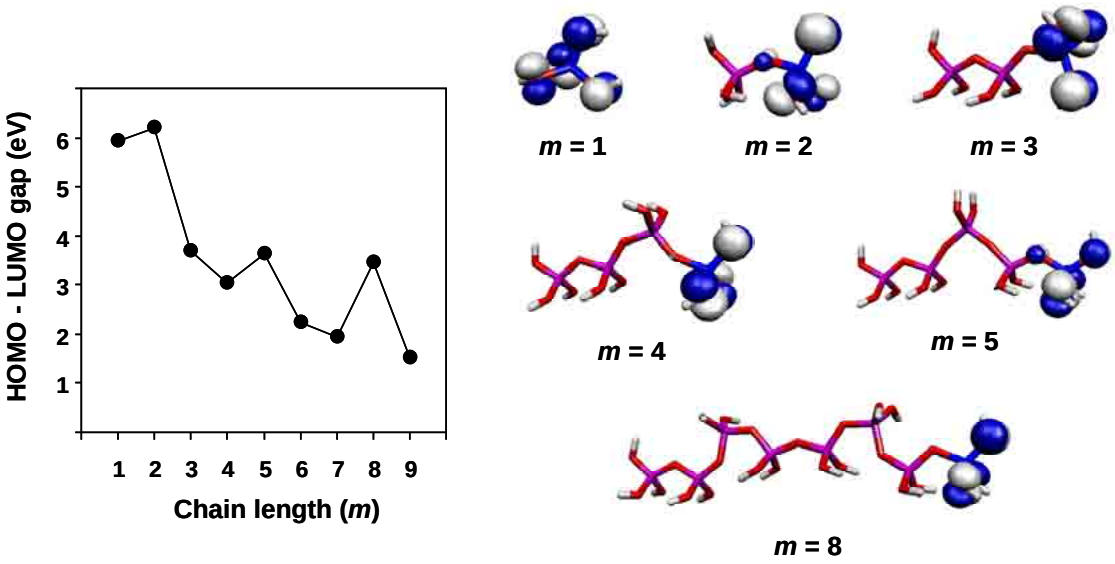

Figure 4.2.3.- In the left, the HOMO-LUMO gap of the alumino-silicate chains versus the chain length. In the right, spatial representation of the HOMO orbital for chains of different lengths. The orbitals are depicted as the blue and white clouds for positive and negative part of the wave function respectively. The chains are represented as sticks, with the red stick corresponding to an oxygen atom, the purple one to silicon, the white one to hydrogen, and the blue one to aluminium.

neighbouring sizes. Therefore, the stability of the chains with lengths following the 3*n* – 1 rule can be explained in terms of their HOMO-LUMO gap. In ***figure 4.2.4*** the HOMO orbitals of the alumino-silicate chains with different lengths are also plotted. The HOMO orbitals are those which would loss electrons more easily. For silicate chains, it was found that the neutral chains had the HOMO orbital delocalized, and the contribution of the bridging oxygen atoms was high [128]. However, the negatively charged chains had a very localized HOMO orbital in the OH groups. The negatively charged species were those that contribute more to the stability, probably due to the fact that bridging oxygen atoms were less reactive [128]. In the case of alumino-silicate chains, which are also charged, the orbital is strongly localized in the oxygen atoms linked to aluminium. Thus, they present the same effect as the charged silicon chains, and are expected to have an important contribution to the stability. In fact, in view of the presented results and those of reference [128], the charged species seem to have a crucial effect on the chain stability (see ***figure 4.2.3***).

Additionally, the bond distances and Mulliken populations of the end positions were analysed. The end position here refers to the last chain tetrahedra with silicon or aluminium atoms. These atoms are bonded to three hydroxyl groups (d_{OH}) and to the next silicon of the chain via an oxygen atom (d_{OSi} and d_{OAl}). These distances versus the alumino-silicate chain length are shown in the ***figure 4.2.5 (a)***. The d_{OH} distance is the average of the three –OH bonds. Both distances, d_{OH} and d_{OSi}, are between 0.1 and 0.15 Å larger for aluminium than for silicon. The O-H bond distances ($d_{O\text{-}H}$) of the hydroxyl groups bonded to the last unit were found to be equal until the third decimal digit ($d_{O\text{-}H}$ = 0.97 Å) for both type of chains, and therefore are not discussed. The d_{OH} lengths do not present a clear tendency neither for silicon nor for aluminium. All the distances are in a range of ± 0.015 Å around the mean value of 1.65 and 1.77 Å for silicon and aluminium respectively. However, in the case of the d_{OSi} and d_{OAl} distances there is a clear tendency with the chain length. The most stable chain lengths, with 2, 5 and 8 tetrahedra, have shorter bonds than the unstable ones.

The T-O-T angles, where T stands for Al or Si, were also analyzed. The Si-O-Si angles with silicon in the end chain tetrahedron range from 140 to 123° and do not show a clear

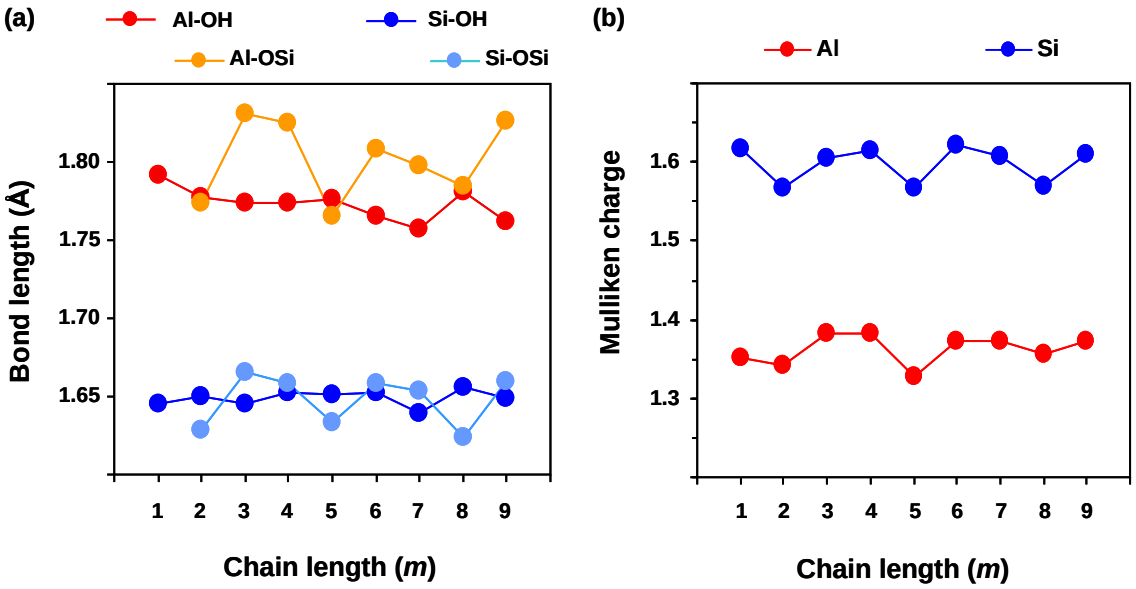

Figure 4.2.5.- (a) Bond distances for the last unit of the alumino-silicate chains versus the chain length. The average Al-OH and Al-OSi distances of the alumino-silicate chains are given in red and orange colours respectively. The Si-OH and Si-OSi distances of the pure silicate chains is shown dark blue and light blue the respectively. **(b)** Mulliken charge of the aluminium and silicon occupying the last position of the chain versus the chain length.

trend with chain size. The replacement of Si by Al changes only slightly the Si-O-Al angles, decreasing less than 8°. Thus, it seems that the tetrahedral structure of the silicate chains arrangements remain unaltered when replacing Si by Al.

The silicon and aluminium charges in the final tetrahedron against the chain length are shown in ***figure 4.2.5 (b)***. As expected, the charges are larger for silicon than for aluminium. The range between the maximum and minimum values of the charge for different lengths is not large, about 0.04 and 0.05 e^- for Al and Si respectively. However, there is a clear trend with the length. For the lengths that follow the $3n - 1$ rule, the atoms have a lower charge. Combining this result with the previous distance analysis, it can be observed that the most stable chains have shorter bonds and less charge in the end Si-Al positions. These are clear signs of a higher covalent character, and thus, stronger bonds. The stronger bond of the end tetrahedra with the rest of the chain may be the reason for the higher stability of the $3n - 1$ lengths.

4.3. Silicate chain growth and structure

In the previous section, it has been discussed the stability of the alumino-silicate chains, concluding that the chain with $3n - 1$ tetrahedra are the most stable ones. Now, the formation of those lengths will be treated. The growth from stable to stable chains by linear condensation (dimer to pentamer for example), implies that unstable structures must be formed during the process (trimers and tetramers). Thus, a different growth process which avoids the formation of unstable chains has been proposed [8, 52]. In it, two dimers are merged together by a linker monomer to form a pentameric chain [8, 52]. To study this process, the merging energies arising from the formation of pentameric chains due to the reaction of two neutral dimers with different linker units, $Si(OH)_4$ $Si(OH)_3O^-$, and $Al(OH)_4^-$, have been calculated.

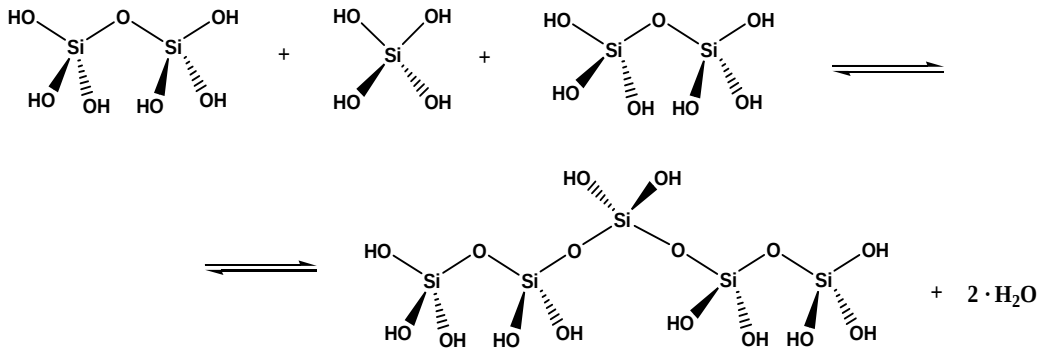

Analogous to the discussed condensation energy, the merging energies were calculated as the energy difference between products and reactants:

$$E_{condensation} = (E_{pentamer} + E_{H_2O}) - (2 \cdot E_{dimer} + E_{monomer}) \qquad (4.2.4)$$

The obtained values are given in the first part of ***table 4.3.1.*** The merging energy when $Al(OH)_4^-$ acts as link, 1.79 eV, is considerably larger than those with either neutral or charged silicon groups. Thus, the merging reactions could be enhanced by the presence of $Al(OH)_4^-$ groups. This finding can be related to the experimental results, which report larger chains when aluminium is present [61, 72, 180, 193]. The process also implies that aluminium would occupy the bridging site of the formed pentameric chain,

in agreement with the experimental data [61, 72, 180, 190-193].

In the previous section the obtained results indicate that chain dimers with aluminium in a Q^1 position are stable, contrary to the experimental results. Therefore, the merging processes when aluminium takes part of one dimer have been also calculated. Two structures could be obtained from the merging processes, either with aluminium in the Q^1 end site or in the Q^2 paired site. The merging energies for the end and paired site are 0.23 and 0.97 eV, respectively (see the second part of ***table 4.3.1)***. Although both processes are thermodynamically favourable, it was found a significant difference (0.74 eV) in the energy gain for Al in the paired position. The most likely process is that one in which aluminium is the reactive extreme of the dimer, resulting in a chain with Al in the Q^2 paired site. The result is in agreement with the experimental observation that aluminium is never situated at Q^1 positions [61, 72, 180, 190-193]. The energy gain of the merging with Al in the paired site is again substantially higher than those of pure silicon processes. Nevertheless, the most energetically favourable reaction is the one with aluminium acting as linker unit, and located in the bridging position of the chain.

Table 4.3.1.- Merging energies of the pentameric chains formation reactions. The first part of the table shows the merging reaction of silicon dimers by means of different linker units: a neutral $Si(OH)_4$ (in blue), a charged $Si(OH)_3O^-$ (in red) and a $Al(OH)_4^-$ (in green). The second part shows the merging reaction when aluminium takes part of the dimer, and a neutral silicate group acts as the linker.

Merging reaction	Merging energy (eV)
Si-Si + **Si** + Si-Si → Si-Si-**Si**-Si-Si + 2 H_2O	0.12
Si-Si + **Si**$^-$ + Si-Si → Si-Si-**Si**$^-$-Si-Si + 2 H_2O	0.32
Si-Si + **Al**$^-$ + Si-Si → Si-Si-**Al**$^-$-Si-Si + 2 H_2O	**1.79**
Si-**Al**$^-$ + Si + Si-Si → **Al**$^-$-Si-Si-Si-Si + 2 H_2O	0.23
Si-**Al**$^-$ + Si + Si-Si → Si-**Al**$^-$-Si-Si-Si + 2 H_2O	0.97

The experimental data [61, 72, 180, 193] and the results from this work indicate that aluminium enhances the merging process. In general, the reactivity of aluminium is faster than that of silicon [215], and it has also tendency to form Q^3 sites [182, 184, 187]. Consequently, longer chains and branched structures are formed in cement pastes or synthetic C-S-H gels when aluminium is present [61, 72, 180, 193]. These effects have been studied in this work following the condensation of $Si(OH)_4$ and $Al(OH)_3$ groups in presence of calcium by Molecular Dynamics. Different to the *ab-initio* simulations, where a given initial chain structure was relaxed, in MD the monomers condense and polymerize freely.

The Mean Chain Length (MCL) of the alumino-silicate chains was calculated according to the formula proposed by Richardson and co-workers [61, 180]:

$$MCL = \frac{Q^1 + Q^2 + (3/2)Q^2_{1Al}}{(1/2)Q^1} \qquad (4.2.5)$$

Experimentally, the relative amounts of Q^n sites are obtained from the area of the correspondent NMR spectra. In the simulations, the number of Q^n sites could be calculated directly. For a given atom T the number of –O–T structures within a given length threshold were counted, where T stands for Si or Al. The number of Q^n sites for aluminium and silicon for all the studied compositions are given as percentages of the total in the ***appendix 4***. The MCL for the studied Al/(Al+Si) ratios versus the Ca/(Al+Si) ratio are shown in ***figure 4.3.1***. The results of a previous work by Dolado et al. for aluminium free simulations are also represented in the figure as black circles. They found that the chain length decreased as the Ca/Si ratio increased [122]. The same trend is followed when aluminium is present during the polymerization, see ***figure 4.3.1***. However, it is clear that the presence of aluminium increases the MCL. The aluminium and calcium concentrations have opposite effects: while the first one increases the MCL, the second one decreases the MCL.

Figure 4.3.1 also shows the degree of high polymerized species, the alumino-silicate tetrahedra linked to more than two other tetrahedra, by looking at the percent of $Q^3 + Q^4$

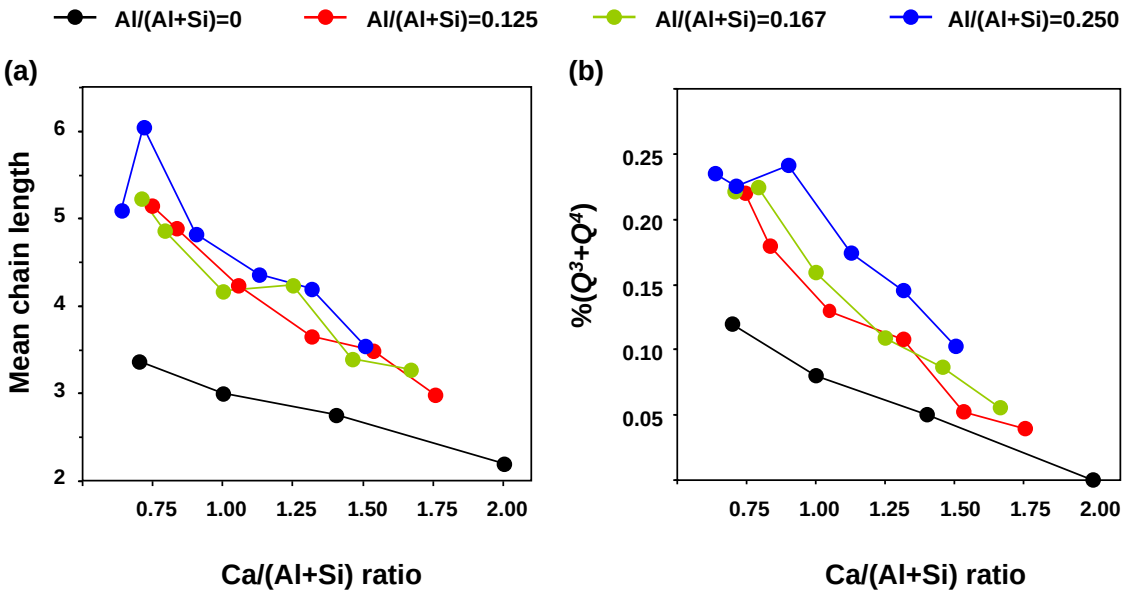

Figure 4.3.1- (a) Mean chain length and **(b)** percent of high polymerization species obtained versus the Ca/(Al+Si) ratio for different aluminium contents as given in the layer.

sites against the Ca/(Al+Si). The existence of Q^3 and Q^4 is related to the formation of two dimensional (2D) and three dimensional (3D) structures. Therefore, the %(Q^3 + Q^4) measures the formation of non-linear chains and interchains crossings. As the aluminium content increases, the number of Q^3 + Q^4 sites increases. Thus, it is clear that aluminium favours the apparition of 2D and 3D features. In fact, the aluminium percent in Q^3 and Q^4 sites is considerably higher than that of silicon, as can be seen in ***appendix 4***. This result agrees with the experimental evidences that find a preference for Al to occupy Q^3 bridging sites linking different alumino-silicate chains [184, 187]. Further analysis both figures can provide additional conclusions. For instance, the differences between the system with and without aluminium are more marked for low Ca/(Al+Si), especially in the case of the high polymerized species. It may indicate that the effects due to the calcium content are stronger than those of aluminium. Thus, linear chains of short lengths, mostly dimers, would be formed at high Ca/(Al+Si) ratio, independently of the aluminium presence.

It is remarkable that at Ca/(Al+Si) below 1.0 the Q^3 + Q^4 sites are more than the 20%.

Thus, the equations to quantify the MCL should account for these features. Gaitero et al. [97] defined a new parameter to quantify the length and structure of the silicate chains including Q^3 and Q^4 features. Studying the degradation of the cement paste due to calcium leaching, they found that as the leaching increased, the content of Ca in the C-S-H gel decreased, and more polymerized silicate chains appear, referring with polymerization to the non-linear structures. Thus, they generalized the MCL equations to the case of planar and three-dimensional structures. They defined the *Average Segment Length* (ASL), which represents the number of length units, i.e. silicate and/or aluminate tetrahedra, between Q^1 and Q^3sites, between Q^1 and Q^4 sites, between Q^3 and Q^4 sites, and between two Q^1, two Q^3 or two Q^4 sites:

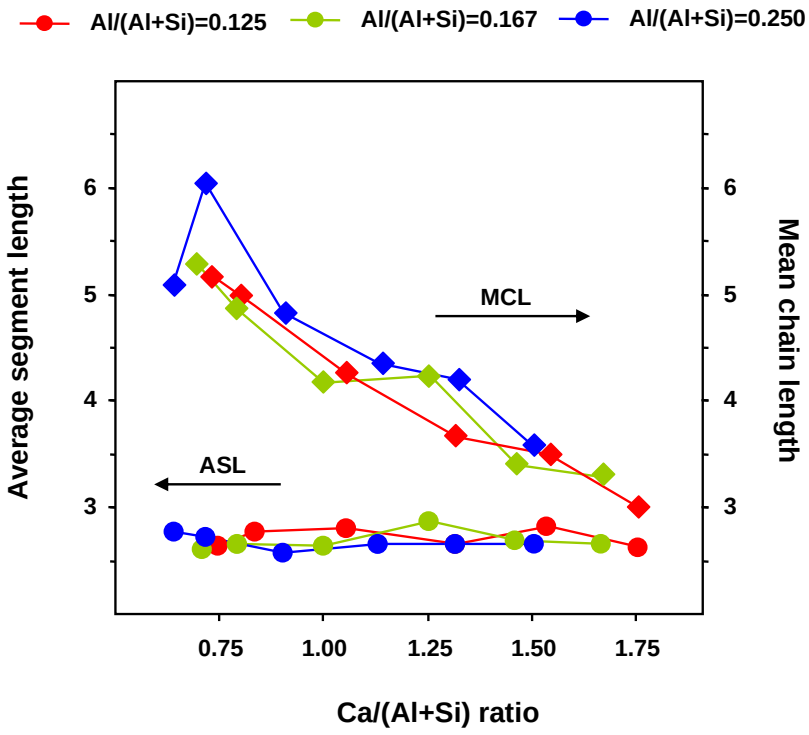

Figure 4.3.2.- Average Segment Length (ASL) of the alumino-silicate chains as a function of the Ca/(Al+Si) ratio for the studied Al/(Al+Si) ratios obtained from the Molecular Dynamics simulations. For comparison, the results obtained for the Mean Chain Length (MCL) with equation (4.2.5) are also shown. The values for the ASL are given as points in the left scale, while those for the MCL as rhombus in the right scale.

$$ASL = \frac{2\left(Q^1 + Q^2 + 1.5Q^2\left(1Al\right) + 3Q^3 + 4Q^4\right)}{Q^1 + 3Q^3 + 4Q^4} \quad (4.2.6)$$

If Q^3 and Q^4 sites are not present, the ASL is exactly the same length as the MCL. As in the case of the MCL, the ASL accounts only for the aluminium units linked to a Q^2 silicon, due to the lack of resolution to determinate other peaks from the ^{29}Si NMR spectra. In our simulation it is possible to considerer all the aluminium and silicon sites, and therefore the equation (4.2.6) is rewritten as:

$$ASL = \frac{2\left(Q^1 + Q^1_{Al} + Q^2 + Q^2_{Al} + 3Q^3 + 3Q^3_{Al} + 4Q^4 + 4Q^4_{Al}\right)}{\left(Q^1 + Q^1_{Al} + 3Q^3 + 3Q^3_{Al} + 4Q^4 + 4Q^4_{Al}\right)} \quad (4.2.7)$$

The result of the ASL for the studied compositions is shown in ***figure 4.3.2***. To compare, the previously calculated MCL values are included again in this figure. The ASL is nearly constant with respect to the Ca/(Al+Si) and Al/(Al+Si) ratios, with a mean value of ~2.8. As the Ca content decreases, the MCL increases while the ASL is kept constant. To unify both trends, the formation of links between different chains must be considered. For the same chain structure, the MCL accounts for Q^2 sites between Q^1 extremes, while the ASL accounts for Q^2 sites between extremes, Q^1 sites, and positions where branches appear, Q^3 and Q^4 sites. Thus, the creation of interchain crossings decreases the segment length, while the chain length is unaffected. Assuming a *Dreierketten* arrangement of the alumino-silicate chains, a value of ASL greater than 2 indicates that the branches appear in inner sites of the chains. These results are in agreement with the experimental findings [184, 187].

4.4. Position of aluminium within the silicate chains

To analyze the stability of the alumino-silicate chains, it was considered that aluminium occupied the end chain tetrahedron. However, from experimental and theoretical results [121, 180, 182, 193], it is well known that aluminium is not located at the

end Q^1 positions. In fact, most of the researches conclude that the incorporation of aluminium only takes place at the bridging Q^2 position [61, 72, 180, 190-193], although paired positions have been found to be stable in some works [121, 195]. The merging process studied in the previous section already point to the bridging position as the most probable one for aluminium, as the energetics of the reactions favour this site. Here, the possible positions of aluminium within a pentameric chain (the first stable length with Q^1, Q^2 paired, and Q^2 bridging positions) were investigated. To this end, the energy, the HOMO-LUMO gap, the spatial location of the HOMO orbital, the bond distances, and the charges were examined.

The energy differences with respect to the low lying structure are shown in ***figure 4.4.1***. The less energetic and therefore most stable structure is the one with aluminium in the bridging position. The chain with aluminium in paired position has a very close energy, just 0.15 eV higher, while the energy for the chain with aluminium in the end position increases considerably, about 1 eV. The HOMO-LUMO gaps change following a similar pattern with the Al position, fully correlated with the previous energy differences. The highest gap corresponds to the chain with aluminium in the bridging site. The gap is slightly smaller (0.05 eV) when aluminium is in the paired position, while when Al is located in the end sites there is substantial decrease (0.59 eV). Thus, both the energies and the HOMO-LUMO gaps indicate a clear preference of aluminium

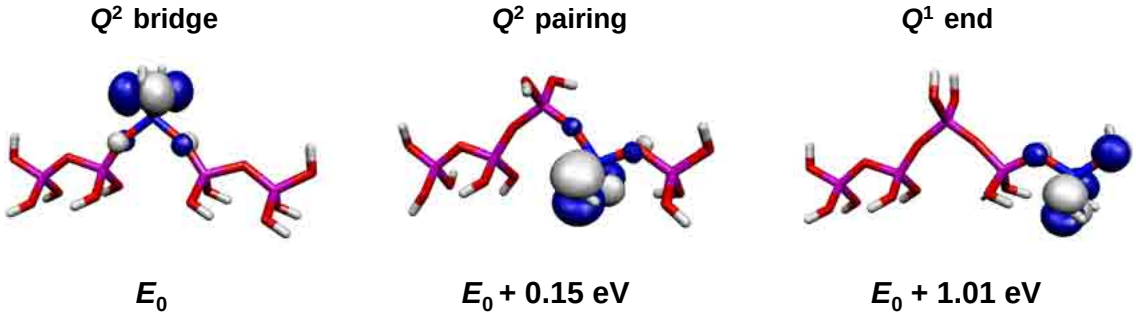

Figure 4.4.1.- Spatial representation of the HOMO orbital for a pentameric chain with aluminium in different positions. Due to the chain symmetry only three different configurations are possible. Below the structure, the energy differences with respect to the grown state energy are also given. The code colours are the same as in ***figure 4.2.3.***

Table 4.4.1.- HOMO-LUMO gaps and charges on Al and Si in different chain positions within a pentameric alumino-silicate chain

Position	HOMO-LUMO (eV)	Charge on Al (e^-)	Charge on Si (e^-)
Q^2 Bridging	4.22	1.40	1.58
Q^2 Paired	4.17	1.38	1.57
Q^1 end	3.63	1.33	1.57

for the inner Q^2 bridging positions, in agreement with the experimental data [61, 72, 180, 190-193]. The small energy and gap difference between the chains with aluminium in the bridging and paired positions may indicate that the latter could be also possible in certain cases, as already stated by some authors [121, 195]. Nevertheless, in view of the results, the Q^1 position is energetically unfavourable, and aluminium would be always flanked by two silicon units in a Q^2 site. From ***figure 4.4.1***, the HOMO orbital is always located at the oxygen atoms bonded to aluminium. Specifically, the orbital is strongly localized in the oxygen atoms of the OH groups, with only a small contribution from the bonding Al-O-Si oxygen atoms. As mentioned in the previous section, this is related to the high stability of charged chains.

As in the stability analysis, the d_{OH}, d_{OSi}, d_{OAl}, and $d_{O\text{-}H}$ bond distances for aluminium and silicon were examined for the different positions within the pentameric chain. The bond lengths are not significantly affected by the atomic position. Changing the position, the Al d_{OH} and d_{OSi} distances change not more than 0.01 Å. The differences for Si are slightly higher, but still less that 0.02 Å. Furthermore, they do not follow any clear trend to extract a conclusion. However, a clear trend was found in the change of the Mulliken population (see ***table 4.4.1***). When aluminium is located in the paired Q^2 sites of the chain, the charge increases, as correspond to a metallic element when the coordination increases. The covalent character of silicon does not change that much with the position within the chain.

The most probable positions of aluminium atoms within the chains could be also

studied from the Molecular Dynamics simulations. It has been discussed in the previous section that the formed alumino-silicate chains were not linear but branched. This makes difficult the analysis in terms of Q^2 paired and bridging sites, as these positions are defined for linear chains. However, the tendency of aluminium to occupy inner positions in the structures instead of Q^1 ends is clear. The fraction of Al and Si in Q^1 sites are shown in ***figure 4.4.2(a)***. The results show that silicon has a higher tendency to occupy the Q^1 end positions than aluminium for all the composition ranges. The effect of high calcium contents is the same as mentioned on the previous section. For high calcium contents most of the silicon sites are Q^1 positions. Even in that case, less than half of the aluminium is located at Q^1 positions, which evolve to less than 20% for lower Ca/(Al+Si) ratios. These amounts of aluminium in Q^1 sites are too high in comparison with the experimental evidences pointing that aluminium is not located at those positions [6, 52, 60, 61, 180, 182, 190-193], and might be due to the high Al/(Al+Si) ratios in the simulations.

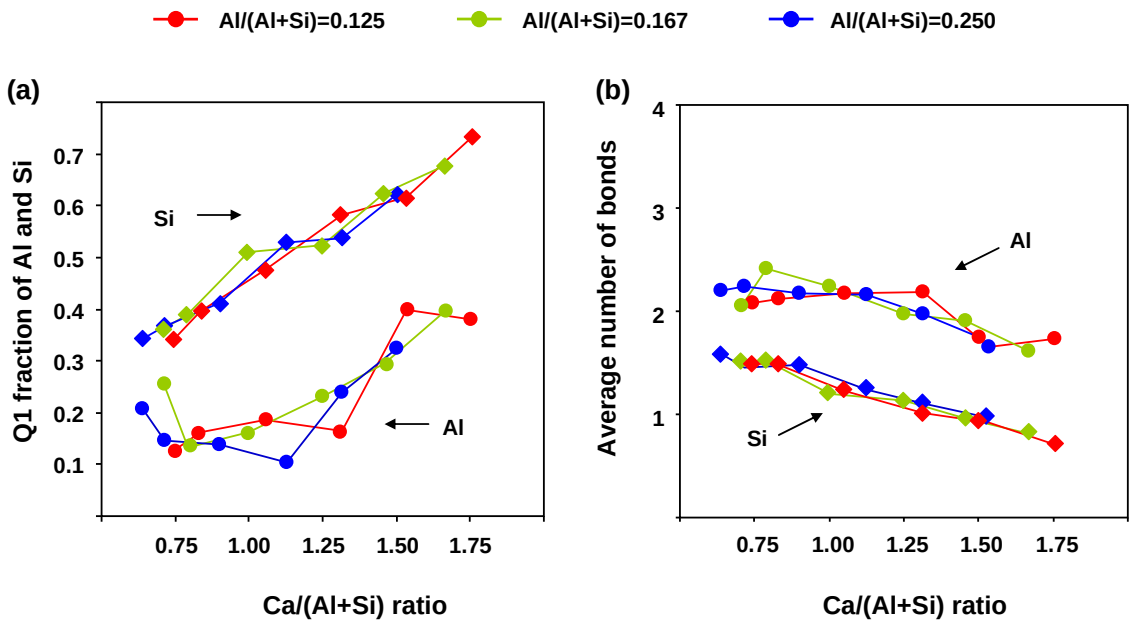

Figure 4.4.2.- (a) Fraction of aluminium and silicon occupying Q^1 end positions in the chains for different compositions as a function of the Ca/(Al+Si) ratio for the studied Al/(Al+Si) ratios. **(b)** Average number of *Al-O-T* and *Si-O-T* bonds, with T is Si or Al, as a function of the Ca/(Al+Si) ratio for the studied Al/(Al+Si) ratios. The values for Al are given as points, while those for the Si as rhombus.

The preference of aluminium for the inner positions in the structures is corroborated by looking at the average number of *Al-O-T* and *Si-O-T* bonds, where *T* is aluminium or silicon:

$$average\ n^o\ bonds = \frac{1Q^1 + 2Q^2 + 3Q^3 + 4Q^4}{Q^1 + Q^2 + Q^3 + Q^4} \qquad (4.2.8)$$

The average number of bonds for is given in ***figure 4.4.2(b)***. The bond number of both Al and Si units increases as the Ca/(Al+Si) ratio decreases, in agreement with previous results. The number of bonds for silicon is in a range between 1 and 1.5, which indicates mostly Q^1 and Q^2 sites. The number of bonds for aluminium is higher than that of silicon. It is about 2 for all the compositions, which corresponds to Q^2 sites. Thus, aluminium must be located inside the alumino-silicate structures. These results indicate a clear preference of aluminium for the inner positions rather than end positions [6, 52, 60, 61, 180, 182, 190-193]. Furthermore, it has been experimentally found that aluminium takes part of Q^3 bridging sites when interchain crossings appear [184, 187]. The calculated high polymerization degree of aluminium is in agreement with this observation.

4.5. Conclusions

The stability, formation, and structure of silicate chains when aluminium substitutes for silicon were investigated by means of *ab-initio* and molecular dynamics methods. According to the obtained results, the general picture of the aluminium incorporation to the C-S-H gel silicate chains could be summarized as follows:

The stability of the chain lengths following the $3n - 1$ rule is also maintained when aluminium is present in the chains. In fact, it has been noticed that charged chains, either with $Al(OH)_4^-$ or $Si(OH)_3O^-$ groups, have a greater contribution to the stability of $3n - 1$ lengths than neutral chains. The stability of these “magic” chain lengths could be correlated to the bond distances and Mulliken populations in the chain extremes. For the

most stable chains a greater covalent character and therefore stronger bonds was found. The results are corroborated by the HOMO-LUMO gaps, which are higher for chains with 2, 5 and 8 tetrahedra. Contrary to the experimental results, dimers containing aluminium were found stable after the simulations. This finding could be rationalized studying the chain growth.

The linear monomer-by-monomer chain growth is thermodynamically favourable for all the considered chains lengths and types, both neutral and charged with Al or Si. However, in such processes less stable chains would be formed. A merging mechanism was proposed to growth beyond the less stable chains: two stable dimers are linked by a monomer to form a pentamer. Thus, the merging process of two silicate dimers with $Si(OH)_4$, $Si(OH)_3O^-$ and $Al(OH)_4^-$ was studied. It was found thermodynamically favourable for all cases, though the energy gain with Al monomers as linker is higher than with Si monomers. The merging energies when Al is in the dimer were smaller than the obtained with $Al(OH)_4$ as a linker. Nevertheless, it was considerably higher than the pure silicon processes if aluminium occupied a Q^2 paired site in the dimer. Thus, there is a clear predilection of Al for the inner Q^2 positions of the chains, especially in the bridging site.

The high tendency of aluminium to react is clear from these results. In fact, the alumino-silicate structures formed by condensation of $Si(OH)_4$ and $Al(OH)_3$ groups in presence of calcium are larger and more polymerized than in Al-free simulations. However, the effect of Ca in the formed structures was predominant. At high calcium contents, linear and short chains, mostly dimers, were formed. However, at low calcium contents, the polymerization degree increased and forms larger two-dimensional and three-dimensional structures. The high reactivity of aluminium might be the reason why no dimers with Al are experimentally found. Although the computed results indicate that those dimers could be thermodynamically stable, their fast reaction by merging processes may make them evolve rapidly to longer chains.

All the presented results suggest that Al would occupy inner chain positions, and no Q^1 end sites. In fact, if a pentameric chain is considered, the obtained lower energy

configuration is the one with Al in the Q^2 bridging position. The energetic differences between Q^2 paired and bridging sites are in favour of the bridging, though the Al location in the paired sites is also favourable for the merging reactions. Nevertheless, both cases are possible, in view of our results. The tendency of $Al(OH)_3$ to react makes the alumino-silicate structures formed in MD simulations non linear. Thus, an analysis of the Al position in terms of paired and bridging sites is difficult. Again, aluminium tends to be at Q^2 and Q^3 sites, and not at the end Q^1 sites.

Our model concerning the aluminium incorporation to the silicate chain structure of the C-S-H gel is in agreement with the experimental data. It must be noted that the results for Dreierketten chains by using *ab-initio* methods could be applied to several minerals that present the same silciate chain arrangement, wollastonite, foshagite, nekoite or xonotlite [217-221].

Chapter 5:

Elastic Properties of the Cement Paste Main Components

5.1. Introduction and computational method

Cement based materials, such as concrete, mortars, or fibre reinforced cement composites are mainly used in construction. Consequently, their most important characteristics are the mechanical properties and durability. Much of the research in the field is focused on the improvement of these properties and their modelling under different conditions. To this end, a good knowledge of the material structure is necessary. Unfortunately, the cement paste is a very complex composite, where many crystalline phases coexist surrounded by an amorphous product, the C-S-H gel. The C-S-H gel is the most important component and hence major responsible for the mechanical properties. Nevertheless, the crystalline phases must be also taken into account, as they contribute to the net performance of the cement paste. Therefore, a precise determination of the elastic properties for all the paste constituents is crucial to

develop accurate models that describe the mechanical material behaviour at the macroscale [106]. The small size and the poor crystallinity of some crystalline phases make difficult their characterization. The problem becomes more complex for the C-S-H gel, whose amorphous nature, associated porosity, and dependence of the water content affect the results of some experimental techniques [41]. Atomistic simulation methods could be a very useful tool to calculate the elastic properties of cement components. This chapter deals with the calculation of the elastic properties for the cement paste components by means of molecular mechanics methods.

The elastic or Young modulus (*E*) of the main clinker components have been determined by nanoindentation and resonance frequencies technique [222, 223]. Velez et al. performed nanoindentation measurements on pure synthetic tricalcium silicate (C_3S), dicalcium silicate (C_2S), tricalcium aluminate (C_3A), and ferrite (C_4AF), as well as synthetic alite and belite with the same stoichiometry as an average industrial clinker. They found values of *E* ranging from 125 to 145 GPa, where the Young modulus of the pure structures was slightly higher than those of alite and belite [222]. With the same technique, Acker obtained identical values of the Young modulus for the unhydrated clinker phases in Ductal cement [223]. Finally, Velez et al. [222] complemented their study with resonance frequencies measurements. Extrapolating to zero the results of samples with different porosities, they found *E* values slightly higher than those by nanoindentation (140 – 160 GPa) though in good agreement.

The most important hydration products, portlandite and ettringite, have been the subject of numerous studies. The elastic properties of portlandite were reviewed by Monteiro and Chang [224]. Their analysis was based on previous Brioullin spectroscopy results [225] and compression tests of portlandite crystals [226]. From those results, they calculate the Reuss [227], Voigt [228] and Hashin-Shtrikman (H-S) [229] upper and lower bounds for the bulk (*K*) and shear (*G*) moduli, as well as their Hill average [230]. They also derived the anisotropic Young modulus and the Poisson's ratio (*v*) [231]. The definitions of these elastic parameters from the elastic tensor coefficients are given in ***appendix 5***. They concluded that the Young modulus is ~41.5 GPa while the Poisson's ratio ~0.32. Compressive tests of compacted powder samples with different porosities

obtained E = 35.2 [232] and 48 GPa [233]. Although these values are close to their results, Monteiro and Chang noticed that they are out from the Hashin-Shtrikman boundaries. They attribute the disagreement to the influence of different pore geometries in the compacting process [224]. Portlandite has been also theoretically studied by DFT methods [234]. After computing elastic tensor coefficients in reasonably agreement with the experimental data, the portlandite Hill average of the Young modulus was 31.55 GPa, somewhat lower than the experimental values. Both the experiments and theory found a strong anisotropy between the young modulus perpendicular and coplanar to the $Ca(OH)_2$ layers, about 3 times higher the latter [226, 234]. Studies of ettringite by ultrasounds of compacted powder with different porosities get a value E = 47.9 GPa [235]. However, a complicated fitting was employed to extrapolate the result to zero porosity. Posterior analysis of these data together with new results using a linear fitting method obtained a Young modulus of 25.2 GPa [106]. This result agrees with the most recent studies, where the elastic tensor of ettringite has been determined by Brioullin spectroscopy. By this technique, the obtained Young modulus is 25.0 GPa for the Hill average [236]. Unfortunately, the experimental elastic properties of other hydrated phases as monosulphoaluminate or hydrogarnet have not yet been determined. The lack of information is related to their poor crystallinity and the small size of their crystals [4].

Little information about the C-S-H gel elastic properties is available. Most of the techniques cannot be applied due to the amorphous nature and the small particle size. Nanoindentation has demonstrated to be very useful. However, the resolution of the technique, with indentations areas ~1 μm and depth ~250 nm, is not enough to determine the elastic properties of C-S-H gel single nanoparticles. Thus, the properties of the C-S-H gel matrix are calculated, including the intrinsic porosity and associated water [88]. The nanoindentation results show a bimodal distribution of the Young modulus with maxima at ~19 and ~29 GPa [58, 87, 88, 237]. These results fit with Jennings's model [84, 85, 90], which proposed the existence of two gels with different densities. According to this result, the C-S-H gel would be formed of the same particles, and the variations of the Young modulus would be associated to the gel porosity [58, 87, 88]. Acker also performed nanoindentation tests on Ductal, an ultrahigh reinforced

cement, with similar results (E = 20 – 31 GPa). In this case the low and high values of E were attributed to C/S ratios < 1 and > 1 respectively [223]. From nanoindentation results, the indentation modulus (M) of a single particle has been estimated by reverse analysis of the data with a self-consistent micromechanical model [58]. The obtained values are 65.9 and 62.9 GPa for the LD and HD C-S-H gel varieties. Both C-S-H gel varieties have close values, which support the suggestion that a single particle builds both types of C-S-H gel [58].

The tobermorite family and ill-crystalline C-S-H type I could be a good approach to understand the elastic properties of the cementitious gel. Plassard et al. measured by nanoindentation methods the Young modulus of C-S-H formed on the surface of a calcite crystal in sodium silicate solution by Atomic Force Microscopy [238]. The C-S-H produced was equilibrated at various concentrations of calcium hydroxide solution to obtain different C/S ratios. They found that the Young modulus increased from ~120 GPa up to 300 GPa as the C/S ratio increased [238]. Recently, Alizadeh et al. measured by Dynamical Mechanical Analysis (DMA) the elastic modulus of samples synthesized by reaction of different amounts of SiO_2 and CaO in water excess [93]. Their dependence for the Young modulus was opposite to that of Plassard et al.: as the C/S ratio increased, E decreased. The values range between 231 and 95 GPa for C/S ratios from 0.8 to 1.5. It must be noted that the values obtained for synthetic C-S-H gels are considerably higher than the suggested for the C-S-H particles. No experimental data regarding the elastic properties of tobermorite was found in the literature. However, they have been calculated by atomistic simulation methods. Two studies [117, 119] by force field methods obtained a value of E = 71.8 GPa [119] for the tobermorite-like Hamid's structure [118], E = 63.5 GPa for a 14 Å tobermorite [117], and 89 GPa for a 12 Å variety with C/S ratio = 1 [117]. Pellenq et al. also reached in his work [117], several interesting conclusions regarding the nature of the cohesive forces in the C-S-H gel. They propose that the nature of the bond network between tobermorite layers is iono-covalent, similar to that of the layers. Thus, tobermorite, and hence the C-S-H gel particles, should be viewed as a continuum material rather than independent layers. Comparing the magnitude order between the tobermorite and the C-S-H gel matrix Young moduli, they concluded that the forces that govern the cohesion between cement particles should be

the same, i.e., iono-covalent [117].

In this chapter, the elastic properties of the cement paste components were calculated by means of force field methods, covering the clinker phases (***section 2***), 31 members of the crystalline Calcium Silicate Hydrates family (***section 3***), the C-S-H gel (***section 4***), and other hydration products (***section 5***), as well as. The discussion was focused on the C-S-H systems. The elastic properties of the crystalline CSH species were discussed as a function of the density, the hydrogen content, and the C/S ratio, and compared with the experimental models for the C-S-H gel nanoparticles. Finally, the elastic properties of a C-S-H gel particle are calculated as a function of the silicate chain length, and rescaled to the gel values applying homogenization procedures.

- ***Computational methods***

The elastic properties of the phases under study have been calculated by molecular mechanics methods. The GULP code has been selected for this purpose [151, 239]. The experimental data for the crystalline structures were optimized by relaxing the unit cell parameters and the atomic positions. The symmetries were eliminated once the experimental full unit cells were generated to allow anisotropic variations and full atomic relaxations, even if they were initially in specific symmetry positions. In some cases the cell symmetry was distorted during the relaxation, and therefore some computed coefficients of the elastic tensor that should be zero have non-zero values. In order to accelerate the convergence of the coulombic energy, the Ewald summation method was chosen [152] with a cut-off radius of 8 Å. The search of local minima followed the Newton-Raphson procedure, updating the Hessian each ten steps with the Broyden-Fletcher-Goldfarb-Shannon (BFGS) scheme [137, 240]. In some cases, especially in structures with high hydrogen content, the convergence was problematic. In those specific cases a prior conjugate gradient (CG) optimization was done. Then, the elastic constant tensor was calculated from the second energy derivative on the optimized structures [150]. From the elastic tensor, the elastic parameters can be derived with the formulas given in ***appendix 5***.

The election of a suitable set of potential energy functional forms and their corresponding parameters (force field) is the tricky part of a molecular mechanics simulation. The main atoms in the studied systems are Ca-Si-O-H set. The force field was chosen from a previous study of the tobermorite structure proposed by Hamid [119]. The interactions between silicate ions were modelled with the well-known potentials for zeolites [241-244]. The Si-O interaction were simulated by two-body Buckingham potentials, including a three-body O-Si-O harmonic potential that penalized deviations from the hybridization bond angle [241-244]. The intermolecular interactions between the water molecules hydrogen and oxygen atoms with other species were described using Buckingham potentials, whereas a Lennard-Jones potential describes the interaction between the atoms from different water molecules. The intramolecular interactions within a water molecule were mimicked by a Morse potential, as well as a three-body harmonic potential to describe H-O-H angle due to the oxygen lone electron pair [242, 244-247]. The coulomb interaction within water molecules was subtracted. Thus, the charges of hydrogen and oxygen atoms serve only to describe their interaction with other atoms, and not to determine the internal structure of the water molecules itself. Therefore, the number of interactions that must be computed were drastically reduced and more flexibility was allowed to the water molecules configuration. The Ca-O ionic interactions were modelled by Buckingham repulsive potentials [246, 247]. Three-body terms were not included in this case due to the random orientation of the ionic interaction. The polarizability of oxygen atoms is described by the core-shell approach [154, 248]. In this model, the atoms are treated as internal cores linked to external mass-less shells. Both the core and the shell are linked by a spring potential and have specific charges. It must be noted that not all oxygen or calcium atoms are equal. The environment surrounding a specific atom has a great influence on its chemical behaviour, bond distances, bond strengths, and other properties. Hence, the differences between atoms were distinguished with different values for the corresponding potential parameters.

The initial force field was extended to Al, S and Fe interactions. The selected potentials from aluminium were those developed for zeolites [241] and brownmillenite (C_4AF) [249], depending on the nature of Al in the structure. Both force fields employed

a Buckigham potential to simulate the Al-O bond. The former includes a three-body harmonic potential to model the O-Al-O bond hybridation. The Fe-O interaction was simulated by a Buckingham potential and their parameters for C_4AF are described in refs. [249, 250]. Finally, the interactions of sulphate groups were modelled using the force field developed by Adam to study the hydration of gypsum [251]. It consists in repulsive Buckingham potentials to simulate the interaction between the oxygen atoms of the SO_4^- with other species, and a Morse and three-body potentials describe the internal tetrahedral structure of the anion. All the potential functional forms and parameters mentioned are listed in ***appendix 4***.

5.2. Clinker phases

The structure, polymorphism, and hydration reactions of the most important clinker components (alite, belite, tricalcium aluminate and ferrite) were described in the introductory chapter. The stable structures at room temperature were selected for the calculations. The pure stoichiometries were employed, although some of them are stable due to guest elements incorporation [4]. The monoclinic superstructure MIII of tricalcium silicate was considered [16]. To avoid fractional occupation numbers of the irregular oxygen positions, those with higher occupation numbers were used when possible. When the occupation number was 0.5, the site selection was made at random. Nevertheless, several tests with different occupations shown negligible divergences for the lattice parameters and elastic properties. The selected atomic structure of the β-belite polymorph and tricalcium aluminate were those described in references [252] and [24]. Finally, the perfect stoichiometry of brownmillenite, C_4AF, was chosen to simulate the ferrite phase [253]. In this structure, all the octahedral positions are occupied by Fe^{+3} and all the tetrahedral positions by Al^{+3}.

After the relaxation, the unit cell parameters and atomic arrangements were checked to assess the transferability of the force field for these structures. The comparison between the crystalline structures and the experimental data is shown in ***appendix 6***. There is an excellent agreement in the lattice parameters, especially in the case of the

Table 5.2.1.- Elastic properties of the clinker phases. The experimental Young modulus and the estimated Poisson coefficients are also given. The bulk (*K*), shear (*G*), and Young modulus (*E*) are in GPa. The Poisson's ratio (ν) is dimensionless.

	K		*G*		*E*		*v*	
	Exp	Comp	Exp	Comp	Exp[a]	Comp	Exp[a]	Comp
C_3S	--	103.0	--	54.5	147-135	138.9	0.30	0.28
β-C_2S	--	111.0	--	53.1	140-130	137.9	0.30	0.30
C_3A	--	133.26	--	63.9	145-160	165.1	0.30	0.29
C_4AF	--	175.6	--	93.5	125	238.2	0.30	0.27

a Values from references [222, 223]

angles. All the errors are lower than the 3% with the exception of the c side of C_2S. Nevertheless, this expansion has little importance in the atomic arrangement, maintaining the silicate structure and the Ca-O coordination unchanged. The symmetries are kept unaltered after the simulations.

The elastic properties of the clinker phases are given in ***table 5.2.1***. The anisotropic Young modulus (E) of C_3S, C_2S and C_3A are in excellent agreement with the nanoindentation results [222, 223]. The results of C_3S and C_2S results are within the range between nanoindentation and resonance frequency measurements. The Young modulus of C_3A is slightly higher than the experimental data, but still in good agreement. The Poisson's ratio are close to the to the estimated averaged value for all the phase constituents of the clinker [254].

The calculated E for ferrite is almost twice the value measured by nanoindentation [222, 223]. The reason of such disagreement is not clear. It must be taken into account that the employed force field reproduces accurately the cell parameters of a broad family of aluminium-iron oxides with different stoichiometries [250]. Alternative

locations of Al and Fe ions within the tetrahedral and octahedral positions were checked, and gave a similar Young modulus. Furthermore, the same potentials were used to calculate the C_3A properties, with results close to the experimental ones. Neither the bulk and shear modulus nor the elastic tensor coefficients of the clinker phases have been yet experimentally determined, and therefore, a comparison between the results cannot be done.

5.3. Crystalline calcium silicate hydrates

The knowledge about the atomic structure of the C-S-H gel is based on models close to the crystalline phases tobermorite and jennite [5, 9, 62]. These natural minerals belong to a wide family known as crystalline hydrated calcium silicates. A recent paper reviews the crystals of this family, and includes other phases related to cement [62]. Although tobermorite and jennite are the compounds that present more similarities with the C-S-H gel, the general trends for the properties of crystalline hydrated calcium silicates might be useful to understand those of the gel. The elastic properties of 21 compounds were calculated, including several varieties of tobermorite. The crystals without any other element different from the Ca, Si, O, and H were chosen from reference [62]. Only those with a fully resolved crystalline structure could be considered, or those with the only the hydrogen position missing. In the latter case, the hydrogen atoms were added to the oxygen atoms of water and hydroxyl groups.

The relaxed unit cell parameters are collected in ***appendix 6***, together with the error percent with the experimental crystalline structure taken as input. The calculated lattice parameters are in good agreement with the experimental ones. The errors are lower than 5%. It can be concluded that the selected force field reproduces well the unit cell and the atomic arrangement of CSH systems. It was not found any experimental data regarding the elastic properties of crystalline C-S-H phases in the literature. Only a theoretical calculation of the elastic tensor of foshagite by DFT methods was found [255]. The calculated elastic tensor coefficients, showed in ***appendix 6***, are in good agreement with those reported in ref. [255]. It can be seen that some coefficients are

different from zero due to the symmetry breaking during the relaxation procedure, though their value are negligible. The Young modulus calculated from the elastic tensor is 101.6 GPa, which is very similar to the value from DFT, E = 111.7 GPa [255].

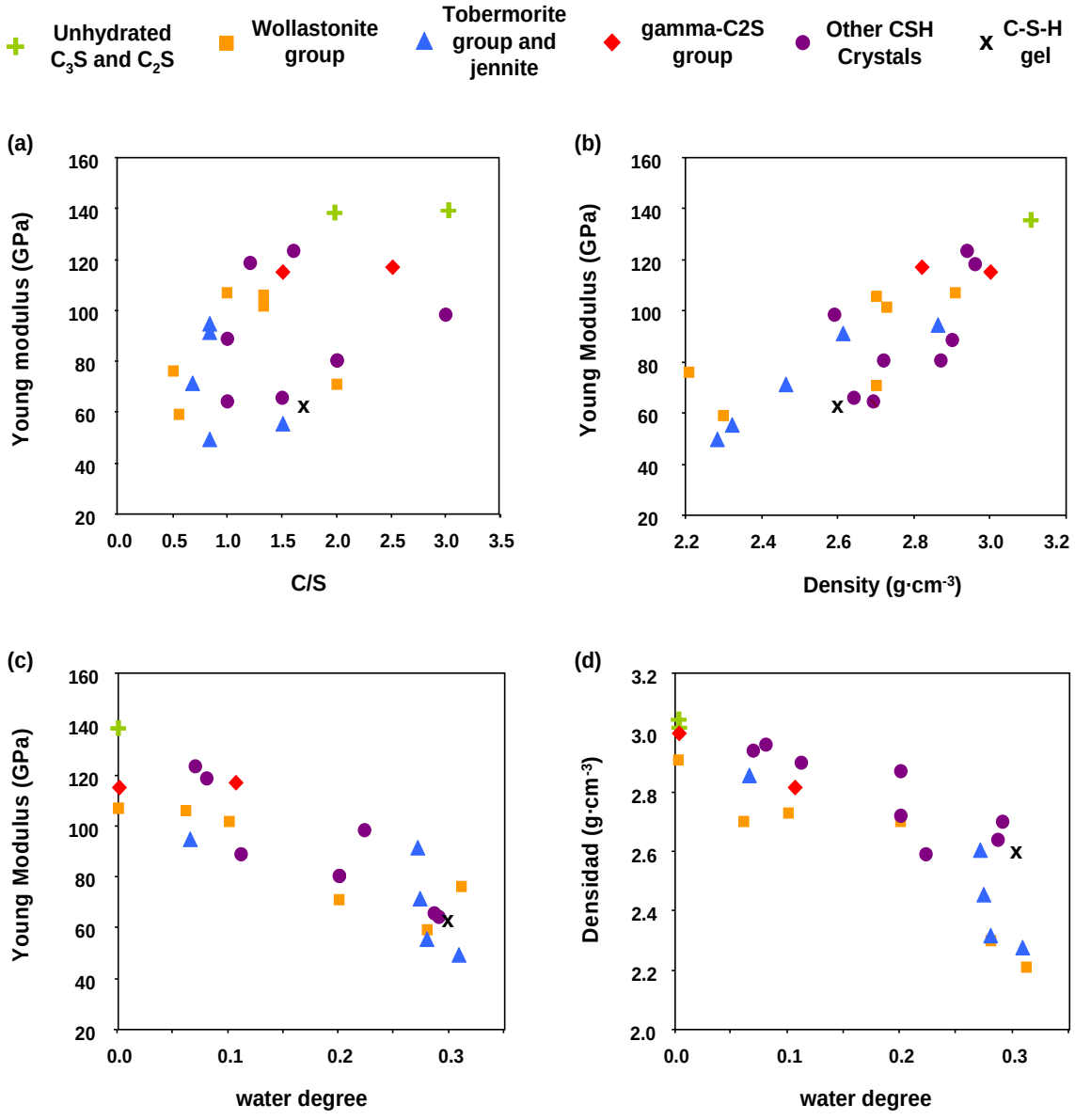

Figure 5.3.1.- Young modulus of the studied C-S-H crystals plotted against their **(a)** C/S ratio, **(b)** density, and **(c)** hydrogen content. The hydrogen content is defined as the number of H atoms per total number of atoms in the unit cell. **(d)** Density of C-S-H crystals with respect to their hydrogen content. The CSH crystals have been grouped in different families according to the classification in ref. [62]. The estimated values for the C-S-H gel are marked with a cross [88, 179].

The elastic properties derived from the elastic tensor calculations are tabulated in ***appendix 6***. The obtained Young moduli were analyzed as a function of several parameters employed to quantify the C-S-H gel structure, such as the C/S ratio, density, and hydrogen content. The results are plotted in ***figure 5.3.1(a)***, including the experimentally estimated values for a C-S-H particle. First, it cannot be seen a clear relationship between the Young modulus and the C/S ratio. For example, jennite (C/S = 1.5, E = 56.03 GPa) has the same calcium to silicon ratio than kilchoanite (C/S = 1.5, E = 115.54 GPa) while its young modulus is about one half. Even for the same subgroups, there are scattered data. In the case of tobermorite, the 14 Å variety has a Young modulus considerably lower than tobermorite 9 Å and clinotobermorite with the same C/S ratio. The silicate chain structure of the CSH crystals was checked as well. The wollastonite and tobermorite groups, as well as rosehnanhite, are formed by *Dreierketten* silicate chains, isolated or linked by the bridging site. The rest of the crystals are built of isolated silicate monomers, dimers or trimmers. No direct correlation was found between the silicate structure of different phases and its elastic properties.

The Young moduli of the crystalline phases are plotted against the experimental density in ***figure 5.3.1(b)***. In our calculations there is a general expansion of the unit cell, with the consequent decrease in the density. Thus, instead the computed values, the experimental density has been plotted for a better comparison with the existing experimental data for the C-S-H gel. The density of the CSH crystals are those reported in the corresponding reference of ***appendix 5.2***, and ranges from 2.21 to 3.0 $g \cdot cm^{-3}$. Although the scattering of the points is quite high, it can be seen that the Young modulus increases as the density of the crystal increases. As the bond nature in all the phases is equal, it is expected that denser structures would present higher elastic properties. At the same time, the Young modulus is also related to the hydrogen content, see ***figure 5.3.1(c)***. Here, the hydrogen content was defined as the number of hydrogen atoms per total number of atoms in the unit cell. In this way, not only the water molecules were considered, but also the hydroxyl groups. For the same hydrogen content, the Young modulus can vary about 30 GPa, though it can be seen that as the hydrogen content increases, the Young modulus decreases. Hence, the hydrogen content

Table 5.3.1.- Young modulus, density, hydrogen content, and C/S ratio of the C-S-H gel and its related structural models tobermorite 14 Å and jennite.

Phase	Young Modulus (GPa)	Density ($g \cdot cm^{-3}$)	Hydrogen content	C/S ratio
Tobermorite 14Å	49.94	2.28	0.31	0.83
Jennite	56.03	2.32	0.28	1.5
C-S-H gel [a]	63	2.60	0.30	1.7

a Values from references [58, 88, 179]

and the density might be considered the variables that control the elastic properties of the crystalline CSH. As the hydrogen content increases and/or the density of the crystal decreases, the elastic properties of the crystal decreases. In fact, both variables are related. Higher hydrogen content reduces the density. This relationship is, however, not linear, as other structural factors also affect the crystal density.

The estimated values for a C-S-H gel particle have been also plotted with crosses in ***figure 5.3.1***. It has been considered the proposed stoichiometry of $C_{1.7}SH_{1.8}$ with a density of 2.6 $g \cdot cm^{-3}$ [179]. The Young modulus calculated by reverse analysis of nanoindentation measurements is ~63 GPa [58, 88]. The results of the Young modulus against the density and hydrogen content are in the range of the crystalline CSH. The comparison of these parameters with those of tobermorite 14 Å and jennite are shown in ***table 5.3.1***. The estimated Young modulus of the gel particle is a little bit higher than the ones of the crystalline phases, tough are of the same order of magnitude. The hydrogen content is very similar too. However, there is a moderate disagreement in the density. The densities of tobermorite 14 Å and jennite are almost the lowest in the crystalline CSH family. The experimental C-S-H gel density is about 0.3 $g \cdot cm^{-3}$ higher. This difference explains why the estimated Young modulus of the C-S-H gel particle is higher than those of the crystals.

5.4. The C-S-H gel

In the previous section, the elastic properties of many crystalline CSH structures were studied as a function of several quantities: the C/S ratio, hydrogen content, and density. However, the gel is usually depicted as an amorphous version of tobermorite 14 Å and jennite crystals [5, 9, 62]. Therefore, the C/S ratio, density, and hydrogen content of the C-S-H gel were analysed taking those crystals as structural models. It is accepted that the C-S-H gel presents a finite chain length following the $3n - 1$ rule, as well as a higher C/S ratio than the related crystals because of the absence of the bridging tetrahedra of the silicate chains [4, 5, 9]. Thus, it was built a bulk material of tobermorite-like species (*T*), and jennite-like species (*J*), formed by dimeric (*T2, J2*), pentameric (*T5, J5*), and octameric (*T8, J8*) chains, as given in ***figure 5.4.1***. The omission of bridging tetrahedra in jennite does not change the total charge of the unit cell, since one silicon atoms (+4 e^-) and two oxygen (–2 e^-) are removed. In the case of tobermorite, the procedure implied to remove one silicon atom (+4 e^-), one oxygen (–2 e^-) and one hydroxyl group (–1 e^-), and therefore the system is negatively charged. To return the unit cell to its neutral state, two possibilities were considered. In the first case, the extra charge was compensated by saturating half of the terminal oxygen atoms in the silicate chains with H, so that they form terminal OH groups (species denoted by T_{OH}). In the second case, the necessary number of calcium atoms has been introduced in the interlayer space to counterbalance the charge (T_{Ca}).

The relaxation of these new tobermorite-like and jennite-like structures with finite chains leads to small changes in their structure. For tobermorite-like species, the main change is the movement of interlayer Ca ions towards the vacancy left after removing the bridging silicon tetrahedron. For jennite-like structures, the absence of bridging tetrahedra implies a slight atomic rearrangement in the Ca-O layer. The new terminal oxygen atoms, previously bonded to the silicon bridging atom, now enter in coordination with the Ca-O layer, and change the orientation of the silicate chains. This possibility of charge compensation makes that the Ca interlayer atoms remain in their positions. The omission of the bridging tetrahedra causes an important decrease on the density of tobermorite and jennite, as can be seen in ***figure 5.4.2***. Not only the

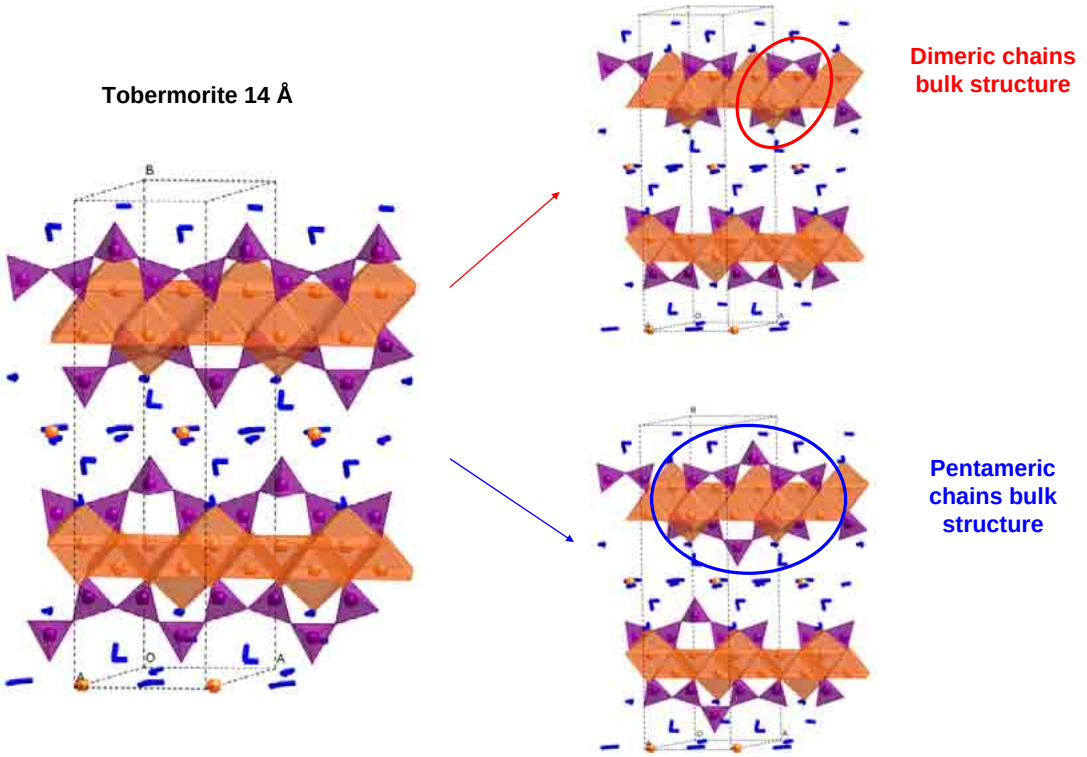

Figure 5.4.1.- Scheme of the method followed to construct the bulk tobermorite-like and jennite-like species. The appropriate number of bridging silicon atoms were removed to build finite silicate chains of length 2, 5 and 8 tetrahedra. Then, the necessary H^{+} or Ca^{+2} ions were included to impose the electroneutrality to the unit cell. In this figure, tobermorite-like dimeric and pentameric species are shown.

molecular weight of the crystal decreased due to the missing atoms, but the lattice parameters of the structure increases. Specifically, the distance between consecutive layers, along the c lattice dimension, is the one that increases more, ~1.5 Å. It can be explained by the cohesion decrease between layers due to the absence of the bridging sites. The cohesive forces between layers are mainly due to interlayer SiO-Ca-OSi ionic bonds [115, 117, 119]. When the bridging silicate tetrahedron is removed, the distance between the terminal oxygen groups of dimers is too high to establish a strong bond, and therefore the hydrogen bongs due to the presence of water are the responsible for the cohesion. These forces are weaker, and therefore the distance between consecutive layers increases. This expansion enhances the disagreement between the measured density of the C-S-H gel and the calculated results.

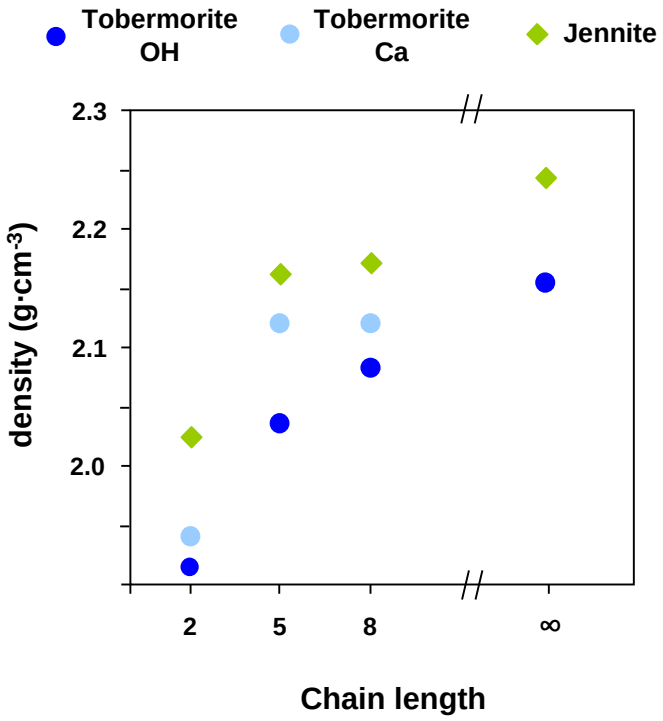

Figure 5.4.2.- Density of the tobermorite and jennite-like structures versus their silicate chain length. The light blue points are for the tobermorite-like species counterbalanced with Ca^{+2} ions, the dark blue points are for the tobermorite-like species counterbalanced with H^{+}, and the green rhombus are for the jennite-like species.

The elastic properties of the tobermorite-like and jennite-like structures with finite chain lengths are given in ***table 5.4.1***. The elastic properties of both structures increase as the chain length increases. This result was expected for two reasons: first, due to the mentioned decrease of the cohesive forces between layers, and second, due to the stability given by the longer silicate chains to the Ca-O layers. The relationship between the mechanical properties and the chain length is not linear. The main improvement in the elastic properties is due to the incorporation of the first bridging tetrahedron, which merges two dimer structures into a pentamer. The elastic properties have the largest change between dimers and pentamers, whereas the rise from pentamers to octamers is smaller. This result is in agreement with the suggested role of the bridging site in the cohesion, as well as with the density increase, also non-linear. For tobermorite-like species, the structures with pentamer chains have almost the same properties as their infinite crystals. For jennite-like structures, the improvement is less pronounced, and the

Table 5.4.1.- C/S ratio, density, and elastic properties of the constructed tobermorite-like and jennite-like structure with finite silicate chains. *T* and *J* denote tobermorite and jennite respectively, and the number with them the silicate chain length. The infinite symbol accounts for the infinite chains in non-defective crystals. The subscript in tobermorite-like species refers to the charge balance method. Further details are given in the text. The bulk (*K*), shear (*G*), and Young modulus (*E*) are given in GPa. The Poisson's ratio (ν) is dimensionless. The density is given in $g \cdot cm^{-3}$

Structure	C/S	Density	*K*	*G*	*E*	*v*
$T_{OH}2$	1.25	1.91	26.0	14.0	35.6	0.27
$T_{Ca}2$	1.50	1.94	25.0	15.7	38.9	0.24
$T_{OH}5$	1.00	2.04	33.7	18.5	46.9	0.27
$T_{Ca}5$	1.10	2.12	33.0	18.0	45.7	0.27
$T_{OH}8$	0.94	2.08	36.8	19.1	48.9	0.28
$T_{Ca}8$	1.00	2.12	47.8	18.5	49.2	0.33
$T\infty$	0.80	2.15	44.8	19.0	49.9	0.31
J2	2.25	2.03	23.9	13.8	34.7	0.26
J5	1.80	2.16	31.8	18.4	46.3	0.26
J8	1.69	2.17	37.8	21.0	53.2	0.27
$J\infty$	1.50	2.24	40.2	22.1	56.0	0.27

elastic properties of octamers should be considered to reach values similar to those of the crystal. This finding could be attributed to the more active role played by the bridging tetrahedra in the stabilization of Ca-O layers for jennite than for tobermorite.

The differences in the elastic properties between tobermorite-like structures balanced by OH (T_{OH}) were also examined. The added calcium ions replace the removed silicon tetrahedra and hold together the silicate chains. Nevertheless, there is no significant improvement in the mechanical properties, which change from E = 35.6 GPa to E = 38.9 GPa in the case of dimers. This effect is even less important in the case of longer chains. Finally, it can be observed that the C/S ratio increases from 0.83 in tobermorite and 1.5 in jennite to values in the range between 0.94 and 2.25 respectively. This rise

supports previous models where the higher C/S ratio of the C-S-H gel with respect to tobermorite and jennite crystals is due to the omission of the bridging tetrahedra and the incorporation of extra Ca ions to balance the charge [4-6, 9, 52].

Nanoindentation technique has not enough resolution to measure the elastic properties of a single C-S-H gel particle. The indentation modulus of the solid phase together with the associated porosity is measured. The Young modulus of a single C-S-H gel particle was obtained by Constantinides et al. performing an inverse analysis homogenization procedure of the nanoindentation measurements [58, 88]. In short, the homogenization procedures are mathematical methods to average the properties of composite materials, usually employed in continuum micromechanics or microporomechanics [256, 257]. Many homogenization procedures have been developed to account for different type,

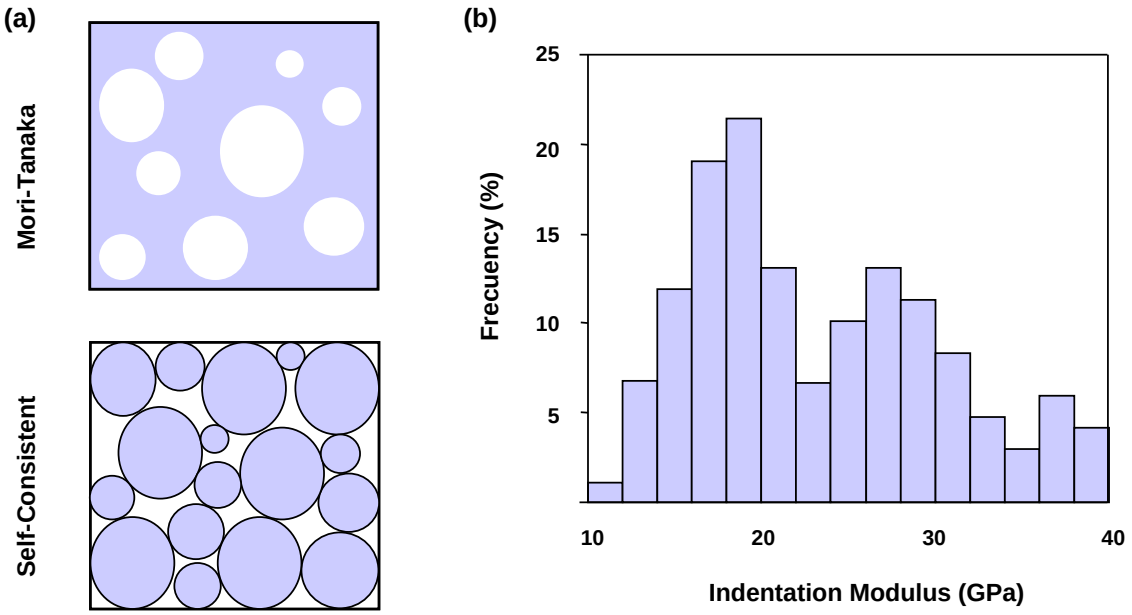

Figure 5.4.3.- (a) Schemes of the homogenization models employed to scale the values of the tobermorite and jennite-like species. Although the Self-consistent model has been proposed as the most suitable one, both are employed in this analysis. **(b)** Typical profile of nanoindentation measurements for the C-S-H matrix. The frequency of a given indentation modulus is plotted versus its value. The bimodal distribution with maxima at ~19 and ~29 GPa can be seen (results courtesy of Dr. J. J. Gaitero from the Centre for Nanomaterials Applications in Construction (**NANOC**) at Labein-Tecnalia

shape, and size of inclusion in the material matrix [258]. Among them, the self-consistent or polycrystalline model was developed to describe the average elastic properties of spherical particles intermixed with some porosity [259]. On the other hand, the Mori-Tanaka schemes models the elasticity of a solid matrix with pore inclusions [260]. A schematic representation of the systems characterized by both models is presented in ***figure 5.4.3 (a)***. Here, the homogenization schemes have been used to rescale the properties of the bulk tobermorite-like and jennite-like particles with finite chain length to those of the C-S-H gel. The self-consistent model has been stated as more suitable to account for the C-S-H gel morphology [88]. Nevertheless, both models were applied to compare the results. The indentation moduli after the homogenization procedure are showed in ***figure 5.4.4***. against the silicate chain length. Two porosities were used in each model, 26% and 36%, suggested as the mean value of the porosity for the HD and LD varieties of C-S-H gel [58, 84, 85, 88, 90]. They are indicated as open circles and solid circles respectively in ***figure 5.4.4***. The indentation modulus ranges of the low stiffness (LS) and high stiffness (HS) features are represented as shadowed regions. Finally, the structure to which corresponds each point is included near them. Instead of the Young modulus, the indentation modulus was calculated and rescaled for a better comparison with the experimental data.

First, it is remarkable that both models capture the range measured for LD- and HD-C-S-H gels. Taking into account both densities and all the chain lengths, the whole range is covered. For both micromechanical models, the stiffness depends clearly on the packing factor and the silicate chain length. As expected, the indentation modulus increases with the packing factor and with the silicate chain length. The dependence of the indentation modulus with the chain length is more accused in the Mori-Tanaka model, while in the self-consistent the difference in the indentation modulus depends more on the porosities. If the self-consistent scheme is assumed to describe better the C-S-H gel nature [88], several conclusion can be drawn. The low density values do not reach the high stiffness region independently of the chain length. The density is the main factor that distinguishes the high-modulus and low-modulus C-S-H gels. Thus, the results agree with the proposed model [58, 87, 88]. Furthermore, the dimers do not reach the high stiffness values. In view of these results, the HD-C-S-H gel could not be

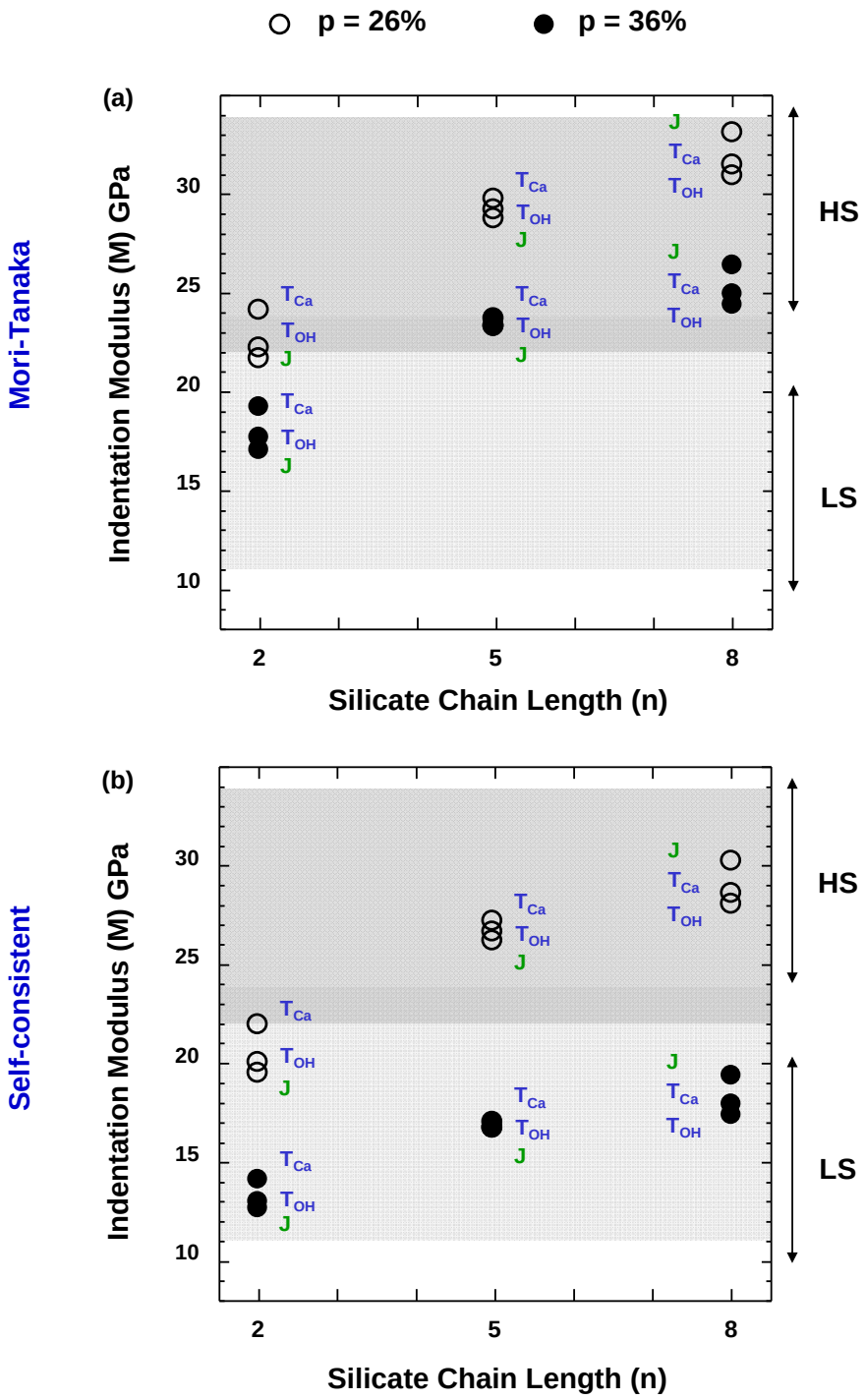

Figure 5.4.4.- Indentation modulus of tobermorite-like and jennite-like structures versus the length of the silicate chains employing **(a)** the Mori-Tanaka and **(b)** the self-consistent homogenization schemes. The solid circles represent the indentation modulus calculated with high porosity value and the empty circles those with low porosity values. They correspond to LD and HD C-S-H gels respectively. A letter near the circles denotes if it is tobermorite balanced by H or Ca (T_{OH} and T_{Ca}) or jennite (J). The shadow regions correspond to the indentation modulus distributions attributed to the LD and HD C-S-H gels.

formed by short chains, and only long chains with low porosities might form the HS gel. In the Mori-Tanaka model, the dimeric chains are in the limit between the high stiffness and low stiffness areas. Longer chains lie in the high stiffness zone, independently from the porosity. Thus, the results indicate that the chain length is determinant in this case, controlling the change between high stiffness and low stiffness C-S-H particles. However, the self-consistent scheme has been stated to fit better with the nature of the C-S-H gel [88], and therefore the results obtained by the Mori-Tanaka scheme should be taken with care. Nevertheless, both homogenization procedures agree in that short chains only reach the low stiffness values. Although the C-S-H gel porosity seems to be the most crucial parameter that controls the matrix properties, the Young modulus of the particle itself is clearly affected by the chain length, and therefore it influences the final material properties.

5.5. Other hydration products

The elastic properties of other hydration products different from the C-S-H gel, i.e., portlandite (CH), ettringite ($C_6A\bar{S}H_{32}$), monosulphoaluminate ($C_4A\bar{S}H_{12}$**)**, and hydrogarnet (C_3AH_6) [4], were calculated. The initial structures of portlandite and hydrogarnet are those of references [95] and [261]. In the case of ettringite, the structure of Hartman and Berliner was employed [100]. They measured deuterated ettringite by neutron diffraction techniques to defined the position of hydrogen atoms within the cell. The proposed composition for ettringite has a partial occupancy of 25.5 water molecules within the unit cell. The calculations were made assuming a stoichiometry with 25 water molecules. As the initial structure for monosulphoaluminate, the coordinates of the natural analogue kuzenite were considered [101]. Kuzenite has 18 water molecules in the interlayer space between the Ca-O-Al sheets, and it corresponds to the most hydrated variety of monosulphoaluminate [4].

The relaxed lattice parameters are shown in ***appendix 6***, together with the experimental value and the percent error between them. The cell parameters of portlandite and hydrogarnet are in good agreement with the experimental data.

Table 5.5.1.- Elastic properties of the main hydrated phases. The bulk (*K*), shear (*G*), and Young (*E*) moduli are given in GPa. The Poisson's ratio (*v*) is dimensionless. The experimental data are given when available for comparison.

	K		*G*		*E*		*v*	
	Exp	Comp	Exp	Comp	Exp	Comp	Exp	Comp
Portlandite [a]	40.0	31.1	16.3	13.3	41.5	35.0	0.31	0.32
Ettringite [b]	27.3	28.4	9.5	6.7	25.0	18.6	0.34	0.39
Hydrogarnet	--	41.2	--	21.7	--	55.5	--	0.35
Monosulpho-aluminate	--	22.8	--	11.5	--	29.1	--	0.27

a ref. [262]; **b** ref. [236]

However, in the case of ettringite and hydrogarnet, there is a mismatch in the c lattice parameter higher than 10%. Such disagreement can be explained by the charged species that appear in the unit cell. Both crystals have positively charged features, columns in ettringite and layers in monosulphoaluminate, with its charge partially delocalized in the water network and balanced by SO_4^{-2} groups [99]. In the force field approach, the atom charge is fixed in the beginning of the simulation and it is not modified to account for the charge transference. Thus, the cell parameters are contracted or expanded due to the columbic interactions. In the case of monosulphoaluminate, the c lattice parameter decreases in order to move the positive layers close to the negative sulphate ions. In ettringite, the dense water mesh hinders the approximation of the SO_4^{-2} groups to the columns, and the c parameter increases due to the repulsion within the column. In general, the disagreement in the lattice parameters is higher for the hydrated species than for the unhydrated crystals, due to the difficulties to describe the weak water dispersive forces [263, 264].

The elastic properties of the hydration products are listed in ***table 5.5.1***. The Young modulus (E = 35.0 GPa) and Poisson ratio (v = 0.31) of portlandite are in good agreement with the experimental results [224, 232, 233], although the bulk and shear

moduli underestimate slightly the experimental values. The results are very similar to those obtained by *ab-initio* methods in ref. [234]. Furthermore, the calculations accurately reproduced the anisotropy of the Young modulus in the crystallographic direction. Laugesen obtained values of 99.39 GPa in the layer planes (x and y crystallographic directions) and 36.29 GPa in the direction perpendicular to the layers (z crystallographic axis). The calculated Young moduli in the same directions were 93.64 and 32.78 GPa respectively.

The experimental and computed elastic tensors coefficients of ettringite are showed in ***appendix 5.2***. The calculated values are similar to the experimental ones [236]. There is an overall agreement for the coefficients which correspond to linear deformations (C_{ij} with i and j = 1, 2 3), while those involving angular strains (i and j = 4, 5, 6) have a considerable mismatch, probably due to the symmetry break during the relaxation. The resulting values of the bulk, shear, and Young moduli are somewhat lower but close to the experimental results [262].

There is not available experimental data to compare the obtained results for hydrogarnet and monosulphoaluminate. Heacker et al. suggested that the elastic properties of the cement paste components that had not been calculated could be assumed to be equal to those of a similar compound [106] . Following such suggestion, the obtained Young modulus for monosulphoaluminate is between those of ettringite and portlandite, the phases to which is structurally related. The result for hydrogarnet is higher than the rest of the hydrated compounds. Such high value is related to its high density, 2.53 $g \cdot cm^{-3}$ [261] with respect to the other hydration products: 2.24, 1.90 and 1.78 $g \cdot cm^{-3}$ for portlandite [95], monosulphoaluminate [101], and ettringite [100] respectively.

5.6. Conclusions

In this chapter the elastic properties of the main cement paste components and other related species have been calculated by atomistic simulation methods in the molecular

mechanics approach. Specifically, The elastic properties of the main clinker phases (C_3S, C_2S, C_3A and C_4AF) and hydration products (CH, $C_6A\bar{S}H_{32}$, $C_4A\bar{S}H_{12}$ and C_3AH_6) are given. The elastic properties of 21 compounds in the crystalline hydrated calcium silicate family have been also calculated, and discussed such as a function of several parameters such as the density or the hydrogen content. Finally, a homogenization procedure has been employed to rescale the Young modulus of tobermorite and jennite crystals with finite silicate chains to those of the amorphous C-S-H gel.

There is an excellent agreement between the experimental and computed lattice parameters for the clinker phases. The Young moduli are in the range of the experimental measurements, with the exception of C_4AF. It can be concluded that the employed force field for the Ca-Al-Si-O set describes well the interactions of the materials. More experimental and theoretical investigations are needed to elucidate the mismatch between the elastic properties of C_4AF.

The cell parameters of the 21 calculated compounds are in good agreement with the experimental data, with errors smaller than the 5%. There is a lack of experimental data about the elastic properties of these crystals. Nevertheless, the calculated elastic properties are in excellent agreement with the computed values for foshagite by *ab-initio* calculations. The Young modulus of the CSH crystals does not correlate with the C/S ratio or the silicate structure (infinite chains, monomers or dimers). From our results, the density and the hydrogen content are the parameters that control the elastic modulus of the CSH family. These quantities are in their turn related. As the hydrogen content increases and the density decreases, the Young modulus of the CSH crystals decreases. The experimental values estimated for a single C-S-H gel particle lie in the calculated range of the CSH crystalline family. However, its Young modulus is slightly higher than those of tobermorite 14 Å and jennite, usually employed as structural models of the C-S-H gel. The disagreement could arise from the difference in the measured density of the C-S-H gel and those of tobermorite and jennite, about 0.3 $g \cdot cm^{-3}$ lower.

From the most accepted models, the finite chain length of the C-S-H gel is the main difference between it and the crystalline tobermorite 14 Å and jennite. Thus, tobermorite-like and jennite-like bulk crystals with finite chains of 2, 5 and 8 tetrahedra were constructed by omission of the bridging silicon tetrahedral following the proposed models. In this way the C/S ratio of the crystals increases up to the range of the C-S-H gel. After relaxing of the initial structures, it was seen that the density of the systems decreased, due to an increment in the separation of the layers. The removal of the bridging tetrahedra implies a decrease in the cohesive forces between layers. As the number of bridging tetrahedral increases (longer chains) the density is more similar to that of the perfect crystal. Therefore, the omission of bridging sites in tobermorite and jennite implies a larger disagreement between their density and the one measured for the C-S-H gel.

The elastic properties of tobermorite-like and jennite-like species were homogenised by the Mori-Tanaka and self-consistent schemes, with the density values proposed for the Low Density and High Density gel varieties. The Young modulus of the structures after the homogenization procedure cover the range obtained experimentally for the indentation modulus. The porosity is the most important factor that differentiates the LS and HS C-S-H gel, in agreement with the experimental data. However, the chain length plays also an important role in the elastic properties. As the silicate chain length increases, the indentation modulus increases, due to higher cohesion between consecutive layers and the stabilization of CaO layers by longer silicate chains. The results from the self-consistent scheme, stated as the most correct one to describe the nanogranular nature of the cement paste, indicate that the HS-C-S-H gel would be only formed by particles with long chains (5 and 8 silicate tetrahedra) packed with low porosity.

For the hydration products, the results of portlandite are in good agreement with the experimental data, and are comparable to those of *ab-initio* results. The employed force field does not describe accurately ettringite and monosulphoaluminate crystals due to the presence of charged species within the unit cell. Some disagreements have been found both in the lattice parameters and elastic properties. Nevertheless, the Young

modulus is in the range of the values for other hydration products such as portlandite and the C-S-H gel. Hence, the use of their elastic parameters as input for other hydrated phases in micromechanical models is justified. The development of a suitable force field for the involved elements (S, Na, Fe) would be necessary to advance in the description of cement paste components.

Chapter 6:

Structure, Elastic Properties, and Reactivity of Tricalcium Aluminate

6.1. Introduction and computational method

Tricalcium Aluminate, C_3A in cement chemistry notation, is typically the third component in amount of the ordinary Portland cement (OPC). The pure C_3A has a stoichiometric formula $Ca_3Al_2O_6$. Its unit cell is cubic with a lattice constant a = 15.263 Å, and the space group is Pa3. It contains 264 atoms (72 Ca, 48 Al, and 144 O) and consists of six-member rings of aluminium-oxide tetrahedral ($Al_6O_{18}^{-18}$), with calcium ions located in the holes between rings counterbalancing the charge, see ***figure 6.1.1.*** There are 80 possible positions for Ca^{+2} ions, and therefore, 8 vacancies appear in the unit cell. It must be noted that these vacancies are not crystalline defects, but intrinsic features of the structure [24-26]. In OPC it does not usually appear in its pure form but in its chemically modified version with substitution of Al and Ca by cations such as Na^+, Si^{+4}, Fe^{+3}, Mg^{+2}, or K^+. The most important substitution is that of $2 \cdot Na^+$ for Ca^{+2}. It induces a symmetry breaking, and consequently the apparition of orthorhombic and monoclinic polymorphs. However, for Na_2O contents lower than 2% the cubic

symmetry is kept [26, 27].

The experimental data regarding the elastic properties of tricalcium aluminate as well as the calculated by force field methods were detailed in ***chapter 5***. Velez et al. [222] and Acker [223] reported the same value for the Young modulus (E = 145 GPa) measuring by nanoindentation pure synthetic samples and unhydrated C_3A grains in Ductal cement samples respectively. Thus, the substitution of Ca^{+2} by Na^{+} ions do not apparently affect to the elastic properties. Measurements by frequency resonances of samples with different porosities gave a slightly higher value, E = 160 GPa [222]. From the force field calculations presented in ***chapter 5***, a value of E = 165.1 GPa was obtained, in good agreement with the experimental data.

The reactivity is the most important characteristic of C_3A. When mixed with water, the tricalcium aluminate reacts very fast and forms calcium hydroaluminates and hydrated alumino-ferrite phases [4, 137]. This process, called *flash setting*, is not desired since it reduces the workability, hindering a proper mixing of cement with water, and decreasing the final strength of cement pastes. To avoid the flash setting, small quantities of gypsum are usually added to the clinker as retardants [4, 137]. Gypsum acts as source of soluble sulphate ions to the solution, which induces the formation of calcium sulphoaluminates instead calcium hydroaluminates, and retards the hydration of C_3A [4, 137]. The reactions involved in these processes were commented in the hydration section of the introductory chapter. The cause for the retarded hydration, however, is not fully elucidated, and it is a reason of controversy despite the numerous studies [36-40, 265-268]. On the one hand, some authors propose that it is due to the formation of a protective layer that might limit the contact between the ionic solution and the C_3A and hinder the C_3A dissolution. Some researches proposed that the layer was formed by crystalline ettringite, [36, 38, 265] or sulphoaluminate [39], while others that the layer crystallinity depends on the pH [37]. On the other hand, other groups pointed out a ‘‘blockage’’ mechanism. The sulphate ions are adsorbed in the tricalcium aluminate surface, and therefore block its reactive sites. This processes results in a decrease of the C_3A dissolution ratio [40, 266-268].

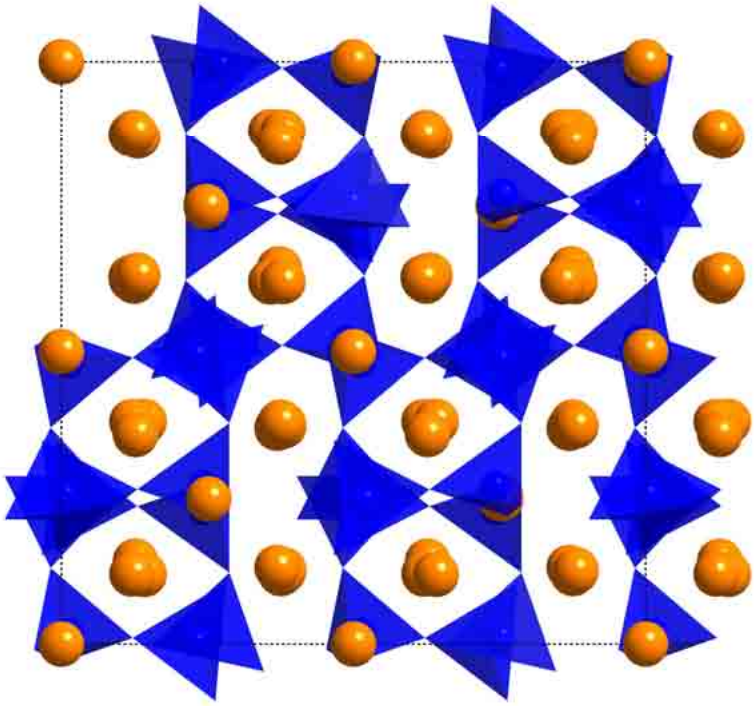

Figure 6.1.1.- Crystalline structure of tricalcium aluminate (C_3A). The calcium atoms are given as orange spheres, while the AlO_4 groups as blue tetrahedra. The aluminium atom is placed in the centre of the tetrahedra, with oxygen atoms occupying the vertexes.

In this chapter *ab-initio* DFT methods were used to investigate the tricalcium aluminate structure and its properties. First, the crystalline structure was studied and the C_3A full elastic tensor was calculated. Second, the bulk reactivity of C_3A was studied, calculating the reactive points under electrophilic and nucleophilic attack. The hydration and retardation mechanisms were analysed in view of these results.

- ***Computational method***

The calculations of tricalcium aluminate were performed in the Density Functional Theory (DFT) approach, using the SIESTA code [201] with the same methodology described in ***chapter 4***. The general gradient approximation (GGA) was adopted using a Perdew-Burke-Ernzerhof (PBE) functional [202]. A double-ξ polarized basis set (DZP) and atomic pseudopotentials (parameterized following the Troullier-Martins method

[203]) were employed to describe the valence and core electrons respectively. The reference configuration for the parameterization and the basis set parameters are given in ***appendix 1***. After convergence tests of the total energy against the number of k points in the Briouillin zone, it was found that a good accuracy was already obtained with the Γ point and a mesh cut-off of 150 Ry.

Additionally to the previous *ab-initio* calculations of C_3A, the OH^- and SO_4^{-2} ions were also studied to analyse the differences that might cause the retardation process. Calculations within the DFT methods were performed for that purpose with the Gaussian code [171]. The Becke 3-parameter, Lee, Yang, and Parr (B3LYP) hybrid scheme was used [174], together with a 6-31G basis set plus an extra polarization d function [175, 176]. The atomic positions were optimized employing the Berny algorithm implemented in the Gaussian code [269]. For the optimized structure, the Mulliken population analysis was performed [167].

6.2. Crystalline structure and Elastic Properties

The initial structure employed for the calculations is the one resolved by Mondal and Jeffery [24] using X-Ray diffraction methods of a pure synthetic C_3A. After relaxing the unit cell the obtained lattice constant are a = b = c = 15.38 Å and α = β = γ = 90º, so the cubic symmetry is kept after relaxations. There is a good agreement between our computed values and the experimental results. The cell sides are overestimated by less than 0.8%, which implies a slight expansion of the unit cell that increases the volume by 2.36%.

The main features of the tricalcium aluminate unit cell are the $Al_6O_{18}^{-18}$ rings. There are eight of such $Al_6O_{18}^{-18}$ rings in each of the subcells with a´ = a/2. The structure found by the calculations for these rings is shown in ***figure 6.2.1***. The labels of the atomic sites follow the nomenclature employed by Mondal and Jeffery [24]. Two aluminium sites can be distinguished within the rings, Al1 and Al2, alternated up and

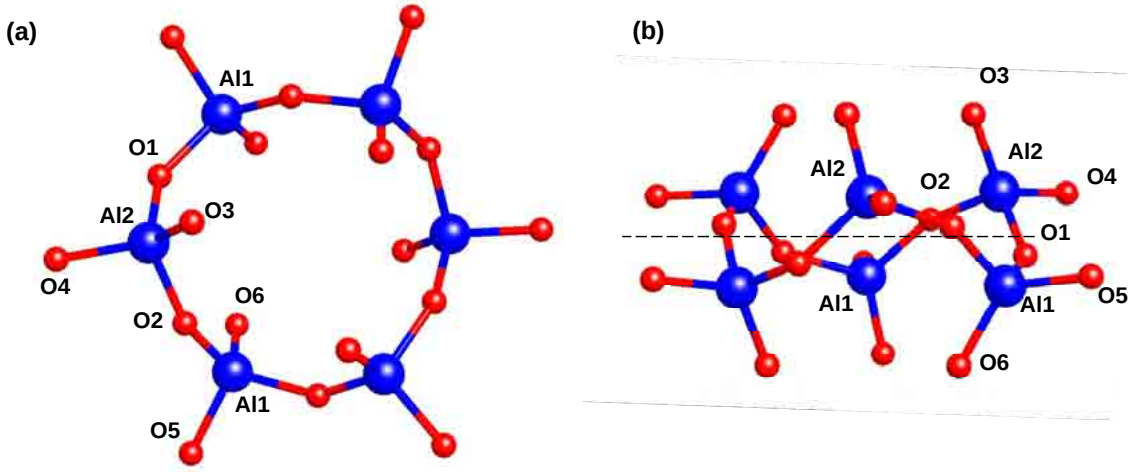

Figure 6.2.1.- Structure of an $Al_6O_{18}^{-18}$ ring in **(a)** a perpendicular view and **(b)** parallel view across the imaginary ring plane. The aluminium (Al1 and Al2) and the six oxygen positions are given in both views. The sites numbers are those of reference [24].

down from an imaginary central plane. For the oxygen atoms six sites can be differentiated (O1, O2, O3,O4, O5, and O6) depending on their position with respect to Al1 and Al2. The values for the Al-O distances and O-Al-O angles between the ring atoms together with the experimental values are given in ***appendix 7***. The calculations show an excellent agreement with the experimental data. The bond distances overestimate slightly and systematically the experimental values, though the discrepancy is always lower than 2%. The calculated mean Al-O length is 1.776 Å, that is, only 0.025 Å larger than the experimental value 1.751 Å [24]. In its turn, the calculated bond angles present small differences with respect to the experimental values which are always below 2º. In this case, the discrepancy of the mean Al-O-Al angle between experiments and theory is only 0.03º. A mean value 109.46º was obtained in comparison with the experimental value of 109.43º [24]. The ring structure is also well described. The results show that the six AlO_4 tetrahedra are alternated 0.4 Å up and down from the imaginary plane of the ring, in agreement with experiments [24]. However, in the calculation the bridging oxygen atoms (O1 and O2) were shifted 0.2 Å up and down from the plane, while the experimental data found them almost coplanar [24]. The radius of the ring was experimentally estimated 1.47 Å assuming an ionic

radius for the oxygen atom of 1.4 Å [24]. With the same ionic radius, and measuring the distance between a bridging oxygen and its opposite in the ring, the measured radius after the relaxation is 1.52 Å, only 0.05 Å higher. It is remarkable that the distances are equal for the three pairs of opposite bridging oxygen atoms, so the ring structure is very regular.

The arrangement and coordination of the calcium ions were also analysed. There are six different types of calcium ions depending on their position within the unit cell, as shown in ***figure 6.2.2***. Ca1 and Ca2 are in high symmetry positions: (i) in the cell vertex, (ii) in the centre of the cell, sides and faces, and (iii) in the 1/4, 1/4, 1/4 and related symmetry positions. They present a perfect octahedral coordination to 6 oxygen atoms. Ca3, 4, 5 and 6 are located in 1/8, 1/8, 1/8 positions and their symmetry equivalents. Ca3 and Ca4 also present an octahedral coordination but irregular in this case, while Ca5 and Ca6 are irregularly coordinated to 8 and 7 oxygen atoms

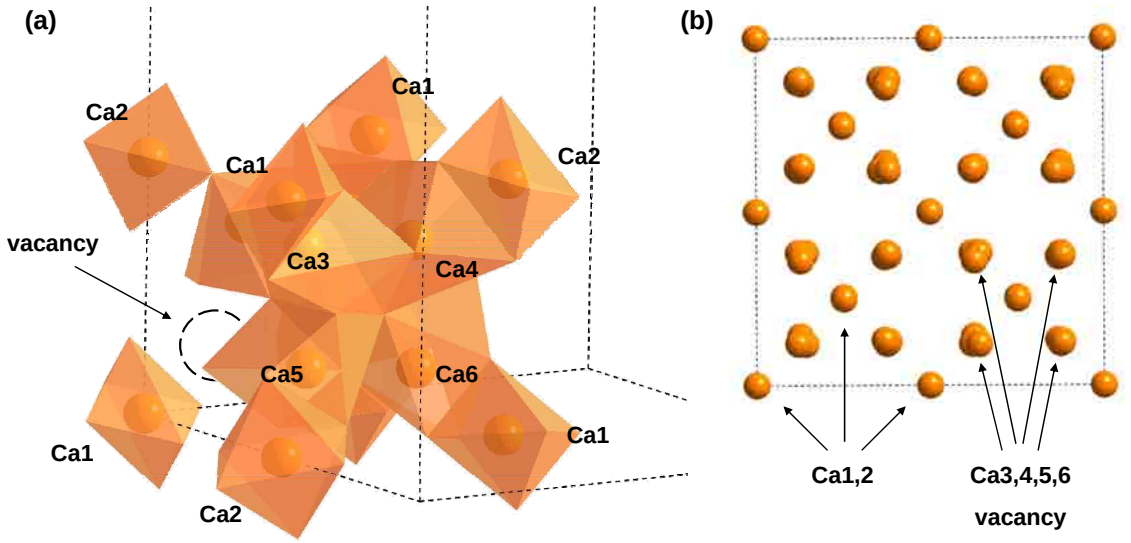

Figure 6.2.2.- Arrangement of the calcium atoms within C_3A unit cell. (a) Representation in perspective of the coordination polyhedra of the calcium atoms in a subcell of a´ = a/4. One of the eight vacancies is also marked. Note that each subcell presents one vacancy. The atomic site numbers follow reference [24]. (b) Projection of the calcium atoms in the unit cell.

respectively. The structural parameters from the calculations and the experimental results [24] are given in ***appendix 7.*** The calculated bond distances overestimate the experimental values bond by 0.15 Å, with the exception of the Ca4-O5 and Ca6-O6 distances which increase up to 0.3 Å. The average value obtained for the Ca-O distance is 2.58 Å, only 0.02 Å higher than the experimental one [24]. The largest mismatch for the O-Ca-O angles between the computed results and the experiment is small, approximately 8º. The average value for the O-Ca-O angles is also in excellent agreement with the experimental value. The experimental average value is 100.09º [24], while the computed one is 99.73º. Hence, it is clear that the calculations reproduce the coordination polyhedron structure of Ca atoms within the unit cell. In principle, the worst description of the structural parameters involving calcium, both bonds lengths and angles, can be ascribed to the weaker ionic character in the Ca-O bond in comparison with the stronger iono-covalent Al-O bond of the rings.

Once the structure was relaxed, the elastic properties of tricalcium aluminate were calculated. The procedure to calculate the elastic tensor is explained in ***appendix 5***. Due to the cubic symmetry of the unit cell, only two components of the strain tensor are needed, *ε1* and *ε4*. Six different degrees for each strain case were applied, in steps of 1%, ranging from – 3% (contraction) to + 3% (expansion). The atomic positions were relaxed for each deformation. Finally, the elastic coefficients have been obtained from linear fits to the computed data. To validate the pseudopotentials and assure their transferability a well-known calcium oxide as lime (CaO) and an aluminium oxide as corundum (Al_2O_3) were studied. For CaO, the volume of the relaxed unit cell V = 112.1 $Å^3$ and the bulk modulus *K* = 110.8 GPa, differ from the experimental data (V = 111.6 $Å^3$ and *K* = 112.0 GPa) by 0.5% and 1.1%, respectively [262, 270]. In the case of corundum, the differences are slightly larger: the obtained results in this work are V = 262.1 $Å^3$ and *K* = 226.6 GPa, while the experimental data are V = 255.0 $Å^3$ and *K* = 251.7 GPa [271, 272]. The differences, 2.7% in the unit cell volume and lower than 10% in the bulk modulus, indicate a good agreement between our calculations and the experimental measurements, and ensure the transferability of the pseudopotential and basis set.

Table 6.2.1.- Elastic tensor coefficients of tricalcium aluminate. Due to the cubic cell symmetry, there are only three irreducible constants [273]. The bulk, shear, and anisotropic Young's moduli, together with the Poisson's ratio derived from the elastic matrix are given. The Young modulus along each crystallographic direction calculated from the compliance matrix is also shown (see ***appendix 5***). Values are given in GPa, with the exception of the Poisson ratio, which is dimensionless.

	This work	Experimental
C_{11}	172.1	--
C_{12}	68.3	--
C_{44}	56.1	--
K	102.9	--
G	54.4	--
E_{ani}	138.7	145 ± 10 ; 160± 10
$E_{x,y,z}$	133.3	[222, 223]
v	0.28	--

The Young modulus (E) is the only elastic property which has been experimentally measured. Two different values have been obtained for the Young modulus depending on the experimental technique. Ultrasound measurements obtained a value of E = 160 ± 10 GPa [222], whereas nanoindentation measurements obtained a value E = 145 ± 10 GPa [222, 223]. The calculated Young modulus is in excellent agreement with the values obtained from nanoindentation, as seen in ***table 6.2.1***. The results underestimate the experimental values by less than the 10%. The average Poisson's ratio (v) is 0.28. This value is in close agreement with the experimentally assumed value of 0.30, and it justifies its choice in order to interpret the nanoindentation experiments [222, 223, 254].

6.3. Electronic structure and reactivity

Before studying C_3A reactivity, a brief analysis of its band structure and Mulliken populations was done. As expected, tricalcium aluminate presents a wide band gap

(3.93 eV) and is therefore an insulator. The average Mulliken charges values (in units of e^-) are 1.653 for Al, –0.913 for O and 0.649 for Ca. The variations for a given specie in different positions are very small, less than 0.075 e^-. However the different environments can be distinguished due to the positions: two different Al environments, six O, and six Ca. The Mulliken population analysis is dependent on the basis set employed to describe the atom. Therefore the iono-covalent bond character cannot be univocally stated from this analysis. However, as their dependence with the atomic site is very small, it can be concluded that the nature of the bonds is similar through the unit cell.

Any chemical reaction or process in a system depends on its electronic density, and involves a change in it, which can be quantified in terms of appropriate reaction descriptors [146, 172]. Thus, the reactivity of a system can be studied by means of its electronic density. The *Top Valence Band* (TVB) and *Bottom Conduction Band* (BCB) are respectively the energy bands from which the electrons can be "easily" removed, and in which electrons can be "easily" accepted. "Easily" means that the energy necessary to remove or accept an electron is the smallest one. These bands are equivalent to the *Highest Occupied Molecular Orbital* (HOMO) and *Lowest Unoccupied Molecular Orbital* (LUMO) orbitals in molecules. If the TVB and BCB are represented in the space, the areas where the system will easily accept or lose electrons are obtained, i.e. the reactive points of the system [146, 172]. The reactive areas which correspond to the TVB, those with tendency to lose electrons, will be reactive under nucleophilic attack. The reactive areas which correspond to the BCV, those with tendency of accept electrons, will be reactive under electrophilic attack.

The spatial location of the top valence band (TVB) is shown as a green isosurface in ***figure 6.3.1***. The TVB gives the areas of the crystal reactive under electrophile attack. In the cement solution the main electrophile species are water and Ca^{+2} ions. The reactive points correspond to the oxygen atoms through the whole unit cell. If one ring is showed in detail, it can be seen that the oxygen atoms have a similar contribution to the reactivity under electrophile attack. High reactivity for the terminal oxygen atoms of the ring (O1, O2, O3, O4) was expected, as they are linked just to one Al and therefore

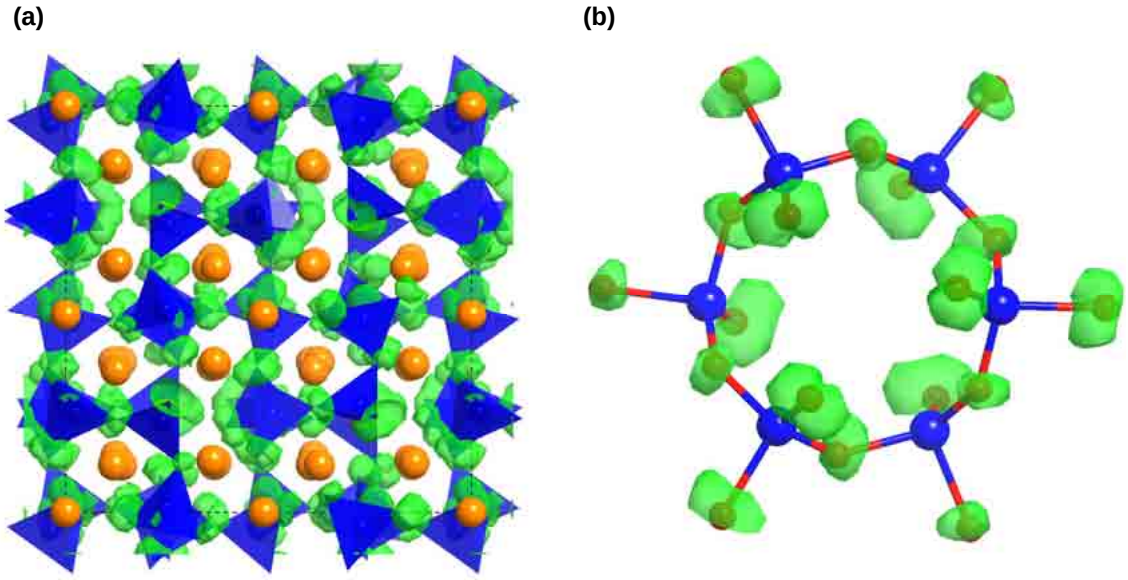

Figure 6.3.1.- Spatial location of the top valence band (TVB) in tricalcium aluminate. The green isosurfaces show the areas where the TVB is larger. The cut off value for the isosurfaces is at 10% of the maximum value. **(a)** General view of the unit cell. **(b)** Detailed view of an $Al_6O_{18}^{-6}$ ring.

should have charge, balanced by the Ca atoms. However, the bridging O1 and O2 which link together two aluminium atoms also contribute equally to the reactivity. From the Mulliken population analysis the charge on oxygen is similar independently of the oxygen position. Thus, the charge is not only located on the terminal oxygen atoms, but shared between all of them, including the O1 and O2 bridging atoms. The Al-O-Al bond has therefore a high ionic character. The high reactivity of the C_3A can be related to this factor. If the O1 and O2 bridging atoms react, the ring will be broken, and more reactive sites will appear.

The bottom conduction band is shown in ***figure 6.3.2***. The oxygen atoms contribute slightly to this band. However, the biggest contribution is due to some reactive areas that appear between calcium atoms. The apparitions of these areas can be related with the arrangement of the calcium ions. The BCB represents the points with tendency to accept electrons, i.e. those areas with charge defect. The calcium atoms are those which present a defect charge in the unit cell. However, the BCB is not located around all the Ca atoms but in some specific areas between Ca1 and Ca4. It can be attributed to the

lowest Ca-Ca distance between them. In ***figure 6.2.2*** Ca3, 4, 5 and 6 ions form some cubic cells. The high symmetry Ca1 and Ca2 are located in the centre of some of these subcells, and therefore, the distance between them and the Ca located in their vertexes is the smallest possible. Furthermore, the subcells with Ca2 in its centre have a missing vertex due to the intrinsic vacancies of the C_3A structure. Thus, those cells have less charge defect and the reactive areas appear only in the subcells with Ca1 inside them, with complete vertexes. Finally, the Ca1-Ca4 path is especially favourable due to the absence of oxygen atoms in its proximity.

The BCB represent the areas where nucleophilic attack takes place. Due to the high alkalinity, the OH^- ions are the main nuclephile groups in the cement paste solution, and, in presence of gypsum, the SO_4^{-2} ions. The existence of the special reactive areas is in agreement with some of the experimental models of the retarding mechanism [40, 266-268]. They stated that there exist some reactive sites in the surface that are blocked by the sulphate groups, slowing down the reaction rate. The difference

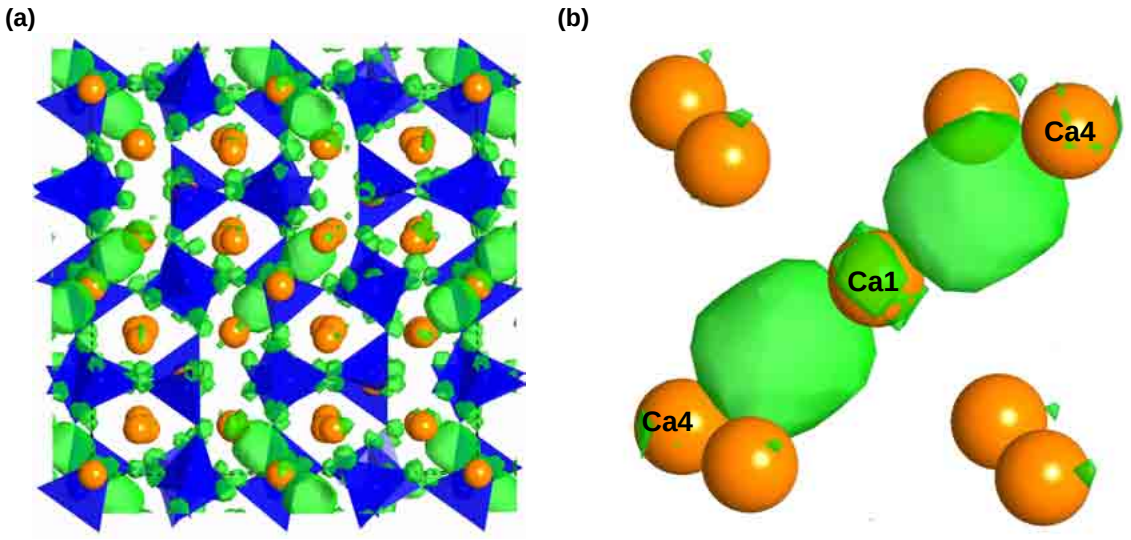

Figure 6.3.2.- Spatial location of the bottom conduction band (BCB) in tricalcium aluminate. As in the previous figure, the green isosurfaces enclose the areas where the BCB is larger, with a cut off value at 10% of the maximum value. **(a)** General view of the unit cell. **(b)** Detailed view of the special reactive areas around Ca1 and Ca4 ions.

between OH^- and SO_4^{-2} ions also points in that direction. On the one hand OH^- groups are small, with a O-H distance ~0.98 Å, and with a negative charge of –1.14 e^- very localized in the oxygen atom. On the other hand SO_4^{-2} ions are bigger, with a S-O distance of 1.54 Å, and their charge is delocalized between the four oxygen atom, –0.75 e^- per oxygen. Thus, the hydroxyl groups could get closer to the reactive points and interact strongly with them than the sulphate ions. Hence, it will be easier for OH to remove the Ca atoms from the solid structure.

The identified reactive sites within the unit cell of C_3A as well as the size differences between hydroxyl and sulphate ions indicate that the blockage mechanism is possible. However, these results cannot state the absence of a protective layer formed when the dissolution starts after the initial blockage. Furthermore, it is known that the retardation does not happen if Na_2SO_4 is added to the clinker instead of $CaSO_4$ [38]. Thus, not only the sulphate group but also the Ca^{+2} ions must play a role in the retardation mechanism. The presence of calcium ions could enhance the formation of portlandite or affect to the local alkalinity of the pore solution, factors that have influence in the retardation [37, 38]. Finally, it must be also taken into account that the reactive points of C_3A were calculated for the bulk structure. In a real system, the reaction between the solution and the crystal will take place on the surface. Interestingly, Cardenas et al. [274], studying alkaline oxide by first-principles simulations, found that the reactive sites of a surface are the same that those of the bulk. The main surface effect is to enhance the already reactive points of the bulk structure. Thus, the presented results can be considered as a first approximation, and be extrapolated to surfaces.

6.5. Conclusions

Tricalcium aluminate is the third component in amount in cement clinker. Its main characteristic is its high reactivity when is mixed with water. In this chapter the structure, elastic properties, and reactivity of bulk tricalcium aluminate have been investigated by *ab-initio* simulations.

The structure of C_3A [24] is perfectly described by the calculations. There is an excellent agreement with the experimental data for the lattice parameters, with disagreements smaller than 1%. Furthermore, the $Al_6O_{18}^{-6}$ ring structure and the calcium coordination polyhedra were investigated. The calculated bond distances present an average error of 0.02 and 0.03Å for Al-O and Ca-O bonds respectively. The mismatches in the O-Al-O and O-Ca-O angles are about 2º and 8º.

The full elastic tensor of tricalcium aluminate was calculated from strain-stress calculations. From the elastic tensor coefficients, the anisotropic Young modulus was calculated, E = 138 GPa. The value is in the range of those obtained by nanoindentation measurements, E = 145 ± 10 GPa [222, 223], and slightly smaller than the one by frequency resonances, E = 160 ± 10 GPa [222].

To study the reactivity of tricalcium aluminate, the spatial location of top valence band (TVB) and bottom conduction band (BCB) were calculated. They represent respectively the reactive areas under electrophile and nucleophilic attack. According to the simulations, all the oxygen atoms across the unit cell are reactive under electrophile attack of species like Ca^{+2} ions and water molecules. It implies a high number of reactive sites per unit cell, and a small resistance of the aluminium rings to the attack, that could be one of the reasons of the high hydraulic activity of C_3A [1, 4]. Some special areas are reactive in the case of nucleophilic attack (OH^- and SO_4^{-2}). The presence of specific sites for the reaction with sulphate ions points to a blockage mechanism for the retardation, as it has been stated in the literature [40, 266-268]. Furthermore, the differences in the charge and the size of OH^- and SO_4^{-2} groups also point in that direction. However, a posterior formation of protective layers cannot be ruled out. Finally, surface calculations would be useful to clarify the complex retardation mechanism.

Summary

Nowadays, the final application of cement-based materials makes sense only at the macroscale. However, the interaction and processes between the atoms that form the material determine cement properties at that scale. In this respect, atomistic simulation methods give us the opportunity to investigate those interactions and processes in detail for any material. The objective of this Thesis was to study cement related problems by means atomistic simulation methods.

This Thesis was mainly focused on the study of the C-S-H gel. The C-S-H gel is the most important hydration product and responsible for most of the cement paste properties. Hence, and accurate description of the C-S-H gel atomic structure is a crucial objective in cement science. In fact, many interesting properties such as the cohesion, the mechanical properties, or the material degradation, are stated to depend on that structure.

To study the formation of the C-S-H gel particles, a C-S-H gel precursor was suggested from tobermorite and jennite structural models. Then, from the assembly of those precursors, the growth and formation of the C-S-H gel nanoparticles has been investigated. Two different mechanisms were identified: (i) at low calcium contents, the rearrangement of the precursors to minimize their dipolar moments gives rise to the formation of tobermorite-like structures, while (ii) at high calcium contents the Ca-O bond formation leads to jennite-like structures. These two mechanisms are likely to govern the C-S-H nanoparticle growth. Unfortunately, the study cannot be further

upscale due to the high computational cost. Different approximations and/or other levels of theory, especially Molecular Dynamics methods, should be employed to study the C-S-H nanoparticles formation at higher scales.

Another topic under study was the relationship between C-S-H gel structure and its elastic properties. The elastic properties of the C-S-H gel were calculated with the tobermorite and jennite structural models as starting point. From them, structures with finite silicate chains lengths following the $3n - 1$ rule were built, and homogenization procedures were applied to include the intrinsic gel porosity. The results indicate that the existence of High Density and Low Density varieties of the C-S-H gel is the main responsible of the bimodal distribution of Young modulus in the cement paste. However, the silicate chain lengths also contribute to the C-S-H gel elastic properties. Specifically, longer silicate chains result in higher elastic properties. In addition to the C-S-H gel investigations, the elastic properties of the most important clinker components and hydrated cement matrix phases were also calculated. The results are in general in good agreement with the experimental measurements.

A correlation between the hydrogen content, the density, and the Young modulus was found for a series of crystalline calcium silicate hydrates (CSH) compounds. The experimentally estimated elastic properties of the amorphous C-S-H gel particles are in the range of the crystalline CSH family. However, experimentally estimated density for a C-S-H gel particle is high with respect to the structural models tobermorite 14 Å and jennite. The water content and density of the C-S-H gel nanoparticles are nowadays important problems in cement science, and therefore, such disagreement should be further investigated both by experimental and simulation methods.

The last studied topic regarding the C-S-H gel structure was the effect of the aluminium incorporation on the silicate chains. By *ab-initio* methods, the structure and electronic properties of the alumino-silicate chains were analyzed: HOMO-LUMO gaps, bond distances and charges, stability, and formation energies. The results confirmed the stability of the chains following the $3n - 1$ rule, and the preference of aluminium for the bridge site within the chains. The Molecular Dynamics simulations of $Si(OH)_4$ and

$Al(OH)_3$ condensations in presence of calcium reproduced the increase of the alumino-silicate mean chain length and the formation of non-linear structures when the Al content increases. Both the *ab-initio* and Molecular Dynamics results are in great agreement with the experiments, and the same trends were obtained: (i) increase of the chain length and polymerization when the Al content increases, and (ii) location of aluminium in central positions of the chains. It was found that the dimers with aluminium in a Q^1 site are stable, tough they are likely to react very fast to form larger chains. That could be the reason why dimers with aluminium are not found in cement pastes.

Besides the C-S-H gel nanostructure and properties, there are other cement-related problems in which atomistic simulations could be useful, for instance in the study of the hydration processes. The reactions of the clinker phases are difficult to track, especially at early ages of hydration, as they take place even during the mixing between cement and water. Here, the reason of the tricalcium aluminate (C_3A) high reactivity was studied by *ab-initio* methods. First, the structural parameters and elastic properties were calculated, with results in excellent agreement with the experimental data. Then, the electronic structure of tricalcium aluminate was analysed to investigate its reactivity. The results point to a blockage mechanism as the reason for the retardation in the C_3A hydration when gypsum is present, due to the existence of some special reactive areas under nucleophilic attack. Surface studies should be carried out to confirm our results and analyse in detail the reaction between the sulphate and hydroxyl groups and the C_3A surface. Although no changes are expected in the reactive points, the key presence of calcium as counterion could be investigated. It must be noted that the approach employed for C_3A can be extended to the remaining clinker phases.

In view of the presented results in this Thesis, it should be drawn that atomistic simulation methods can be very useful to advance in the field of cement science and technology. They will probably play a key role in the resolution of the C-S-H gel nanostructure, the interaction between particles which gives rise to the cohesion, and the explanation of processes such as creep. Creep consists on the rearrangement of the C-S-H gel nanoparticles after the development of the cement paste structure. It is stated to

depend on the interaction between particles, and be very influenced by the water content in the C-S-H gel particles surfaces. The determination of the position and role of water within the C-S-H gel nanoparticles is another topic available to be studied by atomistic simulation methods. In fact, it is nowadays subject of many experimental studies and reason of great controversy. These contributions to the understanding of the C-S-H gel might help in the modification and improvement of its properties in a desired direction. Atomistic simulation methods could contribute as well to the study of the clinker phases reactivity, especially at early ages of hydration. The knowledge of the hydration mechanisms could lead to improve them and achieve a tailored design of cement materials. In this line, the results presented in this Thesis are expected to help in the understanding of the cement paste, and specifically to the C-S-H gel nanostructure and properties and the tricalcium aluminate hydration. Furthermore, this Thesis is expected to be a solid starting point for future research, as it establishes a methodology that could be followed in future studies of cement-related problems by atomistic simulation methods.

Resumen

Pese a que hoy en día el uso final de los materiales en base cemento se centra en la macroescala, las propiedades y el comportamiento a esa escala vienen determinados por las interacciones y los procesos que tienen lugar entre los átomos que componenen el material. En este sentido, los métodos de simulación atomística nos dan la oportunidad de investigar esos procesos e interacciones en detalle para cualquier material o molecula. El objetivo de esta Tesis ha sido estudiar problemas relacionados los materiales cementicios usando como herramienta los métodos de simulación atomística.

El estudio del gel C-S-H ha sido el tema central de esta Tesis. El gel C-S-H es el principal componente y responsable de la mayor parte de las propiedades de pasta del cemento. Por lo tanto, obtener una descripción detallada de su estructura atómica, todavía desconocida, es un objetivo crucial en la ciencia del cemento. De hecho, muchas de las propiedades de los materiales cementicios, como la cohesión, las propiedades mecánicas o la degradación, se relacionan con la estructura atómica del gel C-S-H.

Con el objeto de estudiar el proceso de formación de las partículas de gel C-S-H, se ha propuesto un precursor del gel basado en los modelos estructurales tobermorita y jennita. A partir de la agregación de dicho precursor en diferentes condiciones, se ha estudiado la formación de las nanopartículas del gel C-S-H. Se han identificado dos mecanismos diferentes: (i) para bajos contenidos en calcio, la reordenación de los precursores para minimizar sus momentos dipolares da lugar a estructuras tipo tobermorita, mientras que (ii) para altos contenidos en calcio la formación de enlaces

Ca-O entre los precursores da lugar a estructuras tipo jennita. Estos dos mecanismos son posiblemente los que determinan la formación de las partículas de gel C-S-H. Lamentablemente, no se ha podido ampliar el estudio a escalas mayores debido al alto coste computacional. Para estudiar la formación de nanopartículas de gel C-S-H a escalas mayores es necesario abordar el problema empleando diferentes aproximaciones y/u otros niveles de teoría, como mpor ejemplo métodos de Dinámica Molecular.

Otro de los temas estudiados ha sido la relación entre la estructura del gel C-S-H y sus propiedades elásticas. Las propiedades elásticas del gel C-S-H han sido calculadas empleando como punto de partida los modelos estructurales de tobermorita y jennita. A partir de estos modelos, se han construido estructuras con cadenas de silicato de longitud finita siguiendo la regla $3n - 1$, incluyendo la porosidad intrínseca del gel C-S-H mediante métodos de homogenización. Los resultados indican que la distribución binodal de modulos de Young se debe pricipalmente a la existencia de dos variedades de gel C-S-H de alta y baja densidad. No obstante, la longitud de las cadenas de silicatos también contribuye a las propiedades elásticas. Concretamente, cadenas de silicatos más largas implican mejores propiedades elásticas de las partículas y por tanto del gel. Además de los estudios sobre el gel C-S-H, también se han calculado las propiedades elásticas de los componentes del clínker y las fases de hidratación más importantes. Los resultados obtenidos concuerdan en gran medida con los valores experimentales.

Se ha hallado una correlación entre el contenido de hidrógenos, la densidad y el módulo de Young para una serie de silicatos cálcicos hidratados cristalinos (CSH). Las propiedades elásticas estimadas experimentalmente para una partícula amorfa de gel C-S-H son del orden de las de la familia de cristales CSH. No obstante, la densidad estimada experimentalmente para las partículas de gel C-S-H es alta en relación a los modelos estructurales tobermorita 14 Å y jennita. La densidad y la cantidad de agua en el gel C-S-H son temas importantes en el estudio de los materiales cementicios, y por tanto estas discrepancias deben ser analizadas más en profundidad tanto mediante métodos experimentales como métodos de simulación.

El efecto de la sustitución del aluminio a las cadenas de silicato es el último aspecto

estudiado en relación con la estructura del gel C-S-H. Mediante métodos *ab-initio*, se han analizado la estructura y las propiedades electrónicas de las cadenas de alumino-silicatos: HOMO-LUMO gaps, distancias de enlace y cargas, estabilidad y energías de formación. Los resultados confirman la estabilidad de las cadenas con longitudes acordes a la regla *3n – 1*, y la preferencia del aluminio por la posición puente dentro de las cadenas. Las simulaciones de condensación del $Si(OH)_4$ y $Al(OH)_3$ en presencia de calcio llevadas a cabo mediante Dinámica Molecular reproducen el aumento de longitud de las cadenas de aluminosilicatos y la formación de estructuras no lineales al aumentar el contenido de aluminio. Tanto los cálculos *ab-initio* como los de Dinámica Molecular muestran resultados acordes con los experimentos: (i) aumento de la longitud de la cadena y polimerización al aumentar el contenido en aluminio, y (ii) preferencia del aluminio por las posiciones centrales de la cadena. Según los resultados obtenidos, los dímeros con aluminio en la posición Q^1 son estables, auque que tienen una gran tendencia a reaccionar para formar cadenas más largas. Esta podría ser la explicación a por qué no se han encontrado experimentalmente dímeros con aluminio en pastas de cemento.

Además de la nanoestructura y las propiedades del gel C-S-H, la simulación atomística puede ser un instrumento útil para el estudio de otros problemas relacionados con el cemento, como por ejemplo los procesos de hidratación. Las reacciones hidratación de las fases del clínker son difíciles de monitorizar, especialmente a edades tempranas, ya que ocurren incluso durante la mezcla entre el cemento y el agua. Aquí se ha estudiado el origen de la alta reactividad del aluminato tricálcico (C_3A) mediante métodos *ab-initio*. En primer lugar, se han calculado los parámetros estructurales y las propiedades elásticas del C_3A, obteniendo unos resultados en excelente concordancia con los datos experimentales. En segundo lugar, se ha analizado la estructura electrónica del aluminato tricálcico para estudiar su reactividad. Los resultados apuntan a que la existencia de un mecanismo de bloqueo es la causa de la disminución de la reactividad del aluminato tricálcico en presencia del yeso, debido a la existencia de ciertos puntos reactivos bajo ataque de nucleofílico. Para analizar en detalle la reacción entre el sulfato y los grupos hidroxilos con la superficie del C_3A deberían realizarse estudios de superficie. Pese a no esperar cambios en las zonas reactivas, el efecto clave del calcio

como contraión podría ser estudiado. Es importante tener en cuenta que el método empleado para el estudio del C_3A puede extenderse a las demás fases de clínker.

En vista de los resultados presentados en esta Tesis, debe extraerse como conclusión que los métodos de simulación atomística pueden ser muy útiles para el avance de la ciencia y tecnología del cemento. Probablemente estos métodos jugarán un papel clave en la resolución de la nanoestructura del gel C-S-H, las interacciones entre partículas que dan lugar a la cohesión, y la explicación de procesos como el *creep*. El *creep* consiste en la reorganización de las nanopartículas de gel C-S-H una vez formada la estructura de pasta de cemento. Este proceso depende de la interacción entre las partículas, y esta muy influenciado por del contenido de agua en la superficie del gel C-S-H. Precisamente, la posición y el rol del agua en las nanopartículas de gel C-S-H es otro de los aspectos que pueden ser estudiados mediante métodos de simulación atomística. Este tema es actualmente objeto de gran cantidad de estudios experimentales y motivo de gran controversia. Cualquiera de las mencionadas aportaciones al conocimiento de la estructura gel C-S-H podrían ayudar en la modificación y la mejora de sus propiedades en la dirección deseada. Los métodos de simulación atomística pueden contribuir también al estudio de la reactividad de las fases clínker, especialmente a edades tempranas de hidratación. El conocimiento de los mecanismos de hidratación podría conducir a su mejora, y llegar a alcanzar así un diseño “a la carta” de los materiales en base cemento. En esta línea, se espera que los resultados presentados en esta Tesis contribuyan a la comprensión de la pasta de cemento, y más concretamente a la nanoestructura y propiedades del gel C-S-H y a la hidratación del aluminato tricálcico. También se pretende que esta Tesis sea un punto de partida para futuras investigaciones, al establecer una metodología que puede ser empleada en futuros estudios sobre problemas relacionados con el cemento mediante métodos de simulación atomística.

Appendix 1.

SIESTA Pseudopotentials and Basis set

The SIESTA method is based on a flexible Linear Combination of Atomic Orbitals (LCAO) to construct the Kohn-Sham orbitals, together with pseudopotentials to account for the core electrons [201, 275]. The SIESTA web page can provide the user of pseudopotentials and basis sets for a considerable part of the periodic table. Nevertheless, both the pseudopotentials and the basis set should be carefully tested by the user to asses their transferability

Below, the basis and pseudopotentials used in this work are given. For each atom, a description of the basis set and pseudopotential are given, together with the basis set itself and the input file employed to generate the pseudopotentials with the ATOM program (distributed with the SIESTA code).

ALUMINIUM

==========

Basis Set [276]

Basis set optimized with Simplex for Al in corundum (Al2O3).
Quality of the basis set: DZP (2 radial functions for the 3s state, 2 radial functions for the 3p state and a single radial function for the 3d states). This amounts to 13 atomic orbitals per Al atom.

```
AL     3    0.96730E-01
 n=3   0   2   E    38.42957     5.54399
     7.45113     5.29860
     1.00000     1.00000
 n=3   1   2   E    11.53806     6.32312
     7.99984     5.93909
     1.00000     1.00000
 n=3   2   1   E    42.38228     0.00008
     6.30124
     1.00000
```

Pseudopotential [276]

Flavour of the pseudopotential: Troullier-Martins.
Exchange and correlation functional: GGA (Perdew-Burke-Ernzerhof).
Relativistic: No. Non-linear-core-corrections: Yes.
Cutoff radius for the nlcc: 1.5 bohr.
Reference configuration: 3s2 3p0.5 3d0.5 4f0
Cutoff radii: 3s 2.30 bohrs. 3p 2.30 bohrs. 3d 2.30 bohrs. 4f 2.30 bohrs

```
 pe      Aluminium
        tm2      0.0
   Al   pb
       0.0       0.0       0.0       0.0       0.0       0.0
    3    4
    3    0      2.00      0.00
    3    1      0.50      0.00
    3    2      0.50      0.00
    4    3      0.00      0.00
      2.30      2.30      2.30      2.30      1.00      1.50
```

==========

CALCIUM

==========

Basis Set

Basis set optimized with Simplex for the bulk cubic cell of CaTiO3. The semicore states 3s and 3p are included in the valence. The quality of the basis is DZP for the valence (two radial functions for the 4s, and one radial fuction for the 4p states), and SZ for the semicore states (one radial function for the 3s and the 3p). An extra shell of 3d orbitals are added. This amounts to 14 basis functions per Ca atom.

```
CA   5      1.90213
n=3   0   1   E    61.56667     4.61281
     5.29940
     1.00000
n=4   0   2   E   164.86383     5.38785
     6.76569     4.96452
     1.00000     1.00000
n=3   1   1   E    86.94959     3.48034
     6.32716
     1.00000
n=4   1   1   E   112.03339     4.98424
     7.49434
     1.00000
n=3   2   1   E    87.65847     5.83989
     6.49046
     1.00000
```

Pseudopotential

Flavour of the pseudopotential: Troullier-Martins.
Exchange and correlation functional: LDA (Ceperley-Alder).
Relativistic: yes. Core corrections: no.
Valence reference configuration: 3s2 3p6 3d0 4f0 (ionic configuration, ionic charge +2).
Cutoff radius: 3s 1.30 bohr 3p 1.30 bohr 3d 1.30 bohr 4f 2.00 bohr

```
   pg      Calcium
        tm2      1.5
   Ca   car
       0.0       0.0       0.0       0.0       0.0       0.0
    3    4
    3    0      2.00      0.00
    3    1      6.00      0.00
    3    2      0.00      0.00
    4    3      0.00      0.00
      1.30      1.30      1.30      2.00      0.00      0.00
```

==========

HYDROGEN

==========

Basis Set [275]

Basis set optimized with Simplex for the water molecule.
The quality of the basis is DZP for the valence (two radial functions for the 1s, and one radial function for the 2p). This amounts to 5 basis functions per H atom.

```
H     2      0.22
 n=1    0    2   E      2.07      0.00
   4.971   1.771
   1.000   1.000
 n=2    1    1   E      0.89      0.01
   4.988
   1.000
```

Pseudopotential [275]

Flavour of the pseudopotential: Troullier-Martins.
Exchange and correlation functional: LDA (Ceperley-Alder).
Relativistic: No. Core-corrections: No.
Valence reference configuration: 1s1, 2p0, 3d0, 4f0.
Cutoff radii: 1s 1.25 bohr 2p 1.25 bohr 3d 1.25 bohr 4f 1.25 bohr

```
   pg      Hydrogen
        tm2      2.0
   H    ca
       0.0       0.0       0.0       0.0       0.0       0.0
    0    4
    1    0      1.00
    2    1      0.00
    3    2      0.00
    4    3      0.00
      1.25      1.25      1.25      1.25      0.00      0.00
```

==========

OXYGEN

==========

Basis Set [128]

Basis set optimized for silicates.
The quality of the basis is DZP for the valence (two radial functions for the 2s, two radial function for the 2p state, and one radial function for the 3d shell). This amounts to 13 basis functions per O atom

```
O        3     -0.2062
n=2    0    2   E     89.2503      5.0971
       5.9617503       2.52330170
       1.0000000       1.00000000
n=2    1    2   E     76.3408      7.1750
       7.8532951       2.48682077
       1.00000000       1.00000000
n=3    2    1   E    104.3073      0.0000
       3.92324958
       1.00000000
```

Pseudopotential [275]

Flavour of the pseudopotential: Troullier-Martins
Exchange and correlation functional: LDA (Ceperley-Alder)
Relativistic: No Core-corrections: No
Valence reference configuration: 2s2, 2p4, 3d0, 4f0
Cutoff radii: 2s 1.15 bohr 2p 1.15 bohr 3d 1.15 bohr 4f 1.50 bohr

```
   pe      Oxygen
        tm2      0.0
   O    bl
       0.0       0.0       0.0       0.0       0.0       0.0
    1    4
    2    0      2.00      0.00
    2    1      4.00      0.00
    3    2      0.00      0.00
    4    3      0.00      0.00
      1.15      1.15      1.15      1.15      0.00      1.17
```

==========

SILICON

==========

Basis Set [128]

Basis set optimized for silicates.
The quality of the basis is DZP for the valence (2 radial functions for the 3s state, 2 radial functions for the 3p state and a single radial function for the 3d states) This amounts to 13 atomic orbitals per Al atom.

```
Si       3      0.0000
n=3    0    2   E     18.4973      5.0324
      7.7935252        3.811580
      1.0000000        1.000000
n=3    1    2   E     17.8598      5.2031
      7.9974720        4.198611
      1.0000000        1.000000
n=3    2    1   E      9.7553      0.0000
      4.60610639645471
      1.0000000
```

Pseudopotential [275]

Flavour of the pseudopotential: Troullier-Martins.
Exchange and correlation functional: LDA (Ceperley-Alder).
Relativistic: no. Core corrections: no.
Valence reference configuration: 3s2 3p2 3d0 4f0.
Cutoff radius: 3s 1.90 bohr 3p 1.90 bohr 3d 1.90 bohr 4f 1.90 bohr

```
   pg      Silicon
        tm2      3.0
   Si   ca
       0.0       0.0       0.0       0.0       0.0       0.0
    3    4
    3    0      2.00      0.00
    3    1      2.00      0.00
    3    2      0.00      0.00
    4    3      0.00      0.00
      1.90      1.90      1.90      1.90      0.00      0.00
```

==========

Appendix 2.

Force Fields: Potential Functional Forms and Parameters

As explained in the overview of the atomistic simulation methods, in Molecular Mechanics and classical Molecular Dynamics the interaction between atoms is described by means of a force field. A force field is the sum of the potential functional forms and the specific parameters for the calculation. Two force fields were employed during this Thesis to face different problems.

In ***chapter 4***, the polymerization of $Al(OH)_3$ and $Si(OH)_4$ in presence of calcium and sodium ions was studied by molecular dynamics methods. The used force field was the developed by Garofalini et al. to study the polymerization of alumino-silicate glasses, water interaction with alumino-silicate surfaces, and the properties of intergranular films on ceramic materials [209-214]. The force field consisted in a modified Born-Mayer-Huggins two-body potential to simulate the short range repulsion and coulombic interaction, and a three-body potential to simulate the angle of the silicate and aluminate groups covalent bonds. A screened coulombic potential for the Ca-Na, Al-H and Na-H pairs was included in this work, following the approach of ref [122].

The modified Born-Mayer-Huggins (BMH) potential has the form:

$$U_{AB}^{BMH} = A_{AB}\, exp\left(\frac{-r_{AB}}{\rho_{AB}}\right) + \frac{q_A q_B}{r_{AB}}\xi\left(\frac{r_{AB}}{\beta_{AB}}\right) + U_{AB}^{RSL} \qquad (7.2.1)$$

where A_{AB}, ρ_{AB} and β_{AB} are adjustable pair parameters, given in ***table 2***, ξ is the complementary error function, and r_{AB} is the interatomic distance. U_{AB}^{RSL} is a complementary potential by Rahman, Stillinger, and Lemberg (RSL), employed to make distinctions between inter- and intra-molecular interactions:

$$U_{AB}^{RSL} = \frac{a_{AB}}{1 + exp\left[b_{AB}\left(r_{AB} - C_{AB}\right)\right]} \qquad (7.2.2)$$

where a_{AB}, b_{AB} and C_{AB} are adjustable pair parameters, given in ***table 1***. A three body potential was used to simulate the angle of the covalent bonds in the silicate and aluminate groups:

$$U_{ABC}^{three} = \lambda\, exp\left(\frac{\gamma_{AB}}{r_{AB} - r_{AB}^{0}} + \frac{\gamma_{AC}}{r_{AC} - r_{AC}^{0}}\right)\left(\cos\theta_{ABC} - \cos\theta_{ABC}^{0}\right)^{2} \quad when\ r_{AB} < r_{AB}^{0}\ and\ r_{AC} < r_{AC}^{0}$$

$$U_{ABC}^{three} = 0\ otherwise \qquad (7.2.3)$$

where θ_{ABC} is the angle formed by atoms *A*, *B*, and *C* with atom *A* at the vertex, and λ_{AB} and γ_{AC} are adjustable parameters given in **table 3**.

Table 1.- .- Parameters for the Rahman, Stillinger, and Lemberg potential.

R-S-L	a_{AB} (10^{-12} ergs)	b_{AB} ($Å^{-1}$)	C_{AB} (Å)	Reference
Si – H	-4.6542	6.0	2.20	[277]
H – H	-5.2793	6.0	1.51	[277]
	0.3473	2.0	2.42	
O – H	-2.084	15.0	1.05	[277]
	7.6412	3.2	1.50	
	-0.8336	5.0	2.00	

Table 2.- Parameters for the modified Born-Mayer-Huggins potential. The atomic pairs without A_{AB} and ρ_{AB} are described only by a screened coulombic potential, as given in the second term of equation **(7.2.1)** The selected charge for the atoms were the ionic ones: Si^{+4}, Al^{+3}, Ca^{+2}, Na^{+1}, H^{+1}, and O^{-2}.

B-M-H	A_{AB} (10^{-8} ergs)	β_{AB} (Å)	ρ_{AB} (Å)	Reference
Si – Si	0.1877	2.29	0.29	[277]
Si – O	0.2962	2.34	0.29	[277]
Si – H	0.0069	2.31	0.29	[277]
O – H	0.3984	2.26	0.29	[277]
O – O	0.0725	2.34	0.29	[277]
H – H	0.0034	2.10	0.35	[277]
Al – Al	0.050	0.235	0.29	[214]
Al – O	0.249	0.234	0.29	[214]
Al – H		2.31		
Al – Si	0.2523	0.233	0.29	[214]
Ca – Ca	0.70	0.23	0.29	[214]
Ca – Si	0.2215	0.23	0.29	[214]
Ca – O	0.57	0.234	0.29	[214]
Ca – H		2.31		[122]
Na – O	0.3195	2.34	0.29	[213]
Na – Si	0.2001	2.30	0.29	[213]
Na – Al	0.2178	2.30	0.29	[213]
Na – Ca		2.30		
Na – H		2.31		

Table 3.- Parameters for the three body potential. X stands for Si and Al. Two values are given for the X-O-H set. The first values describe the X-O interaction, while the second one are for the O-H one.

Three Body	r_{AB} (Å)	λ_{AB} (10^{-11} ergs)	γ_{AC} (Å)	θ_{ABC} (º)	Reference
O – X – O	3.0	24.0	2.8	109.5	[213]
X – O – X	2.6	1.0	2.0	109.5	[213]
H – O – H	1.6	35.0	1.5	104.5	[277]
X – O – H	2.6 ; 1.5	5.0	2.0 ; 1.2	109.5	[277]

In ***chapter 5*** the elastic properties of the main components in the cement paste and other related crystals were calculated using molecular mechanics methods. The selected force field was based on those developed for zeolites [241-244], calcium oxides [246, 247]., water-silica interactions [242, 244-247], gypsum [251], and brownmillenite [249, 250]. The coulombic potential was employed to describe coulombic interactions, the Buckingham and the Lennard-Jones potentials to account for the repulsive and dispersive forces, a first order harmonic potential to describe angles due to orbital hybridation in covalent bonds, the Morse potential for the intramolecular interactions in water and SO_4^{-2} ions, and finally, a spring potential for the core-shell interaction. Except the spring potential, all the functional form of the potentials were explained in the overview of the atomistic methods. The new spring potential has the form of the Hooke's equation:

$$U_{AB}^{spring} = \frac{1}{2} k \cdot \left(r - r_0 \right)^2 \qquad (7.2.4)$$

where k is a constant, r is the distance, and r_0 is the equilibrium distance. In the case of a core-shell interaction, r_0 is equal to zero, as the equilibrium position is that with the shell in a central position around the core (see ***chapter 5***). The used functional forms and parameters for the different crystalline species are collected from ***table 4 to 10***.

Table 4.- Parameters to simulate the tricalcium aluminate (C_3A) and ferrite (C_4AF).

Species	Charge core	Charge shell	Spring K (eV·Å^{-2})		Reference
Ca	2.00	--			[250]
Al	3.00	--			[250]
Fe	3.00	--			[250]
O	0.80	-2.800	54.80		[250]
Buckingham	A (eV)	ρ (Å)	C (eV·A^6)	*cut off* (Å)	
Ca– O	1090.0	0.339	0.00	17.52	[250]
Al – O	1730.0	0.290	0.00	17.520	[250]
Fe – O	1410.0	0.313	0.00	17.520	[250]
O – O	9550.0	0.219	32.00	17.520	[250]

Table 5.- Parameters to simulate the tricalcium silicate (C_3S) and dicalcium silicate (C_2S).

Species	Charge core	Charge shell	Spring K (eV·Å^{-2})		Reference
Ca	2.00	--			[250]
Si	4.00	--			[241]
O	0.80	-2.800	54.80		[250]
Buckingham	A (eV)	ρ (Å)	C (eV·A^6)	*cut off* (Å)	
Ca– O	1090.0	0.344	0.00	12.0	[250]
Si – O	1280.0	0.321	10.70	12.0	[241]
O – O	22800.0	0.149	27.90	12.0	[241]

Table 6.- Parameters employed to simulate portlandite (CH).

Species	Charge core	Charge shell	Spring K (eV·Å^{-2})		Reference
Ca	2.00	--			[247]
O	0.87	-2.270	74.90		[247]
H	0.4				[248]
Morse	D (eV)	α (Å^{-2})	r_0 (Å)	*cut off* (Å)	
Ow – Hw	6.20	2.220	0.924	1.4	[248]
Lennard Jones	A (eV·Å^{-6})	B (eV Å^{-12})	*cut off* (Å)		
Ow – Ow	39300.00	42.10	12.0		[248]
Buckingham	A (eV)	ρ (Å)	C (eV·A^6)	*cut off* (Å)	
Ca inter – Ooh	777.00	0.344	0.00	12.0	[247]

Table 7.- Parameters to simulate hydrogarnet (C_3AlH_3).

Species	Charge core	Charge shell	Spring K (eV·Å^{-2})		Reference
Al	3.00	--			[243]
O	0.87	-2.270	74.90		[247]
H	0.4				[242]
Morse	D (eV)	α (Å^{-2})	r_0 (Å)	*cut off* (Å)	
O – H	7.050	3.170	0.943	1.400	[242]
Buckingham	A (eV)	ρ (Å)	C (eV·A^6)	*cut off* (Å)	
Al – O	1142.7	0.299	0.00	12,0	[243]
Ca – O	777.0	0.3440	0.00	12.0	[247]
O – O	22800.0	0.1490	6.97	12.0	[243]

Table 8.- Parameters to describe the intramolecular interaction of the water molecules and SO_4^{-2} groups in C-S-H systems, ettringite, and monosulphoaluminate. The letter following the oxygen atoms distinguish the water (w) and sulphate (s) environment. *Continues in the next page.*

Species	Charge core	Charge shell	Spring K (eV·Å^{-2})		Reference
S	1.36	--			[251]
H	0.40	--			[248]
Ow	1.25	-2.050	209.00		[248]
Os	-0.84	--			[251]
Morse	D (eV)	α (Å^{-2})	r_0 (Å)	*cut off* (Å)	
Ow – Hw	6.20	2.220	0.924	1.4	[248]
S – Os	5.00	1.200	1.505	1.8	[251]
Three body harmonic	k (eV rad^{-2})	θ_0 (º)	*cut off 1-2-3* (Å)		
Ow – Hw – Hw	4.20	108.690	1.2 / 1.2 / 2.4		[248]
S – Os – Os	15.00	109.470	1.8 / 1.8 / 3.2		[251]

Table 9.- Parameters employed to describe the atomic interactions in ettringite and monosulphoaluminate. The letter following the oxygen atoms distinguish the water (w), hydroxyl groups, and sulphate (s) environment. *Continues in the next page.*

Species	Charge core	Charge shell	Spring K (eV·Å^{-2})	Reference
Ca	2.00	--		[247]
Os	-0.84	--		[251]
Ow	1.25	-2.050	209.00	[248]
Ooh	0.87	-2.270	74.90	[242]
Hoh	0.40	--		[242]
Hw	0.40	--		[248]

Al	3.00	--			[243]
S	0.54	--			[251]
Morse	*D* (eV)	α (Å^{-2})	r_0 (Å)	*Cut off* (Å)	
O – H	7.050	3.170	0.943	1.400	[242]
Buckingham	*A* (eV)	ρ (Å)	*C* (eV·A^6)	*Cut off* (Å)	
Al – Os	1142.678	0.2991	0.00	12.0	[243]
Al – Ow	1142.678	0.2991	0.00	12.0	[243]]
Al – Ooh	1142.678	0.2991	0.00	12.0	[243]
Ca – Os	1651.350	0.2931	0.00	12.0	[251]
Ca – Ow	1090.000	0.3440	0.00	12.0	[251]
Ca – Ooh	777.000	0.3440	0.00	12.0	[247]
Os – Os	103585.020	0.2000	25.90	0.0-15.0	[251]
Os – Ow	57143.200	0.2242	75.70	0.0-20.0	[251]
Os – Ooh	57143.200	0.2242	75.70	0.0-20.0	[251]
Ooh – Ooh	22800.000	0.1490	6.97	12.0	[243]
Ooh – Ow	22800.000	0.1490	0.15	12.0	[242]
Os – Hw	2481.270	0.0598	0.00	0.0-20.0	[251]
Os – Hoh	2481.270	0.0598	0.00	0.0-20.0	[251]
Ow – Hw	396.000	0.2500	10.00	0.0-20.0	[248]
Ow – Hoh	312.000	0.2500	0.00	12.0	[242]
Ooh – Hw	312.000	0.2500	0.00	12.0	[242]
Lennard Jones	*A* (eV·Å^{-6})	*B* (eV Å^{-12})	*cut off* (Å)		
Ow – Ow	39300.00	42.10	12.0		[248]

Table 10.- Parameters employed to describe the atomic interactions in the C-S-H systems. The letter following the atoms distinguishes the oxygen and hydrogen atoms according to their nature: water (w), hydroxyl groups (oh). Two different calcium atoms are considered, the one in the Ca-O layers (inter) and the one in the interlaminar space (intra). For non-laminar CSH crystals the Ca inter parameters were employed. *Continues in the next page.*

Species	Charge core	Charge shell	Spring K (eV·Å^{-2})		Reference
Ca inter	2.00	--			[247]
Ca intra	2.00	--			[247]
Ow	1.25	-2.050	209.00		[248]
Ooh	0.87	-2.270	74.90		[242]
Hoh	0.40	--			[242]
Hw	0.40	--			[248]
Si	4.00	--			[241]
Al	3.00	--			[243]
Buckingham	A (eV)	ρ (Å)	C (eV·A^6)	*cut off* (Å)	
Ca inter – Osi	1090.000	0.3440	0.00	12.0	[247]
Ca inter – Ooh	777.000	0.3440	0.00	12.0	[247]
Ca inter – Ow	777.000	0.3440	0.00	12.0	[247]
Ca intra – Osi	1090.000	0.3440	0.00	12.0	[247]
Ca intra – Ooh	1090.000	0.3440	0.00	12.0	[247]
Ca intra – Ow	777.000	0.3440	0.00	12.0	[247]
Si – Osi	1283.907	0.3205	10.66158	12.0	[241]
Si – Ooh	983.557	0.3205	10.66158	12.0	[241]
Si – Ow	984.000	0.3210	10.66158	12.0	[[242]
Al – Osi	1142.678	0.2991	0.00	12.0	[243]
Al – Ow	1142.678	0.2991	0.00	12.0	[243]
Al – Ooh	1142.678	0.2991	0.00	12.0	[243]

Osi – Osi	22800.000	0.3210	27.90	12.0	[241]
Osi – Ooh	22800.000	0.1490	13.90	12.0	[241]
Osi – Ow	22800.000	0.1490	0.149	12.0	[242]
Ooh – Ooh	22800.000	0.1490	6.970	12.0	[241]
Ooh – Ow	22800.000	0.1490	0.149	12.0	[242]
Ooh – Hw	312.000	0.2500	0.00	12.0	[242]
Ow – Hw	396.000	0.2500	0.00	12.0	[248]
Ow – Hoh	312.000	0.2500	0.00	12.0	[242]
Morse	*D* (eV)	α (Å^{-2})	r_0 (Å)	*cut off* (Å)	
O – H	7.050	3.170	0.943	1.400	[242]
Lennard Jones	*A* (eV·Å^{-6})	*B* (eV Å^{-12})	*cut off* (Å)		
Ow – Ow	39300.00	42.10	12.0		[248]
Three body harmonic	*k* (eV rad^{-2})	θ_0 (º)	*cut off 1-2-3* (Å)		
Si – Osi – Osi	2.097	109.470	1.8 /1.8 /3.2		[241]
Si – Osi – Ooh	2.097	109.470	1.8/1.8 /3.2		[241]
Al – Osi – Osi	2.097	109.470	1.8/1.8 /3.2		[243]
Al – Osi – Ooh	2.097	109.470	1.9/1.9/3.5		[243]

Appendix 3.

The Stability Index

In ***chapter 4*** the stability of alumino-silicate chains was investigated. For that purpose, a stability index was defined. The stability index (*S*) quantifies the relative stability of a chain with respect to chains formed by adding or removing one silicon (or aluminium) unit [216]. To set up the local stability condition, the relative chains population and the transition rate per chain and unit time (*T*) between them must be considered. As an example the process for the pure neutral silicate chain will be studied. The transitions are

$$(m-1)_{Si} \rightleftharpoons (m)_{Si} \rightleftharpoons (m+1)_{Si} \tag{7.3.1}$$

where the number in parenthesis is the length of the silicate chain tetrahedra. The chains with length *m* will be more stable when the transition rates to *m* are larger than the ones from *m*:

$$T\left[(m-1)_{Si} \rightarrow (m)_{Si}\right] \times T\left[(m+1)_{Si} \rightarrow (m)_{Si}\right] > T\left[(m)_{Si} \rightarrow (m-1)_{Si}\right] \times T\left[(m)_{Si} \rightarrow (m+1)_{Si}\right] \tag{7.3.2}$$

The left hand side of the equation (7.3.2) represents the transition pathways that lead to chains of length *m*, while the right hand side the pathways that arise from chains of length *m*. If the expression is given as a product of fractions, the condition of stability becomes:

$$\frac{T\left[(m-1)_{Si} \rightarrow (m)_{Si}\right]}{T\left[(m)_{Si} \rightarrow (m-1)_{Si}\right]} \times \frac{T\left[(m+1)_{Si} \rightarrow (m)_{Si}\right]}{T\left[(m)_{Si} \rightarrow (m+1)_{Si}\right]} > 1 \qquad (7.3.3)$$

where the pathways to and from *m* are in the numerator and denominator respectively. At the thermal equilibrium, the number of chains with lengths *m – 1* and *m*, as well as the *m* and *m +1*, must be equilibrated, depending on the transition rate between them:

$$n\left[(m-1)_{Si}\right] T\left[(m-1)_{Si} \rightarrow (m)_{si}\right] = n\left[(m)_{Si} T\right]\left[(m)_{Si} \rightarrow (m-1)_{si}\right] \qquad (7.3.4)$$

$$n\left[(m)_{Si}\right] T\left[(m)_{Si} \rightarrow (m+1)_{si}\right] = n\left[(m+1)_{Si}\right] T\left[(m+1)_{Si} \rightarrow (m)_{si}\right] \qquad (7.3.5)$$

where *n* are the populations of the chains with length between brackets. These populations can be written in terms of the Boltzmann distribution function:

$$n\left[(m)_{Si}\right] = \frac{N}{Z} e^{-\frac{E\left[(m)_{si}\right]}{k_b T}} \qquad (7.3.6)$$

where *N* is the total number of chains, *Z* is the partition function, *E* is the energy of the indicated chain lenght, K_b is the Boltzmann constant and *T* is the temperature. Inserting the expression for the population into equation (7.3.4), it is obtained:

$$\frac{T\left[(m-1)_{Si} \rightarrow (m)_{si}\right]}{T\left[(m)_{Si} \rightarrow (m-1)_{si}\right]} = e^{-\frac{E\left[(m)_{si}\right] - E\left[(m-1)_{si}\right]}{k_b T}} \qquad (7.3.7)$$

Rewriting equation (7.3.3) in terms of (7.3.7), and the corresponding expression for eq.(7.3.5), the following formula is reached after a little algebra:

$$E\left[(m-1)_{si}\right] + E\left[(m-1)_{si}\right] - 2E\left[(m)_{si}\right] > 0 \qquad (7.3.8)$$

The local stability has been defined then in terms of the energy of the alumino-silicate chains. By definition, the stability index (*S*) of the process given in equation (7.3.1) is the right hand side term of equation (7.3.8):

$$S(m) = E\left[(m-1)_{si}\right] + E\left[(m-1)_{si}\right] - 2E\left[(m)_{si}\right] \tag{7.3.9}$$

A chain with length *m* will be stable from adding or removing a monomer if its stability index *S(m)* is positive.

The derivation of the stability index can be extended to all the processes considered in ***chapter 4***, illustrated in ***figure 4.2.1***. Following the same approach, the global stability index is:

$$\begin{aligned} S(m) = {} & 2E\left[(m-1)_{si}\right] + E\left[(m+1)_{si}\right] + E\left[(m-1)_{si^-}\right] + \\ & + 2E\left[(m+1)_{si^-}\right] - 3\left[E(m)_{si}\right] - 3E\left[(m)_{si^-}\right] + E\left[(m-1)_{si}\right] + \\ & + E\left[(m-1)_{Al}\right] + 2E\left[(m+1)_{Al}\right] - E\left[(m)_{si}\right] - 3E\left[(m)_{Al}\right] \end{aligned} \tag{7.3.10}$$

The global stability can be separated in different terms, accounting for a desired group of reaction channels. The discussion of ***chapter 4*** is focused mainly on the role of aluminium in the chain stability. The stability of the processes which involve aluminium is:

$$S_{Al}(m) = E\left[(m-1)_{Al}\right] + E\left[(m+1)_{Al}\right] + E\left[(m-1)_{Si}\right] - 3E\left[(m)_{Al}\right] \tag{7.3.11}$$

And the total stability, including the pure silicon (neutral and charged) chains:

$$S(m) = S_{Si}(m) + S_{Al}(m) \tag{7.3.12}$$

where:

$$S_{Si}(m) = 2E\left[(m-1)_{si}\right] + E\left[(m+1)_{si}\right] + E\left[(m-1)_{si^-}\right] + \\ +2E\left[(m+1)_{si^-}\right] - 3E\left[(m)_{si}\right] - 3E\left[(m)_{si^-}\right] \quad (7.3.13)$$

The result from the analysis is clear: if the stability index is positive, the chain is stable at that size. On the other way, a chain length with negative *S(m)* will evolve towards a more stable length adding or removing alumino-silicate tetrahedra.

Appendix 4.

Connectivity of the Alumino-silicate chains from Molecular Dynamics Simulations

In ***chapter 4***, the polymerization of $Si(OH)_4$ and $Al(OH)_3$ monomers in presence of $Ca(OH)_2 \cdot 5\ H_2O$ and $Na(OH) \cdot 4\ H_2O$ was studied by Molecular Dynamics methods. To analyze the structure of the formed chains and the position of aluminium within them, the Q^n sites of the alumino-silicate chains were calculated. The nomenclature is usually employed in NMR investigations silicate structures such as zeolites, sol-gel systems, and cement materials [215]. A Q^n position denotes a silicon atom linked to *n* other silicon atoms via *n* oxygen atom, $Si\text{-}(O\text{-}Si)_n$. When Aluminium is present, the number of Si-O-Al is indicated by a subscript Q^n_{mAl}, and the remaining $n - m$ bonds are to silicon atoms. An explanatory figure is showed in ***chapter 4***.

In our simulations, the total number of -O-X bonds for each species, with X equal Si or Al, were calculated as the bond number average at each picosecond during the production time (last 50 ps of the simulation). An atom was considered to be chemically linked to another when the latter was located within a sphere from of radius r_c centred in it. The cut-off radii were 2.3 Å for the Si-O distance, 2.6 Å for the Ca-O distance, and 2.5 Å for the Al-O distance. Below, the obtained Q^n of silicon and aluminium for all the studied ratios are showed.

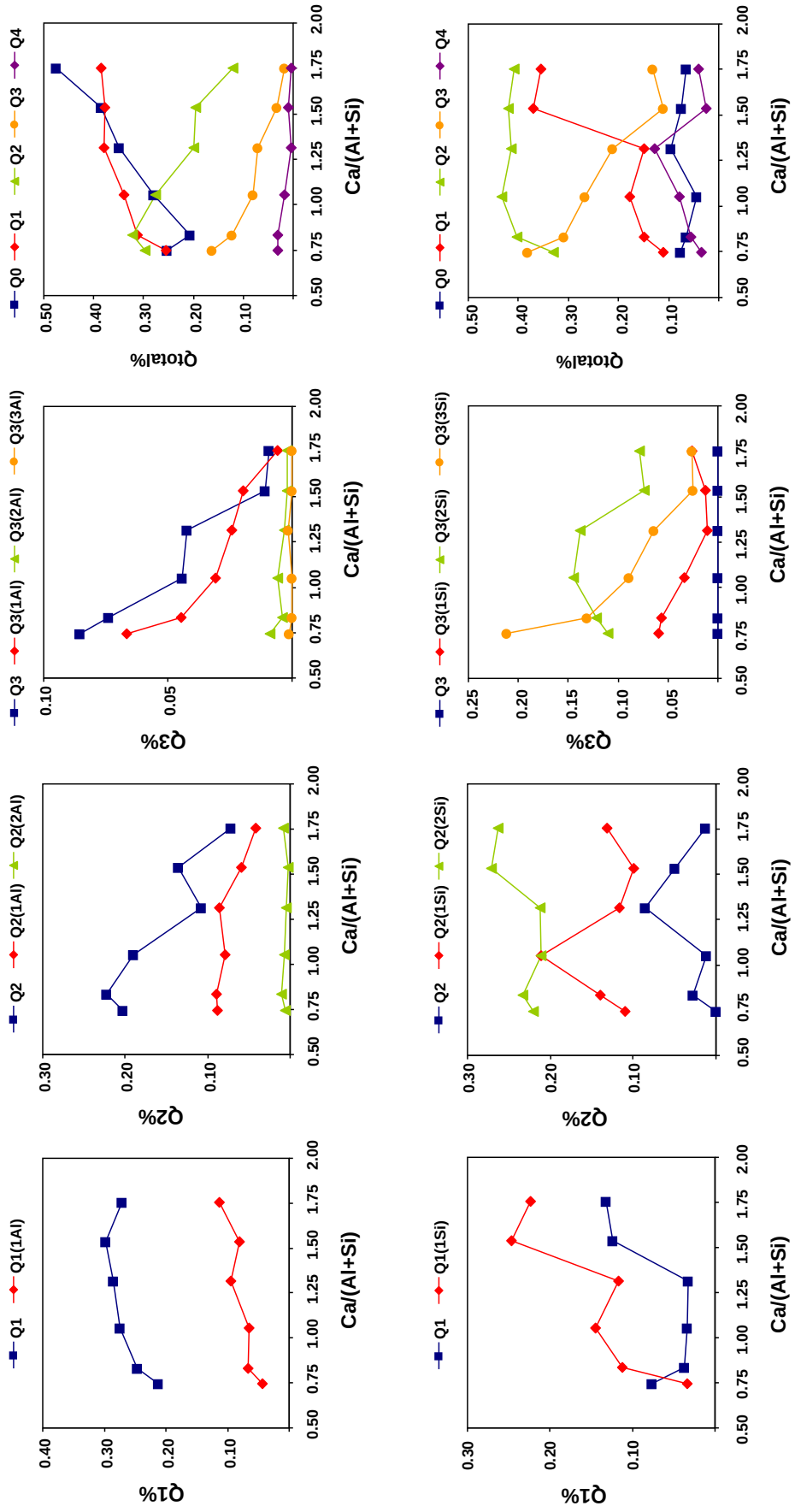

Figure 4.- Fraction of Q^n sites as a function of ther Ca/(Al+Si) ratio with the Al/(Al+Si) ratio fixed at 0.125

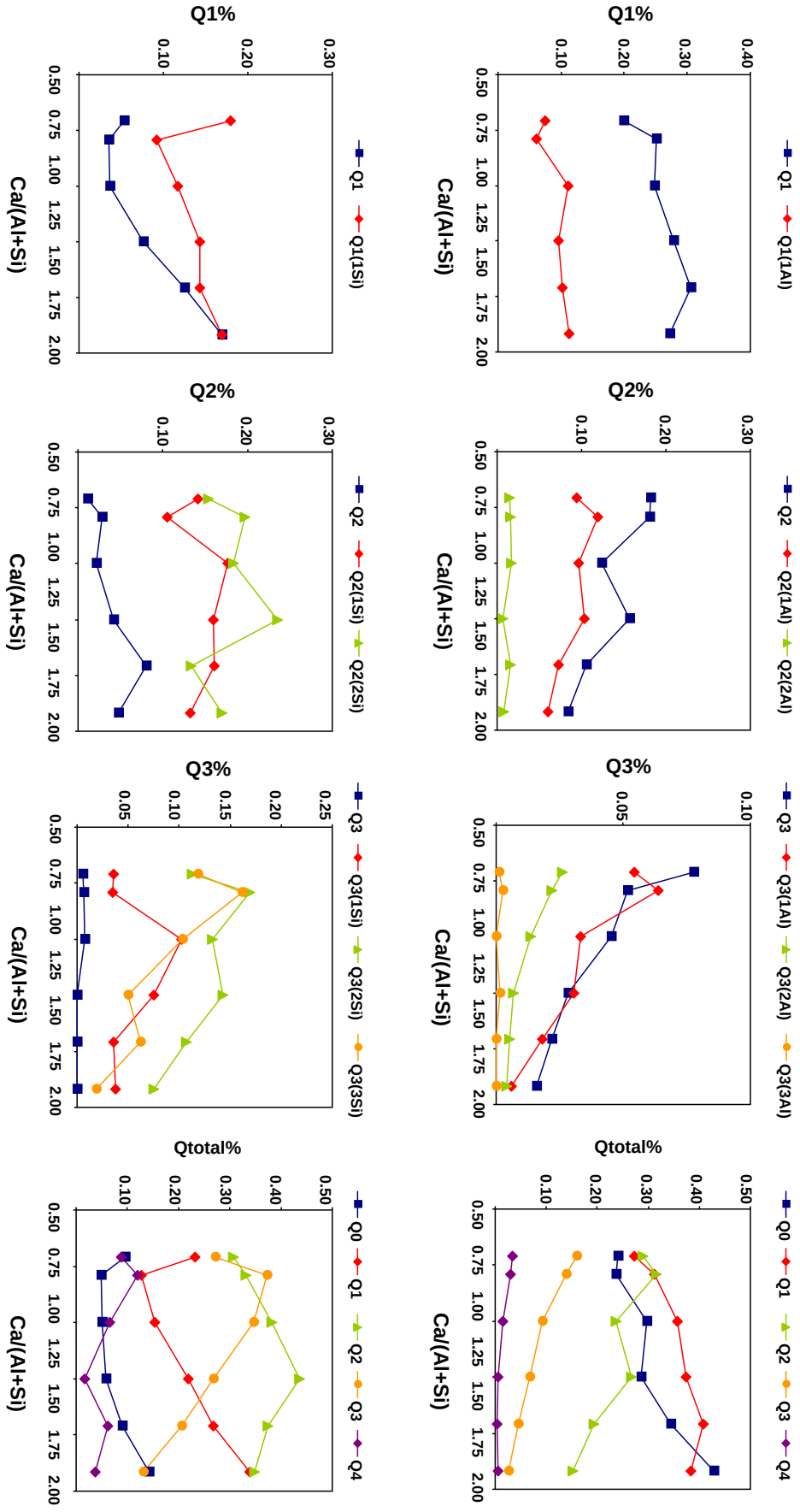

Figure 5.- Fraction of Q^n sites as a function of ther Ca/(Al+Si) ratio with the Al/(Al+Si) ratio fixed at 0.167

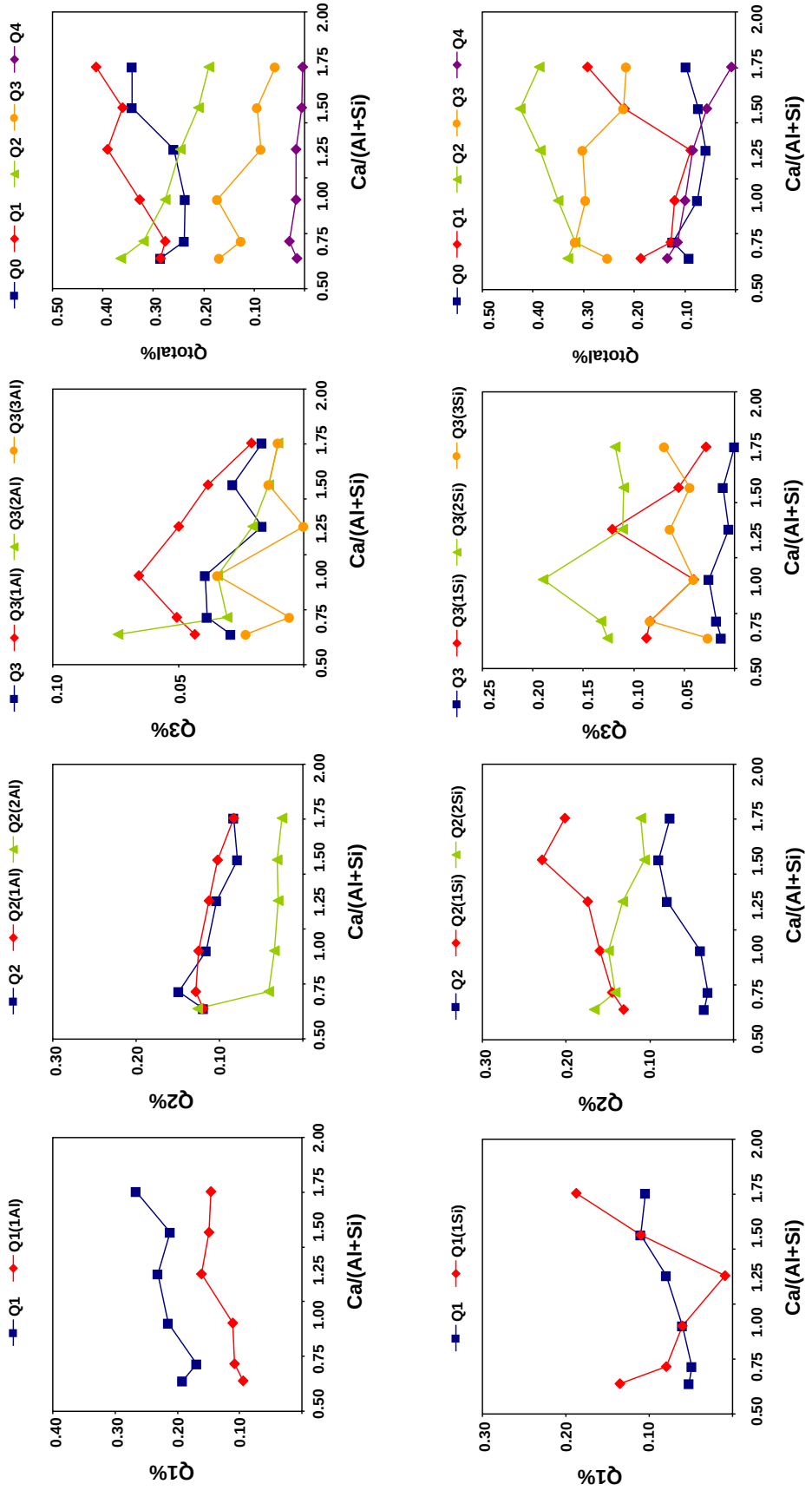

Figure 6.- Fraction of Q^n sites as a function of ther Ca/(Al+Si) ratio with the Al/(Al+Si) ratio fixed at 0.250

Appendix 5.

Elastic Properties Calculations

The most interesting mechanical properties of cement based materials are usually the short-term deformations, controlled by the elastic properties, the long-term deformations, dependent of the viscoelastic properties, and the fracture, which is function of the strength. At early ages the viscoelastic component of the cement paste is important, but at late hydration times the material is well described considering it as elastic [106]. Many micromechanical models deal with the calculation of the elastic properties for the cement paste [87, 104, 229, 278-281]. For this purpose, usually the elastic properties of each individual phase are needed.

The elastic properties describe how a material responds to small reversible deformations. The linear relationship between the stress tensor components σ_i and the strain tensor components ε_j can be written following the tensorial form of Hooke's law:

$$\sigma_i = \sum_{j=1}^{6} C_{ij}\varepsilon_j \qquad (7.5.1)$$

where C_{ij} are the elastic tensor coefficients. If the contracted notation is employed [231], equation (7.5.1) can be written as:

$$\begin{pmatrix}\sigma_1\\ \sigma_2\\ \sigma_3\\ \sigma_4\\ \sigma_5\\ \sigma_6\end{pmatrix}=\begin{pmatrix}C_{11} & C_{12} & C_{13} & C_{14} & C_{15} & C_{16}\\ & C_{22} & C_{23} & C_{24} & C_{25} & C_{26}\\ & & C_{33} & C_{34} & C_{35} & C_{36}\\ & & & C_{44} & C_{45} & C_{46}\\ & & & & C_{55} & C_{56}\\ & & & & & C_{66}\end{pmatrix}\begin{pmatrix}\varepsilon_1\\ \varepsilon_2\\ \varepsilon_3\\ \varepsilon_4\\ \varepsilon_5\\ \varepsilon_6\end{pmatrix} \quad (7.5.2)$$

where the terms under the matrix diagonal are equal to those up by symmetry. A material has, therefore, 21 independent elastic constants, that can be further reduced by crystalline symmetry [273]. The unit cell of the crystal can be deformed in such a way that there is only one strain component different from zero [282]. In that case, the relationship between the applied strain ε_j and the generated stress σ_i depends only on one elastic tensor coefficient C_{ij}:

$$\sigma_i = C_{ij}\varepsilon_j \quad (7.5.3)$$

In ***chapter 6*** the elastic tensor coefficients of tricalcium aluminate were calculated following this procedure. Different degrees of strain were applied, in steps of ±1%, from –3% (contraction) to +3% (expansion) by modifying the lattice parameter of the crystals. The SIESTA code calculates the corresponding stress components from energy derivatives with respect to the strain [231]:

$$\sigma_i = \frac{\partial^2 U}{\partial \varepsilon_i} \quad (7.5.4)$$

Finally, the correspondent coefficient C_{ij} was calculated from the linear fit of the computed obtained data. This procedure was followed in reference [283] to calculate the elastic constants of more than 40 ceramic materials. In ***chapter 5***, the GULP code was used to calculate the elastic properties of the main phases present in the cement paste, as well as 21 hydrated calcium silicate crystals. The only difference with the previous procedure is that GULP calculates directly the elastic tensor from the energy derivatives [239]. Thus, there is no need to make any data fit.

The bulk (*K*) and shear (*G*) moduli can be obtained from the elastic tensor coefficients. Unfortunately, there is not a unique definition to calculate them. The *K* and *G* in the Reuss definition are [227]:

$$K_{Reuss} = \left[S_{11} + S_{22} + S_{33} + 2\left(S_{12} + S_{13} + S_{23} \right) \right]^{-1} \tag{7.5.5}$$

$$G_{Reuss} = \frac{15}{4}\left[\left(S_{11} + S_{22} + S_{33} - S_{12} - S_{13} - S_{23} \right) + 3\left(S_{44} + S_{55} + S_{66} \right) \right]^{-1} \tag{7.5.6}$$

where the S_{ij} denotes the correspondent coefficient of the compliance matrix (the inverse of the elastic tensor). In the Voigt definition, *K* and *G* are [228]:

$$K_{Voigt} = \frac{1}{9}\left[C_{11} + C_{22} + C_{33} + 2\left(C_{12} + C_{13} + C_{23} \right) \right] \tag{7.5.7}$$

$$G_{Voigt} = \frac{1}{15}\left[C_{11} + C_{22} + C_{33} + 3\left(C_{44} + C_{55} + C_{66} \right) - C_{12} - C_{13} - C_{23} \right] \tag{7.5.8}$$

The Reuss and Voight definitions are considered the upper and lower bounds of the bulk (*K*) and shear (*G*) moduli. The average between both values is known as the Hill average [230]. In this Thesis, the Hill definition is shown unless otherwise specified.

$$K_{Hill} = \frac{K_{Voight} + K_{Reuss}}{2} \tag{7.5.9}$$

$$G_{Hill} = \frac{G_{Voight} + G_{Reuss}}{2} \tag{7.5.10}$$

Once the bulk and shear moduli of the material are determined, the Young modulus (*E*) and Poisson's ratio (*v*) can be calculated assuming an isotropous media:

$$E = \frac{9G}{3+G/K} \tag{7.5.11}$$

$$v = \frac{3-2G/K}{6+2G/K} \tag{7.5.12}$$

Finally, for a better comparison with the experimental nanoinoindetation results, the indentation modulus (*M*) of C-S-H gels was calculated [254]:

$$M = \frac{E}{\left(1-v^2\right)} \tag{7.5.13}$$

In ***chapter 5***, two homogenization procedures were applied to rescale the properties of crystalline phases to those of the C-S-H gel [256, 257]. The gel was pictured as a composite made of a solid phase (the tobermorite-like and jennite-like structures with finite chain lengths) with air void inclusions. The self-consistent or polycrystalline model calculates the elastic properties of the material as the average elastic properties of spherical particles intermixed with some porosity [259].

$$\frac{G_{C\text{-}S\text{-}H\ gel}}{G_0} = \frac{1}{2} - \frac{5}{4}(1-\eta) - \frac{3}{16} r_0(2+\eta) + \frac{1}{16}\sqrt{144(1-r_0-480\eta+400\eta^2+408r_0\eta-120r_0\eta^2+9r_0^2\left(2+\eta\right)^2} \tag{7.5.14}$$

$$\frac{K_{C\text{-}S\text{-}H\ gel}}{K_0} = \frac{\frac{4\eta G}{G_0}}{\frac{4G}{Go+3(1-\eta)r_0}} \tag{7.5.15}$$

where η is the packing factor, K_o and G_o the bulk and shear modulus of the crystalline species, and r_o is a parameter defined as the ratio K_o/G_o. On the other hand, the Mori-Tanaka (MT) schemes models the elasticity of a solid matrix with pore inclusions [260]. In the MT approach the bulk and shear modulus are written as:

$$\frac{K_{C\text{-}S\text{-}H\ gel}}{K_0} = \eta \frac{1-\alpha}{1-\alpha\eta} \tag{7.5.16}$$

$$\frac{G_{C\text{-}S\text{-}H\ gel}}{G_0} = \eta \frac{1-\beta}{1-\beta\eta} \tag{7.5.17}$$

where η is again the packing factor, α and β are two parameters dependent on the bulk and shear modulus of the crystalline species (K_o and G_o) given as:

$$\alpha = \frac{3K_0}{(3K_0 + 4G_0)} \tag{7.5.18}$$

$$\beta = \frac{(6K_0 + 12G_0)}{(15K_0 + 20G_0)} \tag{7.5.19}$$

Appendix 6.

Lattice Parameters and Elastic Properties from Force Field Calculations

The presented results in ***chapter 5*** involve the calculation of the lattice parameters and elastic properties of many crystalline phases. Not all the computed parameters were essential in the discussion, and they were only briefly discussed to asses the quality of the results. Furthermore, in some cases big tables are needed to present them. Thus, most of the calculated lattice parameters and elastic properties are included in this appendix.

These values were calculated by force field methods, using the parameters and functional forms described in ***appendix 4***. The calculations were carried out by means of the GULP code [151, 239].

Table 1.- Computed lattice parameters of the clinker phases. The experimental values are also given, together with the error percent between them.

	C_3S			β-C2S		
	Exp [16]	Comp	%error	Exp [252]	Comp	%error
a (Å)	33.08	33.45	+ 1.13	5.50	5.51	+ 0.16
b (Å)	7.02	7.12	+ 1.39	6.76	6.92	+ 2.44
c (Å)	18.50	18.91	+ 2.24	9.32	9.94	+ 6.58
α (º)	90	90	0.0	90	90	0.0
β (º)	94.1	94.9	+ 0.81	94.1	94.0	- 0.17
γ (º)	90	90	0.0	90	90	0.0
	C3A			C4AF		
	Exp [24]	Comp	%error	Exp [253]	Comp	%error
a (Å)	15.26	15.43	+ 0.17	5.58	5.59	+ 0.18
b (Å)	15.26	15.43	+ 0.17	14.60	14.51	- 0.6
c (Å)	15.26	15.43	+ 0.17	5.37	5.43	+ 1.10
α (º)	90	90	0	90	90	0
β (º)	90	90	0	90	90	0
γ (º)	90	90	0	90	90	0

Table 2.- Computed lattice parameter for the studied hydrated calcium silicates. Below the lattice parameter, the error percent with respect to the experimental data are given. The unit cell sides *a*, *b*, and *c* are given in Å, and the angles *α*, *β*, and *γ* in degrees. The reference corresponds therefore to the work that presents a solved crystalline structure, used as starting point for the simulations. *Continues in the next page*

Name	*a*	*b*	*c*	*α*	*β*	*γ*	Ref.
Wollastonite group							
Foshagite	10.47 (1.5)	7.38 (0.3)	7.19 (2.3)	90.2 (0.3)	104.9 (-1.4)	89.8 (-0.2)	[284]
Hillebrandite	7.49 (2.9)	16.22 (-0.6)	11.67 (-1.3)	89.8 (-0.2)	89.9 (-0.1)	89.8 (-0.2)	[285]
Nekoite	7.61 (0.3)	9.75 (-0.5)	7.42 (1.0)	111.3 (-0.5)	103.4 (-0.1)	87.1 (0.7)	[286]
Okenite	9.91 (2.3)	7.35 (1.0)	21.81 (-0.9)	93.51 (0.9)	99.54 (-0.6)	111.08 (0.17)	[218]
Wollastonite	8.03 (1.4)	7.12 (0.9)	7.43 (1.7)	89.5 (-0.5)	103.9 (0.4)	86.3 (1.7)	[287]
Xonotlite	17.18 (3.9)	7.40 (1.0)	7.24 (2.8)	90 (0.0)	88.4 (-1.7)	90 (0.0)	[288]
Tobermorite group and jennite							
Clinotobermorite	11.52 (2.2)	7.33 (-0.1)	11.83 (3.1)	99.1 (-0.1)	100.9 (3.9)	89.9 (-0.2)	[66]
Tobermorite 9Å	6.76 (1.5)	6.74 (1.2)	9.91 (3.5)	96.7 (3.1)	93.5 (-5.2)	114.1 (0.5)	[65]
Tobermorite 11Å	6.81 (1.1)	7.43 (0.6)	23.17 (3.0)	89.78 (-0.2)	88.52 (-1.6)	123.08 (-0.1)	[66]
Tobermorite 14Å	6.76 (0.3)	7.31 (-1.5)	29.14 (4.1)	90 (0.0)	90.3 (0.4)	122.9 (-0.3)	[64]
Jennite	10.63 (0.5)	7.35 (1.1)	11.14 (1.9)	102.6 (1.3)	93.9 (-3.2)	110.1 (0.5)	[68]
γ-C_2S group							
Calcium-chondrodite	8.99 (0.9)	11.75 (2.6)	4.98 (-1.8)	90 (0.0)	90 (0.0)	110.1 (1.6)	[289]

Kilchoanite	12.92 (2.4)	12.92 (2.4)	12.92 (2.4)	126.2 (0.0)	156.8 (0.1)	59.3 (-0.1)	[290]
Other C-S-H crystals							
Afwillite	16.81 (3.2)	5.56 (-1.3)	13.80 (4.1)	90 (0.0)	134.5 (-0.2)	90 (0.0)	[291]
α-C_2SH	9.69 (2.1)	9.38 (2.2)	10.68 (0.2)	90 (0.0)	90 (0.0)	90 (0.0)	[292]
Dellaite	6.90 (0.8)	7.03 (1.2)	13.24 (1.9)	89.2 (-1.7)	96.2 (-1.1)	99.2 (1.0)	[293]
Jaffeite	9.98 (-0.5)	9.98 (-0.5)	7.57 (1.0)	90 (0.0)	90 (0.0)	120 (0.0)	[294]
Killalaite	7.07 (3.9)	15.72 (1.7)	6.87 (0.8)	90 (0.0)	98.1 (0.4)	90 (0.0)	[295]
Poldervaartite	9.69 (3.0)	9.38 (2.6)	10.68 (1.4)	90 (0.0)	90 (0.0)	90 (0.0)	[296]
Rosenhahnite	7.00 (0.8)	9.52 (0.4)	7.01 (3.0)	108.8 (0.1)	97.8 (3.2)	95.4 (-0.5)	[297]
Suolinitie	20.20	6.09	12.12	90.2	90.0	90.9	[298]

Table 3.- Computed elastic properties for the studied hydrated calcium silicates. The bulk (*K*), shear (*G*), and Young (*E*) moduli are given in GPa. The Poisson's ratio is dimensionless. *Continues in the next page*

Name	Formula	*K*	*G*	*E*	*v*
Wollastonite group					
Foshagite	$Ca_4(Si_3O_9)(OH)_2$	73.70	40.00	101.62	0.27
Hillebrandite	$Ca_2(SiO_3)(OH)_2$	59.99	27.19	70.86	0.30
Nekoite	$Ca_3Si_6O_{15}\cdot 7H_2O$	58.90	29.60	76.06	0.28
Okenite	$[Ca_8(Si_6O_{16})(Si_6O_{15})]^{-4}$ $[Ca_2(H_2O)_9\cdot 3H_2O]^{+4}$	48.31	22.85	59.21	0.30

Wollastonite	$Ca_3Si_3O_9$	84.06	41.59	107.10	0.29
Xonotlite	$Ca_6Si_6O_{17}(OH)_2$	72.20	42.20	105.96	0.26
Tobermorite group and jennite					
Clinotobermorite	$Ca_5Si_6O_{17} \cdot 15H_2O$	81.00	35.00	91.78	0.31
Tobermorite 9Å	$Ca_5Si_6O_{16}(OH)_2$	68.95	37.44	95.11	0.27
Tobermorite 11Å	$Ca_4Si_6O_{15}(OH)_2 \cdot 5H_2O$	73.57	29.19	77.34	0.32
Tobermorite 14Å	$Ca_5Si_6O_{16}(OH)_2 \cdot 7H_2O$	44.80	19.00	49.94	0.31
Jennite	$Ca_9Si_6O_{18}(OH)_6 \cdot 8H_2O$	40.20	22.10	56.03	0.27
γ-C_2S group					
Calcium-chondrodite	$Ca_5(SiO_4)_2(OH)_2$	88.00	46.00	117.52	0.28
Kilchoanite	$Ca_6(SiO_4)(Si_3O_{10})$	86.98	45.18	115.54	0.28
Other C-S-H crystals					
Afwillite	$Ca_3(SiO_3OH)_2 \cdot 2H_2O$	61.00	25.00	65.99	0.32
α-C_2SH	$Ca_6(SiO_4)(OH)$	67.00	31.00	80.57	0.30
Dellaite	$Ca_6(Si_2O_7)(SiO_4)(OH)_2$	94.15	46.02	118.72	0.29
Jaffeite	$Ca_6(Si_2O_7)(OH)_6$	68.76	39.08	98.57	0.26
Killalaite	$Ca_7(Si_2O_7)_2(OH)_2$	90.00	48.60	123.56	0.27
Poldervaartite	$Ca_2(HSiO_4)(OH)$	67.00	31.00	80.57	0.30
Rosenhahnite	$Ca_3Si_3O_8(OH)_2$	65.00	35.00	89.02	0.27
Suolinitie	$CaSiO_{2.5}(OH)_{0.5} \cdot H_2O$	52.00	25.00	64.64	0.29

Table 4.- Computed lattice parameters of the main hydration product (except the C-S-H gel). The unit cell sides *a*, *b*, and *c* are given in Å, and the angles *α*, *β*, and *γ* in degrees. The experimental values are also given, together with the error percent between them.

	Portlandite			Ettringite		
	Exp [95]	Comp	%error	Exp [100]	Comp	%error
a (Å)	3.5925	3.5506	- 1.17	11.167	11.303	+ 1.22
b (Å)	3.5925	3.5506	- 1.17	11.167	11.327	+ 1.41
c (Å)	4.905	4.940	+ 0.49	21.354	24.211	+ 13.38
α (º)	90	90	0.0	90	84.7	- 5.88
β (º)	90	90	0.0	90	84.3	- 6.33
γ (º)	120	120	0.0	120	121.8	+ 1.5
	Hydrogarnet			Monosulphoaluminate		
	Exp [261]	Comp	%error	Exp [101]	Comp	%error
a (Å)	12.565	12.995	+ 3.43	5.758	5.856	- 1.69
b (Å)	12.565	12.995	+ 3.43	11.50	12.02	+ 4.57
c (Å)	12.565	12.995	+ 3.43	26.794	23.856	- 10.97
α (º)	90	90	0.0	90	88.95	- 1.17
β (º)	90	90	0.0	90	90.82	0.91
γ (º)	90	90	0.0	120	11.32	-0.57

Portlandite

Exp [225]

$$\begin{pmatrix} 99.3 & 36.2 & 29.7 & \approx 0 & 0 & 0 \\ & 99.3 & 29.7 & \approx 0 & 0 & 0 \\ & & 36.3 & 0 & 0 & 0 \\ & & & 9.9 & 0 & 0 \\ & & & & 9.9 & \approx 0 \\ & & & & & 31.6 \end{pmatrix}$$

This work

$$\begin{pmatrix} 108.7 & 35.5 & 4.5 & 2.0 & 0 & 0 \\ & 108.7 & 4.5 & -2.9 & 0 & 0 \\ & & 32.1 & 0 & 0 & 0 \\ & & & 2.2 & 0 & 0 \\ & & & & 2.2 & 2.0 \\ & & & & & 36.6 \end{pmatrix}$$

Ettringite

Exp [236]

$$\begin{pmatrix} 35.1 & 21.9 & 20.0 & 0.6 & 0 & 0 \\ & 35.1 & 20.0 & 0 & 0 & 0 \\ & & 55.0 & 0 & 0 & 0 \\ & & & 11.0 & 0 & 0 \\ & & & & 11.0 & 0 \\ & & & & & 6.6 \end{pmatrix}$$

This work

$$\begin{pmatrix} 37.7 & 19.8 & 28.9 & -3.7 & 0 & 0 \\ & 34.2 & 29.4 & -18.1 & 4.6 & 5.4 \\ & & 46.9 & 8.6 & -14.4 & 5.4 \\ & & & 3.1 & 1.5 & 5.4 \\ & & & & 7.4 & -10.9 \\ & & & & & 16.9 \end{pmatrix}$$

Foshagite

Exp [255]

$$\begin{pmatrix} 114.3 & 59.0 & 40.7 & 0 & 1.9 & 0 \\ & 190.0 & 43.6 & 0 & -7.1 & 0 \\ & & 123.3 & 0 & -19.3 & 0 \\ & & & 39.1 & 0 & 2.0 \\ & & & & 31.4 & 0 \\ & & & & & 56.9 \end{pmatrix}$$

This work

$$\begin{pmatrix} 126.3 & 59.0 & 37.0 & 0 & 4.4 & 0 \\ & 184.0 & 45.6 & -1.6 & -3.3 & 0 \\ & & 100.1 & -3.0 & -4.4 & 0 \\ & & & 33.6 & 0 & -2.7 \\ & & & & 34.6 & -1.3 \\ & & & & & 48.0 \end{pmatrix}$$

Figure 1.- Experimental and computed elastic tensors of the some phases under study. No data was found in the literature for other crystals.

Appendix 7.

Structural Parameters of Tricalcium Aluminate

Two structural features distinguish tricalcium aluminate: the six membered Al-O rings and the Ca-O coordination polyhedra. In ***chapter 6***, the bond distances and angles of these features were calculated. However, in the discussion, only average values and errors were presented. In this appendix, all the Al/Ca-O distances, as well as O-Al/Ca-O angles are given in detail, comparing them with the experimental data. These values were calculated by *ab-initio* methods by means of the SIESTA code [201].

Table 1.- Distances and angles of the $Al_6O_{18}^{-18}$ rings. The bond lengths are given in Å and the angles in degrees. The atom labels follow those of ***figure 6.2.1*** of ***chapter 6***.The experimental values are from reference [24]

		Bond distances (Å)			angles (º)	
		This work	Exp		This work	Exp
Al1	O1	1.778	1.741	O1 Al1 O2	111.68	109.97
	O2	1.788	1.768	O6 Al1 O5	122.08	122.11
	O5	1.783	1.766	O2 Al1 O6	106.45	105.83
	O6	1.755	1.729	O2 Al1 O5	102.26	103.85
				O6 Al1 O1	111.84	111.62
				O5 Al1 O1	102.17	102.96
Al2	O1	1.786	1.741	O1 Al2 O2	115.66	113.58
	O2	1.782	1.764	O3 Al2 O4	124.57	124.01
	O3	1.757	1.748	O1 Al2 O3	108.12	108.86
	O4	1.785	1.757	O1 Al2 O4	99.91	100.61
				O3 Al2 O2	108.44	107.36
				O4 Al2 O2	100.40	102.46
				Al1 O2 Al2	152.54	-
				Al2 O1 Al1	139.39	-

Table 2.- Structural parameters of the Ca coordination polyhedra. The bond lengths are given in Å and the angles, in degrees. The atom labels follow those of ***figure 6.2.2*** of ***chapter 6***. The experimental values are those of reference [24]. *Continues in the next pages*

		Bonds distances (Å)			angles (º)	
		This work	Exp		This work	Exp
Ca1	O6	2.391	2.338	O6 Ca2 O6	103.21	102.23
				O6 Ca2 O6	76.78	77.77
Ca2	O6	2.468	2.391	O5 Ca2 O5	103.81	99.01
				O5 Ca2 O5	76.23	80.99
Ca3	O3	2.322	2.351	O3 Ca2 O3	104.298	103.42
	O4	2.394	2.357	O3 Ca2 O4	92.35	93.60
				O3 Ca2 O4	161.95	162.50
				O4 Ca2 O4	84.24	86.49
				O3 Ca2 O4	77.21	76.05
Ca4	O1	2.511	2.525	O1 Ca4 O1	114.38	118.23
	O4	2.455	2.543	O1 Ca4 O4	90.94	84.92
	O5	3.324	3.012	O1 Ca4 O4	66.78	64.27
				O1 Ca4 O4	148.36	142.59
				O1 Ca4 O5	54.57	58.48
				O1 Ca4 O5	64.87	69.36
				O1 Ca4 O5	118.09	126.02
				O4 Ca4 O4	81.68	79.43
				O4 Ca4 O5	91.66	90.81
				O4 Ca4 O5	155.51	154.17
				O4 Ca4 O5	120.84	122.53
				O5 Ca4 O5	71.51	74.27

Ca5	O1	2.478	2.471	O1 Ca5 O2	175.95	174.52
	O2	2.444	2.401	O1 Ca5 O2	61.63	63.16
	O2	3.166	2.958	O1 Ca5 O3	104.86	106.33
	O3	2.437	2.429	O1 Ca5 O3	61.61	62.22
	O3	3.043	2.969	O1 Ca5 O4	120.32	120.10
	O4	2.886	2.947	O1 Ca5 O5	107.76	110.49
	O5	2.385	2.569	O1 Ca5 O5	84.87	84.49
	O5	2.266	2.258	O2 Ca5 O2	120.31	120.26
				O2 Ca5 O3	79.01	79.14
				O2 Ca5 O3	120.56	119.33
				O2 Ca5 O4	61.22	60.76
				O2 Ca5 O5	70.31	67.97
				O2 Ca5 O5	91.29	90.05
				O2 Ca5 O3	59.99	62.46
				O2 Ca5 O3	96.91	102.30
				O2 Ca5 O4	135.66	138.60
				O2 Ca5 O5	73.23	72.87
				O2 Ca5 O5	127.91	125.11
				O3 Ca5 O3	83.19	85.68
				O3 Ca5 O4	78.97	78.70
				O3 Ca5 O5	96.36	96.59
				O3 Ca5 O5	170.15	169.31
				O3 Ca5 O4	59.84	58.71
				O3 Ca5 O5	168.58	172.69
				O3 Ca5 O5	100.51	99.19
				O4 Ca5 O5	131.36	128.52
				O4 Ca5 O5	94.91	95.48
				O5 Ca5 O5	81.82	79.79

Ca6	O1	3.300	3.075	O1 Ca6 O2	61.50	62.96
	O2	2.417	2.462	O1 Ca6 O3	117.85	118.54
	O3	2.328	2.320	O1 Ca6 O4	76.53	78.06
	O4	2.267	2.266	O1 Ca6 O6	102.75	104.58
	O6	3.056	2.781	O1 Ca6 O6	137.58	136.92
	O6	2.276	2.294	O1 Ca6 O6	59.28	61.17
	O6	2.403	2.477	O2 Ca6 O3	81.72	80.03
				O2 Ca6 O4	118.07	117.49
				O2 Ca6 O6	61.16	63.94
				O2 Ca6 O6	126.86	133.65
				O2 Ca6 O6	100.27	105.48
				O3 Ca6 O4	80.21	78.44
				O3 Ca6 O6	99.85	99.83
				O3 Ca6 O6	104.51	104.33
				O3 Ca6 O6	174.19	172.40
				O4 Ca6 O6	179.19	177.33
				O4 Ca6 O6	114.96	108.44
				O4 Ca6 O6	94.06	94.26
				O6 Ca6 O6	65.81	69.92
				O6 Ca6 O6	85.86	87.40
				O6 Ca6 O6	78.75	75.83

List of Publications

- ***Refereed Journals***

H. Manzano, J. S. Dolado, and A. Ayuela, *Elastic properties of the main species present in Portland cement pastes*, Acta Materialia, 57(4), 2009

H. Manzano, J. S. Dolado, and A. Ayuela, *Aluminium incorporation to dreierketten silicate chains*, The Journal of Physical Chemistry B, 113(9), 2009

H. Manzano, J. S. Dolado, and A. Ayuela, *Structural, Mechanical and Reactivity Properties of Tricalcium Aluminate Using First-principles calculations*, Journal of the American Ceramic Society, 92(4), 2009

H. Manzano, J. Hamaekers, M. Griebel, and J. S. Dolado, *A molecular dynamics study of the aluminosilicate chains structure in Al-rich calcium silicate hydrated (C-S-H) gel*, Physica Status Solidi (a): Applications and Material Science, 205(6), 2008.

H. Manzano, J. S. Dolado, and A. Ayuela, *On the formation of cementitious C-S-H gel*, Journal of Computer-aided Materials Design, 14(1), 2007

H. Manzano, J. S. Dolado, A. Ayuela, and A. Guerrero, *Mechanical properties of crystalline calcium-silicate-hydrates: comparison with cementitious C-S-H gels*, Physica Status Solidi (a): Applications and Material Science, 204(6), 2007

H. Manzano, J. S. Dolado, A. Ayuela, and A. Porro, *La nanoestructura del cemento explorada mediante simulación computacional*, Dyna 82(3), 2007

J. J. Gaitero, H. Manzano, J. S. Dolado, and I. Campillo, *Multi-scale approach to the study of cement pastes: calcium leaching, a case of study*, International Journal of Materials and Products Technology, Submitted.

- ***Other publications***

H. Manzano, J. J. Gaitero, J. S. Dolado, and I. Campillo, *Silicate structures in C-S-H gels with low calcium content: results from simulations and experiments*, Proceedings of the 9th Cement and Concrete Symposium, Leeds (England), September 2009

H. Manzano, J. S. Dolado, and A. Ayuela, *Prediction of the mechanical properties of the mayor constituent phases of cementitious systems by atomistic simulation* Proceedings of the International Rilem Symposium on Concrete Modelling - CONMOD 08, Delft (The Netherlands), May 2008

J. S. Dolado, H. Manzano, A. Porro, A. Ayuela, J. Hamaekers, and M. Griebel, *On the formation of C-S-H nanoparticles: A bottom up approach* Proceedings of the 12th International Congress in Cement Chemistry, Montreal (Canada), June 2007

References

1. Lea, F.M. and P.C. Hewlett, *Lea's chemistry of cement and concrete*. 4th ed. 1998, Oxford: Elsevier Butterworth-Heinemann. 1053.
2. U.S. Geological Survey, M.R.P. *http://minerals.usgs.gov/minerals/pubs/commodity/cement/*. 2009.
3. Mahasenan, N., S. Smith, and K. Humphreys. *The Cement Industry and Global Climate Change: Current and Potential Future Cement Industry CO2 Emissions*. in *Greenhouse gas control technologies : proceedings of the 6th International Conference on Greenhouse Gas Control Technologies, 1-4 October 2002, Kyoto, Japan*. 2003. Amsterdam ; Boston: Pergamon.
4. Taylor, H.F., *Cement Chemistry*. 2 ed. 1997, London: Thomas Telford Publishing.
5. Taylor, H.F.W., *Proposed structure for calcium silicate hydrate gel.* Journal of the American Ceramic Society, 1986. **69**(6): p. 464-467.
6. Richardson, I.G. and G.W. Groves, *Models for the composition and structure of calcium silicate hydrate (C-S-H) gel in hardened tricalcium silicate pastes.* Cement and Concrete Research, 1992. **22**(6): p. 1001-1010.
7. Richardson, I.G. and G.W. Groves, *Microstructure and microanalysis of hardened ordinary portland cement pastes.* Journal of Materials Science, 1993. **28**(1): p. 265-277.
8. Richardson, I.G., *The nature of the hydration products in hardened cement pastes.* Cement & Concrete Composites, 2000. **22**(2): p. 97-113.
9. Richardson, I.G., *Tobermorite/jennite- and tobermorite/calcium hydroxide-based models for the structure of C-S-H: applicability to hardened pastes of tricalcium silicate, beta-dicalcium silicate, Portland cement, and blends of Portland cement with blast-fumace slag, metakaolin, or silica fume.* Cement and Concrete Research, 2004. **34**(9): p. 1733-1777.
10. Jennings, H.M., et al., *Characterization and modeling of pores and surfaces in cement paste: Correlations to processing and properties.* Journal of Advanced Concrete Technology, 2008. **6**(1): p. 5-29.

11. Chromy, S. and I. Maki, *Determination of the quantitative phase composition of alite and belite in portlnad cement clinker by micro photometry*. Cement and Concrete Research, 1982. **12**(4): p. 511-516.
12. Maki, I. and S. Chromy, *Microscopic study of polymorphism of Ca_3SiO_5*. Cement and Concrete Research, 1978. **8**(4): p. 407-414.
13. Maki, I. *Relationship of processing parameters to clinker properties; influence of minor components.* in *8th International Congress on the Chemistry of Cement*. 1986. Rio de Janeiro.
14. Moranville-Regourd, M. and A.I. Boikova. *Chemistry, structure, properties and quality of clinker*. in *9th International Congress on the Chemistry of Cement*. 1992. New Delhi.
15. Uchikawa, H., S. Hanekara, and T. Shirasaka. *Relationship between zonal structure in alite, lamellar texture in belite and their production process, composition and crystal structure*. in *9th International Congress on the Chemistry of Cement*. 1992. New Delhi.
16. De La Torre, A.G., et al., *The superstructure of C3S from synchrotron and neutron powder diffraction and its role in quantitative phase analyses.* Cement and Concrete Research, 2002. **32**(9): p. 1347-1356.
17. Nishi, F., Y. Takeuchi, and I. Maki, *Tricalcium silicate $Ca_3O(SiO_4)$: the monoclinic superestructure.* Zeitschrift Fur Kristallographie, 1985. **172**(3-4): p. 297-314.
18. Nishi, F. and Y. Takeuchi, *The rhombohedral structure of tricalcium silicate at 1200ºC.* Zeitschrift Fur Kristallographie, 1984. **168**(1-4): p. 197-212.
19. Jeffery, J.W., *The crystal structure of tricalcium silicate.* Acta Crystallographica, 1952. **5**(1): p. 26-&.
20. Barbier, J. and B.G. Hyde, *The structure of the polymorphs of dicalcium silicate, Ca_2SiO_4* Acta Crystallographica Section B-Structural Science, 1985. **41**(DEC): p. 383-390.
21. Feng, X.J., X.M. Min, and C.X. Tao, *Study on the structure and characteristics of dicalcium silicate with quantum chemistry calculations.* Cement and Concrete Research, 1994. **24**(7): p. 1311-1316.
22. Smith, D.K., Majumdar.A, and F. Ordway, *Crystal structure of gamma-dicalcium silicate.* Acta Crystallographica, 1965. **18**: p. 787-&.
23. Jost, K.H., B. Ziemer, and R. Seydel, *Redetermination of structure of beta-dicalcium silicate.* Acta Crystallographica Section B-Structural Science, 1977. **33**(JUN15): p. 1696-1700.
24. Mondal, P. and J.W. Jeffery, *Crystal structure of tricalcium aluminate $Ca_3Al_2O_6$.* Acta Crystallographica Section B-Structural Science, 1975. **B 31**(MAR15): p. 8.
25. Stephan, D. and S. Wistuba, *Crystal structure refinement and hydration behaviour of doped tricalcium aluminate.* Cement and Concrete Research, 2006. **36**(11): p. 2011-2020.

26. Takeuchi, Y., F. Nishi, and I. Maki, *Crystal-chemical characterization of the $3CaO$-Al_2O_3-Na_2O solid solution series.* Zeitschrift Fur Kristallographie, 1980. **152**(3-4): p. 259-307.

27. Lee, F.C., H.M. Banda, and F.P. Glasser, *Substitution of Na, Fe, and Si in tricalcium aluminate and the polymorphism of solid-solutions.* Cement and Concrete Research, 1982. **12**(2): p. 237-246.

28. Aggarwal, S., et al., *Synthesis and properties of dicalcium aluminate.* Cement and Concrete Research, 1972(2): p. 7.

29. Colville, A.A. and S. Geller, *Crystal structures of $Ca_2Fe_{1.43}Al_{0.57}O_5$ and $Ca_2Fe_{1.28}Al_{0.72}O_5$* Acta Crystallographica Section B-Structural Science, 1972. **B 28**: p. 3196-3260.

30. Marinho, M.B. and F.P. Glasser, *Polymorphism and phase changes in the ferrite phase of cements induced by titanium substitution.* Cement and Concrete Research, 1984. **14**(3): p. 360-368.

31. Le Chatelier, H., *Recherches expérimentales sur la constitution des mortiers hydrauliques*. 2nd ed. 1904, Paris: Vve Ch. Dunod.

32. Fujii, K. and W. Kondo, *Kinetics of hydration of tricalcium silicate.* Journal of the American Ceramic Society, 1974. **57**(11): p. 492-497.

33. Thomas, N.L. and D.D. Double, *Calcium and silicon concentrations in solution during the early hydration of portland cement and tricalcium silicate.* Cement and Concrete Research, 1981. **11**(5-6): p. 675-687.

34. Sujata, K. and H.M. Jennings, *Formation of a protective layer during the hydration of cement.* Journal of the American Ceramic Society, 1992. **75**(6): p. 1669-1673.

35. Peterson, V.K., D.A. Neumann, and R.A. Livingston, *Hydration of cement: The application of quasielastic and inelastic neutron scattering.* Physica B-Condensed Matter, 2006. **385**: p. 481-486.

36. Holly, R., et al., *Magnetic resonance in situ study of tricalcium aluminate hydration in the presence of gypsum.* Journal of the American Ceramic Society, 2006. **89**(3): p. 1022-1027.

37. Havlica, J., D. Roztocka, and S. Sahu, *Hydration kinetics of calcium aluminate phases in the presence of various ratios of Ca^{+2} and SO_4^{-2} ions in liquid phase.* Cement and Concrete Research, 1993. **23**(2): p. 294-300.

38. Collepardi, M., et al., *Tricalcium aluminate hydration in presence of lime, gypsum or sodium sulfate.* Cement and Concrete Research, 1978. **8**(5): p. 571-580.

39. Brown, P.W., L.O. Liberman, and G. Frohnsdorff, *Kinetics of the early hydration of tricalcium aluminate in solutions containing calcium-sulfate.* Journal of the American Ceramic Society, 1984. **67**(12): p. 793-795.

40. Minard, H., et al., *Mechanisms and parameters controlling the tricalcium aluminate reactivity in the presence of gypsum.* Cement and Concrete Research, 2007. **37**: p. 1418-1426.

41. Ramachandran, V.S. and J.J. Beaudoin. *Handbook of analytical techniques in concrete science and technology*. 2001; 964].

42. Kondo, R. and S. Ueda. in *5th International Symposium on Cement Chemistry*. 1969. Tokyo (Japan).

43. Brown, P.W., et al., *Analyses of the aqueous phase during early C_3S hydration.* Cement and Concrete Research, 1984. **14**(2): p. 257-262.

44. Jennings, H.M., *Aqueous solubility relationships for 2 types of calcium silicate hydrate.* Journal of the American Ceramic Society, 1986. **69**(8): p. 614-618.

45. Wu, Z.Q. and J.F. Young, *Formation of calcium hydroxide from aqueous suspensions of tricalcium silicate.* Journal of the American Ceramic Society, 1984. **67**(1): p. 48-51.

46. Odler, I. and H. Dorr, *Early hydration of tricalcium silicate. 1. Kinetics of the hydration process and the stoichoimetry of the hydration products.* Cement and Concrete Research, 1979. **9**(2): p. 239-248.

47. Odler, I. and H. Dorr, *Early hydration of tricalcium silicate. 2. Induction period.* Cement and Concrete Research, 1979. **9**(3): p. 277-284.

48. Mehta, P.K. and P. Monteiro, *Concrete : structure, properties, and materials*. 2nd ed. Prentice-Hall international series in civil engineering and engineering mechanics. 1993, Englewood Cliffs, N.J.: Prentice Hall. xxviii, 548 p.

49. Feldman, R.F. and P. Sereda, *A new model for hydrated Portland cement and its practical implications.* Eng J Can, 1970. **53**(8-9): p. 53-59.

50. Jennings, H.M., B.J. Dalgleish, and P.L. Pratt, *Morphological developement of hydrating tricalcium silicate as examined by electron microscopy techniques.* Journal of the American Ceramic Society, 1981. **64**(10): p. 567-572.

51. Goto, S., et al., *Composition and morphology of hydrated tricalcium silicate.* Journal of the American Ceramic Society, 1976. **59**(7-8): p. 281-284.

52. Richardson, I.G., *The nature of C-S-H in hardened cements.* Cement and Concrete Research, 1999. **29**(8): p. 1131-1147.

53. Chatterj. S and J.W. Jeffery, *3-dimensional arrangement of hydration products in set cement paste.* Nature, 1966. **209**(5029): p. 1233-&.

54. Scrivener, K.L. and P.L. Pratt. in *British Ceramic Society Symposium*. 1984. Stoke-on-Trent, Staffs., U.K.: British Ceramic Society.

55. Garboczi, E.J. and D.P. Bentz, *The effect of statistical fluctuation, finite size error, and digital resolution on the phase percolation and transport properties of the NIST cement hydration model.* Cement and Concrete Research, 2001. **31**(10): p. 1501-1514.

56. Daimon, M., et al., *Pore Structure of Calcium Silicate Hydrate in Hydrated Tricalcium Silicate.* Journal of the American Ceramic Society, 1977. **60**(3-4): p. 110-114.

57. Le Chatelier, H. and J.L. Mack, *Experimental researches on the constitution of hydraulic mortars*. 1905, New York,: McGraw Publishing Company. viii, 132 p.

58. Jennings, H.M., et al., *A multi-technique investigation of the nanoporosity of cement paste.* Cement and Concrete Research, 2007. **37**(3): p. 329-336.

59. Rodger, S.A., et al. *Microstructural developement during the Hydration of Cement*. in *Material Research Society Symposium Proceedings*. 1987: Material Research Society.

60. Richardson, I.G. and J.G. Cabrera, *The nature of C-S-H in model slag-cements.* Cement & Concrete Composites, 2000. **22**(4): p. 259-266.

61. Richardson, I.G. and G.W. Groves, *The incorporation of minor and trace elements into calcium silicate hydrate (C-S-H) gel in hardened cement pastes.* Cement and Concrete Research, 1993. **23**(1): p. 131-138.

62. Richardson, I.G., *The calcium silicate hydrates.* Cement and Concrete Research, 2008. **38**: p. 137-158.

63. Long, J.V.P. and J.D.C. McConell, *A mineral application of X-ray absorption microspectroscopy: the hydration of larnite.* Mineralogical Magazine, 1958. **32**: p. 10.

64. Bonaccorsi, E., S. Merlino, and A.R. Kampf, *The crystal structure of tobermorite 14 A (Plombierite), a C-S-H phase.* Journal of the American Ceramic Society, 2005. **88**(3): p. 505-512.

65. Merlino, S., E. Bonaccorsi, and T. Armbruster, *Tobermorites: Their real structure and order-disorder (OD) character.* American Mineralogist, 1999. **84**(10): p. 1613-1621.

66. Merlino, S., E. Bonaccorsi, and T. Armbruster, *The real structure of tobermorite 11 angstrom: normal and anomalous forms, OD character and polytypic modifications.* European Journal of Mineralogy, 2001. **13**(3): p. 577-590.

67. Carpenter, A.B., et al., *Jennite, a new mineral.* American Mineralogist, 1966. **51**: p. 56-74.

68. Bonaccorsi, E., S. Merlino, and H.F.W. Taylor, *The crystal structure of jennite, $Ca_9Si_6O_{18}(OH)_6 \cdot 8H_2O$.* Cement and Concrete Research, 2004. **34**(9): p. 1481-1488.

69. Shpynova, L.G., I.D. Nabitovich, and N.V. Belov, *Microstructure of alite cement stone.* Soviet Physics Crystallography, 1967. **11**(6): p. 4.

70. Grudemo, A., *The crystal structures of cement hydration - A review and a new gel model*, S.C.a.C.R. Institute, Editor. 1986. p. 3-16.

71. Bernal, J.D. *The structure of cement hydration compounds*. in *3rd International Symposium on the Chemistry of Cement*. 1954. London: Cement and Concrete Association, London.

72. Richardson, I.G. and G.W. Groves, *The structure of the calcium silicate hydrate phase present in hardened pastes of white Portland cement/blast-furnace slag blends.* Journal of material science, 1997. **32**: p. 4793-4802.

73. Bernal, J.D., J.W. Jeffery, and H.F.W. Taylor, *Crystallographic research on the hydration of Portland cement. A first report on investigation in progress.*

Magazine of Concrete Research, 1952. **4**(11): p. 5.

74. Fujii, K. and W. Kondo, *Estimation of Thermochemical Data for Calcium Silicate Hydrate (C-S-H).* Communications of the American Ceramic Society, 1983: p. C-220.

75. Kantro, D.L., S. Brunauer, and C.H. Weise, *Developement of surface in the hydration of calcium silicates. II. Extension of investigations to earlier and later stages of hydration.* Journal of Physical Chemistry, 1962. **66**(10): p. 1804-1809.

76. Kurczyk, H.G. and H.E. Schwiete. *Concerning the hydration products of C_3S and β-C_2S.* in *4th International Symposium on the Chemistry of Cement*. 1960. Washington: National Bureau of Standards (now NIST).

77. Taylor, H.F.W. and J.W. Howison, *Relationships between calcium silicates and clay minerals.* Clay Minerals Bulletin, 1956. **3**: p. 98-111.

78. Stade, V.H., *Uber eine aus Poly- und Disilicat bestehende Phase.* Zeitschrift Fur Anorganic Chemistry, 1980. **470**: p. 69-83.

79. Cong, X.D. and R.J. Kirkpatrick, *O-17 MAS NMR investigation of the structure of calcium silicate hydrate gel.* Journal of the American Ceramic Society, 1996. **79**(6): p. 1585-1592.

80. Cong, X.D. and R.J. Kirkpatrick, *^{29}Si MAS NMR study of the structure of calcium silicate hydrate.* Advanced Cement Based Materials, 1996. **3**(3-4): p. 144-156.

81. Chen, J.J., et al., *Solubility and structure of calcium silicate hydrate.* Cement and Concrete Research, 2004. **34**(9): p. 1499-1519.

82. Nonat, A., *The structure and stoichiometry of C-S-H.* Cement and Concrete Research, 2004. **34**(9): p. 1521-1528.

83. Michaelis, W., *The hardening of cement under water* 1909, Chicago : Cement and Engineering News.

84. Tennis, P.D. and H.M. Jennings, *A model for two types of calcium silicate hydrate in the microstructure of Portland cement pastes.* Cement and Concrete Research, 2000. **30**(6): p. 855-863.

85. Jennings, H.M., *A model for the microstructure of calcium silicate hydrate in cement paste.* Cement and Concrete Research, 2000. **30**: p. 101-116.

86. Thomas, J.J., H.M. Jennings, and A.J. Allen, *The surface area of cement paste as measured by neutron scattering: Evidence for two C-S-H morphologies.* Cement and Concrete Research, 1998. **28**(6): p. 897-905.

87. Constantinides, G. and F.J. Ulm, *The effect of two types of C-S-H on the elasticity of cement-based materials: Results from nanoindentation and micromechanical modeling.* Cement and Concrete Research, 2004. **34**(1): p. 67-80.

88. Constantinides, G. and F.J. Ulm, *The nanogranular nature of C-S-H.* Journal of the Mechanics and Physics of Solids, 2007. **55**(1): p. 64-90.

89. Allen, A.J. and J.J. Thomas, *Analysis of C-S-H gel and cement paste by small-*

angle neutron scattering. Cement and Concrete Research, 2007. **37**(3): p. 319-324.

90. Jennings, H.M., *Refinements to colloid model of C-S-H in cement: CM-II.* Cement and Concrete Research, 2008. **38**(3): p. 275-289.

91. Beaudoin, J.J. and R. Alizadeh, *A discussion of the paper "Refinements to colloidal model of C-S-H in cement: CM-II" by Hamlin M. Jennings.* Cement and Concrete Research, 2008. **38**(7): p. 1026-1027.

92. Jennings, H.M., *Reply to the discussion by J.J. Beaudoin and R. Alizeadab of the paper "Refinements to colloid model of C-S-H in cement: CM-II" by H.M. Jennings.* Cement and Concrete Research, 2008. **38**(7): p. 1028-1030.

93. Alizadeh, R., J.J. Beaudoin, and L. Raki, *Dynamic mechanical analysis of calcium silicate hydrates.* Journal of the American Ceramic Society, 2009. **submitted**.

94. Lesko, S., et al., *Investigation by atomic force microscopy of forces at the origin of cement cohesion.* Ultramicroscopy, 2001. **86**(1-2): p. 11-21.

95. Henderson, D.M. and H.S. Gutowsky, *A nuclear magnetic resonance determination of the hydrogen position in $Ca(OH)_2$.* American Mineralogist, 1962. **47**(11-12): p. 1231-1251.

96. Carde, C. and R. Francois, *Modelling the loss of strength and porosity increase due tothe leaching of cement pastes.* Cement & Concrete Composites, 1999. **21**(3): p. 181-188.

97. Gaitero, J.J., I. Campillo, and A. Guerrero, *Reduction of the calcium leaching rate of cement paste by addition of silica nanoparticles.* Cement and Concrete Research, 2008. **38**(8-9): p. 1112-1118.

98. Taylor, H.F.W., C. Famy, and K.L. Scrivener, *Delayed ettringite formation.* Cement and Concrete Research, 2001. **31**(5): p. 683-693.

99. Moore, A. and H.F.W. Taylor, *Crystal structure of ettringite.* Nature, 1968. **218**(5146): p. 1048-&.

100. Hartman, M.R. and R. Berliner, *Investigation of the structure of ettringite by time-of-flight neutron powder diffraction techniques.* Cement and Concrete Research, 2006. **36**(2): p. 364-370.

101. Allmann, R., *Refinement of the hybrid layer structure $[Ca_2Al(OH)_6]^+ \cdot [1/2\ SO_4 \cdot 3H_2O]^-$.* Neues Jahrbuch fur Mineralogie Monatshefte, 1977. **4**: p. 136-144.

102. *Concrete Modelling*. in *Concrete Modelling, ConMod'08*. 2008. Delft, The Netherlands: RILEM publications.

103. Kamali, S., B. Gerard, and M. Moranville, *Modelling the leaching kinetics of cement-based materials - influence of materials and environment.* Cement & Concrete Composites, 2003. **25**(4-5): p. 451-458.

104. Sanahuja, J., L. Dormieux, and G. Chanvillard, *Modelling elasticity of a hydrating cement paste.* Cement and Concrete Research, 2007. **37**: p. 1427-1439.

105. Moranville, M., S. Kamali, and E. Guillon, *Physicochemical equilibria of cement-based materials in aggressive environments - experiment and modeling.* Cement and Concrete Research, 2004. **34**(9): p. 1569-1578.

106. Haecker, C., et al., *Modeling the linear elastic properties of Portland cement paste.* Cement and Concrete Research, 2005. **35**(10): p. 1948-1960.

107. Roussel, N., et al., *Computational modeling of concrete flow: General overview.* Cement and Concrete Research, 2007. **37**: p. 1298-1307.

108. Wittmann, F.H. *Properties of hardened cement paste*. in *7th International Conference on the Chemistry of Cement*. 1980. Paris.

109. van Breugel, K., *Modelling of cement-based systems-the alchemy of cement chemistry.* Cement and Concrete Research, 2004. **34**(9): p. 1661-1668.

110. Bentz, D.P., *Three-dimensional computer simulation of Portland cement hydration and microstructure development.* Journal of the American Ceramic Society, 1997. **80**(1): p. 3-21.

111. Meakawa, K., R. Chaube, and T. Kishi, *Modeling of Concrete Performance - Hydration, Microstructure Formation and Mass Transport.*, in *E&FN SPON*. 1999: London.

112. Van Breugel, K., *Numerical simulation of hydration and microstructural development in hardening cement-based materials.* Cement and Concrete Research, 1995. **25**(2): p. 319-331.

113. Guang, Y., K. van Breugel, and A.L.A. Fraaij, *Three-dimensional microstructure analysis of numerically simulated cementitious materials.* cement and Concrete Research, 2003. **33**(2): p. 215-222.

114. Bullard, J.W., *A determination of hydration mechanisms for tricalcium silicate using a kinetic cellular automaton model.* Journal of the American Ceramic Society, 2008. **91**(7): p. 2088-2097.

115. Pellenq, R.J.M., J.M. Caillol, and A. Delville, *Electrostatic attraction between two charged surfaces: A (N,V,T) Monte Carlo simulation.* Journal of Physical Chemistry B, 1997. **101**(42): p. 8584-8594.

116. Delville, A. and R.J.M. Pellenq, *Electrostatic attraction and/or repulsion between charged colloids.* molecular Simulation, 2000. **24**: p. 1-24.

117. Pellenq, R.J.M., N. Lequeux, and H. van Damme, *Engineering the bonding scheme in C-S-H: The iono-covalent framework.* Cement and Concrete Research, 2008. **38**: p. 159-174.

118. Hamid, S.A., *The crystal structure of 11 A natural tobermorite* $Ca_{2.25}[Si_3O_{7.5}(OH)_{1.5}]\cdot 1\ H_2O$. Zeitschrift Fur Kristallographie, 1891. **154**: p. 189-198.

119. Gmira, A., et al., *Microscopic physical basis of the poromechanical behavior of cement-based materials.* Materials and Structures, 2004. **37**(265): p. 3-14.

120. Faucon, P., J.M. Delaye, and J. Virlet, *Molecular dynamics simulation of the structure of calcium silicate hydrates .1.* $Ca_{(4+x)}\ Si_6O_{(14+2x)}\ (OH)_{(4-2x)}\ (H2O)_2$ *(0<=x<=1).* Journal of Solid State Chemistry, 1996. **127**(1): p. 92-97.

121. Faucon, P., et al., *Study of the structural properties of the C-S-H(I) by molecular dynamics simulation.* Cement and Concrete Research, 1997. **27**(10): p. 1581-1590.

122. Dolado, J.S., M. Griebel, and J. Hamaekers, *A molecular dynamic study of cementitious calcium silicate hydrate (C-S-H) gels.* Journal of the American Ceramic Society, 2007. **90**: p. 3938-3942.

123. Kalinichev, A.G. and R.J. Kirkpatrick, *Molecular dynamics modeling of chloride binding to the surfaces of calcium hydroxide, hydrated calcium aluminate, and calcium silicate phases.* Chemistry of Materials, 2002. **14**(8): p. 3539-3549.

124. Cygan, R.T., J.J. Liang, and A.G. Kalinichev, *Molecular models of hydroxide, oxyhydroxide, and clay phases and the development of a general force field.* Journal of Physical Chemistry B, 2004. **108**(4): p. 1255-1266.

125. Kirkpatrick, R.J., A.G. Kalinichev, and J. Wang, *Molecular dynamics modelling of hydrated mineral interlayers and surfaces: structure and dynamics.* Mineralogical Magazine, 2005. **69**(3): p. 289-308.

126. Kalinichev, A.G., J.W. Wang, and R.J. Kirkpatrick, *Molecular dynamics modeling of the structure, dynamics and energetics of mineral-water interfaces: Application to cement materials.* Cement and Concrete Research, 2007. **37**: p. 337-347.

127. Korb, J.P., et al., *Comparison of proton field-cycling relaxometry and molecular dynamics simulations for proton-water surface dynamics in cement-based materials.* Cement and Concrete Research, 2007. **37**(3): p. 348-350.

128. Ayuela, A., et al., *Silicate chain formation in the nanostructure of cement-based materials.* Journal of Chemical Physics, 2007. **127**(16): p. 164710.

129. Rahmnan, M.M., S. Nagasaki, and S. Tanaka, *Ab Initio Calculations for the Substitutions of $Al(OH)^{-4}$ and SO_2^{-4} with Si Tetrahedra.* Journal of Nuclear Science and Technology, 2001. **38**(7): p. 533-541.

130. Kashihara, S., et al., *Quantum chemical determination of the Al-substituted site in tobermorite.* Journal of the American Ceramic Society, 1994. **77**(11): p. 3023-3026.

131. Frenkel, D. and B. Smit, *Understanding molecular simulation : from algorithms to applications*. 1996, San Diego: Academic Press. xviii, 444 p.

132. Metropolis, N., et al., *Equations of state calculations by fast computing machines.* Journal of Chemical Physics, 1953. **21**(6): p. 1087-1092.

133. Alder, B.J. and T.E. Wainwright. *Molecular dynamics by electronic computers*. in *International Symposium on Statistical Mechanical Theory of Transport Processes*. 1956. Brussels: Interscience, Wiley.

134. Schrodinger, E., *An undulatory theory of the mechanics of atoms and molecules.* Physical Review, 1926. **28**(6): p. 1049-1070.

135. Levine, I.N., *Quantum chemistry*. 4th ed. 1991, Englewood Cliffs, N.J.: Prentice Hall. x, 629 p.

136. Handy, N.C., J.A. Pople, and I. Shavitt, *Samuel Francis Boys.* Journal of Physical Chemistry, 1996. **100**(15): p. 6007-6016.

137. Leach, A.R., *Molecular modelling : principles and applications*. 2nd ed. 2001, Harlow, England ; New York: Prentice Hall. xxiv, 744 p., [16] p. of plates.

138. Koch, W. and M.C. Holthausen, *A Chemist´s Guide to Density Functional Theory*. 2001, Weinheim, Germany: Wiley-VCH Verlag.

139. Sakurai, J.J. and S.F. Tuan, *Modern quantum mechanics*. Rev. ed. 1994, Reading, Mass.: Addison-Wesley Pub. Co. x, 500 p.

140. Born, M. and R. Oppenheimer, *Zur Quantentheorie der Moleküle (On the Quantum Theory of Molecules).* Annalen der Physik, 1927. **84**: p. 27.

141. Cramer, C.J., *Essentials of computationa chemistry: theories and models*. 2002, Chichester, England.: John Wiley & Sons.

142. Jensen, F., *Introduction to computational chemistry*. 2nd ed. 2007, Chichester, England ; Hoboken, NJ: John Wiley & Sons. xx, 599 p.

143. Roothaan, C.C.J., *New developements in molecular orbital theory.* Reviews of Modern Physics, 1951. **23**(2): p. 69-89.

144. Jensen, F., *Introduction to computational chemistry*. 1999, Chichester ; New York: Wiley. xvi, 429 p.

145. Marques, M.A.L. and E.K.U. Gross, *A primer in Density Functional Theory*. Lecture Notes in Physics, ed. C. Fiolhais, M. M.A.L, and Nogueira. 2003, Berlin: Springer-Verlag.

146. Parr, R.G. and W. Yang, *Density-functional theory of atoms and molecules*. International series of monographs on chemistry. 1989, Oxford [England], : Oxford University Press. ix, 333 p.

147. Hohenberg, P. and W. Kohn, *Inhomogeneous electron gas.* Physical Review B, 1964. **136**(3B): p. B864-&.

148. Kohn, W. and L.J. Sham, *Self-consistent equations including exchange and correlation effects.* Physical Review, 1965. **140**(4A): p. 1133-&.

149. Martin, R.M., *Electronic Structure, basic theory and practical methods*. 2004, Cambridge: Cambridge University Press.

150. Ashcroft, N.W. and N.D. Mermin, *Solid State Physics*. 1976, United States: Harcourt College Publishers.

151. Gale, J.D., *GULP: A computer program for the symmetry-adapted simulation of solids.* Journal of the Chemical Society-Faraday Transactions, 1997. **93**(4): p. 629-637.

152. Ewald, P.P., *The calculation of optical and electrostatic grid potential.* Annalen Der Physik, 1921. **64**(3): p. 253-287.

153. London, F., *Some characteristics and uses of molecular force.* Zeitschrift Fur Physikalische Chemie-Abteilung B-Chemie Der Elementarprozesse Aufbau Der Materie, 1930. **11**(2/3): p. 222-251.

154. Dove, M.T., *Structure and dynamics : an atomic view of materials*. Oxford master series in condensed matter physics. 2003, Oxford ; New York: Oxford University Press. xxii, 334 p.

155. Archer, T.D., et al., *An interatomic potential model for carbonates allowing for polarization effects.* Physics and Chemistry of Minerals, 2003. **30**(7): p. 416-424.

156. Elstner, M., et al., *Hydrogen bonding and stacking interactions of nucleic acid base pairs: A density-functional-theory based treatment.* Journal of Chemical Physics, 2001. **114**(12): p. 5149-5155.

157. Rapaport, D.C., *The art of molecular dynamics simulation*. 1995, Cambridge ; New York: Cambridge University Press. xiv, 400 p.

158. Car, R. and M. Parrinello, *Unified Approach for Molecular Dynamics and Density-Functional Theory.* Physical Review Letters, 1985. **55**(22): p. 2471-2474.

159. Verlet, L., *Computer experiments on classical fluids. I. Thermodynamical properties of lennard-jones molecules.* Physical Review, 1967. **159**(1): p. 98-&.

160. Hoover, W.G., *Molecular dynamics*. Lecture notes in physics ;. 1986, Berlin ; New York: Springer-Verlag. vi, 138 p.

161. *Computational Molecular Dynamics: Challenges, methods, ideas*. in *2nd International Symposium on Algorithms for Macomolecular Modelling*. 1997. Berlin: Springer-Verlag.

162. Andersen, H.C., *Molecular Dynamics simulation at constant pressure and/or temperature.* Journal of Chemical Physics, 1980. **72**(4): p. 2384-2393.

163. Nose, S., *A molecular dynamics method for simulations in the canonical ensemble.* Molecular Physics, 1984. **52**(2): p. 255-268.

164. Hoover, W.G., *Canonical dynamics: equilibrium phase space distributions.* Physical Review A, 1985. **31**(3): p. 1695-1697.

165. Hoover, W.G., *Constant-pressure equations of motion.* Physical Review A, 1986. **34**(3): p. 2499-2500.

166. Labbez, C., et al., *Surface charge density and electrokinetic potential of highly charged minerals: Experiments and Monte Carlo simulations on calcium silicate hydrate.* Journal of Physical Chemistry B, 2006. **110**(18): p. 9219-9230.

167. Mulliken, R.S., *Electronic Population Analysis on LCAO-MO Molecular Wave Functions I.* Journal of Chemical Physics, 1955. **23**(10): p. 1833-1840.

168. Gordon, M.S. and M.W. Schmidt, *Recent advances in QM and QM/MM methods.* Computational Science - Iccs 2003, Pt Iv, Proceedings, 2003. **2660**: p. 75-83.

169. Schmidt, M.W., et al., *General atomic and molecular electronic structure system.* Journal of Computational Chemistry, 1993. **14**(11): p. 1347-1363.

170. Dunning, T.H. and P.J. Hay, *Gaussian basis sets for molecular calculations.* Modern Theoretical Chemistry, ed. H.F. Schaefer. Vol. 3. 1977, New York:

Plenum Press. 1-28.

171. Frisch, M.J., et al., *Gaussian 03*. 2003, Gaussian Inc.: Pittsburgh.

172. Parr, R.G. and W.T. Yang, *Density functional approach to the frontier electron theory of chemical reactivity.* Journal of the American Chemical Society, 1984. **106**(14): p. 4049-4050.

173. Breneman, C.M. and K.B. Wiberg, *Determiningatom-centered monopoles from molecular electrostatic potentials. The need for high sampling density in formamide conformational analysis.* Journal of Computational Chemistry, 1990. **11**(3): p. 361-373.

174. Becke, A.D., 5648 (1993). *Density-functional thermochemistry III. The role of exact exchange.* Journal of Chemical Physics, 1993. **98**.

175. Ditchfield, R., W.J. Hehre, and J.A. Pople, *Self-Consistent Molecular-Orbital methods IX. An extended Gaussian-Type basis set for Molecular-Orbital studies of organic molecules.* Journal of Chemical Physics, 1971. **54**(2): p. 724-728.

176. Hehre, W.J., R. Ditchfield, and J.A. Pople, *Self-Consistent molecular orbital methods XII, further extensions of gaussian type basis sets for use in molecular orbital studies of organic molecules.* Journal of Chemical Physics, 1972. **56**(5): p. 2259-2261.

177. Thomas, J.J. and H.M. Jennings, *A colloidal interpretation of chemical aging of the C-S-H gel and its effects on the properties of cement paste.* Cement and Concrete Research, 2006. **36**(1): p. 30-38.

178. Alizadeh, R., J.J. Beaudoin, and L. Raki, *C-S-H (I)-A nanostructural model for the removal of water from hydrated cement paste?* Journal of the American Ceramic Society, 2007. **90**(2): p. 670-672.

179. Allen, A.J., J.J. Thomas, and H.M. Jennings, *Composition and density of nanoscale calcium-silicate-hydrate in cement.* Nature Materials, 2007. **6**(4): p. 311-316.

180. Richardson, I.G., et al., *Location of aluminium in substituted calcium silicate hydrate (C-S-H) gels as determined by Si-29 and Al-27 NMR and EELS.* Journal of the American Ceramic Society, 1993. **76**(9): p. 2285-2288.

181. Copeland, L.E., et al., *Reactions of tobermorite gel with aluminates, ferrites , and sulphates.* J. Res. Dev. Lab., Portland cement Assoc., 1967. **9**: p. 61-74.

182. Sun, G.K., J.F. Young, and R.J. Kirkpatrick, *The role of Al in C-S-H: NMR, XRD, and compositional results for precipitated samples.* Cement and Concrete Research, 2006. **36**(1): p. 18-29.

183. Komarmeni, S. and M. Tsuji, *Selective cation exchange in substituted tobermorite.* Journal of the American Ceramic Society, 1989. **72**: p. 1668-1674.

184. Tsuji, M., S. Komarmeni, and P. Malla, *Substituted tobermorites: ^{27}Al and ^{29}Si MAS NMR, cation exchange, and water sorption studies.* Journal of the American Ceramic Society, 1991. **74**: p. 274-279.

185. Palomo, A., M.W. Grutzeck, and M.T. Blanco, *Alkali-activated fly ashes - A*

cement for the future. Cement and Concrete Research, 1999. **29**(8): p. 1323-1329.

186. Colombet, P., et al. *Nuclear Magnetic Resonance Spectroscopy of Cement-Based Materials*. in *Nuclear Magnetic Resonance Spectroscopy of Cement-Based Materials*. 1998. Bergamo (Italy): Springer-Verlag.

187. Komarmeni, S., et al., *^{27}Al and ^{29}Si magic angle spinning nuclear magnetic resonance spectroscopy of Al-substituted tobermorites.* Journal of Materials Science, 1985. **20**: p. 4209-4214.

188. Stade, H. and D. Müller, *On the coordination of Al in ill-crystallized C–S–H phases formed by hydration of tricalcium silicate and by precipitation reactions at ambient temperature.* Cement and Concrete Research, 1987. **17**: p. 553-561.

189. Skibsted, J., H.J. Jakobsen, and C. Hall, *Direct observation of aluminum guest ions in the silicate phases of cement minerals by ^{27}Al MAS NMR spectroscopy.* Journal of the Chemical Society-Faraday Transactions, 1994. **90**: p. 2095-2098.

190. Andersen, M.D., H.J. Jakobsen, and J. Skibsted, *Incorporation of aluminum in the calcium silicate hydrate (C-S-H) of hydrated Portland cements: A high-field Al-27 and Si-29 MAS NMR Investigation.* Inorganic Chemistry, 2003. **42**(7): p. 2280-2287.

191. Andersen, M.D., H.J. Jakobsen, and J. Skibsted, *Characterization of white Portland cement hydration and the C-S-H structure in the presence of sodium aluminate by Al-27 and Si-29 MAS NMR spectroscopy.* Cement and Concrete Research, 2004. **34**(5): p. 857-868.

192. Andersen, M.D., H.J. Jakobsen, and J. Skibsted, *A new aluminium-hydrate species in hydrated Portland cements characterized by Al-27 and Si-29 MAS NMR spectroscopy.* Cement and Concrete Research, 2006. **36**(1): p. 3-17.

193. Brydson, R., et al., *Parallel electron energy loss spectroscopy study of Al-substituted calcium silicate hydrate (C–S–H) phases present in hardened cement pastes.* Solid State Communications, 1993. **88**: p. 183-187.

194. Schneider, J., M.A. Cincotto, and H. Panepucci, *Si-29 and Al-27 high-resolution NMR characterization of calcium silicate hydrate phases in activated blast-furnace slag pastes.* Cement and Concrete Research, 2001. **31**(7): p. 993-1001.

195. Faucon, P., et al., *Triple-quantum two-dimensional Al-27 magic angle nuclear magnetic resonance study of the aluminum incorporation in calcium silicate hydrates.* Journal of the American Chemical Society, 1998. **120**(46): p. 12075-12082.

196. Faucon, P., et al. *^{27}Al MAS NMR study on cement paste degradation by water*. in *Nuclear Magnetic Resonance Spectroscopy of Cement-Based Materials*. 1998. Bergamo (Italy): Springer-Verlag.

197. Faucon, P., et al., *Characterization of calcium aluminate hydrates and related hydrates of cement pastes by Al-27 MQ-MAS NMR.* Inorganic Chemistry, 1998. **37**(15): p. 3726-3733.

198. Faucon, P., et al., *Silicon substitution for aluminum in calcium silicate hydrates.*

Journal of the American Ceramic Society, 1999. **82**: p. 1307-1312.

199. Faucon, P., et al., *Aluminum incorporation in calcium silicate hydrates (C –S–H) depending on their Ca/Si ratio.* Journal of Physical Chemistry B, 1999. **103**: p. 7796-7802.

200. Lognot, I., I. Klur, and A. Nonat. *NMR and infrared spectroscopies of C-S-H and Al substituted C-S-H synthesized in alkaline solution*. in *Nuclear Magnetic Resonance Spectroscopy of Cement-Based Materials*. 1998. Bergamo (Italy): Springer-Verlag.

201. Soler, J.M., et al., *The SIESTA method for ab initio order-N materials simulation.* Journal of Physics-Condensed Matter, 2002. **14**: p. 2745-2779.

202. Perdew, J.P., K. Burke, and M. Ernzerhof, *Generalized gradient approximation made simple.* Physical Review Letters, 1996. **77**(18): p. 3865-3868.

203. Troullier, N. and J.L. Martins, *Efficient pseudopotentials for plane-wave calculations.* Physical Review B, 1991. **43**: p. 1993-2006.

204. Griebel, M., S. Knapek, and G. Zumbusch, *Numerical Simulation in Molecular Dynamics*. 2007, Berlin, Heidelberg: Springer.

205. Nose, S. and M.L. Klein, *Constant pressure molecular dynamics for molecular systems.* Molecular Physics, 1983. **50**(5): p. 1055-1076.

206. Refson, K., *Molecular dynamics simulation of solid n-butane.* Physica B-Condensed Matter, 1985. **131**: p. 256-266.

207. Beeman, D., *Some multistep methods for use in molecular dynamics calculations.* Journal of Computational Physics 1976. **20**(2): p. 130-139.

208. Pereira, J.C.G., C.R.A. Catlow, and G.D. Price, *Silica condensation reaction: an ab initio study.* Chemical Communications, 1998(13): p. 1387-1388.

209. Litton, D.A. and S.H. Garofalini, *Atomistic structure of sodium and calcium silicate intergranular films in alumina.* Journal of Materials Research, 1999. **14**(4): p. 1418-1429.

210. Garofalini, S.H. and W.W. Luo, *Molecular dynamics simulations of calcium silicate intergranular films between silicon nitride crystals.* Journal of the American Ceramic Society, 2003. **86**(10): p. 1741-1752.

211. Li, W.Q. and S.H. Garofalini, *Molecular dynamics simulation of lithium diffusion in Li_2O-Al_2O_3-SiO_2 glasses.* Solid State Ionics, 2004. **166**(3-4): p. 365-373.

212. Feuston, B.P. and S.H. Garofalini, *Onset of Polymerization in Silica Sols.* Chemical Physics Letters, 1990. **170**(2-3): p. 264-270.

213. Webb, E.B. and S.H. Garofalini, *Effect of adsoption of EAM metal atoms on the structure of sodium alumino silicate glass surface: a molecular dynamics simulation.* Surface Science, 1994. **319**(3): p. 381-393.

214. Zhang, S.H. and S.H. Garofalini, *Molecular dynamics simulations of the effect of the composition of calcium alumino-silicate intergranular films on alumina grain growth.* Journal of Physical Chemistry B, 2006. **110**(5): p. 2233-2240.

215. Brinker, C.J. and G.W. Scherer, *Sol-Gel science*. 1990, San Diego: Academic Press.

216. Alonso, J.A. and M.J. López, *Growth ability and stability indices of clusters.* Journal of Cluster Science, 2003. **14**: p. 31-47.

217. Ohashi, Y. and L.W. Finger, *Role of octahedral cations in pyroxenoid crystal chemistry. 1. Bustamite, wollastonite and pectolite-schizolite-serandite series.* American Mineralogist, 1978. **63**(3-4): p. 274-288.

218. Merlino, S., *Okenite, $Ca_{10}Si_{18}O_{46}\cdot 18H_2O$ - The first example of a chain and sheet silicate.* American Mineralogist, 1983. **68**(5-6): p. 614-622.

219. Dai, Y.S. and J.E. Post, *Crystal-structure of hillebrandite: a natural analog of calcium silicate hydrate (CSH) phases in Portland-cement.* American Mineralogist, 1995. **80**(7-8): p. 841-844.

220. Gard, J.A. and H.F.W. Taylor, *Foshagite: Composition, unit cell and dehydration.* American Mineralogist, 1958. **43**(1-2): p. 1-15.

221. Cong, X.D. and R.J. Kirkpatrick, *Si-29 and O-17 NMR investigation of the structure of some crystalline calcium silicate hydrates.* Advanced Cement Based Materials, 1996. **3**(3-4): p. 133-143.

222. Velez, K., et al., *Determination by nanoindentation of elastic modulus and hardness of pure constituents of Portland cement clinker.* Cement and Concrete Research, 2001. **31**(4): p. 555-561.

223. Acker, P., *Micromechanical analysis of creep and shrinkage mechanisms*, in *Creep, shrinkage and durability mechanics of concrete and other quasi-brittle materials*, F.-J. Ulm, Z.P. Bazant, and W. F.H., Editors. 2001, Elsevier Science.

224. Monteiro, P.J.M. and C.T. Chang, *The elastic moduli of calcium hydroxide.* Cement and Concrete Research, 1995. **25**(8): p. 1605-1609.

225. Holuj, F., M. Drozdowski, and M. Czajkowski, *Brillouin spectrum of $Ca(OH)_2$.* Solid State Communications, 1985. **56**(12): p. 1019- 1021.

226. Meade, C. and R. Jeanloz, *Static compression of $Ca(OH)_2$ at room temperature: observation of amorphization and equation of state measurements to 10.7 GPa.* Geophysical Research Letters, 1990. **17**(8): p. 1157-1160.

227. Reuss, A., *Account of the liquid limit of mixed crystals on the basis of the plasticity condition for single crystal.* Zeitschrift Fur Angewandte Mathematik Und Mechanik, 1929. **9**: p. 49-58.

228. Voigt, W., *Über die Beziehung zwischen den beiden. Elastizitätskonstanten isotroper Körper.* Wiedemanns Annalen der Physik und Chemie, 1889. **38**: p. 573-587.

229. Hashin, Z. and P.J.M. Monteiro, *An inverse method to determine the elastic properties of the interphase between the aggregate and the cement paste.* Cement and Concrete Research, 2002. **32**(8): p. 1291-1300.

230. Hill, R., *The elastic behaviour of a crystalline aggregate.* Proceedings of the Physical Society of London Section A, 1952. **65**(389): p. 349-355.

231. Landau, L.D. and E.M. Lifshitz, *Theory of elasticity*. Second ed. Course of Theoretical Physics. Vol. 7. 1970, Oxford: Pergamon Press.

232. Beaudoin, J.J., *Comparison of mechanical properties of compacted calcium hydroxide and portland cement pastes systems.* Cement and Concrete Research, 1983. **13**(3): p. 319-324.

233. Wittmann, F.H., *Estimation of the modulus of elasticity of Calcium Hydroxide.* Cement and Concrete Research, 1986. **16**(6): p. 971-972.

234. Laugesen, J.L., *Density functional calculations of elastic properties of portlandite, $Ca(OH)_2$.* Cement and Concrete Research, 2005. **35**(2): p. 199-202.

235. Zohdi, T.I., P.J.M. Monteiro, and V. Lamour, *Extraction of elastic moduli from granular compacts.* International Journal of Fracture, 2002. **115**(3): p. L49-L54.

236. Speziale, S., et al., *Single-crystal elastic constants of natural ettringite.* Cement and Concrete Research, 2008. **38**(7): p. 885-889.

237. Ulm, F.J., G. Constantinides, and F.H. Heukamp, *Is concrete a poromechanics material? - A multiscale investigation of poroelastic properties.* Materials and Structures, 2004. **37**(265): p. 43-58.

238. Plassard, C., et al., *Investigation of the surface structure and elastic properties of calcium silicate hydrates at the nanoscale.* Ultramicroscopy, 2004. **100**(3-4): p. 331-338.

239. Gale, J.D. and A.L. Rohl, *The General Utility Lattice Program (GULP).* Molecular Simulation, 2003. **29**(5): p. 291-341.

240. Shannon, D.F., *Conditioning of Quasi-Newton Methods for Functional Minimizations.* Mathematics of computation, 1970. **24**: p. 647-656.

241. Schroder, K.P., et al., *Bridging hydroxyl groups in zeolitic catalysts: a computer simulation of their structure, vibrational properties and acidity in protonated faujasites (HY zeolites).* Chemical Physics Letters, 1992. **188**(3-4): p. 320-325.

242. Du, Z.M. and N.H. de Leeuw, *A combined density functional theory and interatomic potential-based simulation study of the hydration of nano-particulate silicate surfaces.* Surface Science, 2004. **554**(2-3): p. 193-210.

243. Gale, J.D. and N.J. Henson, *Derivation of interatomic potentials for microporous aluminophosphates from the structure and properties of berlinite.* Journal of the Chemical Society-Faraday Transactions, 1994. **90**: p. 3175-3179.

244. Higgins, F.M., N.H. de Leeuw, and S.C. Parker, *Modelling the effect of water on cation exchange in zeolite A.* Journal of Materials Chemistry, 2002. **12**(1): p. 124-131.

245. de Leeuw, N.H., et al., *Modelling the effect of water on the surface structure and stability of forsterite.* Physics and Chemistry of Minerals, 2000. **27**(5): p. 332-341.

246. de Leeuw, N.H., et al., *Density functional theory calculations of adsorption of water at calcium oxide and calcium fluoride surfaces.* Surface Science, 2000. **452**(1-3): p. 9-19.

247. de Leeuw, N.H., G.W. Watson, and S.C. Parker, *Atomistic simulation of the effect of dissociative adsorption of water on the surface structure and stability of calcium and magnesium oxides.* Journal of Physical Chemistry, 1995. **99**(47): p. 17219-17225.

248. De Leeuw, N.H. and S.C. Parker, *Molecular-dynamics simulation of MgO surfaces in liquid water using a shell-model potential for water.* Physical Review B, 1998. **59**: p. 13901-13908.

249. Zacate, M.O. and R.W. Grimes, *Combined Monte Carlo-energy minimization analysis of Al-Fe disorder in Ca2FeAlO5 brownmillerite.* Philosophical Magazine a-Physics of Condensed Matter Structure Defects and Mechanical Properties, 2000. **80**(4): p. 797-807.

250. Zacate, M.O. and A.R. Grimmer, *Intrinsic defect process in Ca-Al-Fe-O cement-phase compounds.* Journal of Materials Science, 1999. **34**: p. 445-449.

251. Adam, C.D., *Atomistic modelling of the hydration of CaSO4.* Journal of Solid State Chemistry, 2003. **174**(1): p. 141-151.

252. Mumme, W.G., et al., *Rietveld structure refinement, crystal chemistry and calculated powder diffraction data for the polymorphs of dicalcium silicate and related phases.* Neues Jahrbuch für Mineralogie, 1995. **169**: p. 35-68.

253. Colville, A.A. and S. Geller, *Crystal structure of brownmillerite, Ca_2FeAlO_5* Acta Crystallographica Section B-Structural Crystallography and Crystal Chemistry, 1971. **B 27**(DEC15): p. 2311-2312.

254. Pharr, G.M., W.C. Oliver, and F.R. Brotzen, *On the generality of the relationship among contact stiffness, contact area, and elastic modulus during indentation.* Journal of Materials Research, 1992. **7**(3): p. 613-617.

255. Laugesen, J.L. *Density functional calculations of elastic properties of portlandite and foshagite*. in *Nanotechnology in Construction*. 2003. Paisley, Scotland: The Royal Society of Chemistry.

256. Dormieux, L., D. Kondo, and F.J. Ulm, *Microporomechanics*. 2006: John Wiley & Sons.

257. Zaoui, A., *Continuum micromechanics: survey.* Journal of Mechanical Engineering, 2002. **128**: p. 808-816.

258. Kanaun, S.K. and V.M. Levin, *Self-Consistent methods for composites*. Solids mechanics and its applications, ed. G.M.L. Gladwell. Vol. 1. 2008: Springer. 382.

259. Kröner, E., *Statistical continuum mechanics*. 1972: Springer-Verlag.

260. Mori, T. and K. Tanaka, *Average stress in matrix and average elastic energy of materials with misfitting inclusions.* Acta Metallurgica, 1973. **21**(5): p. 571-574.

261. Lager, G.A., T. Armbruster, and J. Faber, *Neutron and X-ray diffraction study of hydrogarnet $Ca_3Al_2(O_4H_4)_3$.* American Mineralogist, 1987. **72**(7-8): p. 756-765.

262. Speziale, S., S.R. Shieh, and T.S. Duffy, *High-pressure elasticity of calcium oxide: a comparison between brioullin spectroscopy and radial X-Ray*

diffraction. Journal of Geophysical Research-Solid Earth, 2006. **111**(B2).

263. Mahadevan, T.S. and S.H. Garofalini, *Dissociative water potential for molecular dynamics simulations.* Journal of Physical Chemistry B, 2007. **111**(30): p. 8919-8927.

264. Mahadevan, T.S. and S.H. Garofalini, *Dissociative chemisorption of water onto silica surfaces and formation of hydronium ions.* Journal of Physical Chemistry C, 2008. **112**: p. 1507-1515.

265. Pommershein, J. and J. Chang, *Kinetics of hydration of tricalcium aluminate in the presence of gypsum.* Cement and Concrete Research, 1988. **18**: p. 911-922.

266. Skalny, J. and M.E. Tandros, *Retardation of tricalcium aluminate hydration by sulphates.* Journal of the American Ceramic Society, 1977. **60**(3-4): p. 174-175.

267. Silva, D.A. and P.J.M. Monteiro, *Early formation of ettringite in tricalcium aluminate-calcium-hydroxide-gypsum dispersions.* Journal of the American Ceramic Society, 2007. **90**(2): p. 614-617.

268. Jupe, A.C., et al., *Fast in situ X-ray diffraction studies of chemical reactions: A synchrotron view of the hydration of tricalcium aluminate.* Physica B-Condensed Matter, 1996. **53**(22): p. R14697-R14700.

269. Peng, C., et al., *Using redundant internal coordinates to optimize equilibrium geometries and transition states.* Journal of Computational Chemistry, 1998. **17**(1): p. 49-56.

270. Garrault-Gauffinet, S. and A. Nonat, *Experimental investigation of calcium silicate hydrate (C-S-H) nucleation.* Journal of Crystal Growth, 1999. **200**(3-4): p. 565-574.

271. Wachtman, J.B., et al., *Elastic constants of synthetic single-crystal corundum at room temperature.* Journal of the American Ceramic Society, 1960. **43**(6): p. 334-334.

272. Fiquet, G., P. Richet, and G. Montagnac, *High-Temperature Thermal expansion of lime,periclase, corundum and spinel.* Physical Chemistry of Minerals, 1999. **27**: p. 103-111.

273. Nye, F., *Physical properties of crystals*. 1985, Oxford: Clarendon.

274. Cárdenas, C., et al., *Theoretical study of the surface reactivity of alkaline earth oxides: local density of states evaluation of the local softness.* Journal of Physical Chemistry, 2008. **128**: p. 034708-034715.

275. Junquera, J., et al., *Numerical atomic orbitals for linear-scaling calculations.* Physical Review B, 2001. **64**(23): p. 235111-235120.

276. Paglia, G., et al., *Determination of the Structure of g-Alumina from Interatomic Potential and FirstPrinciple Calculations – The Requirement of Significant Numbers of Non-Spinel Positions to Achieve an Accurate Structural Model.* Physical Review B, 2005. **71**: p. 224115-1 - 224115-16.

277. Litton, D.A. and S.H. Garofalini, *Modeling of hydrophilic wafer bonding by molecular dynamics simulations.* Journal of Applied Physics, 2001. **89**(11): p.

6013-6023.

278. Smilauer, V. and Z. Bittnar, *Microstructure-based micromechanical prediction of elastic properties in hydrating cement paste.* Cement and Concrete Research, 2006. **36**(9): p. 1708-1718.

279. Bernard, O., F.J. Ulm, and E. Lemarchand, *A multiscale mictomechanics-hydration model for the early-age elastic properties of cement-based materials.* Cement and Concrete Research, 2003. **33**(9): p. 1293-1309.

280. Sanahuja, J., L. Dormieux, and G. Chanvillard, *A reply to the discussion "does C-S-H particle shape matter?" F.-J. Ulm and H. Jennings of the paper "modelling elasticity of a hydrating cement paste", CCR 37 (2007).* Cement and Concrete Research, 2008. **38**(8-9): p. 1130-1134.

281. Ulm, F.J. and H.M. Jennings, *Does C-S-H particle shape matter? A discussion of the paper 'Modelling elasticity of a hydrating cement paste', by Julien Sanahuja, Luc Dormieux and Gilles Chanvillard. CCR 37 (2007) 1427-1439.* Cement and Concrete Research, 2008. **38**(8-9): p. 1126-1129.

282. Schlenker, J.L., G.V. Gibbs, and M.B. Boisen, *Strain tensor components expressed in terms of lattice parameters.* Acta Crystallographica Section A, 1978. **34**(JAN): p. 52-54.

283. Yao, H.Z., L.Z. Ouyang, and W.Y. Ching, *Ab initio calculation of elastic constants of ceramic crystals.* Journal of the American Ceramic Society, 2007. **90**: p. 3194-3204.

284. Gard, J.A. and H.F.W. Taylor, *The crystal structure of foshagite.* Acta Crystallographica Section A, 1960. **13**: p. 785-793.

285. Dai, Y.S. and J.E. Post, *Crystal structure of hillebrandite: a natural analogue of calcium silciate hydrate (CSH) phasesin portland cement.* American Mineralogist, 1995. **80**(7-8): p. 841-844.

286. Alberti, A. and E. Galli, *The structure of nekoite, $Ca_3Si_6O_{15}\cdot 7H_2O$, a new type of sheet silicate.* American Mineralogist, 1980. **65**: p. 1270-1276.

287. Ohashi, Y., *Polysynthetically-twinned structures of enstantite and wollastonite.* Physics and Chemistry of Minerals, 1984. **10**(5): p. 217-229.

288. Hejny, C. and T. Armbruster, *Polytypism in xonotlite $Ca_6Si_6O_{17}(OH)_2$.* Zeitschrift Fur Kristallographie, 2001. **216**(7): p. 396-408.

289. Kuznatsova, T.P., et al., *Refinement of the structure of calcium chondrodite, $Ca_5(SiO_4)_2(OH)_2$.* Soviet Ohysics Crystallography, 1980. **25**: p. 91-92.

290. Taylor, H.F.W., *The crystal structure of kilchoanite, $Ca_6(SiO_4)(Si_3O_{10})$, with some commentis on related phases.* Mineralogical Magazine, 1971. **38**: p. 26-31.

291. Malik, K.M.A. and J.W. Jeffery, *A re-investigation of the structure of afwillite.* Acta Crystallographica Section B-Structural Crystallography and Crystal Chemistry, 1976. **32**(2): p. 475-480.

292. Udagawa, S., et al., *Refinement of the crystal structure of gamma Ca_2SiO_4.* Cement and Concrete Research, 1980. **10**(2): p. 139-144.

293. Safronov, A.N., et al., *The refinement of the crystal structure of the cement phase gamma-C_6S_3H.* Doklady Akademii Nauk SSSR, 1981. **256**: p. 1387-1389.

294. Yammova, N.A., et al., *Crystal structure of jaffeite.* Crystallography reports, 1993. **38**: p. 464-466.

295. Taylor, H.F.W., *The crystal structure of killalaite.* Mineralogical Magazine, 1977. **41**: p. 363-369.

296. Dai, Y.S., G.E. Harlow, and A.R. McGhie, *Poldervaartite, $Ca(Ca_{0.5}Mn_{0.5})(SiO_3(OH))(OH)$, a new acid neosilicate from the the Kalahari manganese field, South Africa: crystal structure and description.* American Mineralogist, 1993. **78**: p. 1082-1087.

297. Wan, C., S. Ghose, and G.V. Gibbs, *Rosenhahnite, $Ca_3Si_3O_8(OH)_2$: crystal structure and the stereichemical configuration of the hydroxylated trisilicate group, $Si_3O_8(OH)_2$.* American Mineralogist, 1977. **62**: p. 503-512.

298. Ma, Z., et al., *Crystal structure refinement of suolinite and its significance to the cement techniques.* Chinese Science Bulletin, 1999. **44**(23): p. 2125-2130.